



M I N D A U G A S J U O D Ė N A S

**S U S P E N D E D A N D
A R R A N G E D A g
N A N O P A R T I C L E S :
S E L F - A S S E M B L Y
A N D R E S O N A N C E S
I N N A N O P H O T O N I C S**

D O C T O R A L D I S S E R T A T I O N

K a u n a s
2 0 2 1

KAUNAS UNIVERSITY OF TECHNOLOGY

MINDAUGAS JUODĖNAS

SUSPENDED AND ARRANGED Ag
NANOPARTICLES: SELF-ASSEMBLY AND
RESONANCES IN NANOPHOTONICS

Doctoral Dissertation
Technological Sciences, Materials Engineering (T 008)

2021, Kaunas

This doctoral dissertation was prepared at Kaunas University of Technology, Institute of Materials Science during the period of 2016–2020. The research was supported by the Research Council of Lithuania (PhD student grants: P-DAP-18-306; P-DAP-19-150; P-DAP-20-249; Projects: “2D nanostructures of noble metal nanoparticles for biosensor applications” (S-LLT-18-2); “Plasmonic properties of silver nanoparticles and self-assembled clusters (PLAS)” (LJB-1/2015)).

Scientific supervisor:

Prof. Habil. Dr. Sigitas TAMULEVIČIUS

(Kaunas University of Technology, Technological Sciences, Materials Engineering – T 008).

Edited by: Brigita Brasienė (Publishing house “Technologija”)

Aurelija Gražina Rukšaitė (Publishing house “Technologija”)

Dissertation Defense Board of Materials Engineering Science Field:

Prof. Habil. Dr. Arvidas GALDIKAS – **chairman** (Kaunas University of Technology, Technological Sciences, Materials Engineering – T 008);

Dr. Mindaugas ANDRULEVIČIUS (Kaunas University of Technology, Technological Sciences, Materials Engineering – T 008);

Prof. Habil. Dr. Vidmantas GULBINAS (Center for Physical Sciences and Technology, Natural Sciences, Chemistry – N 003);

Prof. Habil. Dr. Yogendra Kumar MISHRA (Southern Denmark University, Technological Sciences, Materials Engineering – T 008);

Prof. Habil. Dr. Arūnas RAMANAVIČIUS (Vilnius University, Natural Sciences, Physics – N 002).

The official defense of the dissertation will be held at 11 a.m. on the 22nd of February 2021, at the public meeting of Dissertation Defense Board of Materials Engineering Science Field in the Dissertation Defense Hall at Kaunas University of Technology.

Address: K. Donelaičio St. 73-403, 44249 Kaunas, Lithuania.

Tel. no. (+370) 37 300 042; fax. (+370) 37 324 144; e-mail doktorantura@ktu.lt.

Doctoral dissertation was sent on the 22nd of January 2021.

The doctoral dissertation is available on the internet <http://ktu.edu> and at the library of Kaunas University of Technology (K. Donelaičio St. 20, 44239 Kaunas, Lithuania).

KAUNO TECHNOLOGIJOS UNIVERSITETAS

MINDAUGAS JUODĖNAS

SUSPENDUOTOS IR SURIKIUOTOS Ag
NANODALELĖS: SAVIRANKA IR
REZONANSAI NANOFOTONIKOJE

Daktaro disertacija
Technologijos mokslai, medžiagų inžinerija (T 008)

2021, Kaunas

Disertacija rengta 2016–2020 m. Kauno technologijos universiteto Medžiagų mokslo institute. Mokslinius tyrimus rėmė Lietuvos mokslo taryba (doktorantų skatinimas: P-DAP-18-306; P-DAP-19-150; P-DAP-20-249; projektai: „2D nanostruktūros su metalų nanodalelėmis biojutikliams“ (S-LLT-18-2); „Sidabro nanodalelių ir jų klasterių saviorganizacija ir plazmoninės savybės (PLAS)“ (LJB-1/2015)).

Mokslinis vadovas:

Prof. habil. dr. Sigitas TAMULEVIČIUS

(Kauno technologijos universitetas, technologijos mokslai, medžiagų inžinerija – T 008).

Redagavo: Brigita Brasienė (Leidykla “Technologija”)

Aurelija Gražina Rukšaitė (Leidykla “Technologija”)

Medžiagų inžinerijos mokslo krypties disertacijos gynimo taryba:

Prof. habil. dr. Arvidas GALDIKAS – **pirmininkas** (Kauno technologijos universitetas, technologijos mokslai, medžiagų inžinerija – T 008);

Dr. Mindaugas ANDRULEVIČIUS (Kauno technologijos universitetas, technologijos mokslai, medžiagų inžinerija – T 008);

Prof. habil. dr. Vidmantas GULBINAS (Fizinių ir technologijos mokslų centras, gamtos mokslai, chemija – N 003);

Prof. habil. dr. Yogendra Kumar MISHRA (Pietų Danijos universitetas, technologijos mokslai, medžiagų inžinerija – T 008);

Prof. habil. dr. Arūnas RAMANAVIČIUS (Vilniaus universitetas, gamtos mokslai, fizika – N 002).

Disertacija bus ginama viešame medžiagų inžinerijos mokslo krypties disertacijos gynimo tarybos posėdyje, 2021 m. vasario 22 d. 11 val. Kauno technologijos universiteto disertacijų gynimo salėje.

Adresas: K. Donelaičio g. 73-403, 44249 Kaunas, Lietuva.

Tel. (370) 37 300 042; faks. (370) 37 324 144; el. paštas doktorantura@ktu.lt.

Disertacija išsiųsta 2021 m. sausio 22 d.

Su disertacija galima susipažinti internetinėje svetainėje <http://ktu.edu> ir Kauno technologijos universiteto bibliotekoje (K. Donelaičio g. 20, 44239 Kaunas).

ABSTRACT

Interactions between light and metal nanostructures are mediated by a collective motion of free electrons called surface plasmons. The excitation of plasmonic nanoparticles (NPs) with ultrafast laser pulses can induce optomechanical modes (OMs) that modulate their volume and shape. Moreover, NPs arranged in periodic arrays can generate surface lattice resonances (SLRs) that can be modulated by OMs. Capillary force assisted particle assembly (CAPA) is a method that uses a patterned template to generate large area arrays with single particle precision. This method could benefit from microfluidic add-ons to improve control and scalability.

Efficient mixing and high resistance to chemistry is necessary to introduce a microfluidic device into CAPA. Mixing is difficult at the microliter scale, but passive mixers can exploit obstacles to enforce it. The implementation of a three-port microfluidic mixer in alumina is shown, and femtosecond laser ablation as a fabrication method is demonstrated. The device was optimized using the finite element method (FEM). The experimental investigation agreed well with the simulation results indicating that the device could be utilized in a CAPA setup.

The collective NP resonances (i.e., SLR) are interesting, because the associated electromagnetic field is delocalized throughout the array, enabling applications such as biosensing and nanolasing. The author of the dissertation used CAPA to assemble Ag cuboctahedra into $>1\text{ cm}^2$ hexagonal lattices. UV-vis spectroscopy revealed extinction peaks with Q-factors up to 80. It was explained how the extinction changes with light polarizations and angles of incidence and compared to the models based on the coupled dipole approximation and FEM. The observation of SLRs in a self-assembled system demonstrates that a high level of long-range positional control can be achieved at the single-particle level.

Plasmons serve as an optical handle to study the ultrafast electronic and mechanical dynamics of nanoscale systems. Transient absorbance spectroscopy (TAS) is used to track processes on multiple time scales: from the ultrafast creation of hot carriers to their decay into phonons and the formation of OMs. It has been found that a TiO_2 shell surrounding Ag nanocubes causes no appreciable change in the frequency of the OM, but it was strongly attenuated. Up to $\sim 36\%$ of plasmonic energy was lost to the TiO_2 as hot carriers instead of coupling to the OM. The analysis of both ultrafast decay and characterization of optomechanical modes provides a method to track energy dissipation in hybrid metal-semiconductor nanosystems for plasmon-enhanced energy conversion and chemical fuel generation.

TAS was also used to show how OMs affect the dynamic optical properties of SLRs in Ag nanocube arrays. The author of the dissertation compared the OMs of nanocubes in solution versus in arrays and determined their mechanical quality factors. Two dominant mechanical modes were revealed in simulations and imported into an electromagnetic model to examine how shape affects the dispersion diagram. TAS measurements at normal incidence and high angle are compared to the model and illustrate how in-plane and out-of-plane coupling affects OMs and thereby the SLR. The observations demonstrate the effect of ultrafast processes on the photonic length scale, which should be considered in the design of SLR-based devices.

PUBLICATIONS

Article 1 (A1)

M. Juodėnas, T. Tamulevičius, O. Ulčinas, S. Tamulevičius

Implementation of an Optimized Microfluidic Mixer in Alumina Employing Femtosecond Laser Ablation

Journal of Micromechanics and Microengineering, **28**(1), 2018, no. 015013

DOI: 10.1088/1361-6439/aa84fc

Article 2 (A2)

M. Juodėnas, T. Tamulevičius, J. Henzie,
D. Erts, S. Tamulevičius

Surface Lattice Resonances in Self-Assembled Arrays of Monodisperse Ag Cuboctahedra

ACS Nano, **13**(8), 2019, pp. 9038–9047

DOI: 10.1021/acsnano.9b03191

Article 3 (A3)

D. Peckus, H. Rong, L. Stankevičius, M. Juodėnas, S. Tamulevičius,
T. Tamulevičius, J. Henzie

Hot Electron Emission Can Lead to Damping of Optomechanical Modes in Core-Shell Ag@TiO₂ Nanocubes

The Journal of Physical Chemistry C, **121**(43), 2017, pp. 24159–24167

DOI: 10.1021/acs.jpcc.7b06667

Article 4 (A4)

M. Juodėnas, D. Peckus, T. Tamulevičius, Y. Yamauchi,
S. Tamulevičius, J. Henzie

Effect of Ag Nanocube Optomechanical Modes on Plasmonic Surface Lattice Resonances

ACS Photonics, **7**(11), 2020, pp. 3130–3140

DOI: 10.1021/acsp Photonics.0c01187

TABLE OF CONTENTS

Abstract	5
Publications	6
Table of contents	7
List of figures	9
List of symbols and abbreviations	10
1. Introduction	11
1.1. Aim of the research.....	12
1.2. Objectives of the research.....	12
1.3. Scientific novelty	12
1.4. Key statements.....	13
1.5. Structure of the dissertation.....	13
1.6. Author's contribution.....	14
2. Literature review	15
2.1. Nanotechnology and plasmonics	15
2.2. Nanoparticles and self-assembly	15
2.2.1. Nanoparticle plasmonics	15
2.2.2. Nanoparticle self-assembly	16
2.2.3. Capillary force-assisted particle assembly	16
2.2.4. Microfluidic mixing for self-assembly	17
2.3. Surface lattice resonance	17
2.3.1. The collective resonance	17
2.3.2. Producing the SLR	18
2.4. Nanostructure optomechanics.....	18
2.4.1. Optomechanical coupling.....	18
2.4.2. Probing ultrafast dynamics	19
2.4.3. Single particle optomechanics.....	19
2.4.4. Ultrafast influence on plasmonic-photonic modes	20
3. Methods and materials.....	21
3.1. Nanoparticle synthesis.....	21
3.1.1. Ag nanocrystal synthesis	21
3.1.2. Coating of Ag nanoparticles with TiO ₂	21
3.2. Self-assembly template nanofabrication.....	21
3.2.1. E-beam lithography	21
3.2.2. Reactive ion etching	21
3.2.3. Soft lithography	22
3.3. Capillary force assisted particle assembly	22
3.4. Microfluidic device.....	23
3.4.1. Femtosecond laser ablation	23
3.4.2. Microfluidic setup	23
3.5. SEM, TEM, and optical imaging.....	24
3.6. Optical spectroscopy.....	24
3.6.1. UV-vis spectroscopy	24
3.6.2. Transient absorbance spectroscopy	25

3.7. Modeling.....	25
3.7.1. Finite element method	25
3.7.2. Coupled dipole approximation	26
4. Results and discussion.....	28
4.1. Optimized microfluidic mixer for the CAPA setup.....	28
4.1.1. Tesla valve performance optimization	28
4.1.2. Optimization of laser ablation parameters.....	29
4.1.3. Modeling and fabrication of the final device.....	30
4.1.4. Experimental investigation of the full-scale device.....	31
4.2. Plasmonic particles and self-assembly	32
4.2.1. Nanoparticle synthesis and characterization.....	32
4.2.2. Self-assembly	33
4.3. Surface lattice resonance in nanoparticle assemblies	35
4.3.1. Hexagonal lattice of cuboctahedra: Experimental.....	35
4.3.2. Hexagonal lattice of cuboctahedra: Modeling.....	37
4.3.3. Square lattice of nanocubes: Experimental	40
4.3.4. Square lattice of nanocubes: Modeling	42
4.4. Optomechanics of single and arranged nanoparticles.....	44
4.4.1. The mechanical modes of nanocubes	44
4.4.2. Ensemble Ag and Ag@TiO ₂ nanoparticle optomechanics.....	45
4.4.3. TAS measurements of Ag nanocubes in solution versus in arrays...	49
4.4.4. Influence of optomechanical modes on SLRs	51
5. Conclusions	54
6. Acknowledgements	57
7. References	58
8. Santrauka.....	69
8.1. Įvadas.....	69
8.1.1. Tikslas	70
8.1.2. Uždaviniai.....	70
8.1.3. Naujumas.....	70
8.2. Metodika.....	71
8.3. Rezultatai	71
8.3.1. Optimizuotas mikroskystinis įrenginys nanodalelių savirankai	71
8.3.2. Plazmoninės nanodalelės ir jų saviranka	72
8.3.3. Paviršiaus gardelės rezonansas nanodalelių masyvuose.....	72
8.3.4. Suspenduotų ir surikiuotų nanodalelių optomechanika.....	74
8.4. Išvados.....	76
Curriculum vitae.....	81
List of publications	83
Base article copies	86

LIST OF FIGURES

Figure 1. A path through the dissertation	12
Figure 2. Photograph and schematic depiction of capillary force assisted particle deposition setup.	22
Figure 3. Layout of the modeled structures and varied parameters.....	23
Figure 4. Microfluidic experimental setup and method.....	24
Figure 5. Results of the microfluidic mixer optimization.....	28
Figure 6. Laser ablation processing results with respect to the used parameters	29
Figure 7. Final micromachined microfluidic device.....	30
Figure 8. Experimental investigation of the microfluidic device	31
Figure 9. Overview of Ag nanocubes and their core-shell derivatives.....	32
Figure 10. Ag cuboctahedra used in the experiment	33
Figure 11. Ag cuboctahedra assembly.....	34
Figure 12. Ag nanocube self-assembly and their optical properties.....	35
Figure 13. Experimental investigation of angular dependencies	36
Figure 14. Analytical and numerical computations of orthogonal excitation.....	38
Figure 15. Numerical computations of off-normal excitation	39
Figure 16. Energy dispersion diagrams of the self-assembled nanocube arrays	41
Figure 17. FEM modeled nanocubes and their arrays	43
Figure 18. Frequency domain analysis of an Ag nanocube subjected to a uniform initial strain.....	44
Figure 19. Eigenmode analysis of the Ag nanocube	45
Figure 20. π -shifted phases of the tip and face modes of the Ag nanocube	45
Figure 21. Ultrafast absorption properties of Ag and Ag@TiO ₂ nanocubes	46
Figure 22. The investigation of attenuation of OMs.....	48
Figure 23. FEM modeling of Ag@TiO ₂ core-shell assembly coupling	48
Figure 24. Transient absorption measurements exhibit the signature of fundamental optomechanical modes of nanocubes	50
Figure 25. Transient absorption measurements at an angle.....	52
Figure 26. The influence of the isolated eigenmodes on the E - k diagrams	52

LIST OF SYMBOLS AND ABBREVIATIONS

CAPA – capillary force assisted particle assembly
CCP – capacitively coupled plasma
CDA – coupled dipole approximation
D-LSPR – dipolar localized surface plasmon resonance
D-SLR – dipolar surface lattice resonance
DF – dark-field
DMA – dimethyl-amine
DMF – dimethyl-formamide
E-k – energy-momentum space
EM – electromagnetic
FEM – finite element method
FFT – fast Fourier transform
FWHM – full width at half maximum
ICP – inductively coupled plasma
LSP – localized surface plasmon
LSPR – localized surface plasmon resonance
ML – machine learning
MLWA – modified long wavelength approximation
NP – nanoparticle
OM – optomechanical modes
OP – out-of-plane
PDMS – poly-dimethyl-siloxane
PMMA – poly-methyl-methacrylate
PVP – poly-vinyl-pyrrolidone
Q-LSPR – quadrupolar localized surface plasmon resonance
Q-SLR – quadrupolar surface lattice resonance
RA – Rayleigh anomaly
SEM – scanning electron microscopy
SERS – surface enhanced Raman spectroscopy
SLR – surface lattice resonance
TAS – transient absorbance spectroscopy
TBOT – tetra-n-butyl-orthotitanate
TE – transverse electric
TEM – transmission electron microscopy
TM – transverse magnetic
UV-vis – ultraviolet-visible spectroscopy
Yb:KGW – ytterbium doped potassium gadolinium tungstate

1. INTRODUCTION

The field of plasmonics encompasses the interaction of light with metal nanostructures and has generated a lot of interest. Metal nanoparticles can resonate with light if its frequency matches the natural electron plasma oscillation, invoking a localized surface plasmon resonance. This resonance can be modified through hybridization with photonic modes when the nanoparticles are arranged in regular arrays. However, plasmonic structures are not static: they change their shape and optical properties at the ultrafast timescale because of plasmonic heating and thermal expansion. Very short laser pulses can allow observing the processes taking place during the first picoseconds following excitation. Moreover, these ultrafast processes can manifest at the photonic length scale in arranged nanoparticle lattices. This research field has already made great strides but still is young and shows promise in the fields of energy conversion, light emission, biochemistry, cancer treatment, etc.

Standard lithography techniques are usually employed to produce nanoparticle lattices, but template-assisted methods allow using monocrystalline, monodisperse colloidal nanoparticle solutions that can have improved optical qualities. Capillary force assisted particle assembly is one of such methods, but to further expand its applicability, improve its control and ease the upscaling, microfluidic control is necessary. Until now, only simple straight channel microfluidics have been shown, but an optimized mixer in a chemically resistant material, both features required by self-assembly, has not been proposed yet.

Arranged nanoparticles can interact with each other resonantly through photonic Bragg modes. This gives rise to the surface lattice resonance, featuring extreme electromagnetic fields that are delocalized and can extend both in the plane of the array and perpendicular to it. Furthermore, optical extinction spectra can be tuned through the individual nanoparticle and geometric arrangement properties to produce remarkably narrow peaks for applications like nanolasing and biosensing. These features could be achieved using self-assembly of colloidal nanoparticles.

A complex cascade of photophysical processes takes place following excitation of the plasmon resonance. After it dephases, excited electrons rapidly thermalize and create a hot-electron distribution that eventually transfer their energy to phonons, driving the lattice expansion and inducing vibrational modes. These modes change the plasmon resonance at a high frequency. Such modulations can couple with exciting light into optomechanical modes observable in the transient absorbance measurement. A semiconductor shell that is enveloping such a metal nanoparticle could rob it of its hot electrons, which later could be used for catalysis or chemical fuel generation, and this should manifest as a faster decay of optomechanical modes.

The optomechanical modes can also influence the surface lattice resonance. Each nanoparticle in the array, when excited coherently, evolves into a sum of its breathing eigenmodes, following the lattice expansion. This process changes the hybridization condition and shifts the lattice resonance at a gigahertz frequency, providing potential for groundbreaking applications, such as switched lasing. A comparison of nanoparticles in the array vs. in solution can provide insight into the processes taking place at the photonic length scale and ultrafast time scale, while

modeling of nanoparticle shapes can allow predicting the properties of new devices with ultrafast function.

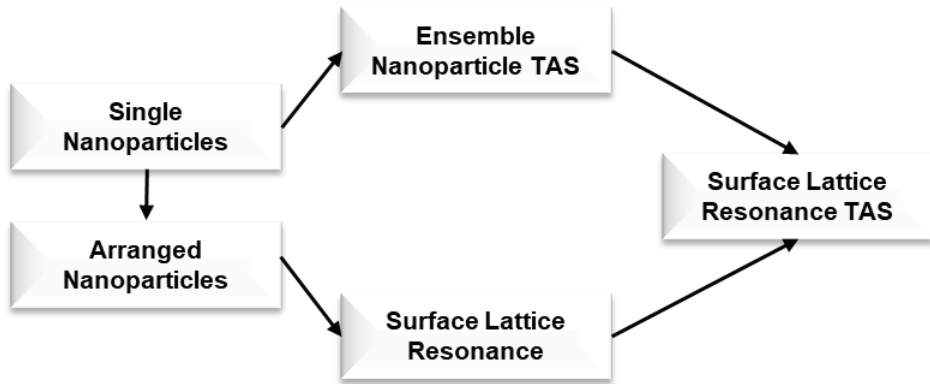


Figure 1. A path through the dissertation: first, a microfluidic improvement for the self-assembly method to go from single to arranged nanoparticles is proposed (published in **A1**); second, a surface lattice resonance is achieved using said self-assembly method (published in **A2**); third, suspended nanoparticles are investigated in the frame of ultrafast optics (published in **A3**); finally, the influence of ultrafast processes on the photonic length scale phenomena is elucidated (published in **A4**)

1.1. Aim of the research

Elucidate the properties of steady-state optical and ultrafast optomechanical resonances of synthesized Ag nanoparticles in a suspended mode in solution and in an arranged mode in self-assembled regular arrays on templates under Bragg coupling condition.

1.2. Objectives of the research

1. Develop a microfluidic add-on device optimized for mixing, applicable for chemically aggressive solvents, and compatible with the capillary force assisted nanoparticle assembly setup.
2. Generate strong surface lattice resonances using a self-assembly technique and synthesized Ag nanoparticles.
3. Investigate steady-state optical and ultrafast optomechanical properties of synthesized Ag nanocubes with a semiconductor shell for nanophotonics.
4. Investigate steady-state optical and ultrafast optomechanical properties of Ag nanoparticle arrays under Bragg coupling condition and compare to free-standing nanoparticle transient absorption.

1.3. Scientific novelty

A novel technique of femtosecond laser micromachining was used to produce a microfluidic add-on for capillary force assisted assembly setup. Alumina was chosen as a material that is highly resistant to aggressive chemical substances, and the finite element method was used to optimize a Tesla valve-based microfluidic mixer.

Capillary force assisted assembly technique was used to produce high quality large area regular arrays of Ag cuboctahedra. It was shown that standard free-space optical techniques can be used to characterize these samples, and strong surface lattice resonances were found. They were characterized in the frame of energy dispersion diagrams, and the coupling to different Bragg modes was explained. The finite element method simulations extend this work and show the electromagnetic field distribution of these modes.

Core-shell Ag@TiO₂ nanocube solutions were produced and investigated using transient absorption spectroscopy. Optomechanical modes are observed in all Ag nanocube solutions, and significant attenuation is measured in core-shell samples. An assumption was made and proven that the energy is lost because of hot-electron transfer to a semiconductor shell.

Transient absorption spectroscopy was employed to extend the self-assembly work with an ultrafast analysis of regular arrays vs. free-standing nanoparticle solutions. Different coupling conditions were explained. Finite element method analysis was used to map mechanical nanocube eigenmodes to the observed optomechanical modes. These eigenshapes were used to model arrays of deformed nanoparticles to show the influence that ultrafast absorption has on the photonic length scale phenomena such as surface lattice resonance.

1.4. Key statements

1. Femtosecond laser ablation can be used to efficiently produce microfluidic structures in alumina.
2. Microfluidic modeling can be used to control the output concentration of a microfluidic device.
3. Capillary force assisted particle assembly can be used to assemble nanoparticles into lattices with single-particle precision.
4. Self-assembled arrays of synthesized nanoparticles can produce high-quality surface lattice resonances.
5. Core-shell Ag@TiO₂ nanoparticles could donate the hot-electrons generated by a dephasing plasmon to a semiconductor shell.
6. Ultrafast optomechanical modes of Ag nanocubes with significant mechanical quality factors modulate the surface lattice resonance at gigahertz frequency.

1.5. Structure of the dissertation

The dissertation is heavily based on the papers published by the author and the co-authors during the doctoral studies. However, the flow of this work does not entirely follow the publications, but rather is grouped by concepts. Overlapping ideas and descriptions have been grouped together, and the results were put under a common heading. Overall, the dissertation follows the research objectives listed above to accomplish the aim of the dissertation. It encompasses 130 pages, 26 figures, and 152 references.

In chapter 1, an introduction to nanoparticle plasmonics is given, followed by self-assembly methods. This leads to the first research objective. A description and overview of the surface lattice resonances lead to the second research objective. A

thorough description of optomechanical modes and their properties leads to the final two objectives. In chapter 2, an overview of the methods used to accomplish the research objectives is given. This includes both technological and analytical equipment as well as modelling. In chapter 3, the results presented in the published papers are provided. The results closely follow the tasks, highlight scientific novelty, and provide the basis for the defense of the key statements. A list of conclusions is given in the final chapter, where the accomplishment of the research objectives is highlighted, and scientific novelty is stressed. This is followed by an acknowledgement and a list of cited references. Next, a summary in Lithuanian is given, which describes the major points of the research and redirects to the figures in the English version to eliminate redundancy. Finally, a *curriculum vitae* and a list of publications by the author is followed by the copies of the published articles.

1.6. Author's contribution

A1: MJ (corresponding author) came up with the idea, assembled the microfluidic experimental setup, carried out the microfluidic experiments, performed the modeling and optical imaging of the device, analyzed the data, prepared the figures, wrote the initial draft, edited, and submitted the final manuscript. TT designed the microfabrication setup, performed SEM imaging, analyzed the data, and edited the manuscript. OU performed the laser ablation experiments and analyzed the data. ST designed the microfabrication setup and edited the manuscript.

A2: MJ (corresponding author) came up with the idea, carried out the self-assembly experiments and optical measurements, performed the modeling, optical and SEM imaging, analyzed the data, prepared the figures, wrote the initial draft, edited, and submitted the final manuscript. TT designed the self-assembly experimental setup and edited the manuscript. JH (corresponding author) performed the nanoparticle synthesis and edited the draft. ST designed the self-assembly experimental setup and edited the draft.

A3: MJ performed the mechanical modeling and edited the manuscript. DP performed the transient absorption measurements. HR performed the nanoparticle synthesis. LS wrote the FFT-based data trace fitting code. ST designed the TAS measurement setup and edited the manuscript. TT (corresponding author) came up with the idea, designed the TAS measurement setup, analyzed the data, prepared the figures (including figures 9, 21, and 22 presented in this dissertation), wrote the initial draft, edited and submitted the final manuscript. JH (corresponding author) came up with the idea, performed optical modeling and TEM imaging, analyzed the data, and edited the manuscript.

A4: MJ (corresponding author) came up with the idea, carried out the self-assembly experiments and steady-state optical measurements, performed the modeling, SEM and optical imaging, analyzed the data, prepared the figures, wrote the initial draft, edited and submitted the final manuscript. DP performed the transient absorption measurements. TT designed the self-assembly and TAS setups and edited the manuscript. ST designed the self-assembly and TAS setups, edited the manuscript. JH (corresponding author) performed the nanoparticle synthesis and edited the draft.

2. LITERATURE REVIEW

2.1. Nanotechnology and plasmonics

The global effort to miniaturize electronics during the last century brought a curious new concept into the scientific world called micro- and later nanotechnology. These fields deal with materials and phenomena at an extremely small scale: from a few microns down to a few atoms thick. A rapid progression in downscaling led to a worldwide breakthrough in micro- and nanodevices as well as new materials.

Eventually, as the material thickness started approaching the optical wavelengths, interesting new phenomena related to metal structures emerged. It was found that the free electron distribution in a metal could sustain surface and volume charge density oscillations following the excitation at optical wavelengths with a distinct resonant response. When considering these oscillations at an interface between the metal and dielectric, strongly enhanced optical near fields were found, which are spatially confined near the metal surface. These charge density fluctuations were called surface plasmons, and the related field plasmonics. Scientists, seeing these properties of plasmonic metals, i.e., gold, silver, aluminum, copper, and others, were quick to speculate that this research will make strides in the fields of biosensing, chemical analysis, light manipulation and generation, and others.

Additional applications emerged with the advance of lithographic and synthetic nanoparticle generation. Similarly to the volume/surface case, if the electron distribution is confined in three dimensions, as in the case of a small particle, the overall displacement of the electrons with respect to the positively charged lattice leads to a restoring force, which in turn gives rise to specific particle-plasmon resonances depending on the geometry of the particle. This led to a branch of the field called nanoparticle plasmonics.

2.2. Nanoparticles and self-assembly

2.2.1. Nanoparticle plasmonics

Metal nanoparticles support collective excitations of free electrons called localized surface plasmons (LSPs) that can couple and focus light down to nanometer length scales.¹⁻⁵ LSPs can be excited by an external electromagnetic (EM) field, leading to strong resonances (LSPRs) when light matches the resonant frequency of the nanostructure. The intensity and spatial distribution of LSPR modes depend sensitively on the size, shape, and the dielectric environment of the nanoparticle.

Nanocubes are interesting in this context because the free-standing cubic shape supports numerous bright plasmon modes,^{6,7} 6 of which constitute 93%⁶ of the total oscillator strength. The lowest energy mode is often called fundamental dipolar mode (D-LSPR), characterized by charge accumulation at the corners and opposite charges residing on the two halves of the cube. Nanocubes support dark plasmon modes, also known as quadrupolar modes (Q-LSPR). These modes possess a net zero dipole moment when the particle is small and therefore cannot interact with the far-field light. When Ag nanocubes come in contact with a surface or are made sufficiently large, hybridization of dipolar (bright) and quadrupolar (dark) LSPR modes is initiated with complex 3D spatial distributions and unusual absorption properties under symmetry-

breaking conditions (e.g., asymmetric dielectric environment, phase retardation).^{8–10} Hybrid modes are interesting because they become interactable from the far-field due to the dipole component but retain a narrow FWHM because of the Fano line shape. Further hybridization can be achieved by arranging nanoparticles into short or long-range order, allowing them to interact through their near-fields to form hot-spots and new hybrid plasmonic modes or through their far-fields, resulting in hybrid plasmonic-photonic modes.

2.2.2. Nanoparticle self-assembly

Researchers have used a variety of methods to generate arrays of single nanocrystals.^{11–13} Standard clean-room lithography procedures are among the most used techniques, but they suffer from high costs and time consumption. Self-assembly using templates is a good route to achieve a sufficient level of control over the position and spacings of NPs, while simultaneously exploiting the advantages of synthesized colloidal nanoparticles. Shaped metal NPs have intrinsically higher single-particle resonance Q -factors ($Q = \lambda/\Delta\lambda$, λ – resonance peak wavelength, $\Delta\lambda$ is its FWHM), because they possess atomically smooth facets and can be monocrystalline. The templates can be generated by replicating patterns in hard materials such as silicon (Si) via soft-lithography using elastomeric polymers, e.g., poly-dimethyl-siloxane (PDMS). This feature helps to limit but not eliminate the need for expensive e-beam lithography steps in the process flow. Assembling NPs on elastomers may have additional advantages in the generation of plasmonic-photonic modes, because stretching/compression can enable dynamic tuning of the interparticle spacing.^{14–16} Such templates have been used to self-assemble arrays of metal and organic NPs¹⁷ with diameters spanning tens of nanometers to microns in 1 cm² scale areas.^{18–20}

2.2.3. Capillary force-assisted particle assembly

Capillary force assisted assembly^{18,21} is a type of template-assisted method that uses convective currents and confining capillary forces at the air/liquid/template interface to selectively deposit NPs inside patterned obstacles (e.g., protrusions or voids) by tailoring the wetting, temperature, and assembly speed conditions in a temperature-controlled single-axis translation setup.²² In the field of plasmonics, CAPA-based methods have been used to generate patterns of NPs for surface enhanced Raman spectroscopy (SERS),²³ anti-counterfeiting security features,²⁴ light upconversion²⁵ etc. In this method, a nanoparticle ink is confined between a glass slide and a patterned template. When these surfaces are translated relative to each other, a meniscus forms at the three-phase interface, which confines nanoparticles in the traps. The dew point and the contact angle are major components contributing to the assembly yield, because sufficient evaporation is necessary to form an accumulation of particles at the meniscus, and the capillary force has to have a sufficient vertical component to confine the particles. These parameters are controlled using a temperature-controlled stage and the surfactant concentration and solvent in the colloid solution. An additional level of control could be achieved using microfluidic devices,^{26–28} but until now, only simple pass-through devices have been proposed with no option for *in-situ* mixing of different solvents and surfactants.

2.2.4. *Microfluidic mixing for self-assembly*

Manipulation of liquids in microfluidics is done at Reynolds numbers ranging from 500 down to 10^{-5} , as dictated by very low flow rates.²⁹ At such Reynolds numbers, the flow regime is completely laminar, making natural mixing of liquids near-impossible, but efficient mixing is essential to implement microfluidic technology for nanoparticle self-assembly. The search for solutions to this problem has attracted a lot of attention.^{30–32}

Several mixing techniques are available. Some involve active, solid components within the channels,^{33,34} others use external fields.^{35–40} These techniques require either a complicated fabrication method or bulky equipment. Another alternative is to use passive structures that manipulate the velocities by splitting and recombining flows to enforce efficient mixing due to velocity gradient.^{41–45}

The use of microfluidics for CAPA of metallic nanoparticles^{23,46} demands materials other than the ones widely used (e.g., PDMS), because the colloid solutions that are based on chloroform, toluene, dimethylformamide, etc. can damage the microfluidic channels by swelling and/or extract the non-crosslinked monomers.⁴⁷ Alumina has exceptional properties like chemical resistance, hardness, electrical insulation, excellent surface flatness and smoothness, strength at high temperatures, and thick film reliability,^{48,49} but it is rather difficult to micromachine.

Over the recent years, direct laser micromachining that is using ultrashort laser pulses has evolved to a point where the quality of structures, range of applicable materials, time consumption and cost are on par or even better than in the conventional methods^{50–53}. Femtosecond laser ablation offers a unique possibility to use a wide array of materials, as it is based on instantaneous evaporation of material, enhancing the current and providing novel applications for microfluidics.

2.3. **Surface lattice resonance**

2.3.1. *The collective resonance*

The extinction peaks of LSPRs are often quite broad due to losses attributed to radiative damping and depolarization; thus, Q -factors greater than 10–20 are seldom observed experimentally.⁵⁴ Decades ago, theorists predicted that the LSPRs^{4,5} of plasmonic nanostructures that are patterned into regular arrays can generate a collective plasmonic response and produce line shapes far sharper than it is possible with single particles. These ideas were initially proposed in theoretical papers of Markel⁵⁵ and Schatz.⁵⁶ They showed that individual NPs in an array could couple diffractively if their LSPRs were within the range of the Rayleigh anomaly (RA). This phenomenon is now commonly called a surface lattice resonance (SLR).^{54,57,58} In these systems, the LSPR⁵⁹ couples to the in-plane diffracted wave (i.e., RA) to generate a new hybrid plasmonic-photonic mode. Under these conditions, each metal NP in the array can experience light scattered by adjacent particles, generating a self-reinforcing collective resonance that creates a narrow dip in the optical transmission spectrum,^{54,58,60} although in some cases, it can enhance transparency.⁶¹

Scientists have used these collective resonances to generate surfaces with very narrow extinction peaks,^{62–66} even supporting Q -factors an order of magnitude larger compared to isolated or disordered nanostructures.⁶⁷ Moreover, these regular arrays

enable relatively easy spectral tunability if one could control parameters such as nanoparticle material, size, spacing, and height.⁵⁴ By changing the lattice parameters in relation to the nanostructures, it is possible to tune this resonant peak across the visible and near infrared spectrum.

2.3.2. *Producing the SLR*

Over time, experimentalists have developed nanofabrication and optical measurement tools to efficiently control these plasmonic-photonic modes with nanoparticle arrays.^{16,60,62,67–69} Researchers can now engineer surfaces supporting SLRs with wide tunability and narrow spectral linewidth for use in novel light-emitting and light-manipulating devices.^{70–74} It appeared in numerous applications in conventional optics,⁷⁵ light emission,^{76,77} protein biosensing,^{78,79} nanolasing,^{80–83} photoluminescence enhancement,⁸⁴ etc. Nevertheless, these are mostly shown on a small scale and often require focusing optics to measure strong resonances. Reproducible results on a large scale using colloidal assembly could allow for additional applications by reducing the cost and time required to produce these devices; however, this has not been demonstrated yet.

Learning how to generate SLRs with arrays of colloidal particles exposed to the environment is especially useful in sensing applications, because the analyte may access EM hotspot and noticeably affect the SLR resonance. Nanoparticle arrays can generate stronger radiative interparticle coupling when the energy associated with the resonance is localized primarily in the superstrate. Thus, arrays composed of taller, high-aspect ratio particles (compared to almost planar vapor-deposited structures) can be considered an acceptable strategy to yield stronger SLRs. Top-down nanofabrication techniques can create tall particles, but masking techniques tend to generate tapered structures whose diameters vary with height.^{68,85} In addition, physical vapor deposition methods generate particles that are highly polycrystalline, which broadens the LSPRs of individual NPs by increasing electron scattering at grain boundaries and lowering the lifetime of the plasmon resonance.⁸⁶ Researchers have used DNA-assisted assembly to generate nanocube arrays. These self-assembled structures can support lattice modes, but the Q-factors are still relatively low compared to the modeled structures.^{12,13} Moreover, SLRs provide insight into the positional control of single-particle assembly with these template-assisted methods.

2.4. **Nanostructure optomechanics**

2.4.1. *Optomechanical coupling*

A mechanical force applied to an optically active system can influence its optical properties and coupling to the electromagnetic fields. However, optical radiation can also influence the mechanical dynamics of the system, e.g., through laser heating or radiation pressure. This kind of coupling of mechanical and optical modes lead to the emerging field of optomechanics.⁸⁷ Plasmonic metal nanoparticles can be a prime example, because they have well-defined elastic mechanical properties as well as being optically active.

Plasmonic resonances serve as a built-in optical “handle” to monitor light-matter interactions in metallic nanosystems.⁸⁸ Light that couples to the LSPR sets off a

complex cascade of relaxation processes, as energy is transferred from the free electron distribution and eventually into lattice vibrations in the metal.⁸⁸ There are numerous routes in this process for energy to dissipate, initially as hot electrons and then as sound and/or heat into the environment. Exploring this process is an essential part in developing high frequency chemical/biological sensors,^{23,89,90} controlling heat dissipation on the nanoscale in thermal devices,⁹¹ improving light absorbance efficiencies in photovoltaics and solar fuel generation.⁹²

These photophysical relaxation processes are still not well understood at neither ensemble, single nanoparticle, nor 2D array level. In particular, the influence of ultrafast processes on the photonic length scale (such as SLR) is still unexplored. The author of the dissertation discusses this concept in 2.4.4. Additionally, hybrid metal/semiconductor systems where the plasmon resonance at least partially overlaps with the band gap of the semiconductor can lead to new applications in nanophotonics.

Explaining the ultrafast transient dynamics of these systems is important to the development of various technologies.⁹³⁻⁹⁵ Plasmon resonances can facilitate hot electron transfer from metal to the semiconductor, effectively circumventing the energy loss mechanisms of the metal and donating that energy to the semiconductor for solar energy conversion or photocatalysis.^{96,97} The ultrafast carrier dynamics occurring at the metal-semiconductor interface should leave some “fingerprint” or “residue” on the slower processes such as optomechanical modes. A comparison of both fast and slow processes should reveal information about the total flow of energy in metal-semiconductor systems.

2.4.2. *Probing ultrafast dynamics*

Transient absorbance spectroscopy (TAS) is one of the most common techniques used to examine the ultrafast electronic dynamics of nanosized systems and has enabled researchers to better understand the properties of individual or isolated metal nanoparticles following the absorption of photons.^{88,98-102} Initial irradiation with the pump pulse excites the LSPR, which after dephasing of the plasmon (~ 20 fs), results in a non-thermal distribution of electrons. These electrons then equilibrate via electron-electron scattering (~ 100 fs), resulting in hot electrons that modify the dielectric constant of the metal¹⁰³ and shift the LSPR resonance. Hot electrons then undergo electron-phonon scattering (~ 1 ps), driving the rise in temperature and lattice expansion,¹⁰⁴ exciting mechanical oscillations. These ultrafast changes in shape, electron density, and deformation potential generate optomechanical modes that modulate the intensity and wavelength of the LSPR at gigahertz frequencies.^{102,105} Finally the mechanical energy couples and dissipates to the environment (~ 1 ns) as the oscillating lattice cools down exponentially.⁸⁸ With a sufficiently short probing pulse, TAS allows to observe these tiny changes in LSPR and indicate the flow of energy over short time scales.

2.4.3. *Single particle optomechanics*

On the individual nanoparticle level, the absorbed energy is transferred from the plasmon to electronic transitions and then to phonons; these phonons raise the lattice temperature and expand the lattice coordinate. When the nanostructure’s vibrational period is longer than the timescale for heating, mechanical modes can be excited

coherently.¹⁰⁶ Cubes have two dominant mechanical modes associated with its corners and faces that appear at different frequencies and modulate the LSPR over time.¹⁰² The optomechanical modes of Ag nanocubes in solution and on surfaces have been studied with TAS.^{88,98,102,107} A detailed examination of optomechanical modes in metals is often performed on single particles, because colloids with narrow size/shape distributions are challenging to synthesize.

In particular, cubic nanoparticles (i.e., nanocubes) are very efficient at converting plasmonic fields into hot carriers.¹⁰⁸ Moreover, the optomechanical modes embody the sum of most, if not all, of the optical energy absorbed by an isolated metal nanoparticle. Thus, a comparison of identical nanoparticles in insulator-like environment versus ones surrounded by a semiconductor shell would allow to observe how much energy is lost to the semiconductor. There have been no comparable TAS investigations of free-standing core-shell nanoparticles where the band gap of the semiconductor shell is near the wavelength of the LSPR resonance.

2.4.4. *Ultrafast influence on plasmonic-photonic modes*

Very little is known about the dynamics of highly ordered plasmonic arrays and how the ultrafast optical response of the nanoparticles affects the hybrid long-range plasmonic-photonic modes of the array. TAS studies demonstrate that plasmonic nanoparticles are not the static structures that are used in computational electromagnetic models. Since the SLR is strongly dependent on the nanoparticle size/shape and its corresponding LSPR,¹⁰⁹ it is hypothesized that the optomechanical modes would affect the plasmonic-photonic properties over time as well. Other researchers have noted that the propagation of optomechanical modes on textured metal films is affected by lattice spacing.¹¹⁰ Researchers in the field of Si-based optomechanical photonic crystals¹¹¹ have experimented with structures that support photonic/plasmonic bandgaps,¹¹² but these rely on high refractive index (n) dielectrics as opposed to a system that is mainly plasmonic and enables stronger light-matter interactions. A comparative study of ultrafast processes between nanoparticles in solution and assembled into regular arrays is difficult, because it necessitates self-assembly; hence, the ultrafast dynamics of synthesized nanoparticle SLR has not been described before.

3. METHODS AND MATERIALS

3.1. Nanoparticle synthesis

3.1.1. Ag nanocrystal synthesis

Monodisperse solutions of Ag nanocubes and cuboctahedra were prepared using a modified procedure based on the Ag polyol synthesis method at the National Institute of Materials Science in Tsukuba, Japan (courtesy of Dr. Joel Henzie and his group).^{113,114} This method generates single-crystal Ag nanoparticles coated with a poly-vinyl-pyrrolidone (PVP; 55,000 MW) surfactant. The average edge length (a) of the cuboctahedra was $122 \text{ nm} \pm 3 \text{ nm}$, and the nanocubes were $a = 39 \pm 3 \text{ nm}$, $77 \pm 3 \text{ nm}$, and $92 \pm 4 \text{ nm}$. The nanoparticles described in **A2** and **A4** were suspended in dimethyl-formamide (DMF) at a concentration of 8.55×10^7 and 3.59×10^{11} p/mL, respectively. The nanoparticles in **A3** were in ethanol. The PVP polymer surfactant also serves as a steric barrier in self-assembly experiments to minimize uncontrolled NP aggregation even at very high concentrations.^{23,60,114}

3.1.2. Coating of Ag nanoparticles with TiO₂

In a typical synthesis to grow the surrounding TiO₂ shell, 2 mL of Ag nanocube seed solution is combined with 50 μL of dimethyl-amine (DMA) in a glass vial sonicated for 5 min and then stirred for 25 min. While the sample was stirring, 5 μL of tetra-*n*-butyl-orthotitanate (TBOT) was combined with 5 mL of ethanol while working in a nitrogen-filled glovebox. This vial of TBOT solution was eventually transferred back into the lab environment (i.e., air), added dropwise to the solution of nanocubes, and stirred for ~ 1 h. The solution was then poured into a Teflon-lined autoclave and heated in an oven at 160°C for 12 h. The Ag@TiO₂ nanocubes were centrifuged and washed with ethanol.

3.2. Self-assembly template nanofabrication

3.2.1. E-beam lithography

The patterns for master stamps were produced using e-beam lithography on a Raith e-Line Plus machine. A 300 nm thick poly-methyl-methacrylate (PMMA) layer was spin coated on a Si(100) wafer. Two exposure approaches were used: one with a metal mask in mind and another with a polymer one. For the former, a dot-based method was used with a 0.05 pC/dot dose. For the latter, a crossed line method was used with a 1000 pC/nm dose. Following exposure, the samples were developed in a 1:3 MIBK:IPA solution at room temperature for 30 s followed by rinsing in IPA and DI. For the dot-based method, this was followed by an e-beam evaporation of 30 nm Al layer and subsequent lift-off in acetone with ultrasonic agitation.

3.2.2. Reactive ion etching

Deep reactive ion etching of the samples was performed using an Apex ICP etcher tool with fluorine-based chemistry. A hybrid polymer C_xF_y inhibitor chemical ion etching approach was used, where both etching and passivating gases are introduced at the same time. The process parameters were as follows: SF₆/C₄F₈ flow rates 50/70 sccm, pressure 20 mT, uncontrolled temperature (varying from room to

$\sim 30^\circ\text{C}$), 1000 W ICP power, and 30 W CCP power, resulting in -110 V bias voltage. This configuration resulted in 80 nm/min etch rate with almost vertical sidewalls.

3.2.3. Soft lithography

Soft lithography was employed to create polymer templates by casting and thermally curing PDMS. Etched stamps were coated with a self-assembled monolayer of perfluoro-octyl-trichloro-silane as an anti-adhesion layer to prevent bonding with the PDMS in subsequent replication cycles. A small droplet containing a 10:1 mixture of polymer base and curing agent (Sylgard 184, Dow-Corning) was put on the stamp and constrained by a thin glass slide; then, the sample was cured at 100°C for 35 minutes. Once the PDMS had fully polymerized, the glass/PDMS pattern could be detached from the master.

3.3. Capillary force assisted particle assembly

PDMS templates patterned with small pits were used to facilitate the assembly of Ag NPs. A custom-built assembly setup (**Figure 2**) was used to generate NP assemblies. Its main components are an optical microscope system (BX51, Olympus), motorized linear precision translator (LS-110, PI Micos), and a temperature control system (TEC-1090, Meerstetter Engineering GmbH).²²

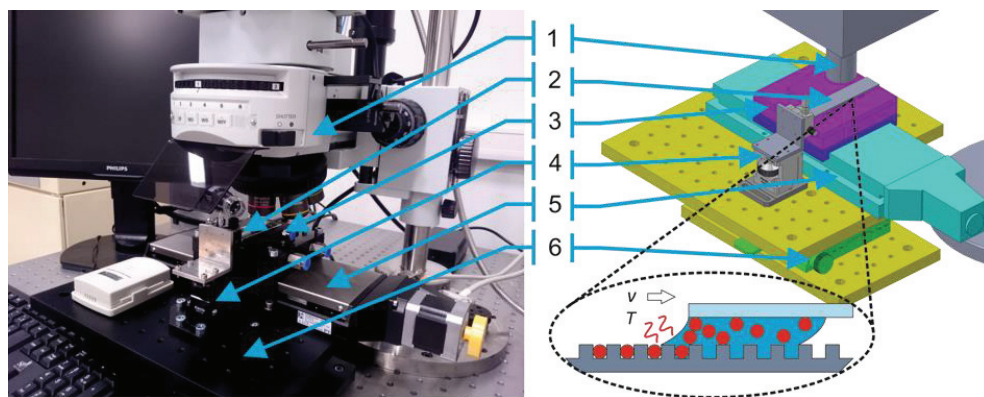


Figure 2. Photograph and schematic depiction of capillary force assisted particle deposition setup. (1) Optical microscope. (2) Glass slide. (3) Controlled temperature sample holder. (4) Height positioner of the glass slide. (5) Motorized precision translator. (6) XY positioning stage. The insert depicts the process of particle deposition, where v denotes the velocity of the translator and T the temperature of the colloidal solution. Reproduced from Virganičius et al.²²

The PDMS pattern was placed on top of the stage, and a 50–100 μL droplet of a concentrated Ag NP colloidal solution (normally $>1 \times 10^{11}$ p/mL) was put on top and confined by a stationary glass slide fixed at a slight inclination, which is used by most doctor-blade patterning methods. DMF was used as the assembly solution, because it is a theta solvent for PVP.²³ The template was then translated $\sim 1 \mu\text{m/s}$ while keeping the glass slide fixed. The droplet moved along the surface with a meniscus orthogonal to the moving direction (**Figure 2**, **Figure 11a**). A combination of viscous drag and evaporation-induced flux causes particles to accumulate at the edge of the meniscus.

Initially, the temperature of the stage was fixed at 10°C above the dew point and then was gradually increased until the number of particles accumulated at the meniscus was high enough and the assembly process in the pits could be observed in situ using dark field. At this point, the translation speed was reduced by 100–200 nm/s to sustain the high-yield deposition. In these experiments, the nanoparticle assembly yield is defined as the ratio of filled traps to the total number of traps in an area. Typically, a high yield >99% could be achieved in large >1 cm² areas.

3.4. Microfluidic device

3.4.1. Femtosecond laser ablation

An optimized microfluidic channel layout was laser micromachined on a 1 mm thick, 30×48 mm² slide of opaque alumina ceramic substrate (VC 100-1 (Policor), 99.6–99.9% Al₂O₃, white, $\rho = 3.89$ g/cm³, Ra<0.01 μ m). Yb:KGW femtosecond laser ($\lambda = 1030$ nm, $\tau = 270$ fs, $P = 4$ W, Pharos 04-500-PP, Light Conversion) together with a galvoscaner (SCANcube III 14, ScanLab) based microfabrication setup (FemtoLAB, Altechna R&D) were employed to impose the designed microfluidic device in the alumina ceramic surface. The same design files that were used for the simulations were imported to a laser fabrication program SCA (Altechna R&D). A detailed description of the applied setup can be found elsewhere.¹¹⁵

The investigation of appropriate laser ablation parameters for microfluidic purposes was performed by varying the pulse overlap (scanning speed 50–250 mm/s) and energy density (0.56–11.2 J/cm²) in a matrix of 500 μ m square structures; 1030 nm wavelength and 40 kHz repetition rate were used. The laser was focused with an f-Theta lens to a diffraction limited 16 μ m diameter spot size.

3.4.2. Microfluidic setup

The investigated structures included 3 basic components: 3 inlets, a mixing structure based on the Tesla valve,¹¹⁶ and an outlet (**Figure 3**). This layout was used for simulations with 2–8 loops varying in angles (α , β), length (L), distance (D) and offset (O).

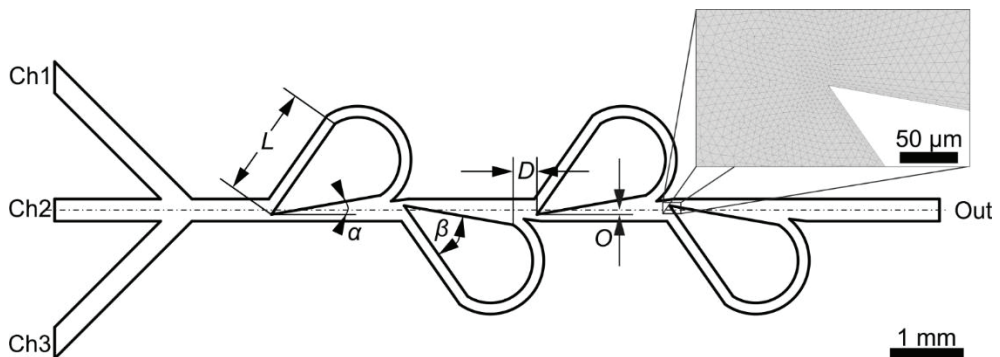


Figure 3. Layout of the modeled structures and varied parameters. L – length of a loop; D – distance between the loops; O – offset from channel axis; α – angle with relation to channel axis; β – structure angle. The inset depicts FEM mesh applied in the simulations. Reproduced from Juodėnas et al.¹¹⁷ (A1)

In order to characterize the fluid mixing performance of the microfluidic channels imposed in alumina ceramics slide, it was covered with a thick (~5 mm) slab of transparent PDMS. Two syringe pumps, LA-100 (single channel) and LA-120 (two channels) from Landgraf Laborsysteme HLL GmbH, were used to drive the fluids through the device (**Figure 4a**). The flow rates were varied (0.17–5.0 $\mu\text{l}/\text{min}$). The focusing fluid supplied from the side channels was deionized water, and the central fluid was stained deionized water. The microfluidic device performance was estimated by observing the change of laminar flows before the mixing structure (see **Figure 4b**) at different flow rate ratios with a USB microscope BW-500X (Brightwell Technology Ltd.). The obtained images were compared to the model (**Figure 4c**).

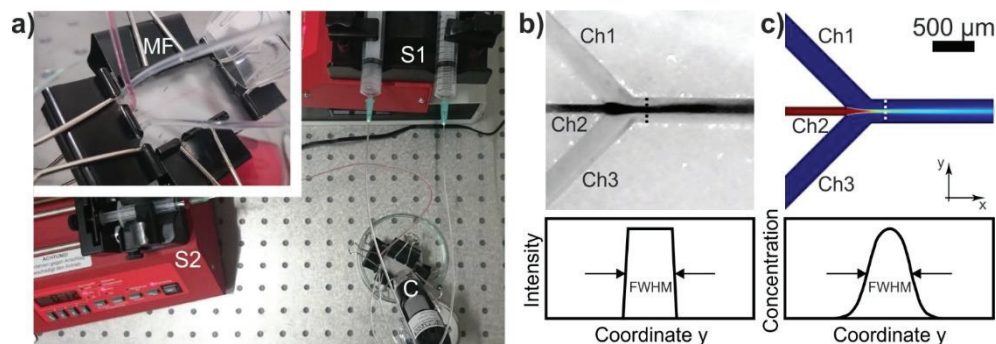


Figure 4. Microfluidic experimental setup and method. **(a)** Photograph of the experimental setup for the evaluation of microfluidic mixing performance (MF - microfluidic device, S1 - two channel syringe pump (clear water), S2 - syringe pump (dyed water), C - USB microscope), USB microscope image **(b)**, and simulated laminar flow **(c)** analysis used for the comparison of geometries. Reproduced from Juodėnas et al.¹¹⁷ (A1)

3.5. SEM, TEM, and optical imaging

Transmission electron microscopy (TEM) measurements were performed on a Hitachi H-7650 operating at 120 kV. The average edge length (a) of the cuboctahedra and nanocubes was measured using a JEOL-1010 TEM operating at 100kV with a minimum magnification of <0.5 nm/pixel. All TEM measurements were performed at the National Institute for Materials Science in Tsukuba, Japan (courtesy of Dr. Joel Henzie and his group). Scanning electron microscopy (Quanta 200 FEG, FEI) imaging of NPs was performed at a low vacuum in a water vapor atmosphere to reduce charging effects. Optical imaging of both nanoparticle deposition process and the final assemblies were performed using a microscope system (BX51, Olympus) equipped with a $100\times$ dark-field objective (MPlanFLN $100\times$ 0.90BD FN26.5, Olympus) and a CCD camera (Micropublisher 3.3, QImaging).

3.6. Optical spectroscopy

3.6.1. UV-vis spectroscopy

Steady state optical properties of Ag nanocube, cuboctahedra, and Ag@TiO₂ particle solutions and assemblies were analyzed with a UV-vis spectrophotometer (AvaSpec-2048, Avantes; 1.2 nm resolution). The angle-dependent transmission properties of 2D arrays were investigated using a custom-built motorized goniometric

setup (**Figure 11c**) consisting of an incandescent light bulb source, a collimator, and a Glan-Taylor polarizer. The source and detector positions were held constant, and the sample was rotated around the vertical axis to change the angle of incidence.¹¹⁸ The acquired spectra were normalized to transmission through an unused template at the same geometry conditions in the case of arrays and to the lamp spectrum in the solution case. The conversion to E-k diagrams was done according to eq. (1, 2). The calculations of the theoretical diffraction edges were done through eq. (3):¹¹⁹

$$E = \hbar\omega \quad (1)$$

$$k_{//} = \frac{2\pi}{\lambda} \sin(\theta) \quad (2)$$

$$E = \frac{\hbar c}{n} |\vec{k}_{//} + \vec{G}| \quad (3)$$

where E is energy, \hbar – reduced Planck’s constant, ω – angular frequency, $k_{//}$ – in-plane projection of the wave vector, λ – wavelength, θ – angle of incidence, c – speed of light in vacuum, n – refractive index of the medium, G – grating vector.

3.6.2. Transient absorbance spectroscopy

Ultrafast processes of the monodisperse Ag and Ag@TiO₂ nanocube colloidal solutions and 2D arrays were investigated with a HARPIA TAS setup built by Light Conversion. The samples were excited using a Pharos ultrafast Yb:KGW laser (Light Conversion) with a regenerative amplifier at a 66.7 kHz repetition rate and 290 fs duration pulses at 1030 nm wavelength. The pump beam wavelength was tuned with an Orpheus collinear optical parametric generator and harmonic generator Lyra (Light Conversion) to 400 nm in **A3** and 350 nm in **A4**, and energy density of 32 $\mu\text{J}/\text{cm}^2$ and 20 $\mu\text{J}/\text{cm}^2$, respectively. The samples were probed with a white light supercontinuum generated using a 2 mm thickness sapphire plate excited with the fundamental laser wavelength (1030 nm). The spectral range of the supercontinuum probe as well as the detection range of the TAS dynamics spanned wavelengths from 489 to 793 nm. The excitation beam was focused to a ~ 700 μm diameter spot, while the diameter of the supercontinuum probe was ~ 500 μm . The steady-state absorption of samples was rechecked after each measurement to ensure there was no damage from the laser irradiation.

3.7. Modeling

3.7.1. Finite element method

3.7.1.1. Microfluidics

FEM method-based physics simulation suite COMSOL Multiphysics was used to model the microfluidic device. The geometries were initially designed and imported as dxf files. Two modules were employed for the simulations, i.e., Creeping Flow and Mixture model, laminar flow. The first module is necessary to calculate the velocity field and the second one to estimate the concentration distribution based on the velocities. Numerically simulated concentration maps of the microfluidic channel path were investigated both qualitatively and quantitatively. Two-dimensional fluid concentration maps were evaluated visually, whereas the concentration distributions

at the outlet were taken as line graphs. A full width at half maximum (FWHM) value of such distribution was measured manually and plotted against the varied geometrical parameter.

3.7.1.2. Single and arranged particle optics

FEM modeling was performed using the COMSOL Multiphysics suite in the wave optics module. For single-particle modeling, a nanoparticle was placed in a uniform dielectric sphere, surrounded by a perfectly matched layer, and the background field was designed as a plane wave. The far-field border layer was designated as the surface between the physical dielectric domain and the perfectly matched layer. For array modeling, the nanoparticle was placed in a dielectric with Floquet boundary conditions relating to either square or hexagonal pattern. The array was illuminated from a port above the nanoparticle at varying incidence angles and polarizations, and a secondary port below collected the transmitted light, yielding transmittance spectra. The optical constants of Ag were taken from literature,¹²⁰ and default piecewise cubic interpolation was used to get values between the data points.

3.7.1.3. Particle mechanics

FEM modeling was performed using COMSOL Multiphysics suite. The Structural Mechanics Module was employed for the mechanical response of the nanoparticle. Eigenmode analysis and the frequency response was modeled using the geometry of the synthesized nanoparticles and mechanical material properties provided by the integrated material library. In order to get the deconvoluted nanoparticle shapes, the author of the dissertation used Rayleigh damping approach, which damps all but two selected frequencies.

3.7.2. *Coupled dipole approximation*

This approximation is an analytical approach to modeling of nanoparticle lattices. In this approximation, every particle is considered a dipole with a polarizability α . When particles have a spheroidal shape, the static polarizability can be expressed as in eq. (4):¹²¹

$$\alpha_{st} = \frac{abc}{3} \cdot \frac{(\epsilon_m - \epsilon_s)}{\epsilon_s + L(\epsilon_m - \epsilon_s)} \quad (4)$$

where a , b , and c are the semi-axes of the spheroid; ϵ_m and ϵ_s are relative permittivities of the NP and the surrounding medium (a non-dispersive refractive index of PDMS $n = 1.4$ was used) respectively; L is the shape factor as defined in¹²¹ (for a sphere $L = 1/3$).

In this case, the particles are too big to ignore retardation effects within the volume of the particle. Therefore, to account for radiative damping and dynamic depolarization, the static polarizability is changed by the modified long wavelength approximation (MLWA)¹²², as defined in eq. (5):

$$\alpha_{MLWA} = \frac{\alpha_{st}}{1 - \frac{2}{3}ik^3\alpha_{st} - \frac{k^2}{a}\alpha_{st}} \quad (5)$$

where k is the wavenumber of the incident light in the medium, α_{st} – static polarizability as defined previously, and a is a size dimension along the polarization direction. When the NPs are in an array, they scatter light in accordance with their dipole moment, and thus, the electric field affecting a particle is a sum of the incident field and scattered fields by every other NP in the array. Under the assumption of an infinite array and orthogonal incidence, the polarizability of a NP in an array can be expressed as in eq. (6):⁵⁶

$$\alpha_{ar} = \frac{1}{1/\alpha_{MLWA} - S} \quad (6)$$

where α_{MLWA} is the modified polarizability as defined previously, S is the contribution of the surrounding NPs, is often called the dipole sum, is mostly dependent on the geometry, and is defined by eq. (7):⁵⁶

$$S = \sum_{j \neq 1} \left[\frac{(1 - ikr_{ij})(3 \cos^2 \theta_{ij} - 1)e^{ikr_{ij}}}{r_{ij}^3} + \frac{k^2 \sin^2 \theta_{ij} e^{ikr_{ij}}}{r_{ij}} \right] \quad (7)$$

where r_{ij} is the distance to a dipole, and θ is the angle between the induced dipole (or polarization of incident field) and the position vector. Finally, a formulation (eq. (8)) introduced in¹²¹ is used to calculate the extinction cross-section, which is a sum of absorption (first term) and scattering (second term) cross-sections:

$$C_{ext} = 4\pi k \cdot \text{Im}(\alpha) + \frac{8}{3} \pi k^4 |\alpha|^2 \quad (8)$$

where α is the polarizability of a particle in an array as defined previously.

4. RESULTS AND DISCUSSION

4.1. Optimized microfluidic mixer for the CAPA setup

4.1.1. Tesla valve performance optimization

The influence of the Tesla valve loop geometry was investigated in order to find an optimal structure. The framework for the simulations was a basic 4-way junction with 3 inlets and one outlet and with the Tesla mixing loops in between. The width of the channels is 300 μm , except when they split in the loops, where it is 150 μm . The simulated two-dimensional concentration maps and the graphs of the FWHM value of the concentration distribution at the outlet are shown in **Figure 5**. A strong dependence of mixing performance was found on the angle with relation to the channel axis (α) (**Figure 5d**), which showed a strong linear dependence. Based on this analysis and some structure size and experimental setup considerations, optimal Tesla loop parameters were selected: $\alpha = 45^\circ$, $\beta = 0^\circ$, $L = 1200 \mu\text{m}$, $D = 480 \mu\text{m}$, $O = 0 \mu\text{m}$, and used for further full-scale device modeling, implementation, and experimental investigation.

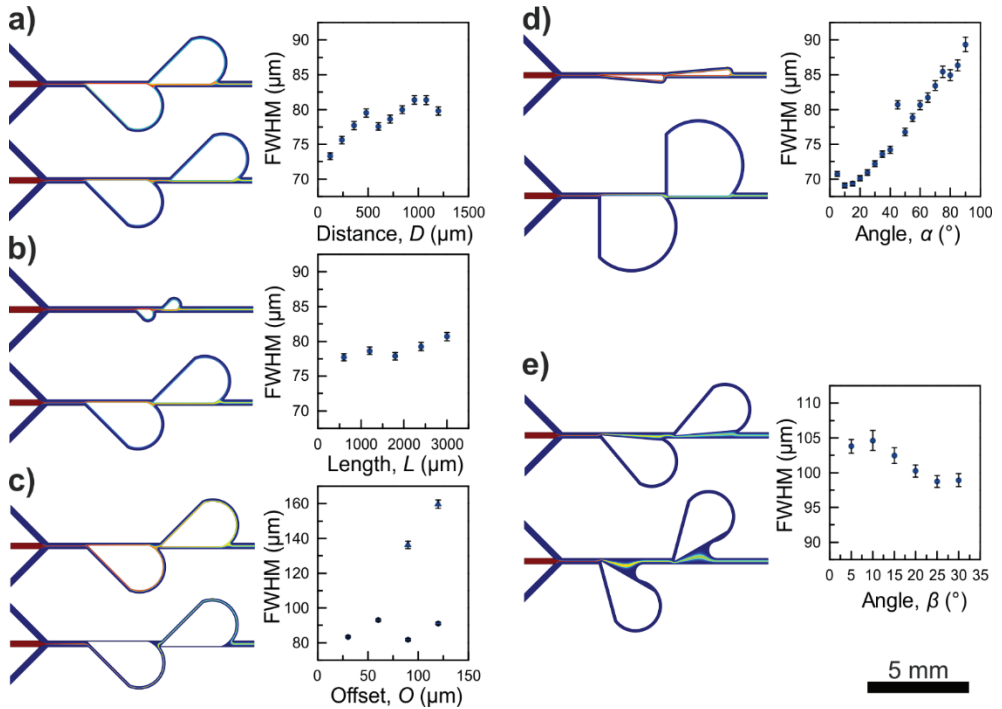


Figure 5. Results of the microfluidic mixer optimization. 2D concentration maps of the lowest (top image) and highest (bottom image) investigated parameter value together with the width of the central flow at the outlet (FWHM value) dependence on the corresponding parameter: **(a)** Distance D (120–1200 μm), **(b)** Length L (600–3000 μm), **(c)** Offset O (30–120 μm), **(d)** Angle α (5–90°), **(e)** Angle β (5–30°). Reproduced from Juodėnas et al.¹¹⁷ (A1)

4.1.2. Optimization of laser ablation parameters

The surface morphology of pulsed laser micromachined structures in alumina highly depends on the spatial distribution of pulses. Furthermore, by changing the pulse energy, the volume ablation rate can be adjusted. Both parameters are of high importance for the manufacturing of microfluidic devices. Therefore, experiments using different laser processing regimes were carried out, which yielded the results allowing for an optimal material processing mode. The surface quality of the ablated areas was dependent on the applied regimes. At high pulse overlap (92% and 90.6%), a layer of melted ablation debris was deposited, which resulted in a decline of surface quality. This agrees well with,¹²³ which states that high pulse overlap as well as high energy density results in an increase of local temperature and unwanted effects, and therefore, these ablation modes are not practical. A further decrease of the pulse overlap (76.6–85.6%) has improved the surface quality, and the melted debris was no longer observed. However, further decrease of the pulse overlap to 68.8–60.9% showed only negligible volume ablation rate at energy densities of 0.56–3.37 J/cm² (**Figure 6a**).

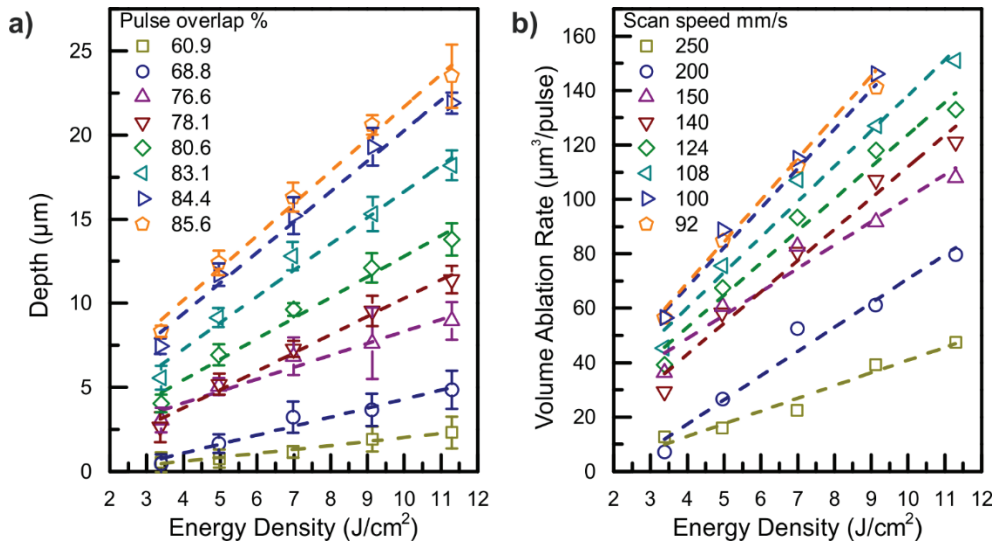


Figure 6. Laser ablation processing results with respect to the used parameters. Structure depth with respect to the energy density and pulse overlap (**a**) and volume ablation rate with respect to the energy density and scanning speed (**b**). The ablation overlap at the corresponding scan speeds is indicated in the legends. Reproduced from Juodėnas et al.¹¹⁷

(A1)

The volume ablation rate can be defined as the volume of material removed per laser pulse (**Figure 6b**). It was evaluated by measuring the depth of structures using a profilometer. The ablated trench depth and volume ablation rate demonstrate linear dependencies with respect to the applied energy density. Higher pulse overlaps (or smaller scan speeds) resulted in deeper structures. Based on these results, 100 mm/s scanning speed (84.4% pulse overlap) and 11.2 J/cm² energy density were selected. The volume ablation rate in this case was 165 μm³/pulse, and in order to reach

~200 μm microfluidic channel depth, the ablation of the designed pattern was repeated 10 times.

4.1.3. Modeling and fabrication of the final device

A microfluidic layout was specifically designed to accommodate the needs for CAPA setup. The length and width of the layout (25 by 75 mm) were selected to fit common microscope glass slide dimensions, which the device is supposed to replace.²² The change of flow direction and branching of the channels are introduced to produce precise droplets of solution on the substrate through the holes where the assembly is to be performed. The laser micromachining parameters and the geometry were selected based on the investigation described in sections 4.1.1 and 4.1.2. A stitched optical micrograph of complete structure is shown in **Figure 7a**.

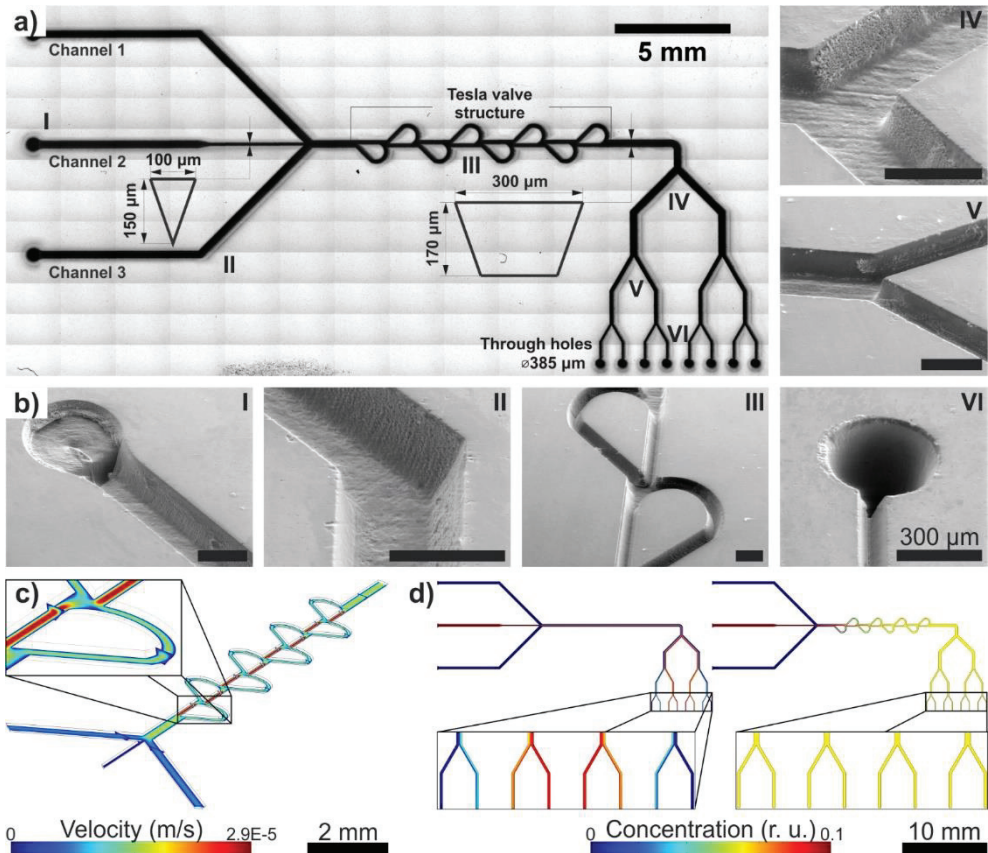


Figure 7. Final micromachined microfluidic device. **(a)** Stitched optical micrograph of the microfluidic device (typical cross-section shapes (V-shape, trapezium) are shown in the insets). **(b)** SEM images of characteristic channels of the microfluidic device. **(c)** 3D velocity profile of a microfluidic flow through the Tesla mixer (inset depicts the first mixing structure). **(d)** Comparison of 2D concentration profiles without and with the Tesla mixer (insets depict magnified branching outlets). Reproduced from Juodėnas et al.¹¹⁷ (A1)

Figure 7c shows a numerically simulated 3D flow velocity distribution of the microfluidic device considering slightly tapered walls of the channels. As it can be

seen from **Figure 7c**, the flow velocity is much higher within the central channel compared to the velocity within the loops. This suggests that mixing occurs due to two effects, i.e., different velocity magnitudes and different velocity directions. Since the flow profile did not show much dependence on the channel cross section geometry, further simulation of the device, not unlike the structure optimization, was performed in 2D. **Figure 7d** shows the contribution of loops to the mixing. A straight channel results in inhomogeneous concentration at the branching outputs, whereas the structure with optimized geometry loops makes the concentration uniform.

4.1.4. Experimental investigation of the full-scale device

The assembled device was investigated by observing the flow profiles within the channels, while changing the flow rates of channels 1 and 2 together or 3 (**Figure 3**). The device performance was compared to the simulated values. The flow profile is consistent with the simulations, when the flow rate of the focusing flows changes (**Figure 8a**). The other mode, where the focused flow rate varied (**Figure 8b**), showed a slight deviation from the simulated values. These errors may be attributed to the inconsistent flow rate delivered by the pump and/or insufficient side pressure from the focusing flows. Overall, the graphs demonstrate the same trends and provide sufficient evidence that: **i**) structures imposed in alumina ceramics do not introduce any changes to regular flow patterns in microfluidics and **ii**) the simulated dependencies of the mean concentration at the output of the microfluidic device (**Figure 8c, d**) may be used as guides for precise selection of the input velocities in order to achieve desired concentration in the output.

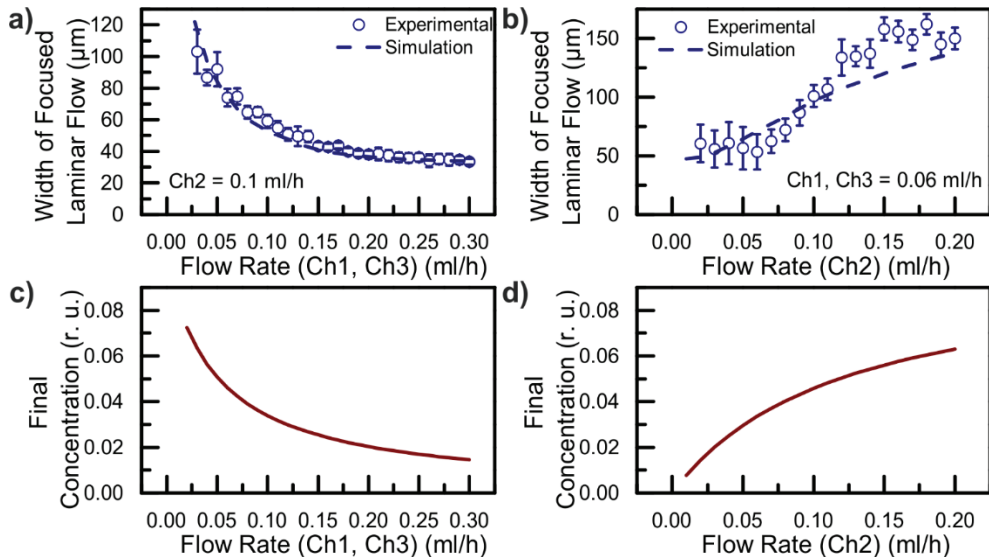


Figure 8. Experimental investigation of the microfluidic device. The widths of the laminar central channel flow (Ch2) while varying focusing channels' flow rates (Ch1, Ch3) **(a)** and central channel flow rate **(b)**, simulated output concentration curves depending on the focusing channels' **(c)** and central channel **(d)** flow rates. Reproduced from Juodėnas et al.¹¹⁷ (A1)

4.2. Plasmonic particles and self-assembly

4.2.1. Nanoparticle synthesis and characterization

4.2.1.1. Ag nanocubes and core-shell nanoparticles

The Ag nanocubes were synthesized using a modified polyol method described in **A3**. They were initially coated with PVP polymer surfactant that stabilizes the colloid.¹¹⁴ The scheme for the TiO₂ coating reaction is shown in Figure 1 of **A3**. The nanocubes appeared to be unchanged by the TiO₂ coating step, retaining their sharp corners and edges in the diaphanous TiO₂. The thickness of the TiO₂ was 12 ± 4 nm for the 39 nm cubes (**Figure 9a**). This coating method was also applied to nanocubes with larger edge lengths: $a = 77 \pm 3$ nm (**Figure 9b**) and $a = 92 \pm 4$ nm (**Figure 9c**). The TEM images show that the particles maintain their shapes, although the TiO₂ shell was thinner: 6 ± 3 and 8 ± 4 nm for $a = 77 \pm 3$ nm and $a = 92 \pm 4$ nm nanocubes, respectively.

The resonant wavelength of LSPR depends sensitively on the local refractive index and provides a simple and independent way to confirm that the particles maintain their shape and acquire the TiO₂ shell.⁴ In UV-vis measurements, the dipolar resonance of the 39 nm Ag cubes shifted by $\Delta\lambda = 47$ nm and $\Delta\lambda = 57$ nm for the 12 and 18 nm TiO₂ shells, respectively (**Figure 9a**). The UV-vis data also shows that the spectra retain a similar shape with multipolar resonances that are characteristic for a cube of this size,⁷ which combined with the TEM results proves that the cubes retain their size and shape after the TiO₂ coating step.

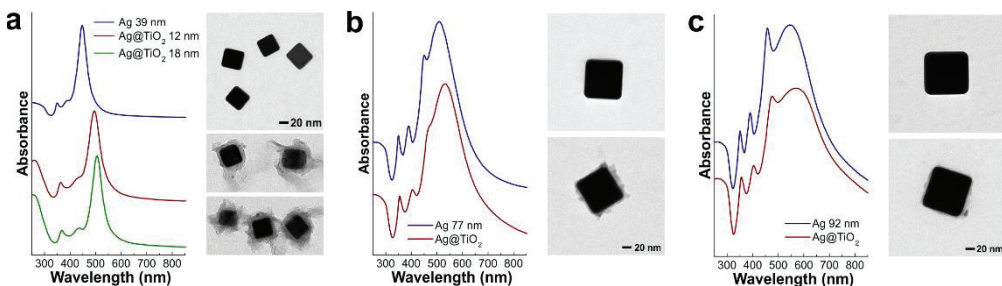


Figure 9. Overview of Ag nanocubes and their core-shell derivatives. Steady-state UV-vis absorption spectra of Ag and Ag@TiO₂ nanocubes with (a) 39 nm, (b) 77 nm, and (c) 92 nm edge lengths. TEM micrographs of the nanocubes are to the right of their corresponding spectra. Reproduced from Peckus et al.⁹⁸ (**A3**)

4.2.1.2. Ag cuboctahedra

Ag cuboctahedra ($a = 122 \text{ nm} \pm 3 \text{ nm}$) were also obtained using the modified polyol method. An overview of the particles and their optical properties is displayed in **Figure 10**. The author has created a model matching the shape of the average particle and simulated its optical properties in FEM. **Figure 10c** shows the extinction spectrum of the NPs in ethanol versus the simulated FEM spectrum. 3D surface polarization plots obtained in the FEM show that the peak at 602 nm is a dipolar mode, while the peaks at 408 nm and 468 nm are quadrupolar modes (**Figure 10d**). The experimental and calculated spectra do not differ significantly aside from a slight

redshift of the experimental spectrum, which may be due to inaccurate definition of edge rounding in the model or influence of the surfactant.

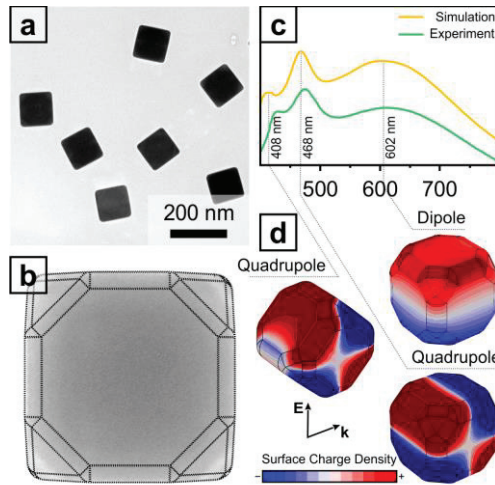


Figure 10. Ag cuboctahedra used in the experiment. **(a)** TEM micrograph of colloidal Ag cuboctahedra with an edge length of $123 \text{ nm} \pm 2 \text{ nm}$. **(b)** TEM micrograph of a single NP with overlaid contours of the model shape. **(c)** Modeled and measured optical extinction spectra of the NPs dispersed in ethanol. **(d)** Charge density plots of the quadrupolar and dipolar plasmonic modes denoted in (c). Reproduced from Juodėnas et al.¹²⁴ (A2)

4.2.2. Self-assembly

Bare Ag cuboctahedra ($a = 122 \pm 3 \text{ nm}$) and Ag nanocubes ($a = 77 \pm 3 \text{ nm}$) were used for self-assembly. **Figure 11a** shows an illustration of the CAPA¹⁸ method used to organize the cuboctahedra into 270 nm diameter pits with 600 nm center-to-center spacing in a hexagonal arrangement. The method had a >99% yield in a >1 cm² deposition area. Dark-field (DF) optical microscopy is used to initially assess the quality of the deposition. **Figure 11d** shows a DF image of the hexagonal periodic array of NPs. SEM images were collected in different places around the pattern and show that the cuboctahedra are oriented randomly and are typically in an off-center position within the traps (**Figure 11b**). The trap size in this case was large enough to accommodate up to two NPs. Dimers did assemble in some locations of the patterned template, but these areas were quite rare. Throughout the sample, about 10% of all filled traps were dimers. For dimers to contribute to the SLR, they must be aligned, which is difficult to achieve with circular traps, because the dimers are highly anisotropic. Moreover, if dimers were contributing to the optical spectra in any way other than serving as a defect, the polarization dependence at orthogonal excitation due to different short-axis and long-axis resonances could be seen. As it is shown later, such dependence is not observed; thus, only single NPs are considered.

The CAPA technique with PDMS patterns consisting of a square array of pits with 400, 350, and 300 nm spacings (center-to-center) was used as well (**Figure 12**). These patterns were filled with monodisperse Ag nanocubes ($a = 77 \text{ nm} \pm 3 \text{ nm}$). The CAPA experiments were performed using a dense solution of nanoparticles

(3.59×10^{11} p/mL). **Figure 12A** shows a real photograph of the CAPA assembly in progress on a 15×15 mm² array next to the SEM image of the assembled array. Dark-field optical micrographs of these assemblies are shown in **Figure 12B**. These images indicate a high assembly yield, which is estimated to be >99% in a >1 cm² area. Steady-state optical measurements on the nanocube solutions (**Figure 12C**) were performed in DMF (0.28×10^{11} p/mL).

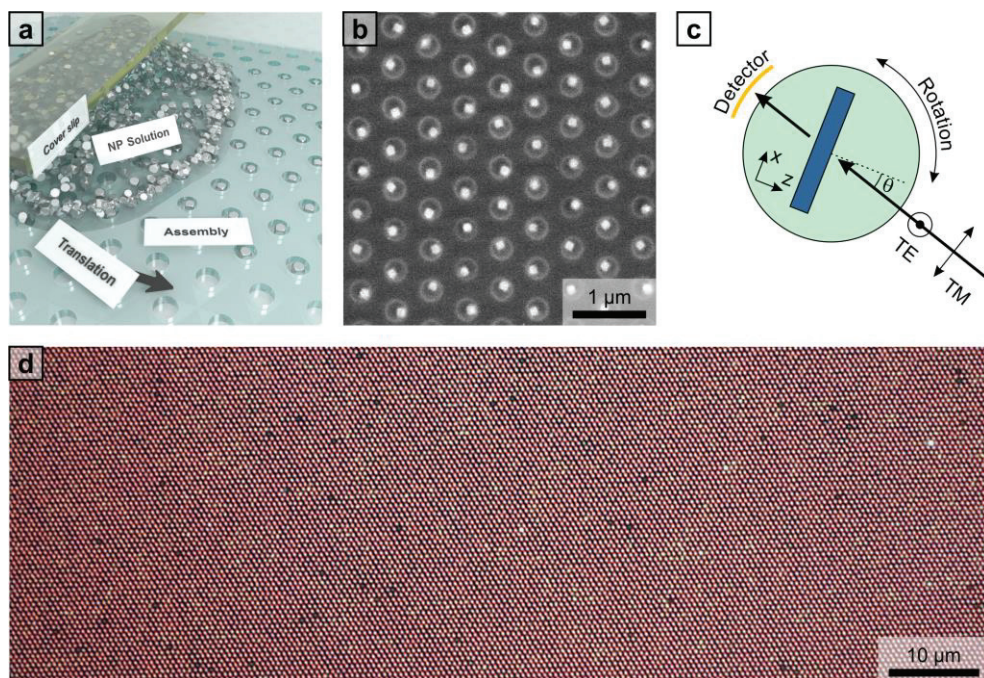


Figure 11. Ag cuboctahedra assembly. **(a)** A 3D visualization of the CAPA assembly method. **(b)** SEM micrograph of a randomly selected assembly area showing the deposition of single NPs. **(c)** A simplified layout of the optical measurement setup used to characterize the angle and polarization dependence of the NP arrays. TE or TM polarized light beam excites the sample at an incident angle θ , which changes by rotating the sample around the vertical axis. The transmitted light is collected by a stationary detector. **(d)** Dark-field optical micrograph of a randomly selected assembly area. Each red point is a single NP, while yellowish points correspond to dimers. Reproduced from Juodėnas et al.¹²⁴ (A2)

In both cases, the assembled nanoparticle patterns could be left exposed to air to generate an asymmetric dielectric environment or fully encapsulated by polymerizing an additional layer of PDMS following the deposition to create a uniform dielectric environment. The author mainly focused on the asymmetric patterns with nanoparticles exposed to the environment, because this configuration may be advantageous for sensing applications as it leaves the superstrate open for the introduction of different media.

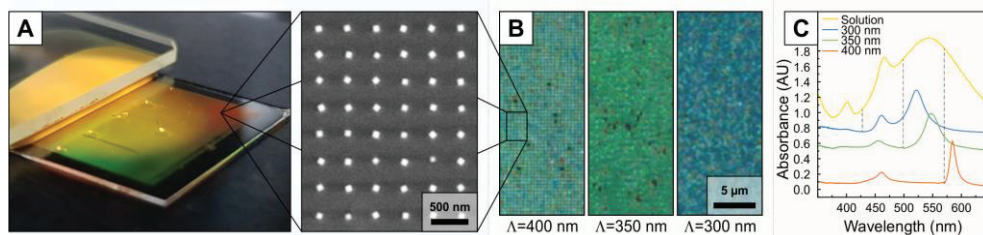


Figure 12. Ag nanocube self-assembly and their optical properties. **(A)** Photograph of the CAPA assembly process drawing a nanoparticle ink across a 15×15 mm² template and an SEM micrograph of a self-assembled nanocube lattice. **(B)** Dark-field optical micrographs (100 \times , NA = 0.9) of nanocube arrays with 400, 350, and 300 nm spacings. **(C)** Steady-state UV-Vis spectra of the nanocube arrays and a solution of the same nanocubes suspended in DMF. The nanocube array samples were excited at normal incidence. The dashed vertical lines indicate the locations of the Rayleigh anomaly (RA) for the Γ points of each lattice spacing. Reproduced from Juodėnas et al.¹²⁵ (A4)

4.3. Surface lattice resonance in nanoparticle assemblies

4.3.1. Hexagonal lattice of cubooctahedra: Experimental

The samples are large enough that free-space optical methods, such as UV-vis spectrophotometry, can be used to study them. This feature is important, because it allows to avoid the use of focusing optics that might broaden the SLR peaks.¹²⁶ The patterns were illuminated with a collimated incandescent source with a diameter of 5 mm. This corresponds to 6×10^7 assembled NPs (in 600 nm spacing hexagonal lattice) under orthogonal incidence (particle density = $3.2 \text{ p}/\mu\text{m}^2$). The optical investigations were performed in transmission mode, where the source and detector are both stationary, and the sample is rotated to change the angle of incidence (**Figure 11c**).

The author has converted the obtained transmission data to momentum space in order to generate dispersion diagrams in **Figure 13a** and **b** for Γ -M and Γ -K k -space directions, respectively, and for TM (left) and TE (right) polarized illumination. The author of the dissertation will be referring to these four cases as Γ -M_{TM}, Γ -M_{TE}, Γ -K_{TM}, and Γ -K_{TE}. The author only plots the 1st Brillouin zone to avoid redundancy. **Figure 13a** and **b** also show the corresponding reciprocal lattice diagrams. Lattice vectors \mathbf{g}_1 and \mathbf{g}_2 were plotted in these diagrams and were used to define the other members of the lattice. The author has added in-plane wave vector component to the resulting lattice vectors to produce the diffraction directions, which are color coded for degeneracy and plotted on top of the experimental dispersion diagrams.

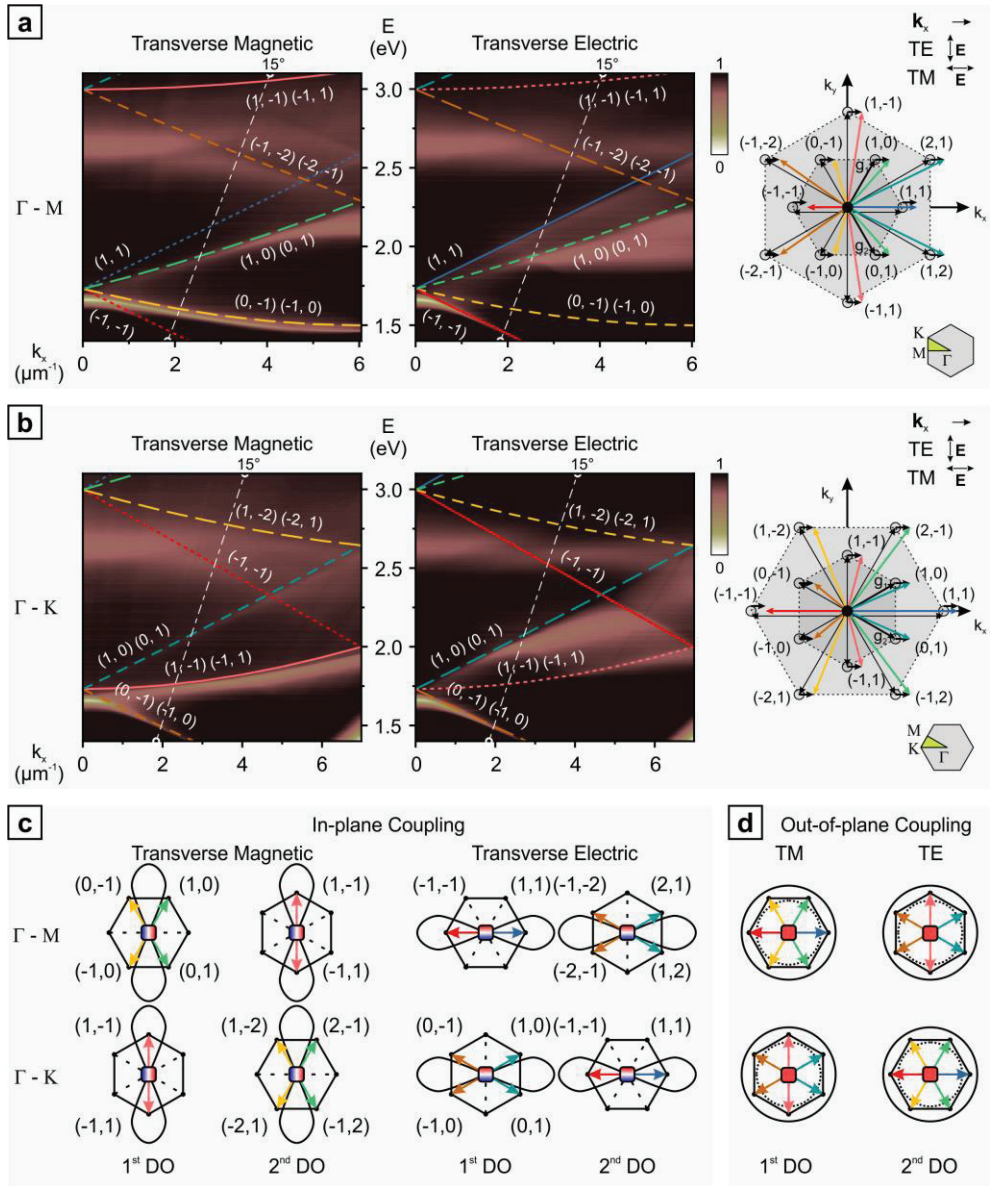


Figure 13. Experimental investigation of angular dependencies. **(a, b)** The dispersion diagrams obtained from the transmission data for **(a)** Γ -M_{TM}, Γ -M_{TE} and **(b)** Γ -K_{TM}, Γ -K_{TE} cases. White dashed line signifies the cut for modeling analysis. Colored dashed lines overlaid on top of the graphs correspond to the diffraction orders (“DO”) plotted on the reciprocal lattice diagrams. Lines with longer dashes indicate modes with stronger in-plane coupling and are color coded for degeneracy. **(c)** Comparison between in-plane coupling strengths corresponding to the alignment of dipolar scattering patterns for all explored cases. **(d)** Illustration of out-of-plane coupling. Reproduced from Juodėnas et al.¹²⁴ (A2)

The quadrupolar LSPR (Q-LSPR) can be observed in all spectra as a broad feature at ~ 2.6 eV (475 nm) that only weakly interacts with the RAs. This may be due

to a complicated quadrupolar scattering pattern as well as possible mode hybridization because of asymmetric interaction with PDMS. The author has elaborated on the Q-SLR behavior in section 4.3.4. The dipolar SLR (D-SLR) can be observed at 1.65 eV (757 nm) at the orthogonal angle of incidence (i.e., $\mathbf{k}_x = 0$). The energy of the SLR best matches the Γ point ($E_\Gamma = \frac{\hbar c}{n} \cdot \frac{2\pi}{\Lambda \cdot \sin(\frac{2\pi}{3})}$) for the lattice geometry when the refractive index of PDMS ($n = 1.4$) is used. Furthermore, there were no observable air-propagating SLR peaks ($E_\Gamma^{air} = 2.39$ eV). It was concluded that the NP arrays behave like they are in a homogenous environment for in-plane dipolar interactions, even though they are obviously not, because SEM measurements show they are physically exposed inside the holes. The gained insight suggests that SLR arrays in recessed holes may be a fruitful research direction for sensing applications, because the analyte will still be able to access the particles, which support the strongest EM fields in the array.

It is important to note that in the four different cases that were presented, the coupling strength as determined by the alignment of the NP scattering pattern to the diffraction mode propagation direction is not the same (**Figure 13c**). For in-plane coupling, when the scattering pattern of the NPs lies on a plane that is perpendicular to the surface, 4 coupling strengths indicated by the dash length of RAs on the dispersion diagrams are shown. The solid line represents the strongest coupling. In case of out-of-plane polarization, all nanoparticle dipoles are aligned perpendicular to the surface (**Figure 13d**); thus, the scattered light is primarily located in the plane of the array. This feature of the out-of-plane dipolar coupling leads to stronger overall coupling compared to in-plane coupling. This discussion will be expanded in the modeling section of a square nanocube lattice (4.3.4).

The highest Q -factor peaks (up to ~ 80) follow either the $(-1, -1)$ mode in the Γ - M_{TE} , or $(0, -1)$ $(-1, 0)$ for both Γ - K_{TM} and Γ - K_{TE} . This peak is absent in the case of Γ - M_{TM} , because the scattered light is orthogonal to the mode direction; hence, there is no coupling. Regardless, some modicum of coupling can still be observed at very small angles of incidence, which could be an evidence of out-of-plane coupling. Instead, the excitation of Γ - M_{TM} generates very strong and high-quality coupling at the $(0, -1)$ $(-1, 0)$ modes. This mode is narrow throughout the 1st Brillouin zone, maintaining high Q -factor even up to very large excitation angles. This allowed to tune the SLR response in the near-infrared spectrum between 1.5 and 1.65 eV.

4.3.2. Hexagonal lattice of cuboctahedra: Modeling

In order to expand the experimental observations and improve the understanding of the underlying phenomena, the author of the dissertation has performed numerical calculations with CDA and FEM. **Figure 14a** (top) shows the CDA-calculated extinction cross sections of a single dipole and a dipole in an array excited by an orthogonally incident ($\mathbf{k}_x = 0$) plane wave. The CDA calculations assume an infinite array of particles with individual polarizabilities (α) that express the properties of the nanoparticle, and the dipole sum (S), which represents the collective contributions of the lattice. The total polarization of a particle in an array (α_{ar}) is then expressed as in eq. 6 (section 3.7.2).

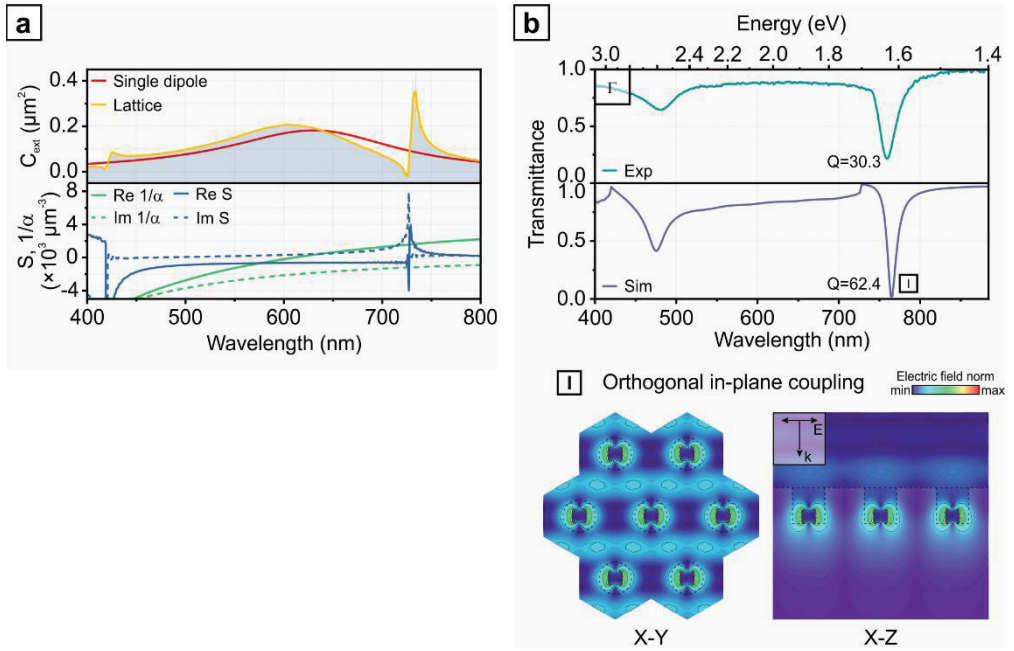


Figure 14. Analytical and numerical computations of orthogonal excitation. **(a)** Spectra of CDA calculated extinction generated by the isolated and in-array dipole; real and imaginary parts of the dipole sum and inverse polarizability. **(b)** FEM modeled (below) and experimental (above) transmission spectra at orthogonal incidence and FEM modeled electric field distributions for the peak indicated by (I): orthogonal in-plane coupling at 764 nm. Dashed contours depict the PDMS template. Reproduced from Juodėnas et al.¹²⁴

(A2)

Figure 14a (bottom) plots the members of the denominator in eq. 6, showing the real and imaginary components of $1/\alpha$ and S . SLRs are possible, when the real contributions of $1/\alpha$ and S intersect, and SLR at ~ 740 nm is observed, because the α_{ar} is large, and the imaginary parts of $1/\alpha$ and S are negative and similar in magnitude. The CDA result matches the hexagonal resonance at 764 nm relatively well, considering it is an analytical solution.

For a glimpse at a microscopic picture of the lattice and EM fields associated with these experimental peaks, COMSOL software was employed to model the periodic unit cell with FEM. The sample was modeled as a hexagonal array of cuboctahedra in a homogeneous environment with the refractive index of PDMS. **Figure 14b** shows the transmission spectrum of the array at orthogonal incidence ($\mathbf{k}_x = 0$). The modeled spectrum closely matches the experimental data, including the SLR at ~ 757 nm. The calculated Q -factor is higher in the model, which may be due to deviations in the periodicity of the self-assembled array or some rotational disorder of the particles. The EM field distribution maps were plotted for this sample at 764 nm in the plane of the array (X-Y) and in the plane of incidence (X-Z) in **Figure 14b** (I). It matches the standing wave pattern of a dipolar SLR mode. The electric field is strongest around the nanoparticles compared to the interstitial space.

In order to explore all the major SLR peaks, the author of the dissertation has modeled a spectrum for each of the cases at 15° angle of incidence as indicated by the dashed white lines in **Figure 13a** and **Figure 13b**. The transmission spectra are displayed in **Figure 15a** and **Figure 15b**. Most of the simulated peaks can be mapped to the experimental ones (dashed lines). The subtle divergence of spectral positions could be attributed to inaccuracies of the experimental optical setup. When comparing the two simulated polarization cases, it is easy to recognize that the same RAs have associated SLRs with different strengths. This is due to the coupling strengths discussed earlier and displayed in **Figure 13c**.

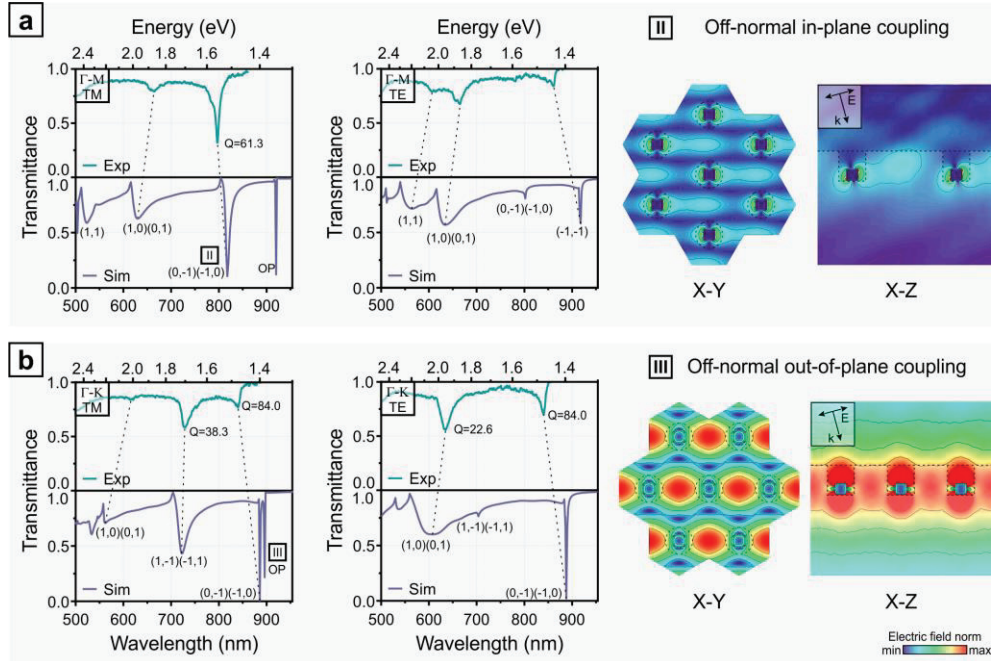


Figure 15. Numerical computations of off-normal excitation. **(a, b)** FEM modeled and experimental transmission spectra at 15° angle of incidence for **(a)** Γ -M_{TM}, Γ -M_{TE} and **(b)** Γ -K_{TM}, Γ -K_{TE} cases and FEM modeled electric field distributions for the selected cases: (II) off-normal in-plane coupling at 818 nm (Supplementary Animation SA3, Supplementary Animation SA4), (III) off-normal out-of-plane coupling at 896 nm (Supplementary Animation SA5, Supplementary Animation SA6). Dashed contours depict the PDMS template. Reproduced from Juodėnas et al.¹²⁴ (A2)

The strongest experimental peak at this specific 15° excitation angle occurs at 818 nm in Γ -M_{TM} case and has a Q -factor ~ 60 . The EM field distribution cuts corresponding to this case are displayed in **Figure 15a** (II). In contrast to the example discussed above, the electric field is much more delocalized between the NPs but still significantly weaker than around them. It should be noted how the dipolar EM field around the nanoparticle matches the polarization direction of the incident light in the X-Z cut, which will not be the case for the narrowest peaks.

The narrowest simulated peaks are associated with the most red-shifted RAs in all four excitation/polarization conditions. Although corresponding experimental

peaks are not as sharp, they do generate relatively large Q -factors of ~ 80 . Upon thorough investigation of each peak, two cases of OP coupling were found in the simulations, both excited using TM polarized illumination. **Figure 15b** (III) shows the EM field plot of this OP resonance. It generates an enormous local electric field intensity that is strongest between the particles and extends both vertically and horizontally. The OP peak in Γ -M_{TM} is clearly visible in the simulation but is absent in the experiments; thus, it was concluded it is just the in-plane peak that has been observed in the experiment of Γ -K_{TM}. The inability to excite out-of-plane resonances is likely due to the asymmetry of the refractive index in the normal direction of the samples. Addition of an index-matching layer could enable these out-of-plane peaks; however, it would deny analyte accessibility to the strongest EM fields, although for nanolasing applications it could turn out to be beneficial. Strong OP peaks were registered using smaller particles and lattices and will be described in the following sections.

4.3.3. Square lattice of nanocubes: Experimental

Once again, the large area of the nanoparticle array samples ($\sim 2 \text{ cm}^2$) enabled the use of a free-space optical spectrophotometer to measure the optical response. **Figure 12C** shows the transmission spectra of the assembled Ag nanocube arrays under normal incidence vs. the spectrum of free-standing Ag nanocubes in DMF. All spectra were offset for clarity. The RA wavelengths at normal incidence for square gratings in PDMS are $\lambda_{RA} = \Lambda \cdot n$. Thus, for $\Lambda = 400 \text{ nm}$, 350 nm , and 300 nm square gratings in PDMS ($n = 1.425$), λ_{RA} is 570 nm , 499 nm , and 428 nm (**Figure 12C**; dashed lines). The relative spectral position between the RA and LSPR resonance is the most critical factor for SLR coupling.^{55,56,62} In this case, only the 400 nm lattice RA is on the red side of the single nanoparticle LSPR at normal incidence, giving a narrow D-SLR peak ($Q = \lambda/\Delta\lambda \approx 48$). The other two cases show similar linewidths ($Q \approx 18$ and $Q \approx 14$ for 350 nm and 300 nm lattices, respectively) at different spectral positions, which is associated with the relative positions of their respective RAs. Neither of the normal incidence RAs matches the wavelength of the narrow Q-LSPR peak at $\sim 460 \text{ nm}$. Therefore, the Q-SLR can only be observed with off-normal excitation, because it affects the spectral position of the RA according to the energy dispersion relation: $E = \frac{\hbar c}{n} |\vec{G} + \vec{k}_{//}|$ (**Figure 16A**). The air-propagating RAs are also included in this diagram.

The energy dispersion diagrams for each array were collected from 0° – 90° incidence with TM and TE polarization in transmission mode (**Figure 16B**). The calculated RA lines are overlaid on top. In between each dispersion diagram, there is a grayscale bar representing the UV-vis absorption spectrum of the free-standing Ag nanocubes in solution for reference to compare the location of the LSPRs with the SLRs. The author of the dissertation has only plotted the first Brillouin zone of the square unit cell (i.e., the in-plane k -vector range $-\pi/\Lambda$ – π/Λ). These results clearly show the dependence of coupling on the in-plane polarization of the nanoparticle arrays, which were previously described using a hexagonal lattice of Ag cuboctahedra.¹²⁴ When the nanocube is excited with TM polarized light, its radiation pattern couples most strongly to the $(0, \pm 1)$ modes. TE polarized nanoparticles couple most strongly

to the $(\pm 1, 0)$ modes. This is easily observed in the dispersion diagram of the $\Lambda = 400$ nm lattice, because its RA is on the red side of the nanocube D-LSPR; hence, the peak is very narrow. The TM case shows a parabolic SLR following the $(0, \pm 1)$ modes, whereas the TE case has a strongly red-shifting SLR peak following the $(\pm 1, 0)$ modes. This coupling preference persists in all NP array samples that were examined.

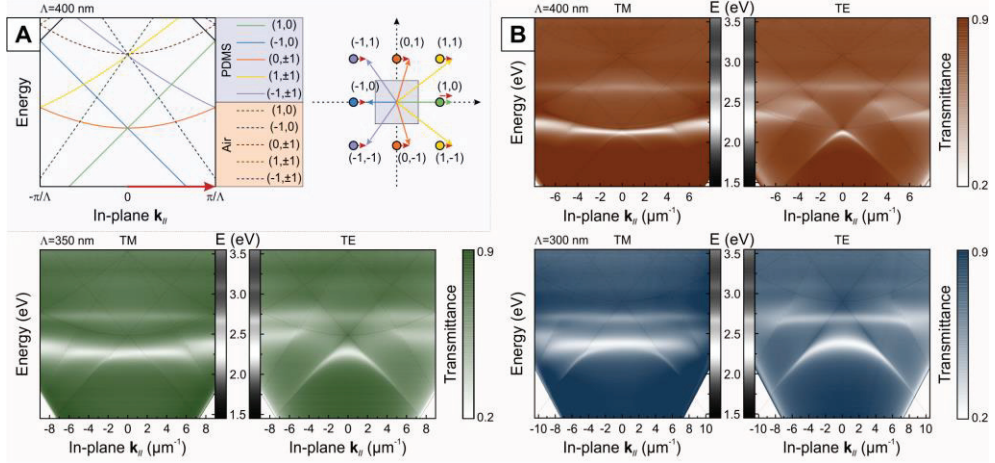


Figure 16. Energy dispersion diagrams of the self-assembled nanocube arrays. **(A)** Energy dispersion structure of a square lattice; diffraction orders propagating in two interfacing media are plotted: PDMS $n = 1.425$ and air $n = 1$. A reciprocal lattice diagram shows the modification of lattice vectors because of additional in-plane light momentum provided by off-normal excitation; **(B)** steady-state E - k dispersion diagrams of nanocube arrays with 400, 350, and 300 nm spacings. The E - k diagrams were collected in transmission mode using a collimated white light that is TM or TE polarized. The vertical grayscale bars represent the transmission of the solution of the same nanocubes. Reproduced from Juodėnas et al.¹²⁵ **(A4)**

When the arrays are excited with TM polarized light at higher angles of incidence, the electric field vector becomes increasingly polarized perpendicular to the plane of the array. These conditions enable out-of-plane (OP) SLRs that have been observed by¹²⁴ and other research groups.^{69,127–131} In OP excitation, the radiation pattern of a dipole lies in the array plane, enabling coupling to any of the modes. It manifests in the experiment as coupling to unexpected directions, such as coupling to $(\pm 1, 0)$ modes using TM polarization. OP resonances are challenging to observe experimentally because the nanoparticle patterns are typically designed to achieve the narrowest SLR peaks at normal incidence; thus, the RA is further to the red side of particle LSPR. Exciting OP modes requires off-normal excitation so that the incident electric field has an OP component. As the angle of incidence is increased, by the time the nanoparticles can be polarized OP, the RA will have already redshifted away from the single nanoparticle LSPR, causing the coupling to weaken significantly, albeit retaining the narrow linewidth. This phenomenon is evident in the TM polarized excitation of the $\Lambda = 400$ nm and 350 nm spaced arrays. There are sharp features following the $(\pm 1, 0)$ modes. However, they quickly fade because the RA redshifts too far away from the single-particle LSPR. Strong OP coupling extends further in the 300 nm spaced lattice ($Q \approx 78$ at $\theta = 35^\circ$) because the RAs still intersect the single-

particle LSPR at oblique angles of incidence, allowing the nanoparticles to be polarized normal to the surface. These types of SLR resonances are particularly interesting, because their EM field is concentrated OP instead of in-plane, which may enable extreme sensitivity to changes in the dielectric environment.

The Q-LSPR peak observed in the dispersion diagrams remained relatively constant and independent of array spacing. The solution spectrum in **Figure 12C** shows that the Q-LSPR and D-LSPR should be similar in intensity, whereas the latter is invisible in the arrays. The number of particles probed in solution (5.42×10^8 nanoparticles) vs. in the arrays (1.23×10^8 , 1.6×10^8 , and 2.18×10^8 nanoparticles for 400, 350, and 300 nm patterns, respectively) is on the same order of magnitude. Thus, this feature is attributed to the combined effects of phase retardation and substrate-induced quadrupole-dipole hybridization.^{8,132} The Q-SLR could be observed at higher angles and appears in the TE illumination in the 300 nm spaced arrays. Interestingly, the Q-SLR interacts with the air-RA ($\pm 1, 0$) but not the PDMS-RA ($\pm 1, 0$). This behavior can be explained by extending the hybridization theory for single nanocubes on surfaces to SLRs.⁸ The nanocube array is partially exposed to air; thus, there are two RAs available in this asymmetric dielectric environment, i.e., one propagating above the array in the air and one propagating in PDMS below. Their energy dispersion lines are illustrated in **Figure 16A**. The D-LSPR EM intensity is expected to be localized in the higher n medium and interacts strongly with the PDMS-RA. **Figure 16B** illustrates this point, because the strong dipolar SLR peaks are close to the PDMS-RAs. In contrast, substrate-induced hybridization causes the Q-LSPR mode to shift primarily into the superstrate (i.e., air);⁸ thus, it interacts most strongly with the air-RA.

4.3.4. Square lattice of nanocubes: Modeling

The author of the dissertation has performed EM modeling using FEM with a single nanocube and nanocubes in $\Lambda = 300$ nm spaced square arrays. The arrays were suspended in a homogenous dielectric environment ($n = 1.43$) to simplify the calculations and make them comparable to a nanocube array encapsulated in PDMS (**Figure 17A**). The optical constants derived from Johnson and Christy (JC) were used to model the optical properties of Ag.¹²⁰ The modeled $E-k$ dispersion maps match the experiment almost perfectly. However, there is a slight redshift in the modeled peaks due to the unavoidable mismatch between nanoscale features and bulk-derived optical constants such as JC. The red-shift is also observed in the single-nanocube model (**Figure 17B**). As expected, the features previously attributed to air-RAs have disappeared in uniform n , and the D-SLRs remain mostly unaffected because the PDMS-RAs dominate the air-exposed samples described in **Figure 16**.

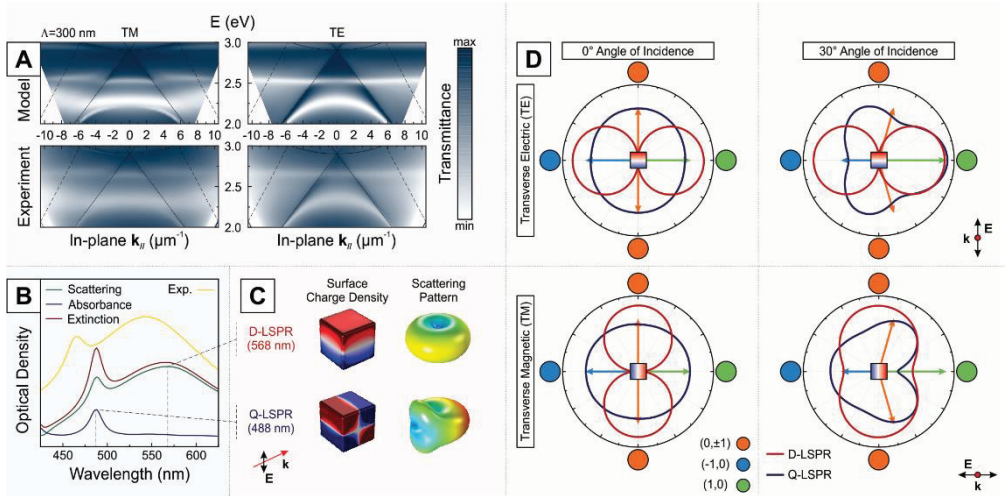


Figure 17. FEM modeled nanocubes and their arrays. **(A)** Simulated (top) and experimental (bottom) energy dispersion diagrams of a 300 nm spaced nanocube lattice in a homogeneous slab of PDMS. Transmittance is normalized (actual value ranges are 0.015–0.98 in the model and 0.15–0.625 in the experiment). **(B)** Experimental and simulated absorption spectra of the nanocube colloid solution. **(C)** Respective surface charge density (red and blue mark positive and negative charge accumulation) and radiation pattern surfaces (blue to red rainbow scheme shows an increasing scattering strength). **(D)** Polar plots of in-plane radiation patterns generated by the Q-LSPR and D-LSPR modes at normal incidence and at 30° incidence. Reproduced from Juodėnas et al.¹²⁵ **(A4)**

Interestingly, the Q-SLR coupling has shifted from TE to TM polarization in both simulation and experiment. The radiation patterns of the D-LSPR and Q-LSPR modes were used to help explain this observation. The radiation pattern of the nanocube D-LSPR mode has a characteristic torus shape that allows it to best couple to RAs that match the radiation direction (**Figure 17C, D**). As a result of symmetry of D-LSPR in TE excitation, coupling preference does not change with the angle of incidence. In the TM case, the toroidal radiation pattern progressively rotates with the angle of incidence, allowing OP coupling described earlier. **Figure 17D** shows cross-sections of the radiation patterns when the angle of incidence is normal (left) and 30° (right). The radiation pattern of the nanocube in the lattice will be different due to the fields generated by the neighboring particles, but the coupling rules should be similar. The radiation pattern of the quadrupole is different: it has a fishtail-like shape in the back-scattering direction, which shifts the radiation pattern node away from the center of the particle. Thus, the radiation pattern cross-section in the plane of the array is an ellipse at normal incidence, which means that the quadrupole radiates in-plane in all directions, enabling it to couple to any RA. The quadrupolar peak at normal incidence is very narrow and extremely sensitive to lattice spacing. Predicting the correct lattice spacing with imperfect optical constants like JC is challenging; the author of the dissertation has not observed it in the tested arrays, but it should be possible. **Figure 17D** also shows the profile of the Q-LSPR radiation pattern at 30° angle. In TE excitation, scattering is strongest in the (1, 0) direction. However, this direction

corresponds to the RA with energy that increases with the angle of incidence. The quadrupole is already lower in energy than the RA; thus, coupling is not possible in the TE excitation. In TM excitation, there is a stronger radiation in the $(-1, 0)$ direction, which corresponds to the RA with decreasing energy, allowing it to intersect with the quadrupolar LSPR and couple into the Q-SLR at high angles of incidence. The reason for the switch of Q-SLR from TE to TM is not completely clear; it is speculated that the radiation pattern of Q-LSPR in an asymmetric environment might be modified in a way that reverses the coupling priority that has been observed in a homogeneous environment.

4.4. Optomechanics of single and arranged nanoparticles

4.4.1. The mechanical modes of nanocubes

Ultrafast heating of nanocubes caused by the electronic processes excited by the pump pulse in TAS measurements induces stress across the nanoparticle. Consequently, the nanoparticle expands and later evolves into its breathing eigenmodes. The breathing modes are symmetric relative to the center of mass. A finite element method study in the frequency domain to get the displacement of characteristic nanocube points reveals the resonances attributed to the breathing eigenmodes (**Figure 18**).

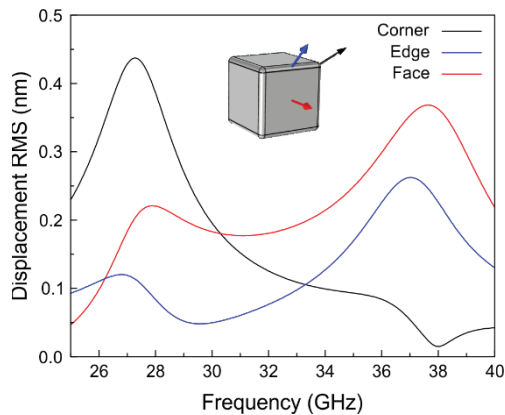


Figure 18. Frequency domain analysis of an Ag nanocube subjected to a uniform initial strain. RMS displacements of three high symmetry points (corner, edge, face) are plotted vs. the frequency. Reproduced from Juodėnas et al.¹²⁵ (A4)

The mechanical modes of a cube are universal, regardless of size or material. The frequencies may change, but the eigenmodes stay the same. The eigenmode analysis has been performed to find the pure, non-convoluted breathing modes of a cube. Thus, 100 cube modes are listed in **Figure 19**, in frequency order (increasing left to right, top to bottom). Based on the frequencies acquired using the frequency domain, the tip mode, the face mode, and the edge mode have been found; they are squared in **Figure 19**. It has been shown that the tip mode contributes to the optical measurements much more compared to the face mode.¹⁰⁵ The author has only considered the tip and the face mode (**Figure 20**), because the edge mode contributes to the optical measurements even less than the face mode.

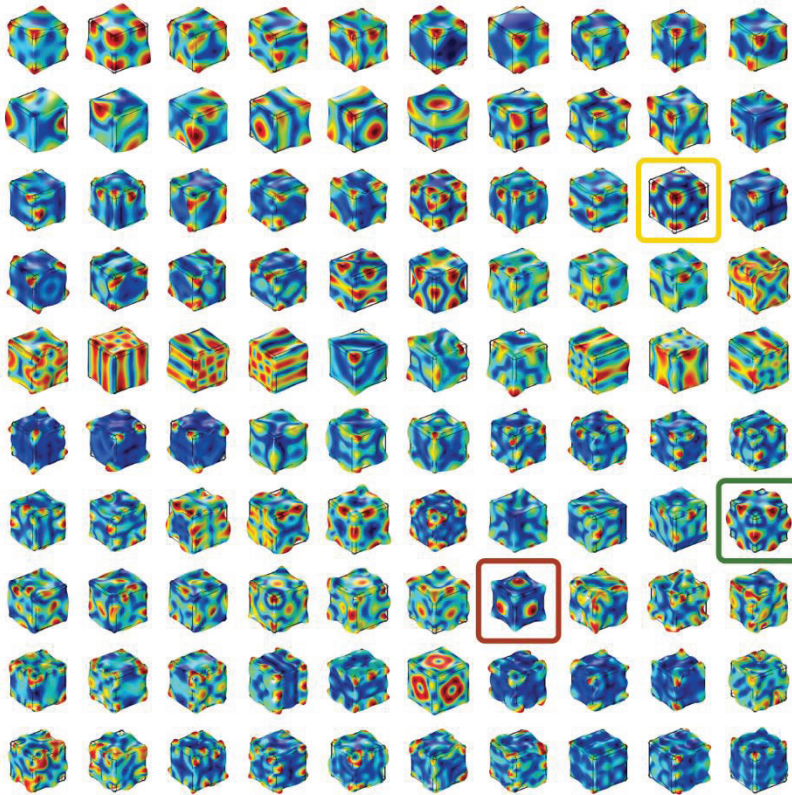


Figure 19. Eigenmode analysis of the Ag nanocube with $a = 77$ nm and edge rounding $r = 5$ nm. The major breathing eigenmodes are squared. Reproduced from Juodėnas et al.¹²⁵ (A4)

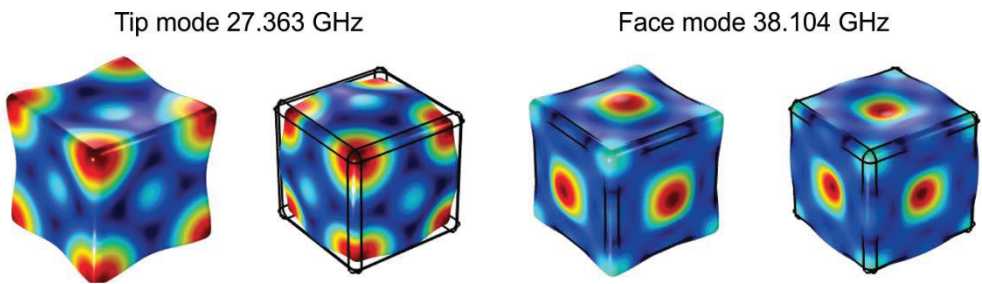


Figure 20. π -shifted phases of the tip and face modes of the Ag nanocube with $a = 77$ nm. The tip mode is characterized by opposite motions of tips and faces, whereas the face mode is characterized by parallel motions of tips and faces. Reproduced from Juodėnas et al.¹²⁵ (A4)

4.4.2. Ensemble Ag and Ag@TiO₂ nanoparticle optomechanics

In order to assess the impact of the TiO₂ shell on the ultrafast electron dynamics of the Ag nanocubes, the author of the dissertation has measured both Ag and

Ag@TiO₂ cubes using TAS. **Figure 21** shows the change in the TAS spectra of Ag nanocubes (**Figure 21a**) and core-shell Ag@TiO₂ nanocubes (**Figure 21b**) in ethanol over time. The samples were excited with a $\lambda = 400$ nm pump laser and monitored with a continuum white light probe ($\lambda = 480\text{--}765$ nm). This setup enabled efficient excitation of the nanocube and ability to observe the breathing modes by monitoring wavelengths associated with the lower energy dipolar LSPR mode. **Figure 21c** shows TAS traces for multiple Ag and Ag@TiO₂ nanocubes ($a = 39 \pm 3$, 77 ± 3 , and 92 ± 4 nm) collected nearest to the wavelength where the cube dipole exhibited maximum ΔA . The initial increase in amplitude is caused by excitation of the electron distribution, which quickly relaxes via electron-electron scattering followed by electron-phonon scattering. The second peak originates from the expansion of the lattice coordinate that is determined by the electron-phonon coupling constant of the particle. The pulse width of the pump laser is faster than the period of expansion/contraction of the particle; thus, it is possible to efficiently excite coherent optomechanical modes that modulate absorbance by shifting the position of the LSPR peak.

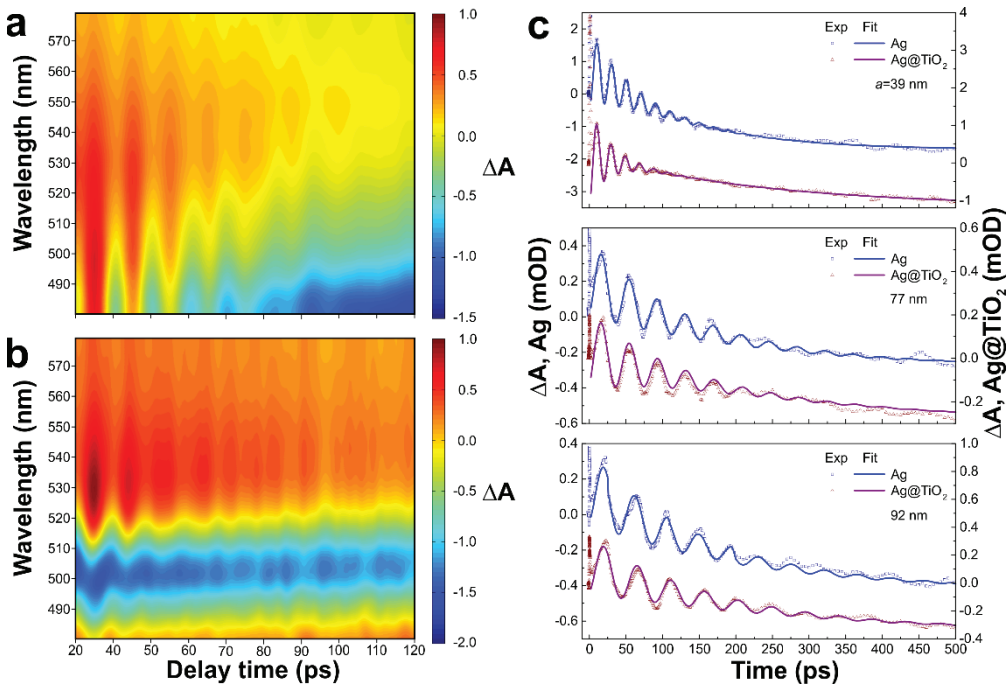


Figure 21. Ultrafast absorption properties of Ag and Ag@TiO₂ nanocubes. TAS carpets for (a) solution of 39 nm Ag nanocubes and (b) the same cubes coated with a 12 nm TiO₂ shell. (c) TAS relaxation traces were chosen at the maximum positive ΔA value for Ag (blue) and Ag@TiO₂ (red) with three different edge lengths. The solid lines show the data fit to a damped oscillator function in eq. 9. Reproduced from Peckus et al.⁹⁸ (A3)

A function describing the fast exponential decay (τ_{b0}) and the slow exponential decay (τ_b) modulated by a damped harmonic oscillator function (τ , T) was used to fit the TAS traces (eq. 9).

$$\Delta A(t) = a_0 \exp\left(-\frac{t}{\tau_{b0}}\right) + a \exp\left(-\frac{t}{\tau_b}\right) + A \exp\left(-\frac{t}{\tau}\right) \cos\left(\frac{2\pi t}{T} - \varphi\right) \quad (9)$$

Fitting the TAS traces for the smallest Ag and Ag@TiO₂ nanocubes ($a = 39 \pm 3$ nm) shows that the period of oscillation (T) was almost unchanged by the TiO₂ shell (20.0 ps for Ag and 19.5~19.6 ps for Ag@TiO₂), hinting that the Ag nanocube core and the TiO₂ shell are not mechanically coupled. However, the Q-factor ($Q = \pi\tau/T$) of the Ag@TiO₂ nanocubes decreased by ~40%; thus, the TiO₂ shell causes significant damping overall (**Figure 22a**). Furthermore, the Fourier transforms (**Figure 22b**) show that the same ($a = 39 \pm 3$ nm) Ag cube has a sharp resonance at ~50 GHz, but the TiO₂ shell broadens the peak in FFT significantly. Previously, Petrova et al. used finite element analysis to show that the reduced frequency of the Ag cube fundamental breathing mode (tip mode) is $\varpi = 6.04$ when excited by a uniform initial strain.¹⁰² The author has fitted the TAS traces for three Ag nanocube sizes ($a = 39 \pm 3$, 77 ± 3 , and 92 ± 4 nm) and showed that T is linearly correlated with size. Using this plot, $\varpi = 6.17 \pm 0.13$ was obtained for Ag nanocubes and $\varpi = 6.16 \pm 0.01$ for Ag@TiO₂ nanocubes. The ϖ values are roughly the same, adding further proof that the core and shell are decoupled (**Figure 22c**, top).

It was surprising that the frequency of the breathing mode of the Ag nanocube was largely unaffected by the TiO₂ coating. These observations suggest that the increased decay of the optomechanical mode is not caused by the shell enhancing the radiation of sound but rather by some other phenomena. The author has gone further and modeled the influence of coupling strength on the oscillation frequency of a bare Ag cube ($a = 39$ nm) and one surrounded by a TiO₂ shell ($t = 12$ nm) using FEM. The weakly coupled core-shell Ag@TiO₂ nanocubes had an oscillation frequency similar to the bare Ag cube (**Figure 23a**). By steadily increasing the coupling strength from 0.01 to 10 GPa/nm in the frequency domain, a shift in the frequency of the tip breathing mode with increasing coupling strength was observed. The analysis in the time domain (**Figure 23b**) confirms the change of the frequency of oscillations. The inset shows the deformed state of the core-shell assembly in the strong coupling regime. **Figure 23c** shows that the frequency increases with the coupling strength, and only a marginal frequency increase in experiments has been observed. These results show that the shell cannot enhance the decay of photoexcitation energy mechanically via sound waves, but rather some other effect is driving the attenuation of the optomechanical mode.

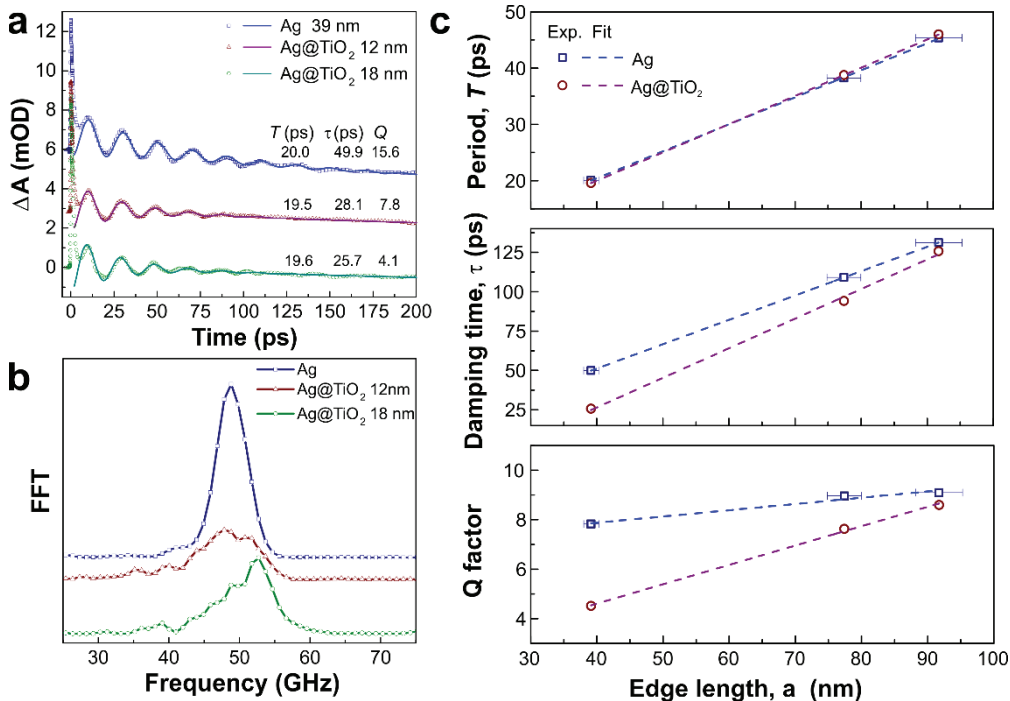


Figure 22. The investigation of attenuation of OMs **(a)** TAS traces for Ag and Ag@TiO₂ nanocubes ($a = 39$ nm) with 12 and 18 nm thick TiO₂ shells. The solid lines correspond to the damped oscillator fitting. **(b)** FFT spectra of the TAS traces in **(a)**. **(c)** Size-dependent optomechanical properties of Ag and Ag@TiO₂ nanocubes. Reproduced from Peckus et al.⁹⁸ (A3)

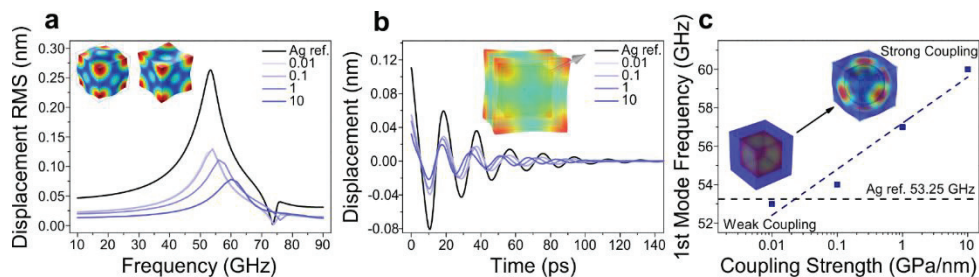


Figure 23. FEM modeling of Ag@TiO₂ core-shell assembly coupling ($a = 39$ nm and $t = 12$ nm TiO₂ shell thickness). **(a)** Displacement RMS of the corner of the Ag core is plotted against frequency. **(b)** The total displacement of the corner of the Ag core is plotted against time in different coupling strength regimes. **(c)** The shifted frequency is plotted against the coupling strength showing a log-linear dependency. 3D images show the displacement magnitude in weak and strong coupling regimes. Reproduced from Peckus et al.⁹⁸ (A3)

The damping time τ is known to be strongly affected by the surrounding medium (homogeneous broadening) and dephasing due to the size distribution of the nanoparticles (inhomogeneous broadening).¹³³ The Ag nanocubes are monodisperse, and the dimensions of Ag core are largely unchanged by the coating step, as illustrated

by TEM and the lack of change in T . It was hypothesized that the oscillations of the Ag@TiO₂ nanocubes are damped from the very beginning because of electron losses. Since conventional energy loss via mechanical vibrations is not important in this particular system (for mechanical losses, $t > \tau_b$), the primary loss mechanism should be energy transfer to the TiO₂ shell (for electronic losses, $t < \tau_b$) (**Figure 22c**, middle). The homogeneous Q -factor allows removing the influence of size and isolating the effect of energy loss (**Figure 22c**, bottom). It can be seen that the Q -factors of the Ag cubes are relatively unchanged by size ($Q = 8\sim 9$). Interestingly, the Q -factors for Ag@TiO₂ nanocubes had a much wider range ($Q = 5\sim 9$). If the systems are equivalent; then, the smaller nanocubes have additional energy loss due to the enhanced absorption losses of small metal nanoparticles. In this system, energy will be lost as hot electrons and is not mechanical as explained above. Following the initial light excitation, the local plasmon resonance of the particle can either scatter the photon or transfer its energy into nonradiative relaxation processes. As mentioned, for smaller metal particles (<50 nm), this nonradiative relaxation channel is dominant and creates hot carriers that would normally redistribute energy via electron-electron scattering and dissipate into the environment as heat/sound. However, hot electrons extend further from the surface than the normal electron distribution and can transfer into the electronic states of an adjacent electron acceptor, as clearly illustrated by emerging applications such as plasmon-enhanced photodetection and photocatalysis.^{134–139}

In order to find evidence of enhanced hot electron loss, the ultrafast TAS traces of the 39 nm Ag and Ag@TiO₂ nanocubes were reexamined (Figure 5 in **A3**). The normalized traces show that the initial decay is faster for both Ag@TiO₂ nanocube solutions. Moreover, the intensity of the first part of the breathing mode (at ~10 ps) was highly attenuated, representing a decrease in $\Delta A \sim 36\%$. Faster decay and smaller oscillations for Ag@TiO₂ nanocubes reveals that electron-phonon coupling has less impact on the TAS signal, because there is an alternative relaxation path. The TAS results show that the TiO₂ shell can harvest hot electrons from the LSPR of the Ag nanocube. However, the fate of hot electrons and specifically how efficiently they move into the semiconductor, or migrate back into the metal, is still an open area of research and will impact the efficiency of the conversion process from light into hot electrons. Optomechanical oscillations can serve as an additional accounting tool to observe the effects of hot electron emission in mechanically uncoupled interfaces to help engineer the performance of plasmonic devices for energy and chemical fuel generation.¹⁴⁰

4.4.3. *TAS measurements of Ag nanocubes in solution versus in arrays*

In order to compare the ultrafast processes between suspended, uncoupled nanoparticles with arranged nanoparticles under Bragg coupling condition, TAS signals of $a = 77$ nm nanocubes in solution and in self-assembled arrays were measured. **Figure 24A** shows TAS plots with ΔA modulations that are characteristic to OMs supported by plasmonic nanoparticles. The author of the dissertation has measured all array samples presented in 4.3.3 ($\Lambda = 400, 350, \text{ and } 300$ nm) in addition to the free-standing nanocubes suspended in DMF (Solution).

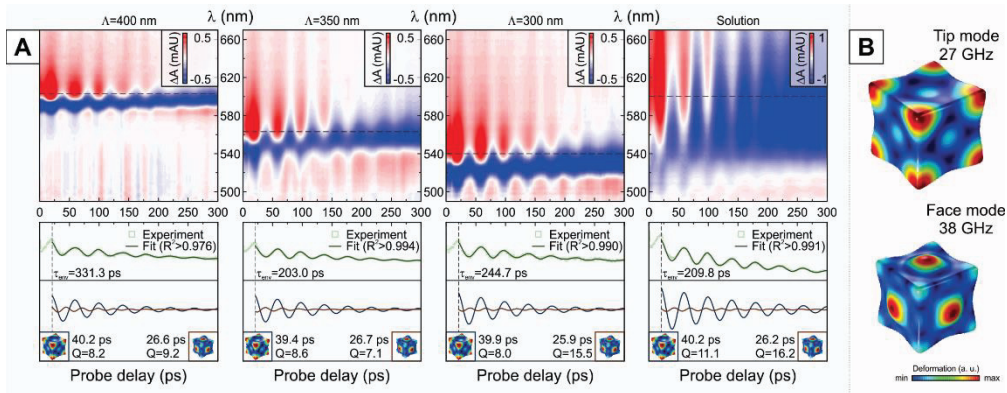


Figure 24. Transient absorption measurements exhibit the signature of fundamental optomechanical modes of nanocubes. **(A)** Transient absorption spectroscopy carpets were collected on arrays with spacings $\Lambda = 400, 350,$ and 300 nm at normal probe incidence and compared to the solution of the same nanocubes. The dashed lines indicate the traces used to fit the optomechanical modes. The traces were fit using a sum of a decaying exponential and two damped cosines starting from $t = 21$ ps to eliminate the uncertainties introduced by a mixed contribution to the TAS signal from e-ph equilibration and lattice expansion. **(B)** The two dominant eigenshapes were modeled with FEM: tip mode (27 GHz) and face mode (38 GHz). Reproduced from Juodėnas et al.¹²⁵ (A4)

Cubes are known to support two vibrational modes that dominate its mechanical response.^{102,105} The strongest mode results from the deformation of the eight corners of the cube, i.e., the ‘tip mode,’ which is known to strongly affect optical response. The second mode is generated by a deformation of the six faces of the cube, i.e., the ‘face mode,’ which behaves like a high-frequency overtone with a weaker optical response. The two dominant modes are plotted in **Figure 24B**. In order to understand the impact of each vibrational mode on TAS data, TAS traces with the highest signal amplitude were selected and plotted in the bottom row of **Figure 24A**. Each trace was analyzed using a machine learning (ML) algorithm (Eureqa) by fitting it with a decaying exponential ($e^{-t/\tau_{env}}$; τ_{env} is the decay constant) and two damped cosine functions.¹⁰² The fit was initiated at $t = 21$ ps to minimize the contribution of e-ph equilibration and focus on the lattice expansion/contraction. In the ML code, the face mode was constrained to be lower in amplitude than the tip mode. In addition, the frequencies were selected to best match those acquired after performing fast Fourier transform (FFT) on the data. The ML code was allowed to run until it achieved high goodness-of-fit ($R^2 > 0.97$). The mechanical quality factors for each mode are used to compare how each array affects the damping of the OMs.

The mechanical Q-factors of nanoparticles depend on the materials properties, dimensions, and the viscoelastic properties of the surrounding medium. Previously, Hartland et al. measured individual Ag nanocubes cast with poly-vinyl-alcohol on glass substrates and observed Q-factors from 14 to 25.¹⁰⁷ Damping of the Q-factor of metal nanostructures is highly dependent on the orientation of the particle and its interaction with a solid substrate. In solution, the D-LSPR of the nanocubes is very broad due to the intrinsic radiative damping of bright plasmon modes. The Q-factors

of the tip and face modes were 10.7 and 16.8, respectively, at $\lambda_{\text{probe}} = 600$ nm. The Q -factor is higher in DMF than ethanol,⁹⁸ in part because DMF has a lower viscosity. In addition, DMF swells the PVP polymer because it is a theta solvent, reducing inhomogeneous damping.

The Q -factors of the optomechanical modes in arrays excited at normal incidence (0°) are smaller than solution measurements ($Q \approx 8$ for the tip mode and $Q \approx 7\text{--}15$ for the face mode). A few points are worth noting: (i) the tip mode has a near-constant Q -factor in all array samples; (ii) the face mode varies between samples and becomes strongest in the $\Lambda = 300$ nm pattern. The author of the dissertation surmises that the tip-mode at normal incidence is not strongly affected by the mechanical environment because the tips have a smaller contact area with the PDMS compared to the face-mode.

4.4.4. Influence of optomechanical modes on SLRs

The SLR depends on the RA and LSPR in a nanoparticle array. The position of the RA is fixed in this experiment. Thus, any change in the LSPR will affect coupling to the RA and modify the SLR peak. The effect of chemically deforming Ag nanocubes on the LSPR has been studied by colloidal chemists and serves as a useful guide.¹⁴¹ They show that the LSPR progressively red-shifts as the faces become concave and tips extend away from the body center of the cube. Conversely, Ag nanocubes with rounded edges and tips have blue shifted LSPRs. In order to understand how the dynamic mechanical deformation of the nanocube affects the SLR, TAS was used to measure the $\Lambda = 300$ nm array using a pump/probe incidence angle of 30° with TE and TM excitation (**Figure 25**). At 30° incidence, TM polarization produces two peaks, i.e., one in-plane and one OP, the former will be considered and compared to TE-generated in-plane coupling. The EM intensity plots in **Figure 25** demonstrate the characteristic in-plane and OP intensity distribution, and the OP mode generates stronger fields. Regarding OMs, the tip mode maintained the same Q -factor in both in-plane and OP coupling and matched the previous experiments at 0° incidence ($Q \approx 9$). Interestingly, the face mode Q -factor was stronger in the in-plane case ($Q \approx 12$). The higher Q in-plane could be a consequence of increased elastic environment homogeneity in the plane of the array vs. out of plane, because the latter has one facet strongly adsorbed to the polymer surface.

A frequency-domain study was performed on a $\Lambda = 300$ nm square array with the tip and face mode eigenshapes to study how they affected the SLR over time. As predicted by the eigenmode analysis, the edge mode and face mode are very close in frequency and become convoluted when isotropic damping is used, yielding a combined shape at the face mode frequency.^{102,105} Therefore, in order to produce pure tip and face mode shapes, the frequencies of dominant eigenmodes with Rayleigh damping were used, which damps all but two predefined frequencies. The initial strain was selected to yield a deformation of 3 nm to observe clear shapes. The phase of both modes with the tips of the nanocubes extended outwards was selected (**Figure 20**). Each array was modeled using an incident excitation from $0\text{--}30^\circ$ and then subtracted from the E-k diagram of the un-deformed Ag cube (**Figure 26A**).

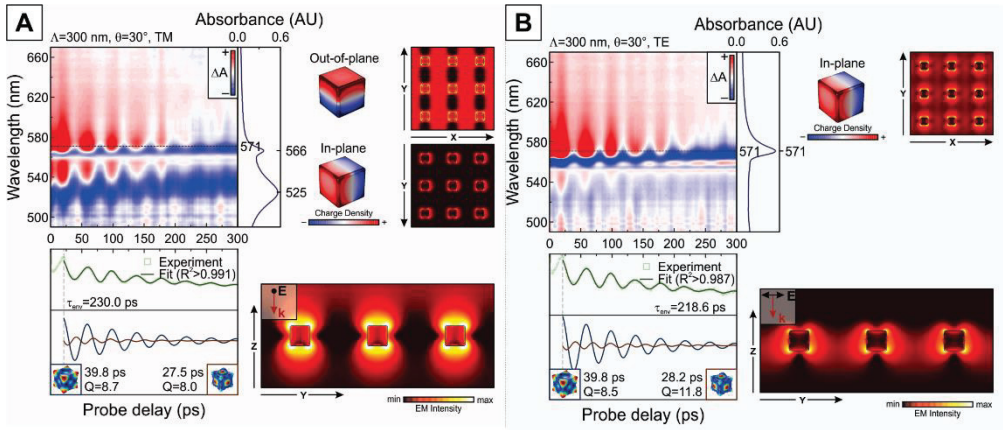


Figure 25. Transient absorption measurements at an angle. Transient absorption data taken from 300 nm spacing nanocube arrangements at 30° probe angle of incidence and two polarizations: (A) TM and (B) TE. The traces used for fitting are marked with a dashed line. The absorption spectra next to the 2D maps are steady-state measurements taken at the same angle of incidence. Surface charge density maps of the nanocubes are presented next to the respective absorption peaks, and the electric field time average is plotted in the XY and YZ planes of the nanoparticle array. Reproduced from Juodėnas et al.¹²⁵ (A4)

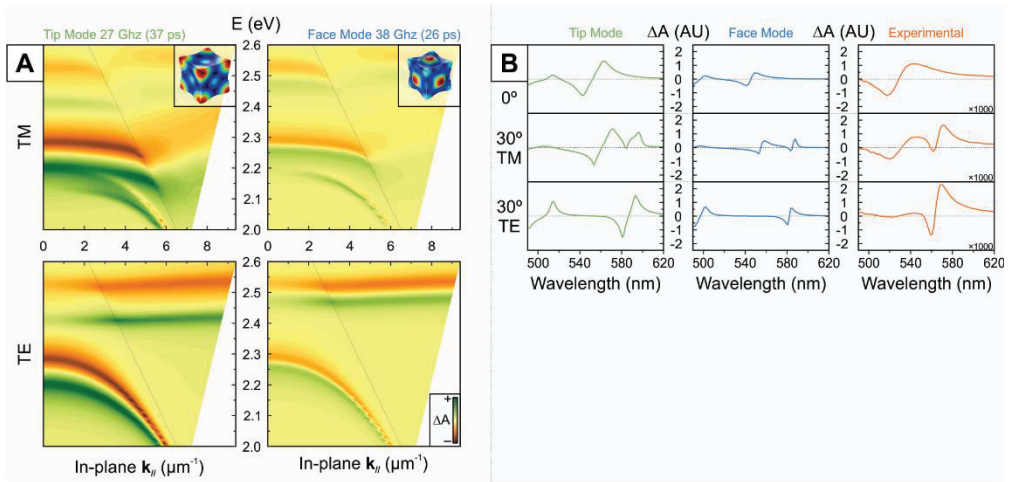


Figure 26. The influence of the isolated eigenmodes on the E - k diagrams. (A) Absorbance difference maps on E - k diagrams, showing the individual contribution of the two primary modes to the TAS signal; (B) absorbance difference traces generated by tip mode (left), face mode (middle), and experimental measurement (right) at normal (top) and 30° incidence with TM/TE polarizations (bottom). Reproduced from Juodėnas et al.¹²⁵ (A4)

The dispersion diagrams are strongly affected by the deformed shapes that represent the OMs. Both modes cause a red shift in the spectrum. Only the influence of shape on LSPR was considered, but changes in electron density and interband transitions will also play a role but to a lesser degree in cubes.¹⁰⁵ The tip mode dominates the overall change of the optical response, which is demonstrated by the

amplitude and distance between the positive and negative ΔA peaks. The D-SLRs of both tip and face modes generate similar patterns in both TE and TM excitation, including the OP mode. The Q-SLR available in TM excitation is most strongly affected; $+\Delta A$ contributions from the tip and face mode almost do not overlap in energy. This strong contrast difference between the Q-SLRs of the tip and face modes could be caused by the Fano lineshape of quadrupolar modes,⁸ which is very sensitive to changes in the shape of the corners and edges of nanocubes.¹⁴²

The simulated ΔA spectra from 0° and 30° (TM/TE) illumination schemes were compared to the $\Lambda = 300$ nm arrays in the experiments (**Figure 26B**). The focus was on the D-SLR because its features are well within the bandwidth of the probe in the experimental setup. Under normal excitation, both arrays cause the SLR to red shift versus the un-deformed nanocube array, matching the shape and general shift in the experiment. The experimental trace also features a slightly asymmetrical line shape, indicating a broadening of the SLR peak. TE and TM excitation generated slightly weaker red shifting of the SLR in the simulated arrays. Probing at an angle and especially at the sharpest OP mode wavelength enables to exploit the narrow line shape of the SLR: even though the shift is smaller, the amplitude of the signal is larger than the normal case, because even very small changes of a sharp feature can generate strong TAS signals. Overall, the simulations have an excellent qualitative match with the experiments, even with the strong deformation of the simulated eigenmodes. These results indicate that the dynamic shape of the nanoparticle should be considered when designing SLR-employing devices for ultrafast applications. Indeed, SLRs could be designed with strong ΔA that modulate the loss of the SLR. This may enable pulsed light emission at gigahertz frequencies in a gain medium with sufficient population inversion.

5. CONCLUSIONS

1. A microfluidic add-on device, featuring a static three-port mixer based on the Tesla valve structure, was designed and optimized for the capillary force assisted particle assembly system and implemented in alumina. It was found that femtosecond laser ablation can be used to produce microfluidic structures in alumina efficiently, and microfluidic modeling can be used to predict the output concentration in microfluidic devices of this type.
 - a. The finite element method was used to explain and optimize the mixer's performance, and it was found that the structure angle with respect to the channel axis has the highest impact on it. Considering these results, the optimal structure parameters ($\alpha = 45^\circ$, $\beta = 0^\circ$, $L = 1200 \mu\text{m}$, $D = 480 \mu\text{m}$, $O = 0 \mu\text{m}$) for the full-scale device were defined.
 - b. The author of the dissertation has introduced a novel approach to produce microfluidic structures in unorthodox materials and used femtosecond laser micromachining to implement the designed structure in exceptionally hard and chemically inert material, i.e., alumina. The processing conditions were optimized for processing rate and surface quality: 84.4% pulse overlap, 11.2 J/cm^2 energy density resulted in $165 \mu\text{m}^3/\text{pulse}$ volume ablation rate with reasonable surface finish.
 - c. Microfluidic experiments on a complete device matched the modelled flow geometry curves. This proved that the selected microfabrication method is a viable way to produce chemically resistant microfluidic structures. Furthermore, based on this good match, it was concluded that the numerically calculated values could serve as a guide to select appropriate flow rates for capillary force assisted particle assembly.
2. Monodisperse Ag nanocubes and cuboctahedra were assembled into lithographically predefined templates using capillary force assisted nanoparticle assembly and generated strong surface lattice resonances. It has been established that plasmonic lattices with long-range order and single particle resolution can be produced via this method and can generate high-quality extinction peaks.
 - a. The capillary force assisted nanoparticle assembly method was improved to achieve an exceptional assembly yield (>99% filled traps) at a large scale (>1 cm²) with long range single particle control in dense patterns. $123 \pm 2 \text{ nm}$ edge length synthesized Ag cuboctahedra were deposited into 600 nm center-to-center hexagonal patterns, and $77 \pm 3 \text{ nm}$ edge length synthesized Ag nanocubes were deposited into 300, 350, and 400 nm center-to-center square patterns.
 - b. A surface lattice resonance has been registered for the first time in a self-assembled system. Numerical computations confirmed its hybrid plasmonic-photonic nature. The author has performed a thorough analysis and characterization of energy and in-plane wavevector maps and explained the dependencies on pattern orientation and incident light polarization. This

out-of-plane case, but the latter has the advantage of narrower spectral linewidth.

- c. The dominant eigenmodes have been determined via finite element modelling, and they were used to show how the dynamic shape of each individual mode affects the surface lattice resonance over time in electromagnetic simulations. The impact was found to be significant and matched experimental transient absorbance data. This shows that the dynamic nature of metal nanostructures must be considered when designing SLR-based devices for potential applications in active plasmonics and nanophotonics in the gigahertz frequency.

6. ACKNOWLEDGEMENTS

The research presented in this dissertation has been mostly conducted at the Institute of Materials Science of Kaunas University of Technology. The author of the dissertation would like to first thank the colleagues and co-workers who were very friendly and supportive and made the Institute a great place to work.

Specifically, the author wants to express his gratitude to Prof. Sigitas Tamulevičius and Prof. Tomas Tamulevičius for continuous support, starting from the first steps in the labs as an undergraduate student all the way up to finishing this dissertation. They always encouraged to strive for the best, were exceptionally patient to read the author's work for a substantial number of times and always showed interest in it.

Most of the outstanding results and publications in top journals could not have been possible without the help of Dr. Joel Henzie from the National Institute for Materials Science in Tsukuba, Japan. He is an exceptional scientist as well as a friendly, thoughtful, and honest person. The author of the dissertation is proud to say that he helped him to grow and improve as a researcher for which he is thankful.

On a more personal note, the author is extremely thankful for the chance that allowed him to meet his fiancée Paulina. She stood by his side every single day during these past 4 years, supported him in every step, and gave him a reason not to stay at work for too long.

Most importantly, the author wants to thank his mother and father, who set him up for a career as a scientist from his very first appearance on Earth.

7. REFERENCES

- (1) BARNES, W. L.; DEREUX, A.; EBBESEN, T. W. Surface Plasmon Subwavelength Optics. *Nature* **2003**, *424* (6950), 824–830.
- (2) SCHULLER, J. A.; BARNARD, E. S.; CAI, W.; JUN, Y. C.; WHITE, J. S.; BRONGERSMA, M. L. Plasmonics for Extreme Light Concentration and Manipulation. *Nat. Mater.* **2010**, *9* (3), 193–204.
- (3) HENZIE, J.; LEE, J.; LEE, M. H.; HASAN, W.; ODOM, T. W. Nanofabrication of Plasmonic Structures. *Annu. Rev. Phys. Chem.* **2009**, *60* (1), 147–165.
- (4) ANKER, J. N.; HALL, W. P.; LYANDRES, O.; SHAH, N. C.; ZHAO, J.; VAN DUYN, R. P. Biosensing with Plasmonic Nanosensors. *Nat. Mater.* **2008**, *7* (6), 442–453.
- (5) MAYER, K. M.; HAFNER, J. H. Localized Surface Plasmon Resonance Sensors. *Chem. Rev.* **2011**, *111* (6), 3828–3857.
- (6) FUCHS, R. Theory of the Optical Properties of Ionic Crystal Cubes. *Phys. Rev. B* **1975**, *11* (4), 1732–1740.
- (7) CORTIE, M. B.; LIU, F.; ARNOLD, M. D.; NIIDOME, Y. Multimode Resonances in Silver Nanocuboids. *Langmuir* **2012**, *28* (24), 9103–9112.
- (8) ZHANG, S.; BAO, K.; HALAS, N. J.; XU, H.; NORDLANDER, P. Substrate-Induced Fano Resonances of a Plasmonic Nanocube: A Route to Increased-Sensitivity Localized Surface Plasmon Resonance Sensors Revealed. *Nano Lett.* **2011**, *11* (4), 1657–1663.
- (9) SHERRY, L. J.; CHANG, S.-H.; SCHATZ, G. C.; VAN DUYN, R. P.; WILEY, B. J.; XIA, Y. Localized Surface Plasmon Resonance Spectroscopy of Single Silver Nanocubes. *Nano Lett.* **2005**, *5* (10), 2034–2038.
- (10) NICOLETTI, O.; DE LA PEÑA, F.; LEARY, R. K.; HOLLAND, D. J.; DUCATI, C.; MIDGLEY, P. A. Three-Dimensional Imaging of Localized Surface Plasmon Resonances of Metal Nanoparticles. *Nature* **2013**, *502* (7469), 80–84.
- (11) ZHANG, H.; KINNEAR, C.; MULVANEY, P. Fabrication of Single-Nanocrystal Arrays. *Adv. Mater.* **2020**, *32* (18), 1904551.
- (12) LIN, Q.-Y.; LI, Z.; BROWN, K. A.; O'BRIEN, M. N.; ROSS, M. B.; ZHOU, Y.; BUTUN, S.; CHEN, P.-C.; SCHATZ, G. C.; DRAVID, V. P.; AYDIN, K.; MIRKIN, C. A. Strong Coupling between Plasmonic Gap Modes and Photonic Lattice Modes in DNA-Assembled Gold Nanocube Arrays. *Nano Lett.* **2015**, *15* (7), 4699–4703.
- (13) LIN, Q.-Y.; MASON, J. A.; LI, Z.; ZHOU, W.; O'BRIEN, M. N.; BROWN, K. A.; JONES, M. R.; BUTUN, S.; LEE, B.; DRAVID, V. P.; AYDIN, K.; MIRKIN, C. A. Building Superlattices from Individual Nanoparticles via Template-Confined DNA-Mediated Assembly. *Science* (80-.). **2018**, *359* (6376), 669–672.
- (14) ALEXANDER, K. D.; SKINNER, K.; ZHANG, S.; WEI, H.; LOPEZ, R. Tunable SERS in Gold Nanorod Dimers through Strain Control on an Elastomeric Substrate. *Nano Lett.* **2010**, *10* (11), 4488–4493.
- (15) YANG, A.; HRYN, A. J.; BOURGEOIS, M. R.; LEE, W.-K.; HU, J.; SCHATZ, G. C.; ODOM, T. W. Programmable and Reversible Plasmon Mode Engineering. *Proc. Natl. Acad. Sci.* **2016**, *113* (50), 14201–14206.
- (16) MALYNYCH, S.; CHUMANOV, G. Light-Induced Coherent Interactions between Silver Nanoparticles in Two-Dimensional Arrays. *J. Am. Chem. Soc.* **2003**, *125* (10), 2896–2898.
- (17) FLAURAUD, V.; MASTRANGELI, M.; BERNASCONI, G. D.; BUTET, J.; ALEXANDER, D. T.

- L.; SHAHRABI, E.; MARTIN, O. J. F.; BRUGGER, J. Nanoscale Topographical Control of Capillary Assembly of Nanoparticles. *Nat. Nanotechnol.* **2017**, *12* (1), 73–80.
- (18) NI, S.; ISA, L.; WOLF, H. Capillary Assembly as a Tool for the Heterogeneous Integration of Micro- and Nanoscale Objects. *Soft Matter* **2018**, *14* (16), 2978–2995.
- (19) HANSKE, C.; TEBBE, M.; KUTTNER, C.; BIEBER, V.; TSUKRUK, V. V.; CHANANA, M.; KÖNIG, T. A. F.; FERY, A. Strongly Coupled Plasmonic Modes on Macroscopic Areas via Template-Assisted Colloidal Self-Assembly. *Nano Lett.* **2014**, *14* (12), 6863–6871.
- (20) MAYER, M.; TEBBE, M.; KUTTNER, C.; SCHNEPF, M. J.; KÖNIG, T. A. F.; FERY, A. Template-Assisted Colloidal Self-Assembly of Macroscopic Magnetic Metasurfaces. *Faraday Discuss.* **2016**, *191*, 159–176.
- (21) MALAQUIN, L.; KRAUS, T.; SCHMID, H.; DELAMARCHE, E.; WOLF, H. Controlled Particle Placement through Convective and Capillary Assembly. *Langmuir* **2007**, *23* (23), 11513–11521.
- (22) VIRGANAVIČIUS, D.; JUODĖNAS, M.; TAMULEVIČIUS, T.; SCHIFT, H.; TAMULEVIČIUS, S. Investigation of Transient Dynamics of Capillary Assisted Particle Assembly Yield. *Appl. Surf. Sci.* **2017**, *406* (11), 136–143.
- (23) HENZIE, J.; ANDREWS, S. C.; LING, X. Y. Y.; LI, Z.; YANG, P. Oriented Assembly of Polyhedral Plasmonic Nanoparticle Clusters. *Proc. Natl. Acad. Sci.* **2013**, *110* (17), 6640–6645.
- (24) KUEMIN, C.; NOWACK, L.; BOZANO, L.; SPENCER, N. D.; WOLF, H. Oriented Assembly of Gold Nanorods on the Single-Particle Level. *Adv. Funct. Mater.* **2012**, *22* (4), 702–708.
- (25) GREYBUSH, N. J.; SABOKTAKIN, M.; YE, X.; DELLA GIOVAMPAOLA, C.; OH, S. J.; BERRY, N. E.; ENGHETA, N.; MURRAY, C. B.; KAGAN, C. R. Plasmon-Enhanced Upconversion Luminescence in Single Nanophosphor–Nanorod Heterodimers Formed through Template-Assisted Self-Assembly. *ACS Nano* **2014**, *8* (9), 9482–9491.
- (26) NI, S.; KLEIN, M. J. K.; SPENCER, N. D.; WOLF, H. Capillary Assembly of Cross-Gradient Particle Arrays Using a Microfluidic Chip. *Microelectron. Eng.* **2015**, *141*, 12–16.
- (27) NI, S.; KLEIN, M. J. K.; SPENCER, N. D.; WOLF, H. Cascaded Assembly of Complex Multiparticle Patterns. *Langmuir* **2014**, *30* (1), 90–95.
- (28) KLEIN, M. J. K.; KUEMIN, C.; TAMULEVICIUS, T.; MANNING, M.; WOLF, H. Note: A Microfluidic Chip Setup for Capillarity-Assisted Particle Assembly. *Rev. Sci. Instrum.* **2012**, *83* (8), 086109.
- (29) MARASSO, S. L.; GIURI, E.; CANAVESE, G.; CASTAGNA, R.; QUAGLIO, M.; FERRANTE, I.; PERRONE, D.; COCUZZA, M. A Multilevel Lab on Chip Platform for DNA Analysis. *Biomed. Microdevices* **2011**, *13* (1), 19–27.
- (30) XIA, H. M.; WAN, S. Y. M.; SHU, C.; CHEW, Y. T. Chaotic Micromixers Using Two-Layer Crossing Channels to Exhibit Fast Mixing at Low Reynolds Numbers. *Lab Chip* **2005**, *5* (7), 748–755.
- (31) BHAGAT, A. A. S.; PETERSON, E. T. K.; PAPAUTSKY, I. A Passive Planar Micromixer with Obstructions for Mixing at Low Reynolds Numbers. *J. Micromechanics Microengineering* **2007**, *17* (5), 1017–1024.
- (32) WANG, S.; HUANG, X.; YANG, C. Mixing Enhancement for High Viscous Fluids in a Microfluidic Chamber. *Lab Chip* **2011**, *11* (12), 2081–2087.

- (33) NGUYEN, N. T.; WU, Z. Micromixers - A Review. *J. Micromechanics Microengineering* **2005**, *15* (2), R1–R16.
- (34) LEE, C. Y.; CHANG, C. L.; WANG, Y. N.; FU, L. M. Microfluidic Mixing: A Review. *Int. J. Mol. Sci.* **2011**, *12* (5), 3263–3287.
- (35) SONATO, A.; AGOSTINI, M.; RUFFATO, G.; GAZZOLA, E.; LIUNI, D.; GRECO, G.; TRAVAGLIATI, M.; CECCHINI, M.; ROMANATO, F. A Surface Acoustic Wave (SAW)-Enhanced Grating-Coupling Phase-Interrogation Surface Plasmon Resonance (SPR) Microfluidic Biosensor. *Lab Chip* **2016**, *16* (7), 1224–1233.
- (36) LEE, C.-Y.; CHANG, T.-C.; WANG, S.-C.; CHIEN, C.-W.; CHENG, C.-W. Using Femtosecond Laser to Fabricate Highly Precise Interior Three-Dimensional Microstructures in Polymeric Flow Chip. *Biomicrofluidics* **2010**, *4* (4), 046502.
- (37) MATSUBARA, K.; NARUMI, T. Microfluidic Mixing Using Unsteady Electroosmotic Vortices Produced by a Staggered Array of Electrodes. *Chem. Eng. J.* **2016**, *288*, 638–647.
- (38) VENANCIO-MARQUES, A.; BARBAUD, F.; BAIGL, D. Microfluidic Mixing Triggered by an External LED Illumination. *J. Am. Chem. Soc.* **2013**, *135* (8), 3218–3223.
- (39) WEN, C. Y.; YEH, C. P.; TSAI, C. H.; FU, L. M. Rapid Magnetic Microfluidic Mixer Utilizing AC Electromagnetic Field. *Electrophoresis* **2009**, *30* (24), 4179–4186.
- (40) JUODĖNAS, M.; HOYLAND, J. D.; JURENAS, V.; BUBULIS, A. Piezoelectric Actuation for Microfluidic Cell Sorting. *J. Meas. Eng.* **2013**, *1* (4), 228–232.
- (41) CHUNG, Y. C.; HSU, Y. L.; JEN, C. P.; LU, M. C.; LIN, Y. C. Design of Passive Mixers Utilizing Microfluidic Self-Circulation in the Mixing Chamber. *Lab Chip* **2004**, *4* (1), 70–77.
- (42) HONG, C. C.; CHOI, J. W.; AHN, C. H. A Novel In-Plane Passive Microfluidic Mixer with Modified Tesla Structures. *Lab Chip* **2004**, *4* (2), 109–113.
- (43) PARK, S. G.; LEE, S. K.; MOON, J. H.; YANG, S. M. Holographic Fabrication of Three-Dimensional Nanostructures for Microfluidic Passive Mixing. *Lab Chip* **2009**, *9* (21), 3144–3150.
- (44) LIN, Y. C.; CHUNG, Y. C.; WU, C. Y. Mixing Enhancement of the Passive Microfluidic Mixer with J-Shaped Baffles in the Tee Channel. *Biomed. Microdevices* **2007**, *9* (2), 215–221.
- (45) LEE, C. Y.; WANG, W. T.; LIU, C. C.; FU, L. M. Passive Mixers in Microfluidic Systems: A Review. *Chem. Eng. J.* **2016**, *288*, 146–160.
- (46) KUEMIN, C.; STUTZ, R.; SPENCER, N. D.; WOLF, H. Precise Placement of Gold Nanorods by Capillary Assembly. *Langmuir* **2011**, *27* (10), 6305–6310.
- (47) LEE, J. N.; PARK, C.; WHITESIDES, G. M. Solvent Compatibility of Poly(Dimethylsiloxane)-Based Microfluidic Devices. *Anal. Chem.* **2003**, *75* (23), 6544–6554.
- (48) YOSHIMURA, M.; BOWEN, H. K. Electrical Breakdown Strength of Alumina at High Temperatures. *J. Am. Ceram. Soc.* **1981**, *64* (7), 404–410.
- (49) DÖRRE, E.; HÜBNER, H. *Alumina - Processing, Properties, and Applications*; Springer-Verlag Berlin Heidelberg, 1984.
- (50) SURIANO, R.; KUZNETSOV, A.; EATON, S. M.; KIYAN, R.; CERULLO, G.; OSELLAME, R.; CHICHKOV, B. N.; LEVI, M.; TURRI, S. Femtosecond Laser Ablation of Polymeric Substrates for the Fabrication of Microfluidic Channels. *Appl. Surf. Sci.* **2011**, *257*

- (14), 6243–6250.
- (51) WADDELL, E. A. Laser Ablation as a Fabrication Technique for Microfluidic Devices. In *Microfluidic Techniques*; Humana Press: New Jersey, 2006; Vol. 321, pp 27–38.
- (52) CHEN, Q.; CHEN, Q.; MACCIONI, G.; SACCO, A.; SCALTRITO, L.; FERRARIS, M.; FERRERO, S. Fabrication of Large-Area Microfluidics Structures on Glass by Imprinting and Diode-Pumped Solid State Laser Writing Techniques. *Microsyst. Technol.* **2011**, *17* (10–11), 1611–1619.
- (53) CHEN, Q.; CHEN, Q.; MACCIONI, G.; SACCO, A.; FERRERO, S.; SCALTRITO, L. Fabrication of Microstructures on Glass by Imprinting in Conventional Furnace for Lab-on-Chip Application. *Microelectron. Eng.* **2012**, *95*, 90–101.
- (54) KRAVETS, V. G.; KABASHIN, A. V.; BARNES, W. L.; GRIGORENKO, A. N. Plasmonic Surface Lattice Resonances: A Review of Properties and Applications. *Chem. Rev.* **2018**, *118* (12), 5912–5951.
- (55) MARKEL, V. A. Coupled-Dipole Approach to Scattering of Light from a One-Dimensional Periodic Dipole Structure. *J. Mod. Opt.* **1993**, *40* (11), 2281–2291.
- (56) ZOU, S.; JANEL, N.; SCHATZ, G. C. Silver Nanoparticle Array Structures That Produce Remarkably Narrow Plasmon Lineshapes. *J. Chem. Phys.* **2004**, *120* (23), 10871–10875.
- (57) CHERQUI, C.; BOURGEOIS, M. R.; WANG, D.; SCHATZ, G. C. Plasmonic Surface Lattice Resonances: Theory and Computation. *Acc. Chem. Res.* **2019**, *52* (9), 2548–2558.
- (58) WANG, W.; RAMEZANI, M.; VÄKEVÄINEN, A. I.; TÖRMÄ, P.; RIVAS, J. G.; ODOM, T. W. The Rich Photonic World of Plasmonic Nanoparticle Arrays. *Mater. Today* **2018**, *21* (3), 303–314.
- (59) MULVANEY, P. Surface Plasmon Spectroscopy of Nanosized Metal Particles. *Langmuir* **1996**, *12* (3), 788–800.
- (60) HICKS, E. M.; ZOU, S.; SCHATZ, G. C.; SPEARS, K. G.; VAN DUYN, R. P.; GUNNARSSON, L.; RINDZEVICIUS, T.; KASEMO, B.; KÄLL, M. Controlling Plasmon Line Shapes through Diffractive Coupling in Linear Arrays of Cylindrical Nanoparticles Fabricated by Electron Beam Lithography. *Nano Lett.* **2005**, *5* (6), 1065–1070.
- (61) KRAVETS, V. G.; SCHEDIN, F.; PISANO, G.; THACKRAY, B.; THOMAS, P. A.; GRIGORENKO, A. N. Nanoparticle Arrays: From Magnetic Response to Coupled Plasmon Resonances. *Phys. Rev. B* **2014**, *90* (12), 125445.
- (62) AUGUÉ, B.; BARNES, W. L. Collective Resonances in Gold Nanoparticle Arrays. *Phys. Rev. Lett.* **2008**, *101* (14), 143902.
- (63) CHU, Y.; SCHONBRUN, E.; YANG, T.; CROZIER, K. B. Experimental Observation of Narrow Surface Plasmon Resonances in Gold Nanoparticle Arrays. *Appl. Phys. Lett.* **2008**, *93* (18), 181108.
- (64) MARKEL, V. A. Divergence of Dipole Sums and the Nature of Non-Lorentzian Exponentially Narrow Resonances in One-Dimensional Periodic Arrays of Nanospheres. *J. Phys. B At. Mol. Opt. Phys.* **2005**, *38* (7), L115–L121.
- (65) RODRIGUEZ, S. R. K.; SCHAAFSMA, M. C. C.; BERRIER, A.; GÓMEZ RIVAS, J.; GO, J. Collective Resonances in Plasmonic Crystals: Size Matters. *Phys. B Condens. Matter* **2012**, *407* (20), 4081–4085.
- (66) HUMPHREY, A. D.; BARNES, W. L. Plasmonic Surface Lattice Resonances on Arrays of Different Lattice Symmetry. *Phys. Rev. B* **2014**, *90* (7), 075404.

- (67) KRAVETS, V. G.; SCHEDIN, F.; GRIGORENKO, A. N. Extremely Narrow Plasmon Resonances Based on Diffraction Coupling of Localized Plasmons in Arrays of Metallic Nanoparticles. *Phys. Rev. Lett.* **2008**, *101* (8), 087403.
- (68) HENZIE, J.; LEE, M. H.; ODOM, T. W. Multiscale Patterning of Plasmonic Metamaterials. *Nat. Nanotechnol.* **2007**, *2* (9), 549–554.
- (69) ZHOU, W.; ODOM, T. W. Tunable Subradiant Lattice Plasmons by Out-of-Plane Dipolar Interactions. *Nat. Nanotechnol.* **2011**, *6* (7), 423–427.
- (70) GOERLITZER, E. S. A.; MOHAMMADI, R.; NECHAYEV, S.; VOLK, K.; REY, M.; BANZER, P.; KARG, M.; VOGEL, N. Chiral Surface Lattice Resonances. *Adv. Mater.* **2020**, 2001330.
- (71) WANG, D.; BOURGEOIS, M. R.; GUAN, J.; FUMANI, A. K.; SCHATZ, G. C.; ODOM, T. W. Lasing from Finite Plasmonic Nanoparticle Lattices. *ACS Photonics* **2020**, *7* (3), 630–636.
- (72) GUAN, J.; SAGAR, L. K.; LI, R.; WANG, D.; BAPPI, G.; WATKINS, N. E.; BOURGEOIS, M. R.; LEVINA, L.; FAN, F.; HOOGLAND, S.; VOZNYI, O.; MARTINS DE PINA, J.; SCHALLER, R. D.; SCHATZ, G. C.; SARGENT, E. H.; ODOM, T. W. Engineering Directionality in Quantum Dot Shell Lasing Using Plasmonic Lattices. *Nano Lett.* **2020**, *20* (2), 1468–1474.
- (73) LIU, Y.; TEITELBOIM, A.; FERNANDEZ-BRAVO, A.; YAO, K.; ALTOE, M. V. P.; ALONI, S.; ZHANG, C.; COHEN, B. E.; SCHUCK, P. J.; CHAN, E. M. Controlled Assembly of Upconverting Nanoparticles for Low-Threshold Microlasers and Their Imaging in Scattering Media. *ACS Nano* **2020**, *14* (2), 1508–1519.
- (74) VASKIN, A.; KOLKOWSKI, R.; KOENDERINK, A. F.; STAUDE, I. Light-Emitting Metasurfaces. *Nanophotonics* **2019**, *8* (7), 1151–1198.
- (75) CHEN, W.; TYMCHENKO, M.; GOPALAN, P.; YE, X.; WU, Y.; ZHANG, M.; MURRAY, C. B.; ALU, A.; KAGAN, C. R. Large-Area Nanoimprinted Colloidal Au Nanocrystal-Based Nanoantennas for Ultrathin Polarizing Plasmonic Metasurfaces. *Nano Lett.* **2015**, *15* (8), 5254–5260.
- (76) MA, Z.; NI, X.; ZHANG, W.; JIANG, X.; YANG, H.; YU, J.; WANG, W.; XU, L.; XU, J.; CHEN, K.; FENG, D. Hexagonal Ag Nanoarrays Induced Enhancement of Blue Light Emission from Amorphous Oxidized Silicon Nitride via Localized Surface Plasmon Coupling. *Opt. Express* **2014**, *22* (23), 28180.
- (77) VECCHI, G.; GIANNINI, V.; GÓMEZ RIVAS, J. Shaping the Fluorescent Emission by Lattice Resonances in Plasmonic Crystals of Nanoantennas. *Phys. Rev. Lett.* **2009**, *102* (14), 146807.
- (78) ADATO, R.; YANIK, A. A.; AMSDEN, J. J.; KAPLAN, D. L.; OMENETTO, F. G.; HONG, M. K.; ERRAMILI, S.; ALTUG, H. Ultra-Sensitive Vibrational Spectroscopy of Protein Monolayers with Plasmonic Nanoantenna Arrays. *Proc. Natl. Acad. Sci.* **2009**, *106* (46), 19227–19232.
- (79) YANIK, A. A.; CETIN, A. E.; HUANG, M.; ARTAR, A.; MOUSAVI, S. H.; KHANIKAEV, A.; CONNOR, J. H.; SHVETS, G.; ALTUG, H. Seeing Protein Monolayers with Naked Eye through Plasmonic Fano Resonances. *Proc. Natl. Acad. Sci.* **2011**, *108* (29), 11784–11789.
- (80) HAKALA, T. K.; REKOLA, H. T.; VÄKEVÄINEN, A. I.; MARTIKAINEN, J.-P. P.; NEČADA, M.; MOILANEN, A. J.; TÖRMÄ, P. Lasing in Dark and Bright Modes of a Finite-Sized Plasmonic Lattice. *Nat. Commun.* **2017**, *8*, 1–7.

- (81) ZHOU, W.; DRIDI, M.; SUH, J. Y.; KIM, C. H.; CO, D. T.; WASIELEWSKI, M. R.; SCHATZ, G. C.; ODOM, T. W. Lasing Action in Strongly Coupled Plasmonic Nanocavity Arrays. *Nat. Nanotechnol.* **2013**, *8* (7), 506–511.
- (82) RAMEZANI, M.; HALPIN, A.; FERNÁNDEZ-DOMÍNGUEZ, A. I.; FEIST, J.; RODRIGUEZ, S. R.-K.; GARCIA-VIDAL, F. J.; GÓMEZ RIVAS, J. Plasmon-Exciton-Polariton Lasing. *Optica* **2017**, *4* (1), 31.
- (83) SCHOKKER, A. H.; KOENDERINK, A. F. Lasing at the Band Edges of Plasmonic Lattices. *Phys. Rev. B* **2014**, *90* (15), 155452.
- (84) LEE, B.; PARK, J.; HAN, G. H.; EE, H.-S.; NAYLOR, C. H.; LIU, W.; JOHNSON, A. T. C.; AGARWAL, R. Fano Resonance and Spectrally Modified Photoluminescence Enhancement in Monolayer MoS₂ Integrated with Plasmonic Nanoantenna Array. *Nano Lett.* **2015**, *15* (5), 3646–3653.
- (85) KWAK, E.-S.; HENZIE, J.; CHANG, S.; GRAY, S. K.; SCHATZ, G. C.; ODOM, T. W. Surface Plasmon Standing Waves in Large-Area Subwavelength Hole Arrays. *Nano Lett.* **2005**, *5* (10), 1963–1967.
- (86) CHEN, K.-P.; DRACHEV, V. P.; BORNEMAN, J. D.; KILDISHEV, A. V.; SHALAEV, V. M. Drude Relaxation Rate in Grained Gold Nanoantennas. *Nano Lett.* **2010**, *10* (3), 916–922.
- (87) KIPPENBERG, T. J.; VAHALA, K. J. Cavity Opto-Mechanics. *Opt. Express* **2007**, *15* (25), 17172.
- (88) HARTLAND, G. V. Optical Studies of Dynamics in Noble Metal Nanostructures. *Chem. Rev.* **2011**, *111* (6), 3858–3887.
- (89) PELTON, M.; SADER, J. E.; BURGIN, J.; LIU, M.; GUYOT-SIONNEST, P.; GOSZTOLA, D. Damping of Acoustic Vibrations in Gold Nanoparticles. *Nat. Nanotechnol.* **2009**, *4* (8), 492–495.
- (90) WU, H.-J.; HENZIE, J.; LIN, W.-C.; RHODES, C.; LI, Z.; SARTOREL, E.; THORNER, J.; YANG, P.; GROVES, J. T. Membrane-Protein Binding Measured with Solution-Phase Plasmonic Nanocube Sensors. *Nat. Methods* **2012**, *9* (12), 1189–1191.
- (91) MALDOVAN, M. Sound and Heat Revolutions in Phononics. *Nature* **2013**, *503* (7475), 209–217.
- (92) ATWATER, H. A.; POLMAN, A. Plasmonics for Improved Photovoltaic Devices. *Nat. Mater.* **2010**, *9* (3), 205–213.
- (93) HARUTYUNYAN, H.; MARTINSON, A. B. F.; ROSENMANN, D.; KHORASHAD, L. K.; BESTEIRO, L. V.; GOVOROV, A. O.; WIEDERRECHT, G. P. Anomalous Ultrafast Dynamics of Hot Plasmonic Electrons in Nanostructures with Hot Spots. *Nat. Nanotechnol.* **2015**, *10* (9), 770–774.
- (94) LI, J.; CUSHING, S. K.; MENG, F.; SENTY, T. R.; BRISTOW, A. D.; WU, N. Plasmon-Induced Resonance Energy Transfer for Solar Energy Conversion. *Nat. Photonics* **2015**, *9* (9), 601–607.
- (95) WU, K.; CHEN, J.; MCBRIDE, J. R.; LIAN, T. Efficient Hot-Electron Transfer by a Plasmon-Induced Interfacial Charge-Transfer Transition. *Science* (80-.). **2015**, *349* (6248), 632–635.
- (96) LINIC, S.; ASLAM, U.; BOERIGTER, C.; MORABITO, M. Erratum: Photochemical Transformations on Plasmonic Metal Nanoparticles. *Nat. Mater.* **2015**, *14* (7), 744–744.
- (97) WU, K.; LIAN, T. Quantum Confined Colloidal Nanorod Heterostructures for Solar-to-

- Fuel Conversion. *Chem. Soc. Rev.* **2016**, *45* (14), 3781–3810.
- (98) PECKUS, D.; RONG, H.; STANKEVIČIUS, L.; JUODĖNAS, M.; TAMULEVIČIUS, S.; TAMULEVIČIUS, T.; HENZIE, J. Hot Electron Emission Can Lead to Damping of Optomechanical Modes in Core–Shell Ag@TiO₂ Nanocubes. *J. Phys. Chem. C* **2017**, *121* (43), 24159–24167.
- (99) LINK, S.; EL-SAYED, M. A. Spectral Properties and Relaxation Dynamics of Surface Plasmon Electronic Oscillations in Gold and Silver Nanodots and Nanorods. *J. Phys. Chem. B* **1999**, *103* (40), 8410–8426.
- (100) VOISIN, C.; DEL FATTI, N.; CHRISTOFILOS, D.; VALLÉE, F. Ultrafast Electron Dynamics and Optical Nonlinearities in Metal Nanoparticles. *J. Phys. Chem. B* **2001**, *105* (12), 2264–2280.
- (101) BESTEIRO, L. V.; KONG, X.-T.; WANG, Z.; HARTLAND, G.; GOVOROV, A. O. Understanding Hot-Electron Generation and Plasmon Relaxation in Metal Nanocrystals: Quantum and Classical Mechanisms. *ACS Photonics* **2017**, *4* (11), 2759–2781.
- (102) PETROVA, H.; LIN, C.-H. H.; DE LIEJER, S.; HU, M.; MCLELLAN, J. M.; SIEKKINEN, A. R.; WILEY, B. J.; MARQUEZ, M.; XIA, Y.; SADER, J. E.; HARTLAND, G. V. Time-Resolved Spectroscopy of Silver Nanocubes: Observation and Assignment of Coherently Excited Vibrational Modes. *J. Chem. Phys.* **2007**, *126* (9), 094709.
- (103) BAIDA, H.; MONGIN, D.; CHRISTOFILOS, D.; BACHELIER, G.; CRUT, A.; MAIOLI, P.; DEL FATTI, N.; VALLÉE, F. Ultrafast Nonlinear Optical Response of a Single Gold Nanorod near Its Surface Plasmon Resonance. *Phys. Rev. Lett.* **2011**, *107* (5), 057402.
- (104) VOISIN, C.; DEL FATTI, N.; CHRISTOFILOS, D.; VALLÉE, F. Time-Resolved Investigation of the Vibrational Dynamics of Metal Nanoparticles. *Appl. Surf. Sci.* **2000**, *164* (1–4), 131–139.
- (105) AHMED, A.; PELTON, M.; GUEST, J. R. Understanding How Acoustic Vibrations Modulate the Optical Response of Plasmonic Metal Nanoparticles. *ACS Nano* **2017**, *11* (9), 9360–9369.
- (106) ANTONELLI, G. A.; MARIS, H. J.; MALHOTRA, S. G.; HARPER, J. M. E. Picosecond Ultrasonics Study of the Vibrational Modes of a Nanostructure. *J. Appl. Phys.* **2002**, *91* (5), 3261–3267.
- (107) STALEVA, H.; HARTLAND, G. V. Transient Absorption Studies of Single Silver Nanocubes. *J. Phys. Chem. C* **2008**, *112* (20), 7535–7539.
- (108) ZHANG, H.; GOVOROV, A. O. Optical Generation of Hot Plasmonic Carriers in Metal Nanocrystals: The Effects of Shape and Field Enhancement. *J. Phys. Chem. C* **2014**, *118* (14), 7606–7614.
- (109) TRETNAK, V.; HOHENESTER, U.; KRENN, J. R.; HOHENAU, A. The Role of Particle Size in the Dispersion Engineering of Plasmonic Arrays. *J. Phys. Chem. C* **2020**, *124* (3), 2104–2112.
- (110) ROBILLARD, J.-F.; DEVOS, A.; ROCH-JEUNE, I.; MANTE, P. A. Collective Acoustic Modes in Various Two-Dimensional Crystals by Ultrafast Acoustics: Theory and Experiment. *Phys. Rev. B* **2008**, *78* (6), 064302.
- (111) EICHENFIELD, M.; CHAN, J.; CAMACHO, R. M.; VAHALA, K. J.; PAINTER, O. Optomechanical Crystals. *Nature* **2009**, *462* (7269), 78–82.
- (112) EL-JALLAL, S.; MRABTI, A.; LÉVÊQUE, G.; AKJOUJ, A.; PENNEC, Y.; DJAFARI-ROUHANI, B. Phonon Interaction with Coupled Photonic-Plasmonic Modes in a

- Phoxonic Cavity. *AIP Adv.* **2016**, *6* (12), 122001.
- (113) TAO, A.; SINSERMSUKSAKUL, P.; YANG, P. Polyhedral Silver Nanocrystals with Distinct Scattering Signatures. *Angew. Chemie Int. Ed.* **2006**, *45* (28), 4597–4601.
- (114) HENZIE, J.; GRÜNWARD, M.; WIDMER-COOPER, A.; GEISLER, P. L.; YANG, P. Self-Assembly of Uniform Polyhedral Silver Nanocrystals into Densest Packings and Exotic Superlattices. *Nat. Mater.* **2012**, *11* (2), 131–137.
- (115) TAMULEVIČIUS, T.; ŠIMATONIS, L.; ULČINAS, O.; TAMULEVIČIUS, S.; ŽUKAUSKAS, E.; REKUVIENĖ, R.; MAŽEIKA, L. Micromachining and Validation of the Scanning Acoustic Microscope Spatial Resolution and Sensitivity Calibration Block for 20-230 MHz Frequency Range. *Microscopy* **2016**, *65* (5), 429–437.
- (116) WANG, C. T.; CHEN, Y. M.; HONG, P. A.; WANG, Y. T. Tesla Valves in Micromixers. *Int. J. Chem. React. Eng.* **2014**, *12* (1).
- (117) JUODĖNAS, M.; TAMULEVIČIUS, T.; ULČINAS, O.; TAMULEVIČIUS, S. Implementation of an Optimized Microfluidic Mixer in Alumina Employing Femtosecond Laser Ablation. *J. Micromechanics Microengineering* **2018**, *28* (1), 015013.
- (118) TAMULEVIČIUS, T.; GRAŽULEVIČIŪTĖ, I.; URBONAS, D.; GABALIS, M.; PETRUŠKEVIČIUS, R.; TAMULEVIČIUS, S. Numerical and Experimental Analysis of Optical Response of Sub-Wavelength Period Structure in Carbonaceous Film for Refractive Index Sensing. *Opt. Express* **2014**, *22* (22), 27462.
- (119) GUO, R.; HAKALA, T. K.; TÖRMÄ, P. Geometry Dependence of Surface Lattice Resonances in Plasmonic Nanoparticle Arrays. *Phys. Rev. B* **2017**, *95* (15), 155423.
- (120) JOHNSON, P. B.; CHRISTY, R. W. Optical Constants of the Noble Metals. *Phys. Rev. B* **1972**, *6* (12), 4370–4379.
- (121) BUFFMAN, D. R.; BOHREN, C. F.; HUFFMAN, D. R. Particles Small Compared with the Wavelength. In *Absorption and Scattering of Light by Small Particles*; Wiley-VCH Verlag GmbH: Weinheim, Germany, 1998; pp 130–157.
- (122) MOROZ, A. Depolarization Field of Spheroidal Particles. *J. Opt. Soc. Am. B* **2009**, *26* (3), 517.
- (123) LEONE, C.; GENNA, S.; TAGLIAFERRI, F.; PALUMBO, B.; DIX, M. Experimental Investigation on Laser Milling of Aluminium Oxide Using a 30 W Q-Switched Yb:YAG Fiber Laser. *Opt. Laser Technol.* **2016**, *76* (2016), 127–137.
- (124) JUODĖNAS, M.; TAMULEVIČIUS, T.; HENZIE, J.; ERTS, D.; TAMULEVIČIUS, S. Surface Lattice Resonances in Self-Assembled Arrays of Monodisperse Ag Cuboctahedra. *ACS Nano* **2019**, *13* (8), 9038–9047.
- (125) JUODĖNAS, M.; PECKUS, D.; TAMULEVIČIUS, T.; YAMAUCHI, Y.; TAMULEVIČIUS, S.; HENZIE, J. Effect of Ag Nanocube Optomechanical Modes on Plasmonic Surface Lattice Resonances. *ACS Photonics* **2020**, *7* (11), 3130–3140.
- (126) HAYNES, C. L.; MCFARLAND, A. D.; ZHAO, L.; VAN DUYN, R. P.; SCHATZ, G. C.; GUNNARSSON, L.; PRIKULIS, J.; KASEMO, B.; KÄLL, M. Nanoparticle Optics: The Importance of Radiative Dipole Coupling in Two-Dimensional Nanoparticle Arrays †. *J. Phys. Chem. B* **2003**, *107* (30), 7337–7342.
- (127) HUTTUNEN, M. J.; DOLGALEVA, K.; TÖRMÄ, P.; BOYD, R. W. Ultra-Strong Polarization Dependence of Surface Lattice Resonances with out-of-Plane Plasmon Oscillations. *Opt. Express* **2016**, *24* (25), 28279.
- (128) LI, G. H. Y.; LI, G. Necessary Conditions for Out-of-Plane Lattice Plasmons in Nanoparticle Arrays. *J. Opt. Soc. Am. B* **2019**, *36* (4), 805.

- (129) ZHOU, W.; HUA, Y.; HUNTINGTON, M. D.; ODOM, T. W. Delocalized Lattice Plasmon Resonances Show Dispersive Quality Factors. *J. Phys. Chem. Lett.* **2012**, *3* (10), 1381–1385.
- (130) YANG, X.; XIAO, G.; LU, Y.; LI, G. Narrow Plasmonic Surface Lattice Resonances with Preference to Asymmetric Dielectric Environment. *Opt. Express* **2019**, *27* (18), 25384.
- (131) HUA, Y.; FUMANI, A. K.; ODOM, T. W. Tunable Lattice Plasmon Resonances in 1D Nanogratings. *ACS Photonics* **2019**, *6* (2), 322–326.
- (132) MCMAHON, J. M.; WANG, Y.; SHERRY, L. J.; VAN DUYN, R. P.; MARKS, L. D.; GRAY, S. K.; SCHATZ, G. C. Correlating the Structure, Optical Spectra, and Electrodynamics of Single Silver Nanocubes. *J. Phys. Chem. C* **2009**, *113* (7), 2731–2735.
- (133) MARTY, R.; ARBOUET, A.; GIRARD, C.; MLAYAH, A.; PAILLARD, V.; LIN, V. K.; TEO, S. L.; TRIPATHY, S. Damping of the Acoustic Vibrations of Individual Gold Nanoparticles. *Nano Lett.* **2011**, *11* (8), 3301–3306.
- (134) GOYKHMANN, I.; DESIATOV, B.; KHURGIN, J.; SHAPPIR, J.; LEVY, U. Locally Oxidized Silicon Surface-Plasmon Schottky Detector for Telecom Regime. *Nano Lett.* **2011**, *11* (6), 2219–2224.
- (135) KNIGHT, M. W.; SOBHANI, H.; NORDLANDER, P.; HALAS, N. J. Photodetection with Active Optical Antennas. *Science (80-.)*. **2011**, *332* (6030), 702–704.
- (136) LINIC, S.; CHRISTOPHER, P.; INGRAM, D. B. Plasmonic-Metal Nanostructures for Efficient Conversion of Solar to Chemical Energy. *Nat. Mater.* **2011**, *10* (12), 911–921.
- (137) MUKHERJEE, S.; LIBISCH, F.; LARGE, N.; NEUMANN, O.; BROWN, L. V.; CHENG, J.; LASSITER, J. B.; CARTER, E. A.; NORDLANDER, P.; HALAS, N. J. Hot Electrons Do the Impossible: Plasmon-Induced Dissociation of H₂ on Au. *Nano Lett.* **2013**, *13* (1), 240–247.
- (138) WANG, G.; WANG, X.; LIU, J.; SUN, X. Mesoporous Au/TiO₂ Nanocomposite Microspheres for Visible-Light Photocatalysis. *Chem. - A Eur. J.* **2012**, *18* (17), 5361–5366.
- (139) BRONGERSMA, M. L.; HALAS, N. J.; NORDLANDER, P. Plasmon-Induced Hot Carrier Science and Technology. *Nat. Nanotechnol.* **2015**, *10* (1), 25–34.
- (140) MOSKOVITS, M. The Case for Plasmon-Derived Hot Carrier Devices. *Nat. Nanotechnol.* **2015**, *10* (1), 6–8.
- (141) RYCENGA, M.; LANGILLE, M. R.; PERSONICK, M. L.; OZEL, T.; MIRKIN, C. A. Chemically Isolating Hot Spots on Concave Nanocubes. *Nano Lett.* **2012**, *12* (12), 6218–6222.
- (142) PELLARIN, M.; RAMADE, J.; RYE, J. M.; BONNET, C.; BROYER, M.; LEBEAULT, M.-A.; LERMÉ, J.; MARGUET, S.; NAVARRO, J. R. G.; COTTANCIN, E. Fano Transparency in Rounded Nanocube Dimers Induced by Gap Plasmon Coupling. *ACS Nano* **2016**, *10* (12), 11266–11279.
- (143) YANG, A. S.; CHUANG, F. C.; CHEN, C. K.; LEE, M. H.; CHEN, S. W.; SU, T. L.; YANG, Y. C. A High-Performance Micromixer Using Three-Dimensional Tesla Structures for Bio-Applications. *Chem. Eng. J.* **2015**, *263*, 444–451.
- (144) HOSSAIN, S.; ANSARI, M. A.; HUSAIN, A.; KIM, K. Y. Analysis and Optimization of a Micromixer with a Modified Tesla Structure. *Chem. Eng. J.* **2010**, *158* (2), 305–314.
- (145) TESLA, N. Valvular Conduit, February 1920.

- (146) CHRISTOPHER, P.; INGRAM, D. B.; LINIC, S. Enhancing Photochemical Activity of Semiconductor Nanoparticles with Optically Active Ag Nanostructures: Photochemistry Mediated by Ag Surface Plasmons. *J. Phys. Chem. C* **2010**, *114* (19), 9173–9177.
- (147) GOMATHI DEVI, L.; KAVITHA, R. A Review on Plasmonic Metal@TiO₂ Composite for Generation, Trapping, Storing and Dynamic Vectorial Transfer of Photogenerated Electrons across the Schottky Junction in a Photocatalytic System. *Appl. Surf. Sci.* **2016**, *360*, 601–622.
- (148) MUBEEN, S.; LEE, J.; SINGH, N.; KRÄMER, S.; STUCKY, G. D.; MOSKOVITS, M. An Autonomous Photosynthetic Device in Which All Charge Carriers Derive from Surface Plasmons. *Nat. Nanotechnol.* **2013**, *8* (4), 247–251.
- (149) UNG, T.; LIZ-MARZÁN, L. M.; MULVANEY, P. Controlled Method for Silica Coating of Silver Colloids. Influence of Coating on the Rate of Chemical Reactions. *Langmuir* **1998**, *14* (14), 3740–3748.
- (150) YIN, Y.; LU, Y.; SUN, Y.; XIA, Y. Silver Nanowires Can Be Directly Coated with Amorphous Silica to Generate Well-Controlled Coaxial Nanocables of Silver/Silica. *Nano Lett.* **2002**, *2* (4), 427–430.
- (151) MONGIN, D.; JUVÉ, V.; MAIOLI, P.; CRUT, A.; DEL FATTI, N.; VALLÉE, F.; SÁNCHEZ-IGLESIAS, A.; PASTORIZA-SANTOS, I.; LIZ-MARZÁN, L. M. Acoustic Vibrations of Metal-Dielectric Core–Shell Nanoparticles. *Nano Lett.* **2011**, *11* (7), 3016–3021.
- (152) CRUT, A.; JUVÉ, V.; MONGIN, D.; MAIOLI, P.; DEL FATTI, N.; VALLÉE, F. Vibrations of Spherical Core-Shell Nanoparticles. *Phys. Rev. B* **2011**, *83* (20), 205430.

8. SANTRAUKA

8.1. Įvadas

Plazmonikos mokslas apima šviesos sąveiką su metalinėmis nanostruktūromis. Metalinės nanodalelės gali rezonuoti su šviesa, kurios dažnis artimas natūraliam elektronų plazmos svyravimų dažniui. Šis rezonansas gali hibridizuotis su fotoninėmis modomis, kai nanodalelės išdėstomos į tvarkingas gardeles. Be to, plazmoninės struktūros nėra statinės – po sužadavimo jos keičia formą ir savo optines savybes. Šie ultraspartieji procesai gali pasireikšti ir tvarkinguose nanodalelių masyvuose.

Nanodalelių masyvams gaminti paprastai pasitelkiamos standartinės litografijos technologijos, tačiau šablonais pagrįsti savirankos metodai gali leisti išnaudoti koloidinių nanodalelių privalumus. Nanodalelių saviranka kapiliarinėmis jėgomis yra vienas tokių metodų. Šiuo metodu pagrįstoms sistemoms gali praversti valdymas mikroskystiniais prietaisais. Optimizuotas mikroskystinis prietaisais su efektyvaus maišymo funkcionalumu, pagamintas iš chemiškai atsparios medžiagos, dar nebuvo pasiūlytas.

Periodiškai surikiuotos nanodalelės gali sąveikauti tarpusavyje per fotonines Brego modas, o šis reiškinys vadinamas paviršiaus gardelės rezonansu. Paviršiaus gardelės rezonansas pasižymi itin stipriais elektriniais laukais, galinčiais pasklisti nanodalelių masyvo plokštumoje. Itin mažo spektrinio pločio smailėmis pasižymintys tokių struktūrų optinės sugerties spektrai gali būti valdomi keičiant ir nanodalelių, ir masyvo geometrijos savybes. Visa tai gali būti pasiekta pasinaudojant nanodalelių saviranka, tačiau tai dar nebuvo pademonstruota.

Sužadinus plazmonų rezonansą nanodalelėse, kyla kompleksiška fotofizinių reiškinų kaskada. Gėstant plazmonui, sužadinti elektronai termalizuoja ir sugeneruoja karštų elektronų skirstinį, kurie galop perduoda energiją metalo gardelei (fononams). Pastarieji sukelia gardelės plėtimąsi bei mechaninius virpesius – nanodalelės formos ir dydžio pokyčius. Ši moduliacija gali sąveikauti su vėliau ateinančia šviesa ir generuoti optomechanines modas, kurias galima stebėti skirtuminės sugerties spektroskopijos metodu. Puslaidininkinis nanodalelių apvalkalas galėtų surinkti generuojamus karštus elektronus, kurie vėliau galėtų būti panaudoti katalizei ar cheminio kuro generavimui. Kaip šio energijos pernašos būdo įrodymas galėtų būti spartesnis optomechaninių modų gesimas.

Dinamiškos optomechaninės modos taip pat gali daryti įtaką paviršiaus gardelės rezonansui. Kiekvienos koherentiškai sužadintos dalelės forma masyve kinta dėl sukiamų virpesių. Dėl to paviršiaus gardelės rezonansas gali būti moduluojamas gigahercų dažniu. Tai gali būti panaudota inovatyviuose įrenginiuose, tokiuose kaip pulsuojantys nanolazeriai. Nanodalelių palyginimas suspenduotu ir surikiuotu režimu gali suteikti žinių apie procesus, vykstančius ultrasparčioje laiko skalėje ir fotoninėje erdvės skalėje, o tokių masyvų modeliavimas leidžia nuspėti naujų įrenginių su ultrasparčiomis funkcijomis savybes.

8.1.1. Tikslas

Apibūdinti susintetintų Ag nanodalelių pastovias optines ir ultrasparčias optomechanines savybes, kai jos suspenduotos tirpale arba savirankos būdu surikiuotos į masyvus ant šablonų, tenkinančių Brego sąlygą.

8.1.2. Uždaviniai

1. Sukurti mikroskystinį prietaisą, optimizuotą skysčiams maišyti, galintį veikti su chemiškai agresyviomis terpėmis ir suderinamą su nanodalelių savirankos kapiliarinėmis jėgomis sistema.
2. Sugeneruoti paviršiaus gardelės rezonansą panaudojant susintetintas Ag nanodaleles ir savirankos metodą.
3. Ištirti pastovias optines ir ultrasparčias optomechanines susintetintų Ag nanodalelių su puslaidininkiniu apvalkalu savybes nanofotonikos taikymams.
4. Ištirti pastovias optines ir ultrasparčias optomechanines susintetintų Ag nanodalelių masyvų, tenkinančių Brego sąlygą, savybes bei palyginti su suspenduotų nanodalelių skirtumine sugertimi.

8.1.3. Naujumas

Panaudota nauja technologija mikroskystinių įrenginių gamybai – mikroapdirbimas femtosekundiniu lazeriu. Pasirinkta aliuminio keramikos medžiaga siekiant įgalinti tokį prietaisą veikti su chemiškai agresyviomis medžiagomis ir paversti suderinamu su nanodalelių savirankos kapiliarinėmis jėgomis sistema. Baigtinių elementų metodu atlikta Teslos vožtuvo geometrija pagrįsto maišytuvo optimizacija.

Nanodalelių saviranka kapiliarinėmis jėgomis panaudota didelio ploto tvarkių Ag nanodalelių masyvams sukurti. Parodyta, kad standartiniai optinio charakterizavimo metodai gali būti panaudoti tokiems bandiniams tirti ir pademonstruoti stiprūs paviršiaus gardelės rezonansai. Jie charakterizuoti energijos dispersijos diagramomis, remiantis jomis paaiškinta sąveika su difrakcinėmis Brego modomis. Baigtinių elementų metodo skaičiavimais pademonstruotas elektromagnetinio lauko pasiskirstymas sužadinus šias modas.

TiO₂ kiautu apvilktos Ag nanodalelės buvo suformuotos ir ištirtos naudojant skirtuminės sugerties spektroskopiją. Pastebėtos optomechaninės modos visuose Ag nanodalelių mėginiuose. Apvilktose dalelėse pastebėtas ryškus optomechaninių modų slopinimas. Paaiškinta, kad energijos praradimas gali būti siejamas su karštųjų elektronų pernaša į puslaidinikinį apvalką.

Skirtuminės sugerties spektroskopija panaudota pratęsti savirankos tyrimams su ultrasparčių procesų analize ir jų palyginimu tvarkiuose masyvuose ir koloidiniame tirpale. Paaiškintos skirtingų optomechaninių sąveikų sąlygos. Baigtinių elementų metodo analizė panaudota priskiriant mechanines nanokubų modas pastebėtoms optomechaninėms oscilacijoms. Apskaičiuotos deformuotų nanokubų formos panaudotos optiniam masyvų modeliavimui, kur parodyta ultrasparčių procesų įtaka fotoninio nuotolio reiškiniams, tokiems kaip paviršiaus gardelės rezonansas.

8.2. Metodika

Monodispersiniai Ag nanodalelių tirpalai susintetinti naudojant modifikuotą „polyol“ sintezės metodą.^{113,114} Suformuoti Ag kuboktahedrai (kraštinės ilgis $a = 122$ nm) ir Ag nanokubai ($a = 92$ nm, 77 nm ir 39 nm). Nanodalelės, priklausomai nuo eksperimento, buvo paskleistos etanolyje arba dimetilformamide. Ag nanokubai buvo apvilkti TiO₂ apvalkalu, panaudojant procesą, aprašytą **A3** publikacijoje. Šablonai nanodalelių savirankai buvo formuojami naudojant elektronų litografijos įrenginį (e-Line Plus, Raith), gilųjų ėsdinimą reaktyviaisiais jonais (Apex ICP) bei minkštąją litografiją polidimetilsiloksane (PDMS) (Sylgard 184). Nanodalelėms surikiuoti panaudota savirankos kapiliarinėmis jėgomis sistema, susidedanti iš optinio mikroskopo (BX51, Olympus), precizinio motorizuoto stalio (LS-110, PI Micos) ir temperatūros valdiklio (TEC-1090, Meerstetter Engineering GmbH). Judant staleliui, o ant polimerinio šablono užlašintą koloidinio tirpalo lašą prilaikant mikroskopiniu stikleliu, laše kyla konvekcinės srovės, atnešančios daleles į aplinkų ribą, kur jos įkalinamos skylėse ant šablono. Mikroskystinis prietaisas, tinkantis šiai sistemai, buvo suformuotas aliuminio oksido keramikoje (VC 100-1 (Policor)), panaudojant Yb:KGW femtosekundinį lazerį (Šviesos konversija) ir galvoskenneriu (SCANcube III 14, ScanLab) pagrįstą mikroapdirbimo sistemą (Altechna R&D). Disertacijoje demonstruojamoms nuotraukoms gauti panaudoti transmisiniai elektronų mikroskopai (Hitachi H-7650 ir JEOL-1010), optinis mikroskopas (BX51, Olympus) su tamsaus lauko objektyvais ir CCD kamera (Micropublisher 3.3, QImaging), skenuojantis elektronų mikroskopas (Quanta 200 FEG, FEI). Pastovios optinės savybės ištirtos naudojant UV-vis spektrofotometrą (AvaSpec-2048, Avantes) ir motorizuotą goniometrinių stendą, susidedantį iš kaitrinės lempučių, kolimatoriaus ir poliarizatoriaus.¹¹⁸ Ultraspartūs procesai tyrinėti naudojant HARPIA TAS eksperimentinį stendą su Yb:KGW femtosekundiniu lazeriu (Šviesos konversija). Mikroskystinio prietaiso, Ag nanodalelių optinių ir mechaninių savybių modeliavimas atliktas baigtinių elementų metodu pagrįstu programiniu paketu COMSOL Multiphysics.

8.3. Rezultatai

8.3.1. Optimizuotas mikroskystinis įrenginys nanodalelių savirankai

Mikroskystinis įrenginys buvo suprojektuotas su trimis įėjimo kanalais, vienu išėjimo kanalu bei su Teslos vožtuvo tipo maišančia struktūra. Jos geometrija buvo optimizuota efektyviam maišymui. Pasinaudojant baigtinių elementų metodu (FEM), buvo ištirtos mikroskystinio prietaiso veikimo tendencijos kintant kiekvienam iš parametrų, pavaizduotų **Figure 4** (čia ir toliau naudojamos nuorodos į angliškoje versijoje įterptas iliustracijas „Figure“). Modeliavimo rezultatai pavaizduoti **Figure 5**. Nustatytas pagrindinis parametras, darantis įtaką prietaiso veikimui – kilpos kampas kanalo ašies atžvilgiu. Remiantis modeliavimo rezultatais ir atsižvelgiant į struktūrų dydį, parinkti ir kiti geometrijos parametrai: $\alpha = 45^\circ$, $\beta = 0^\circ$, $L = 1200$ μm , $D = 480$ μm , $O = 0$ μm .

Siekiant panaudoti įrenginį nanodalelių savirankai, pasirinkta aliuminio keramikos medžiaga. Struktūros juose suformuotos femtosekundiniu lazeriu, prieš tai

optimizavus apdirbimo parametrus. Optimizavimo rezultatai pavaizduoti **Figure 6**. Buvo pasirinktas 100 mm/s skenavimo greitis ir 11,2 J/cm² energijos tankis, leidžiantis pašalinti 165 μm³ medžiagos su kiekvienu lazerio impulsu. Apdirbant šiuo režimu, pasiektas 200 μm mikroskystinių kanalų gylis. Suformuotos struktūros optinė nuotrauka bei modeliai be maišančios struktūros ir su ja pavaizduoti **Figure 7**. Akivaizdu, kad, į kanalą įterpus Teslos vožtuvu pagrįstą struktūrą, išsišakojančiuose išėjimo kanaluose koncentracija tampa vienoda.

Suformuotas įrenginys ištirtas ir realiame eksperimentiniame stende. Buvo keičiami centrinio arba šoninių kanalų debitai ir stebimas mikroskystinio prietaiso veikimas (**Figure 8**). Palyginus gautus rezultatus, gautas pakankamai geras atitikimas su modeliuojant gautais parametrais. Remiantis šiais ir aukščiau aprašytais tyrimais, padarytos tokios išvados: **i)** struktūros, suformuotos lazerinio apdirbimo būdu aliuminio keramikoje, gali būti naudojamos mikroskystiniams taikymams; **ii)** modeliuojant gaunamos priklausomybės gali būti naudojamos kaip gairės, siekiant valdyti koncentraciją parenkant debitus įėjimo kanaluose.

8.3.2. *Plazmoninės nanodalelės ir jų saviranka*

Tyrimuose panaudotų Ag nanodalelių sintezė išsamiai aprašyta **A3** publikacijoje. Suformuoti Ag kuboktahedrai (kraštinės ilgis $a = 122$ nm) ir Ag nanokubai ($a = 92$ nm, 77 nm ir 39 nm). Dalis nanokubų buvo apvilkti TiO₂ sluoksniu, kurio storis atitinkamai $t = 8$ nm, 6 nm ir 12 nm (**Figure 9**). Pagal TEM nuotraukas nustatyta, kad po apvilkimo žingsnio Ag šerdis išlaikė aštirus kampus ir kraštines. Lokalaus plazmonų rezonanso (LSPR) dažnis priklauso nuo aplinkos lūžio rodiklio, taigi jį galima panaudoti kaip patvirtinimą, kad plazmoninė šerdis liko nepakitusi, tik įgavo TiO₂ apvalkalą.⁴ Tai įrodyta UV-vis matavimu – dipolis LSPR (D-LSPR) pasislinko spektre, tačiau išlaikė tokią pačią formą, įskaitant daugiapolių rezonansus, kurie yra charakteringi tokio dydžio nanokubams.⁷ Ag kuboktahedrai yra apžvelgti **Figure 10**, kur demonstruojama jų TEM nuotrauka bei optinis spektras. Buvo suformuotas modelis, kuris atitinka tokios nanodalelės formą, ir apskaičiuotos jo optinės savybės, naudojant FEM. Suskaičiuotas sugerties grafikas gerai atitinka eksperimentinį. Tuo remiantis galima teigti, kad ir sudėtingesnių struktūrų optiniai skaičiavimai teisingi.

Pliki Ag kuboktahedrai ($a = 122 \pm 3$ nm) ir Ag nanokubai ($a = 77 \pm 3$ nm) buvo panaudoti savirankos eksperimentams. **Figure 11** pavaizduotas nanodalelių savirankos kapiliarinėmis jėgomis¹⁸ metodas, kuris panaudotas kuboktahedrams surikiuoti į 600 nm periodiškumo heksagoninę gardelę su >99% našumu >1 cm² plote. Ag nanokubai ta pačia metodika buvo surikiuoti į 400 nm, 350 nm ir 300 nm kvadratinės gardeles (**Figure 12**). Abiem atvejais nanodalelių masyvai gali būti arba palikti sąlytyje su oru, arba uždengti polimerizuojant papildomą PDMS sluoksnį iš viršaus, taip sudarant vienalytę lūžio rodiklio aplinką. Didžioji dalis eksperimentų atlikta su atvirais bandiniais, išskyrus vieną atvejį, kai tiesiogiai lyginta su homogeninėje aplinkoje atliekamais skaičiavimais.

8.3.3. *Paviršiaus gardelės rezonansas nanodalelių masyvuose*

Tvarkingi Ag nanodalelių masyvai suformuoti pakankamai dideliame plote, kad būtų galima jų optines savybes matuoti įprastu UV-vis stendu be fokusuojančios

optikos. Tyrimas atliktas pralaidumo režimu, o kritimo kampas keistas sukant bandinį (**Figure 11**). Gauti pralaidumo spektrai buvo paversti į energijos dispersijos diagramas. Šešiakampės kuboktahedrų gardelės atveju gautos 4 diagramos: dvi orientacijos su dviem skirtingomis šviesos poliarizacijomis (Γ - M_{TM} , Γ - M_{TE} , Γ - K_{TM} , ir Γ - K_{TE}). Jos pavaizduotos **Figure 13**. Visose diagramose matomas kvadrupolinis LSPR (Q-LSPR) (475 nm), kurio rezonansas nepriklauso nuo kritimo kampo ir nesąveikauja su Reilėjaus anomalijomis (RA). Dipolis paviršiaus gardelės rezonansas (D-SLR) aiškiai matomas 757 nm, kai šviesa krinta statmenai bandiniui. Toks bangos ilgis atitinka RA, sklindančią PDMS lūžio rodiklio aplinkoje ($n = 1.4$). Taigi, nanodalelės elgiasi lyg būtų apsuptos PDMS, nors iš SEM nuotraukų aiškiai matyti, kad jas šablono duobutėje supa oras. Tai įdomus reiškinys, parodantis, kad galima išnaudoti paviršiaus gardelės rezonanso elektromagnetinius laukus jutiklių taikymams, kadangi prie nanodalelių galėtų laisvai patekti tiriamą medžiaga.

Norint geriau paaiškinti eksperimentinius pastebėjimus, atliktas heksagoninės nanodalelių gardelės modeliavimas analitiniu susietųjų dipolių metodu (CDA) ir FEM. **Figure 14** pavaizduoti pirmuoju metodu suskaičiuoti vienos nanodalelės ir jų masyvo ekstinkcijos skerspjūviai. Spektrinėje vietoje, kur egzistuoja RA, ekstinkcijos skerspjūvio spektre atsiranda aštri smailė, atitinkanti eksperimentinius rezultatus. Naudojant FEM buvo suskaičiuoti elektromagnetiniai laukai, atsirandantys masyvą žadinant plokščiąja banga vienalyčio lūžio rodiklio aplinkoje. **Figure 14** pavaizduotas pralaidumo spektras šviesai krintant statmenai, kuris, kaip ir analitiniu būdu suskaičiuotasis, gerai atitinka eksperimentinį. Modeliuose gautas kokybės faktorius ($Q = \lambda/\Delta\lambda$) didesnis nei eksperimente dėl deviacijų nuo periodiškumo, rotacinės tinkamos ar neidealios dalelių kokybės.

Atidžiau paanalizuoti sumodeliuoti ir eksperimentiniai pralaidumo spektrai, kai šviesos kritimo kampas 15° (**Figure 15**). Visos eksperimentiškai užregistruotos smailės turi savo atitikmenį sumodeliuotame spektre. Diverguojantys neatitikimai gauti dėl kampinio pozicionavimo netikslumų. Stipriausi eksperimentiniai rezonansai (atsižvelgiant į amplitudę) tokio kritimo kampo atveju užfiksuoti Γ - M_{TM} konfigūracijoje ($Q \sim 60$). Siauriausi rezonansai modelyje (su didžiausiu kokybės faktoriumi) užfiksuoti tie, kurie susieti su labiausiai į raudonąją pusę pasislinkusiomis RA. Nors eksperimentiniai jų atitikmenys ne tokie siauri, vis dėlto generavo gana įspūdingą $Q \sim 80$. Atidžiau įvertinus elektrinio lauko pasiskirstymus kiekvienoje iš sumodeliuoto rezonanso sąlygų, pastebėta, kad kai kuriais atvejais dalelės gali būti poliarizuojamos statmenai masyvo plokštumai (OP) ir generuoti ypač stiprius elektrinius laukus. Esminė tokio sužadavimo sąlyga – TM poliarizacija ir nenulinis šviesos kritimo kampas. **Figure 15** parodytas šis elektrinis laukas. Vis dėlto nustatyta, kad eksperimente registruojamos smailės atitinkamose spektrinėse pozicijose yra sukeltos plokštumoje pasklidusio elektrinio lauko. Tačiau OP elektrinius laukus pavyko išgauti su mažesnėmis, nanokubo formos dalelėmis.

Ag nanokubai buvo surikiuoti savirankos būdu į kvadratinis masyvus su tokiais pat dideliu našumu. **Figure 12** parodyti jų pralaidumo spektrai, šviesai krintant statmenai, ir pažymėtos RA sąlygos. $\Lambda = 400$ nm, 350 nm, and 300 nm gardelėms jos atitinkamai yra 570 nm, 499 nm ir 428 nm bangos ilgyje. Šiuo atveju tik 400 nm SLR sąlyga yra į raudonąją pusę nuo D-LSPR, o tai yra esminė sąlyga, norint išgauti

siauriausius paviršiaus gardelės rezonansus.^{55,56,62} Šiuo atveju išmatuota $Q \sim 48$, o kitais dviem atitinkamai $Q \sim 18$ ir $Q \sim 14$. Nė vienos gardelės RA statmenai krintančiai šviesai neatitiko Q-LSPR (~ 460 nm), taigi kvadrupolinis paviršiaus gardelės rezonansas (Q-SLR) galėtų būti stebimas tik apšviečiant kamu, kadangi tokiu atveju gardelės rezonansas slenka pagal dispersijos ryšį $E = \frac{\hbar c}{n} |\vec{G} + \vec{k}_{//}|$. Pagal šį ryšį kintanti energijos priklausomybė pavaizduota **Figure 16** kartu su išmatuotomis energijos dispersijos diagramomis. Iš jų aiškiai matyti priklausomybė nuo poliarizacijos, kuri buvo aptarta ir kuboktahedrų gardelės atveju (**A2**).

Apšvietus Ag nanodalelių gardelių bandinius TM poliarizuota šviesa kamu, pastebėta SLR šalia tų RA sąlygų, kurių šviesos sklaidimo kryptis nesutampa su plokštumoje poliarizuoto dipolio sklaidoma šviesa (tai yra LSPR-RA sąveikos sąlyga). Toks neatitikimas yra OP SLR požymis.^{69,124,127–131} Šį reiškinį paprastai sunku užfiksuoti, kadangi, norint daleles poliarizuoti OP, reikalingas pasviręs švietimo kampas, tačiau, didinant kritimo kampą, RA slenka į raudonąją spektro pusę (paprastai tolyn nuo D-LSPR). Toks variantas pastebėtas 400 nm ir 350 nm gardelėse, kur OP SLR pasireiškė labai neryškiai. Tačiau 300 nm gardelės atveju šis rezonansas tęsiasi gerokai ilgiau ir pasiekia $Q \sim 78$ šviesai krintant $\theta = 35^\circ$ kamu.

8.3.4. *Suspenduotų ir surikiuotų nanodalelių optomechanika*

Skirtuminės sugerties spektroskopijos (TAS) būdu išmatuoti Ag ir Ag@TiO₂ tirpalai, norint įvertinti TiO₂ apvalkalo įtaką ultrasparčiai elektronų dinamikai. **Figure 21** pavaizduota optinio spektro pokyčio evoliucija laike. Žadinančio lazerio impulso trukmė yra trumpesnė nei nanodalelių mechaninių osciliacijų periodas. Tai leidžia sužadinti optomechanines modas (OM) koherentiškai. Mechaninės modos keičia nanodalelių LSPR smailių poziciją, o tai matoma kaip OM osciliacijos TAS spektre. Pasirinkus vieną iš zonduojančio lazerio bangos ilgių, atliktas funkcijos pritaikymas, ją sudaro greitai gęstanti eksponentė (atitinkanti elektronų-fononų sklaidą), lėtai gęstanti eksponentė (atitinkanti nanodalelės traukimąsi dėl aušimo) bei slopstanti harmoninio osciliatoriaus funkcija (atitinkanti slopstančias mechanines vibracijas). Tai aprašyta 9 lygtimi.

Šios funkcijos pritaikymas parodė, kad OM periodas lyginant plikas ir apvilktas nanodaleles beveik nepakito (20,0 ps Ag ir 19,5~19,6 ps Ag@TiO₂). Tai leidžia manyti, kad šerdis ir apvalkalas nėra tvirtai mechaniškai susieti. Tačiau pastebėta, kad mechaninis kokybės faktorius ($Q = \pi\tau/T$) sumažėjo $\sim 40\%$ apvilktų dalelių atveju (**Figure 22**). Atliktas mechaninis sistemos modeliavimas FEM, norint atmesti mechaninius energijos nuostolius, kurie galėtų būti Q sumažėjimo priežastis (**Figure 23**). Modelyje aprašytas $a = 39$ nm plikas Ag nanokubas ir apvilktas $t = 12$ nm TiO₂ sluoksniu. Apvilktos sistemos mechaninis susietumas keistas 0,01–10 GPa/nm ir pastebėta, kad silpnai susietos sistemos rezonansinis dažnis beveik nepakinta (tai atitinka eksperimento rezultatus), o stipriai susietos sistemos dažnis gerokai pasikeičia. Remiantis šiuo modeliu ir kitais aprašytais svarstymais, galima teigti, kad Ag@TiO₂ nėra mechaniškai susieta sistema ir kad kažkoks kitas reiškinys turėjo lemti Q sumažėjimą.

Iškelta hipotezė, kad energija, reikalinga aukšto kokybės faktoriaus OM sukelti, prarandama ankstyviausiuose ultrasparčiųjų procesų etapuose – dėl karštų elektronų

netekimo. Po pradinio sužadavimo LSPR gali arba išsklaidyti fotoną, arba perduoti šią energiją nespinduliniams relaksacijos procesams. Mažesnėms nanodalelėms antrasis variantas pasireiškia stipriau nei pirmasis. Tai paaiškina, kodėl Q -faktorius sumažėjimas aptiktas tik mažiausioms nanodalelėms. Šie nespinduliniai relaksacijos procesai sugeneruoja karštus elektronus, kurie netrukus perskirsto energiją, išildo nanodalelės gardelę, sukelia jos plėtimąsi, ir energija perleidžiama į aplinką kaip šiluma arba garsas. Tačiau karšti elektronai gali pasklisti už nanodalelės paviršiaus ribų ir pereiti į šalia esančio elektronų akceptorius elektronines būsenas.^{134–139} Dar kartą peržiūrėję pirmąsias skirtuminės sugerties laikinio grafiko pikosekundes, pastebėjome, kad pradinis eksponentinis gesimas greitesnis Ag@TiO_2 mėginiuose. Be to, pirmoji su nanodalelės plėtimusi susijusi smailė taip pat buvo $\Delta A \sim 36\%$ mažesnė. Šie du požymiai rodo, kad elektronų ir fononų sklaida vyksta su mažesne energija, nes karšti elektronai turi alternatyvų relaksavimo kelią – pereiti į TiO_2 apvalkalą. Taigi, TAS matavimai parodė, kad puslaidininkinis Ag nanodalelių apvalkalas gali surinkti karštus elektronus, sugeneruotus dėl plazmonų rezonanso, kuriuos galima panaudoti nanofotonikos taikymuose.¹⁴⁰

Norint suprasti ultrasparčiųjų procesų skirtumus tarp suspenduotų ir surikiuotų nanodalelių, pamatuotas $a = 77$ nm Ag nanokubų TAS, kai jie koloidiniame tirpale ir kai yra tvarkingai surikiuoti į prieš tai aprašytas gardeles. **Figure 24** pavaizduoti žemėlapiai, rodantys TAS moduliacijas, kurios yra charakteringos OM nanodalelių modoms. Kubai pasižymi dviem pagrindinėmis vibracinėmis modomis.^{102,105} Stipresnioji iš jų susijusi su aštuonių kubo kampų deformacija, ir ji daro didžiausią įtaką optiniam atsakui. Antroji moda susijusi su šešių kubo paviršių deformacija. Gautiems TAS laikiniams grafikams pritaikyta funkcija su gėstančia eksponente ir dviem eksponentiškai slopstančių harmoninių svyravimų dėmenimis.¹⁰² Iš pritaikytos funkcijos apskaičiuoti mechaniniai kokybės faktoriai tirpale atitinkamai siekė $Q \sim 10,7$ ir $Q \sim 16,8$ kampų ir paviršių modoms, ir yra didesni nei gauti ankstesniame tyrime dėl mažesnio DMF klampumo. Q -faktoriai apšviečiant nanodalelių gardeles statmenai krintančia šviesa gauti mažesni nei tirpale ($Q \sim 8$ kampų modai ir $Q \sim 7–15$ paviršių modai). Svarbu pastebėti, kad **i**) kampų moda tarp skirtingų periodų gardelių praktiškai nekinta ir **ii**) paviršių moda kinta tarp skirtingų gardelių ir tampa stipriausia, kai $\Lambda = 300$ nm. Taip yra dėl to, kad kampų moda nėra stipriai susijusi su mechanine aplinka – kampų sąlyčio su PDMS plotas sąlyginai nedidelis, palyginti su paviršiais.

Taip pat atlikti TAS matavimai, apšviečiant $\Lambda = 300$ nm dalelių gardelę 30° kampų TE ir TM poliarizuota šviesa (**Figure 25**). Kaip aprašyta anksčiau, TM poliarizacija generuoja dvi SLR smailės – vieną plokštumoje, kitą OP. Pastaroji palyginta su TE poliarizacija gaunamu rezonansu plokštumoje, kadangi jų optiniai spektrai panašūs, bet elektrinio lauko pasiskirstymas skiriasi. Abiem atvejais kampų Q -faktorius išliko panašus, kaip ir visuose eksperimentuose $Q \sim 9$. Įdomu tai, kad paviršiaus Q -faktorius buvo stipresnis TE atveju ($Q \sim 12$) palyginti su TM, nors OP SLR skleidžia stipresnius elektrinius laukus. Taip gali būti dėl to, kad plokštumoje nanodaleles supa vienalytiškesnė mechaninė aplinka, palyginti su vertikalia kryptimi, nes pastaruoju atveju viena nanodalelės plokštuma yra stipriai prikibusi prie polimerinio paviršiaus.

Galiausiai atliktas $\Lambda = 300$ nm nanodalelių gardelės modeliavimas FEM, kad būtų galima geriau suprasti, kaip OM paveikia SLR. Iš mechaninio modeliavimo gautos nanodalelės, deformuotos pagal kampų ir paviršių modas, buvo surikiuotos į gardelę ir apšviestos $0\text{--}30^\circ$ kampu krintančia šviesa. Gauti pralaidumo spektrai atimti iš identiško modelio su nedeformuotomis nanodalelėmis, taip gauta laike užšaldyta TAS energijos dispersijos diagrama (**Figure 26**). Kaip ir tikėtasi, abi modos sukėlė SLR (įskaitant ir OP SLR) raudonąjį poslinkį, tiesa, kampų moda spektrą paslinko labiau nei paviršiaus moda.

Sumodeliuoti TAS spektrai, kai gardelės apšviečiamos 0° ir 30° kritimo kampais bei TM arba TE poliarizacijomis, palyginti su eksperimentiniais rezultatais (**Figure 26**). Visais atvejais sumodeliuotų grafikų forma gerai atitinka eksperimentus, išskyrus bendrą raudonąjį poslinkį modeliuose dėl optinių konstantų netikslumų. Eksperimentiniai grafikai yra šiek tiek asimetriniai, tai rodo, kad slinkdamas SLR taip pat ir išplatėja. Apšviečiant kampu, ypač OP SLR atveju, atsiveria galimybės išnaudoti itin mažus spektrinius pločius ultraspartiems taikymams – net ir pats mažiausias poslinkis generuoja stiprų TAS signalą. Šie rezultatai rodo, kad dinaminė nanodalelių forma vaidina svarbų vaidmenį ultrasparčiuose procesuose, ir į tai reikia atsižvelgti projektuojant paviršiaus gardelės rezonansu pagrįstus įrenginius.

8.4. Išvados

1. Mikroskystinis įrenginys, turintis trijų įvadų Teslos vožtuvu pagrįstą maišančią struktūrą, buvo suprojektuotas ir optimizuotas nanodalelių savirankos kapiliarinėmis jėgomis metodui bei realizuotas aliuminio oksido keramikoje. Nustatyta, kad mikroapdirbimas femtosekundiniu lazeriu yra tinkama technologija mikroskystiniams prietaisams efektyviai formuoti aliuminio keramikoje bei tai, kad mikroskystinis modeliavimas gali būti naudojamas tokio tipo mikroskystinių prietaisų išėjimo koncentracijai nuspėti.
 - a. Baigtinių elementų metodu paaiškintas ir optimizuotas maišančiosios struktūros funkcionalumas. Nustatyta, kad kilpinės struktūros kampas su centriniu kanalu turi didžiausią įtaką maišymo efektyvumui. Remiantis optimizacijos rezultatais, parinkti parametrai įrenginiui realizuoti ($\alpha = 45^\circ$, $\beta = 0^\circ$, $L = 1200 \mu\text{m}$, $D = 480 \mu\text{m}$, $O = 0 \mu\text{m}$).
 - b. Pasiūlytas inovatyvus būdas formuoti mikroskystines struktūras netradicinėse medžiagose ir panaudotas mikroapdirbimas femtosekundiniu lazeriu kanalams formuoti itin kietoje ir chemiškai atsparioje medžiagoje – aliuminio oksido keramikoje. Optimizuotos mikroapdirbimo sąlygos, siekiant išgauti pakankamai didelį apdirbimo našumą, nesumažinant struktūrų kokybės: parinktas 84,4% impulsų persidengimas ir $11,2 \text{ J/cm}^2$ energijos tankis leido pasiekti $165 \mu\text{m}^3/\text{imp}$. tūrinį abliacijos greitį su gera paviršiaus kokybe.
 - c. Atlikti laminarinės tėkmės mikroskystiniuose kanaluose matavimai gerai atitiko apskaičiuotas vertes. Tai rodo, kad pasirinktas mikroapdirbimo metodas gali būti naudojamas gaminant itin atsparius mikroskystinius prietaisus. Be to, nustatyta, kad sumodeliuotos tėkmės vertės galima naudoti kaip gaires, siekiant

parinkti tinkamus debitus nanodalelių nusodinimo kapiliarinėmis jėgomis eksperimentuose.

2. Ag kuboktahedrai ir nanokubai buvo surikiuoti ant litografiškai parengtų šablonų naudojant nanodalelių savirankos kapiliarinėmis jėgomis metodą ir sugeneravo stiprų paviršiaus gardelės rezonansą. Parodyta, kad, naudojantis šia metodika, gali būti kuriamos didelio nuotolio tvarkos plazmoninės gardelės su pavienių nanodalelių skyra bei tai, kad jos gali generuoti aukšto kokybės faktoriaus ekstinkcijos smailes.
 - a. Patobulintas nanodalelių savirankos kapiliarinėmis jėgomis metodas ir pasiektas itin aukštas savirankos našumas (>99% spąstų buvo užpildyti) dideliame plote (>1 cm²) bei pademonstruotas didelio nuotolio pavienių dalelių suvaldymas tankiuose masyvuose. 123 ± 2 nm kraštinės ilgio susintetinti Ag kuboktahedrai savirankos būdu buvo surikiuoti į 600 nm periodo šešiakampės geometrijos masyvus, o 77 ± 3 nm kraštinės ilgio susintetinti Ag nanokubai savirankos būdu buvo surikiuoti į 300, 350 ir 400 nm periodo kvadratinės geometrijos masyvus.
 - b. Pirmą kartą užregistruotas plazmoninis paviršiaus gardelės rezonansas savirankos būdu suformuotoje sistemoje. Šis reiškinys detalai ištirtas ir charakterizuotos šviesos energijos ir banginio vektoriaus projekcijos ryšio priklausomybės nuo masyvo orientacijos ir šviesos poliarizacijos. Tai leido nustatyti sąlygas, generuojančias spektriškai aštriausias sugerties smailes su optiniais kokybės faktoriais (iki ~80), sulygintiniais su pasiekiamais tradicine litografija formuojamose struktūrose.
 - c. Elektromagnetinis modeliavimas baigtinių elementų metodu parodė elektrinio lauko charakteristikas plokštumoje ir statmenai jai generuojamo rezonanso atvejais. Pademonstruota, kad pastarasis pasižymi itin stipriais laukais, plytinčiais virš ir po nanodalelių masyvu, ir gali atverti galimybes didelio jautrumo jutikliams, tačiau tokio rezonanso efektyvus sužadanimas reikalauja tam tikros geometrijos.
3. Monodispersiški Ag nanokubų ir Ag@TiO₂ koloidiniai tirpalai buvo ištirti ultrasparčiųjų procesų kontekste. Aprašyti optomechaniniai procesai, bylojantys apie karštųjų elektronų generavimą, kurie gali būti naudingi nanofotonikos taikymams. Pademonstruota, kad gėstančio plazmono generuojami karšti krūvininkai gali būti atiduodami į šalia esančią puslaidininkinę medžiagą.
 - a. Skirtuminės sugerties tyrimai parodė, kad TiO₂ kiautu apvilktos nanodalelių optomechaninės modos, palyginti su plikomis nanodalelėmis, yra ~40% labiau slopinamos, taigi jos praranda energiją greičiau.
 - b. Nustatyta, kad optomechaninių virpesių dažnis yra pastovus, nepriklausomai nuo to, ar nanodalelės apvilktos. Atlikta baigtinių elementų metodo analizė parodė, kad tik silpno mechaninio ryšio tarp Ag šerdies ir apvalkalo atveju virpesių dažnis gali išlikti nepakitęs. Taigi, parodyta, kad turi egzistuoti

- alternatyvus, nemechaninis relaksacijos kanalas, besivaržantis su elektronų ir fononų sąveika, lemiančia optomechaninių osciliacijų gyvavimo trukmę.
- c.* Pateikta ir paaiškinta stebėtų reiškinių interpretacija, susijusi su karštųjų elektronų emisija į puslaidinikinį apvaskalą pirminėse ultraspartaus sužadavimo fazėse. Tai gali lemti energijos, vėliau panaudojamos mechaniniams virpesiams žadinti, sumažėjimą. Šie karštieji elektronai galėtų būti surinkti ir panaudoti nanofotonikos taikymuose, tokiuose kaip katalizė.
4. Surikuiotų Ag nanokubų masyvai buvo išanalizuoti naudojant skirtuminės sugerties metodą ir buvo užfiksuota ultraspartai paviršiaus gardelės rezonanso moduliacija. Ši optomechaninė sąveika buvo palyginta su suspenduotų nanodalelių atveju bei apibūdintos ultrasparčiosios paviršiaus gardelės rezonanso dinamikos ypatybės. Nustatyta, kad aukšto mechaninio kokybės faktoriaus optomechaninės vibracijos moduliuoja šį tolumo nuotolio plazmoninį-fotoninį reiškinį gigahercų eilės dažniu.
- a.* Nustatyta, kad pagrindinės mechaninės modos virpesių kokybės faktoriai masyvuose (~ 8) yra sulyginami su išmatuotais koloidiniuose tirpaluose su tomis pačiomis dalelėmis (~ 10). Be to, parodyta, kad optinis dalelių atsakas yra moduluojamas ne vieno, o dviejų mechaninių virpesių modų; antrosios iš jų kokybės faktorius gali net viršyti pirmosios (~ 15).
- b.* Pirmą kartą užfiksuota ultraspartai paviršiaus gardelės rezonanso moduliacija ~ 30 GHz dažniu. Nustatyta, kad, žadinant kampu krintančia šviesa, gardelės plokštumoje generuojamas rezonansas sąveikauja su mechaninėmis modomis stipriau, palyginti su rezonansu, generuojamu statmenai plokštumai. Tačiau pastarasis turi siauresnį sugerties smailės spektrinį plotį.
- c.* Baigtinių elementų metodu išskirtos dominuojančių mechaninių modų figūros ir jos panaudotos pademonstruoti, kaip kiekviena iš jų daro įtaką paviršiaus gardelės rezonansui. Modeliavimo rezultatai gerai atitiko eksperimentinius rezultatus ir parodė, kad ultrasparčioji nanostruktūrų dinamika yra pakankamai reikšminga. Tai reiškia, kad į šiuos procesus reikia atsižvelgti projektuojant paviršiaus gardelės rezonansu pagrįstus įrenginius potencialiems aktyviosios plazmonikos ir nanofotonikos taikymams gigahercų dažniu.

CURRICULUM VITAE

MINDAUGAS JUODĖNAS

E-mail: mindaugas.juodenas@ktu.lt

Location: Kaunas, Lithuania

Education

- 2020 PhD in Materials Engineering
(expected 2021-02-22)
*Institute of Materials Science
Kaunas University of Technology*
- European doctorate program “Physics and Chemistry of Advanced Materials” (PCAM)
- ERASMUS+ internship at Mads Clausen Institute of the University of Southern Denmark, Sønderborg, Denmark
- 2016 Master of Materials Technology
Kaunas University of Technology
- Diploma with honors
- 2014 Bachelor of Mechatronics
Kaunas University of Technology
- Diploma with honors
- ERASMUS studies at the University of Southern Denmark, Sønderborg, Denmark
- 2010 High School
Utena Adolfas Šapoka Gymnasium
- Diploma with honors

Employment

- 2019–present Junior Research Staff Member
*Institute of Materials Science
Kaunas University of Technology*
- Development of nanophotonics in self-assembled plasmonic architectures
- Electron beam lithography, reactive ion etching, femtosecond laser microfabrication machinery operation and recipe development
- 2018–2019 Invited Junior Research Staff Member
*Institute of Materials Science
Kaunas University of Technology*
- 2016–2018 Senior Engineer
*Institute of Materials Science
Kaunas University of Technology*

Participation in National and International Projects

- 2020–2022 Ultra-Broadband Antireflection Coatings Based on Highly Absorbing Thin Layers – Plasmonic Blackbody (PlasmoBlack)
led by Prof. T. Tamulevičius
- 2019–2020 Experimental characterization of thin films and structures used in vacuum chamber for particle accelerators (DAFU-2)
led by Prof. S. Tamulevičius
- 2019 Development, Investigation and Application of Polymer Templates for Plasmon Nanolasers (TemplatedNanoLaser)
led by M. Juodėnas
- 2019–2022 New generation smart composite ultrasonic heat and water meters
led by Prof. A. Ragauskas
- 2019 Formation and Modification of Nanoparticles via Femtosecond Laser Ablation of Targets in Liquids (FemtoColloid)
led by Prof. T. Tamulevičius
- 2018–2020 Multifunctional coatings based on ZnO nanowires for selective sensing and efficient solar harvesting (MultiFun)
led by Dr. S. Račkauskas

2018–2021 Creation and development of innovative optical security devices and next generation micro/nano devices and structures for optical applications
led by Prof. S. Tamulevičius

2018–2020 2D nanostructures of noble metal nanoparticles for biosensor applications
led by Prof. S. Tamulevičius

2017–2018 Regular metal oxide nanotube arrays for gas sensing (Gas-Sens)
led by Prof. T. Tamulevičius

2017 Creation of algorithm for rendering of the hologram image and its realization in mobile devices (HoloApp)
led by Prof. T. Tamulevičius

2015–2017 Plasmonic properties of silver nanoparticles and self-assembled clusters (PLAS)
led by Prof. S. Tamulevičius

2016 Calibration of 3D acoustic microscope visualization employing buried lithographic microstructures (3DSonic)
led by Prof. T. Tamulevičius

2014–2015 Fundamental investigation of surface relief and molecular forces influence on the self-organization of nanoparticles and nanofibers (PARMO)
led by Prof. S. Tamulevičius

2014–2015 Regular 3D Structures for Optical Sensors (3DSens)
led by Dr. M. Andrulevičius

Internships, Trainings, and Summer Schools Abroad

2018 SoFun School – Soft Matter for Functional Materials
Bordeaux, France

2017 PCAM / Thinface Summer School on Surfaces and Interfaces
San Sebastian/Donostia, Spain

2015 ERASMUS+ Intensive Course “TL-IRMP”
Warsaw, Poland
Palermo, Italy

2015 Summer School “PolyNano”
Kgs. Lyngby, Denmark

2012 ERASMUS intensive course “WALT”
Bialystok, Poland

Awards

2017–2019 Best Poster/Oral Presentation Awards
“Advanced Materials and Technologies”
“Nanotechnology and Innovation in the Baltic Sea Region”
“EMRS Spring Meeting”

2017-2020 Academic Excellence of PhD Students
Kaunas University of Technology
Research Council of Lithuania

2012–2015 Academic Excellence of Undergraduate/Graduate Students
Kaunas University of Technology Rector’s Scholarship

2011–2013 Patron’s Scholarship
JSC “Pirmas žingsnis”
V. Baršauskienė
JSC “Enerstena”

2012 National Materials Mechanics Competition
1st place

LIST OF PUBLICATIONS

Peer-reviewed publications forming the basis of this dissertation

A1. Juodėnas, Mindaugas; Tamulevičius, Tomas; Ulčinas, Orestas; Tamulevičius, Sigitas. Implementation of an optimized microfluidic mixer in alumina employing femtosecond laser ablation // *Journal of Micromechanics and Microengineering*. 2018, vol. 28, iss. 1, art. no. 015013, pp. 1-10. DOI: 10.1088/1361-6439/aa84fc. [IF: 2.141]

A2. Juodėnas, Mindaugas; Tamulevičius, Tomas; Henzie, Joel; Erts, Donats; Tamulevičius, Sigitas. Surface lattice resonances in self-assembled arrays of monodisperse Ag cuboctahedra // *ACS Nano*. 2019, vol. 13, iss. 8, pp. 9038-9047. DOI: 10.1021/acsnano.9b03191. [IF: 14.588]

A3. Peckus, Domantas; Rong, Hongpan; Stankevičius, Lukas; Juodėnas, Mindaugas; Tamulevičius, Sigitas; Tamulevičius, Tomas; Henzie, Joel. Hot electron emission can lead to damping of optomechanical modes in core-shell Ag@TiO₂ nanocubes // *Journal of Physical Chemistry C*. 2017, vol. 121, iss. 43, pp. 24159-24167. DOI: 10.1021/acs.jpcc.7b06667. [IF: 4.484]

A4. Juodėnas, Mindaugas; Peckus, Domantas; Tamulevičius, Tomas; Yamauchi, Yusuke; Tamulevičius, Sigitas; Henzie, Joel. Effect of Ag nanocube optomechanical modes on plasmonic surface lattice resonances // *ACS Photonics*. 2020, vol. 7, iss. 11, pp. 3130-3140. DOI: 10.1021/acsp Photonics.0c01187. [IF: 6.864]

Peer-reviewed publications not related to this dissertation

1. Stankevičius, Lukas; Tamulevičius, Tomas; Žutautas, Andrius; Juodėnas, Mindaugas; Juškevičius, Kęstutis; Drazdys, Ramutis; Tamulevičius, Sigitas. Diffraction efficiency optimization of multilayer dielectric mirror-based gratings for 1030 nm femtosecond lasers // *Optics & Laser Technology*. 2020, vol. 126, art. no. 106071, pp. 1-8. DOI: 10.1016/j.optlastec.2020.106071. [IF: 3,233]

2. Peckus, Domantas; Chauvin, Adrien; Tamulevičius, Tomas; Juodėnas, Mindaugas; Ding, Junjun; Choi, Chang-Hwan; El Mel, Abdel-Aziz; Tessier, Pierre-Yves; Tamulevičius, Sigitas. Polarization-dependent ultrafast plasmon relaxation dynamics in nanoporous gold thin films and nanowires // *Journal of Physics D: Applied Physics*. 2019, vol. 52, iss. 22, art. no. 225103, pp. 1-13. DOI: 10.1088/1361-6463/ab0719. [IF: 3,169]

3. Tamulevičius, Tomas; Juodėnas, Mindaugas; Klinavičius, Tomas; Paulauskas, Andrius; Jankauskas, Kęstutis; Ostreika, Armantas; Žutautas, Andrius; Tamulevičius, Sigitas. Dot-matrix hologram rendering algorithm and its validation through direct laser interference patterning // *Scientific Reports*. 2018, vol. 8, art. no. 14245, pp. 1-11. DOI: 10.1038/s41598-018-32294-5. [IF: 4,011]

4. Virganičius, Dainius; Juodėnas, Mindaugas; Tamulevičius, Tomas; Schiff, Helmut; Tamulevičius, Sigitas. Investigation of transient dynamics of capillary assisted particle assembly yield // *Applied Surface Science*. 2017, vol. 406, pp. 136-143. DOI: 10.1016/j.apsusc.2017.02.100. [IF: 4,439]

5. Juodėnas, Mindaugas; Hoyland, James D.; Jūrėnas, Vytautas; Bubulis, Algimantas. Piezoelectric actuation for microfluidic cell sorting // Journal of measurements in engineering. 2013, vol. 1, iss. 4, pp. 228-232.

Conferences related results have been presented in by the author (* marks conferences abroad)

Juodėnas, Mindaugas, et al. Arrays of self-assembled Ag nanoparticles produce a surface lattice resonance // 43rd National physics conference of Lithuania, October 3–5, 2019, Kaunas, Lithuania. DOI: 10.5755/e01.9786090216385.

Juodėnas, Mindaugas, et al. Single particle self-assembly proved by surface lattice resonance // Advanced materials and technologies, August 19–23, 2019, Palanga, Lithuania.

* Juodėnas, Mindaugas, et al. Dispersive plasmonic resonance in a self-assembled hexagonal lattice // NanoTech Poland & Nanotechnology and innovation in the Baltic Sea region, June 5–9, 2019, Poznań, Poland.

* Juodėnas, Mindaugas, et al. Templated assembly of Ag nanoparticles in porous anodized alumina // Self-Assembly of Colloidal Systems, September 20–22, 2018, Bordeaux, France.

Juodėnas, Mindaugas, et al. Investigation of Ag nanoparticle assemblies in porous anodized alumina // Advanced materials and technologies, August 27–31, 2018, Palanga, Lithuania.

* Juodėnas, Mindaugas, et al. Dark field optical spectroscopy of deposited Ag nanocube arrays and their Raman enhancement // Developments in optics and communications, April 12–13, 2018, Riga, Latvia.

Juodėnas, Mindaugas, et al. Formation and investigation of regular Ag nanocube arrays // 42nd National physics conference of Lithuania, October 4–6, 2017, Vilnius, Lithuania. DOI: 10.15388/proceedings/LNFK.42.

Juodėnas, Mindaugas, et al. Deposition of Ag nanocubes into regular arrays by tailored self-assembly // Advanced materials and technologies, August 27–31, 2017, Palanga, Lithuania.

Juodėnas, Mindaugas, et al. Laser modification of self-assembled nanocube arrays // Nanotechnology and innovation in the Baltic Sea region, June 14–16, 2017, Kaunas, Lithuania.

* Juodėnas, Mindaugas, et al. Fabrication of static microfluidic mixer in alumina ceramics for precise fluid mixing employing ultra-short pulse ablation // Advances in Optofluidics, September 14–15, 2016, Cetraro, Italy.

Ulčinas, Orestas; Juodėnas, Mindaugas; et al. Femtosecond laser micromachining of microstructures for acoustic microscope calibration and microfluidic devices // Advanced materials and technologies, August 27–31, 2016, Palanga, Lithuania.

Virganavičius, Dainius; Juodėnas, Mindaugas; et al. Template assisted ordering of nanoparticle arrays // Advanced materials and technologies, August 27–31, 2016, Palanga, Lithuania.

Juodėnas, Mindaugas, et al. Directed assembly of micro particles into well-organized arrays // Open readings, March 15–18, 2016, Vilnius, Lithuania.

Juodėnas, Mindaugas, et al. Investigation of microparticle assembly on polymer replicas employing capillary forces // 41st National physics conference of Lithuania, June 17–19, 2015, Vilnius, Lithuania.

Juodėnas, Mindaugas, et al. Micro particle arrangement via capillary force assisted particle deposition on replicated polymer templates // Open readings, March 24–27, 2015, Vilnius, Lithuania.

Conferences related results have been presented in by the co-authors

Tamulevičius, Tomas; Juodėnas, Mindaugas, et al. Laser imposed micro and nano patterns: from nanoparticles and hydrophobic surfaces to anti-counterfeiting applications // Nanomaterials for biosensor and biomedical applications, July 2–4 2019, Jūrmala, Latvia.

Tamulevičienė, Asta; Juodėnas, Mindaugas, et al. Silver nanostructures for SERS applications // Nanomaterials for biosensor and biomedical applications, July 2–4, 2019, Jūrmala, Latvia

Tamulevičius, Tomas; Juodėnas, Mindaugas, et al. Optical properties of silver nanoparticles: tailored self-assembly and nanocomposite thin films // NanoTech Poland 2019 & Nanotechnology and innovation in the Baltic Sea region, June 5–9 2019, Poznań, Poland.

Tamulevičius, Sigitas; Juodėnas, Mindaugas, et al. Technologies for 2-D nanostructures // International workshop on advanced magnetic oxides, April 15–17, 2019, Aveiro, Portugal.

Tamulevičius, Tomas; Juodėnas, Mindaugas, et al. Investigation of Ag nanoparticle assemblies in top down and bottom-up prepared templates // EMN meeting on photonics, October 21–25, 2018, Kaohsiung, Taiwan.

Tamulevičienė, Asta; Mikalkevičius, Mantas; Juodėnas, Mindaugas, et al. Investigation of different nature silver nanostructures for enhancement of Raman scattering signal // EMN meeting on photonics, October 21–25, 2018, Kaohsiung, Taiwan.

Juodėnas, Mindaugas, et al. Directional scattering of assembled Ag nanocubes observable in the far-field // Nanotechnology and innovation in the Baltic Sea region, May 30–June 1, 2018, Sønderborg, Denmark.

Tamulevičius, Tomas; Juodėnas, Mindaugas, et al. Optomechanical properties of plasmonic Ag nanocubes and regular assemblies // E-MRS Fall Meeting, September 18–21, 2017, Warsaw, Poland.

Tamulevičius, Tomas; Stankevičius, Lukas; Peckus, Domantas; Juodėnas, Mindaugas, et al. Excitation of optomechanical resonances in monodisperse plasmonic nanocubes // Nanotechnology and innovation in the Baltic Sea region, June 14–16, 2017, Kaunas, Lithuania.

Peckus, Domantas; Tamulevičius, Tomas; Stankevičius, Lukas; Juodėnas, Mindaugas, et al. Ultrafast dynamics of coherent oscillations of highly monodispersed plasmonic Ag nanocubes and their assemblies // E-MRS Spring Meeting, May 22–26, 2017, Strasbourg, France.

M. Juodėnas, T. Tamulevičius, O. Ulčinas, S. Tamulevičius

Implementation of an Optimized Microfluidic Mixer in Alumina Employing Femtosecond Laser Ablation

In this work, an implementation of a full-scale optimized micromixer via femtosecond laser ablation, which is one of the few techniques that allows precise direct fabrication of structures on alumina ceramics is presented. Laser ablation processing conditions for microfluidic channel fabrication were investigated and the most appropriate parameters were selected. Optimization of mixing microfluidic structures was performed by modelling the mixing capabilities of various geometry Tesla valve based structures^{33,34,42,45,116,143–145} employing Finite Element Method (FEM). Using these results, the efficiency of mixing of liquids and its dependence on the valve structure geometry is discussed. Obtained results of the numerically simulated mixing performance of different structures were used to select the configuration for the experimental implementation. A microfluidic device, including the modelled mixer, was designed for precise dosing and dilution of colloidal solutions in CAPA experimental setup described in²², which enables one to manipulate and position micro-/nanoparticles in well-defined, ordered arrays^{21,26–28,46}. The device, containing three inlet channels, a Tesla valve based passive mixer and a branching outlet channel system with through holes at the ends of each channel, was successfully implemented in a scarcely used material in microfluidics – alumina. The experimental results demonstrated close conformity with the numerical simulations, i.e., the geometry of laminar flows within the channel as well as mixing behavior, indicating that the suggested microfluidic device prototyping technology can be employed as an alternative for conventional methods especially when hard, chemically inert materials, such as alumina, are in use, as well as proving the viability of such micromixer for manipulation of substances required by CAPA.

Implementation of an optimized microfluidic mixer in alumina employing femtosecond laser ablation

M Juodėnas¹ , T Tamulevičius^{1,2} , O Ulčinis¹ and S Tamulevičius^{1,2} 

¹ Institute of Materials Science of Kaunas University of Technology, K. Baršausko St. 59, LT-51423 Kaunas, Lithuania

² Department of Physics, Kaunas University of Technology, Studentų St. 50, LT-51368 Kaunas, Lithuania

E-mail: mindaugas.juodenas@ktu.lt

Received 12 May 2017, revised 7 August 2017

Accepted for publication 8 August 2017

Published 15 December 2017



CrossMark

Abstract

Manipulation of liquids at the lowest levels of volume and dimension is at the forefront of materials science, chemistry and medicine, offering important time and resource saving applications. However, manipulation by mixing is troublesome at the microliter and lower scales. One approach to overcome this problem is to use passive mixers, which exploit structural obstacles within microfluidic channels or the geometry of channels themselves to enforce and enhance fluid mixing. Some applications require the manipulation and mixing of aggressive substances, which makes conventional microfluidic materials, along with their fabrication methods, inappropriate. In this work, implementation of an optimized full scale three port microfluidic mixer is presented in a slide of a material that is very hard to process but possesses extreme chemical and physical resistance—alumina. The viability of the selected femtosecond laser fabrication method as an alternative to conventional lithography methods, which are unable to process this material, is demonstrated. For the validation and optimization of the microfluidic mixer, a finite element method (FEM) based numerical modeling of the influence of the mixer geometry on its mixing performance is completed. Experimental investigation of the laminar flow geometry demonstrated very good agreement with the numerical simulation results. Such a laser ablation microfabricated passive mixer structure is intended for use in a capillary force assisted nanoparticle assembly setup (CAPA).

Keywords: tesla valve, microfluidic mixing, femtosecond laser ablation, alumina

 Supplementary material for this article is available [online](#)

(Some figures may appear in colour only in the online journal)

1. Introduction

With the ever-advancing field of nanotechnology, research in microfluidics has brought a wide array of improvements in techniques involving the manipulation of minuscule amounts of fluids, often in the range of femtoliters [1, 2]. Applications of microfluidic devices are revolutionizing areas of clinical diagnostics, genetics, biology, etc, since the very low consumption of reagents, their fast response, low cost and disposability are all very important aspects in practical

science [3–6]. More often than not, the manipulation of liquids in microfluidics is done at Reynolds numbers ranging from 500 down to 10^{-5} , as dictated by ever decreasing flow rates [7]. As a rule, at such Reynolds numbers the flow regime is completely laminar, giving rise to the troublesome mixing of liquids. Although this can be defined as an advantage of microfluidics, enriching the ways to manipulate fluids, there are however applications where efficient mixing is essential. The search for solutions to this problem has attracted a lot of attention [8–10]. Moreover, it might be necessary to have a

completely homogeneous concentration distribution along the lateral channel axis in order to feed an identical concentration to further microfluidic functional elements [11].

In cases where mixing is mandatory—several mixing techniques are available. One of them involves active, solid components within the channels—rotating discs, dimers, particles, etc [12, 13]. Another way of achieving fluid mixing is by using external fields: acoustic, electric and magnetic [14–19]. Although these techniques usually provide a very good mixing performance, they require either a complicated fabrication method for the introduction of active components or bulky equipment, further evolving into chip-in-the-lab rather than the lab-on-a-chip concept of the system. Fortunately, there are alternative ways to achieve mixing in microfluidic channels, even at very low Reynolds numbers, that is by using passive, easily implementable mixing structures (e.g. the Tesla valve), that manipulate the velocities of separate fluids within a single channel, thus exploiting the effect of mixing due to the velocity gradient [20–24].

Furthermore, as the field of microfluidics advances, more and more complicated structures as well as manufacturing strategies and novel materials are required for sophisticated applications. As a rule, depending on the specific requirements, silicon, glass or polymers are often used in the fabrication of microfluidic devices. The use of a specific class of materials dictates the compatible technologies and, until recently, the only widely used techniques for the manufacturing of microfluidic devices were well established lithography based methods employing standard cleanroom facilities: i.e. optical and nanoimprint, very often followed by soft lithography for fast replication or injection molding for a more industrial approach [25–27]. Although these methods are well-known and reliable, they involve several steps, which are expensive, lengthy and resource consuming. Furthermore, the use of microfluidics for non-biological species, e.g. capillary force assisted nanoparticle assembly (CAPA) of metallic nanoparticles [28, 29], demands materials other than the ones widely used (e.g. polydimethylsiloxane (PDMS)), because the colloid solutions that are based on chloroform, toluene, dimethylformamide, etc can damage the microfluidic channels and/or extract the non-crosslinked monomers that can afterwards pollute the experiments [30]. Certainly, novel materials and novel fabrication technologies are required. One material, often overlooked in microtechnology due to its fabrication difficulties, despite possessing impressive characteristics, is alumina. It is the most widely used ceramic due to its exceptional properties such as its chemical resistance, hardness, electrical insulation, excellent surface flatness and smoothness, strength at high temperatures and thick film reliability [31, 32]. It is found that many applications and many products made from it are commercially available, including parts for medical diagnostic equipment, medical and surgical devices, parts for implantable devices, substrates for thermal printheads, thin film devices, printed substrates for automotive parts, sensor parts, general thick film applications, etc [33]. No doubt, the use of such a material in a field with high future expectations like microfluidics would open new

horizons in its application, especially for the transport and manipulation of extremely aggressive species.

Over recent years, direct laser micromachining using ultra-short laser pulses has evolved to a point where the quality of structures, range of applicable materials, time consumption and cost are on a par with or even better than the conventional methods [34–37]. What is more, relatively new techniques, such as femtosecond laser induced chemical etching and water-assisted femtosecond laser drilling, offer the fabrication of 3D micro channels within the bulk of a material, bringing a huge advantage over the surface constrained traditional methods [38–42]. Additionally, femtosecond laser ablation, unlike standard lithography techniques, offers a unique possibility to use a wide array of materials, as it is based on the instantaneous evaporation of a material, enhancing the current and providing novel applications for microfluidics.

In this work, implementation of a full scale optimized micromixer via femtosecond laser ablation, which is one of the few techniques that allows precise direct fabrication of structures on alumina ceramics, is presented. Laser ablation processing conditions for microfluidic channel fabrication were investigated and the most appropriate parameters were selected. Optimization of the mixing microfluidic structures was performed by modeling the mixing capabilities of various geometry Tesla valve based structures [12, 13, 21, 24, 43–46] employing the finite element method (FEM). Using these results, the efficiency of the mixing of liquids and its dependence on the valve structure geometry is discussed. The obtained results of the numerically simulated mixing performance of the different structures were used to select the configuration for the experimental implementation. A microfluidic device, including the modeled mixer, was designed for precise dosing and dilution of colloidal solutions in the CAPA experimental setup described in [47], which enables one to manipulate and position micro-/nanoparticles in well-defined, ordered arrays [28, 48–51]. The device, containing three inlet channels, a Tesla valve based passive mixer and a branching outlet channel system with through holes at the ends of each channel, was successfully implemented in a scarcely used material in microfluidics—alumina. The experimental results demonstrated close conformity with the numerical simulations, i.e. the geometry of laminar flows within the channel as well as mixing behavior, indicating that the suggested microfluidic device prototyping technology can be employed as an alternative for conventional methods especially when hard, chemically inert materials, such as alumina, are in use, as well as proving the viability of such a micromixer for the manipulation of aggressive substances required by CAPA.

2. Methods and materials

2.1. Mixer geometry

The investigated structures included three basic components: three inlets, a mixing structure and an outlet. The inlets were designed with the aforementioned application in mind—dilution of colloidal suspensions—therefore the middle inlet containing the concentrated colloidal suspension (see figure 1

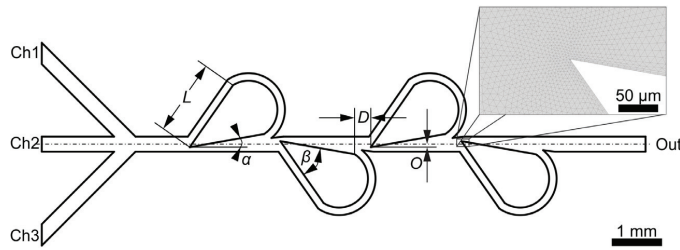


Figure 1. Basic layout (Ch1, Ch2, Ch3—inlets; out—outlet) of the modeled structures and varied parameters: L —length of a loop; D —distance between the loops; O —offset from channel axis; α —angle with relation to channel axis; β —structure angle. The inset depicts FEM mesh applied in the simulations.

‘Ch2’) was surrounded by two inlets for the diluting liquid (figure 1 ‘Ch1’, ‘Ch3’) forming a focusing effect after the joining of the three channels. The mixing structure was based on the Tesla valve, originally invented and patented by Nikola Tesla [43]. The structures, albeit heavily modified, retained the original idea—flow diodicity, where forward flow has a high hydraulic resistance due to liquid forcefully flowing through specifically designed loops, whereas the backwards flow has little to no resistance. For our designs (see figure 1), 2–8 loops were used, varying in angles (α , β), length (L), distance (D) and offset (O). The geometry also contained one or several outlets, depending on whether the whole microfluidic device or just the mixing part was modeled.

2.2. Modeling method

Even though more accurate methods exist for computational fluid simulations [52, 53], the commercially available FEM method based physics simulation suite COMSOL Multiphysics 5.0 was selected due to its straightforward simulations and modeling compatibility with CAD. Furthermore, FEM simulations have already been proven to be viable for small scale fluid flows [54, 55]. The geometries were initially designed using Autodesk AutoCAD 2016 and imported to COMSOL as ‘*.dxf’ files. Two modules were employed for the simulations—‘creeping flow’, which was used for simulating fluid flows at very low Reynolds numbers for which the inertial term in the Navier–Stokes equations could be neglected, and ‘mixture model, laminar flow’, which was used to model the flow at low and moderate Reynolds numbers of liquids containing a dispersed phase. The dispersed phase can be bubbles, liquid droplets, or solid particles and it is assumed that they travel at terminal velocity. The first module was necessary to calculate the velocity field and the second one to estimate the concentration distribution based on the velocities. Both modules employ the Navier–Stokes equations (1) and (2). The first one describes the conservation of momentum and the second one—the conservation of mass:

$$\rho \left(\frac{\partial \mathbf{u}}{\partial t} + \mathbf{u} \cdot \nabla \mathbf{u} \right) = -\nabla p + \nabla \cdot \left(\mu (\nabla \mathbf{u} + (\nabla \mathbf{u})^T) - \frac{2}{3} \mu (\nabla \cdot \mathbf{u}) \mathbf{I} \right) + \mathbf{F} \tag{1}$$

$$\frac{\partial \rho}{\partial t} + \nabla \cdot (\rho \mathbf{u}) = 0, \tag{2}$$

where \mathbf{u} is the fluid velocity, p is the fluid pressure, ρ is the fluid density, and μ is the fluid dynamic viscosity. The different terms correspond to the inertial forces (1–1), pressure forces (1–2), viscous forces (1–3), and the external forces applied to the fluid (1–4). For the very low Reynolds number simulations, such as this one, the first term can be neglected and that side of the equation is equal to 0.

For the creeping flow module, an incompressible flow, non-turbulent model and inertial flow term neglectation (Stokes flow) were selected. As for the mixture model, laminar flow module, a dispersed phase of solid particles, homogeneous flow mode and non-turbulent flow model type were selected. The boundary conditions for both modules are presented in table 1.

The mesh was selected for physics-induced fluid dynamics applications, which is proposed by the program itself. The predefined mesh parameters were selected as extremely fine (minimum element size 0.08 μm , maximum element growth rate 1.05, curvature factor 0.2, resolution of narrow regions 1). A sensible maximum element size was determined by performing a mesh convergence test (see figure 2). The test showed a 10 μm element size to be the saturation point and therefore this value was selected across all of the simulations, which resulted in a convergent mesh. The physics-induced sequence added a rectangular shaped mesh for boundary layers, whereas the rest of the mesh was free triangular (figure 1). All solutions yielded a convergent result with a 0.1% error.

The numerically simulated concentration maps of the microfluidic channel path were investigated both qualitatively and quantitatively. 2D fluid concentration maps were evaluated visually, whereas concentration distributions at the outlet were taken as line graphs (such as in the inset of figure 2). A full width at half maximum (FWHM) value of such a distribution was measured manually and plotted against the varied geometrical parameters.

2.3. Femtosecond laser ablation

An optimized microfluidic channel layout was laser micro-machined on a 1 mm thick, 30 × 48 mm² slide of opaque alumina ceramic substrate (VC 100-1 (Policor), 99.6–99.9% Al₂O₃, white, $\rho = 3.89 \text{ g cm}^{-3}$, $Ra < 0.01 \mu\text{m}$). A Yb:KGW femtosecond laser ($\lambda = 1030 \text{ nm}$, $\tau = 270 \text{ fs}$, $P = 4 \text{ W}$, Pharos

Table 1. Boundary conditions (BC) and properties for the simulation of concentration profiles.

Physics module	Inlet BC	Wall BC	Fluid properties	Outlet BC
Creeping flow	Laminar inflow $Ch_{1,3} = 0.045 \mu\text{l min}^{-1}$ $Ch_2 = 0.03 \mu\text{l min}^{-1}$ Entrance length $10 \mu\text{m}$, entrance thickness $200 \mu\text{m}$	No slip	$\rho = 1000 \text{ kg m}^{-3}$ $\mu = 0.001 \text{ Pa} \cdot \text{s}$	Atmospheric pressure, suppress backflow
Mixture model, laminar flow	Velocity distribution input from creeping flow simulated velocity distribution Dispersed phase concentration $\Phi_d = 0.1$	No slip, no dispersed phase flux	Continuous phase (water): $\rho = 1000 \text{ kg m}^{-3}$ $\mu = 0.001 \text{ Pa} \cdot \text{s}$ Dispersed phase (polystyrene): $\rho = 1050 \text{ kg m}^{-3}$ $\phi = 10^{-7} \text{ m}$	Atmospheric pressure, no viscous stress, dispersed phase outlet

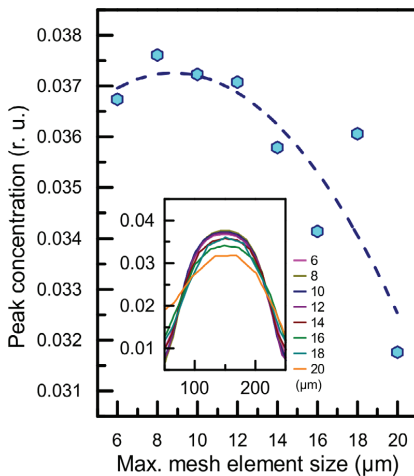


Figure 2. Mesh convergence test: peak concentration dependence on the maximum mesh element size taken from concentration distributions along the lateral channel axis (y) (inset).

04-500-PP, Light Conversion) together with a galvoscaner (SCANcube III 14, ScanLab) based microfabrication setup (FemtoLAB, Altechna R&D) was employed to impose the designed microfluidic device in the alumina ceramic surface. The same design files that were used for the simulations were also imported to a laser fabrication program SCA (Altechna R&D). A detailed description of the applied setup can be found in [56].

The investigation of the appropriate laser ablation parameters for microfluidic purposes was performed by varying the pulse overlap (scanning speed $50\text{--}250 \text{ mm s}^{-1}$) and energy density ($0.56\text{--}11.2 \text{ J cm}^{-12}$) in a matrix of $500 \mu\text{m}$ square structures. The detailed experimental parameters can be found in table 2. For this particular task, a 1030 nm wavelength and 40 kHz repetition rate were used. The laser was focused with a f-Theta lens to a diffraction limited $16 \mu\text{m}$ diameter spot size. The resulting square matrix of pits was evaluated using an SEM (Quanta 200 FEG, FEI) and a profilometer (TR200, Time Group).

2.4. Setup for experimental evaluation of device performance

In order to characterize the fluid mixing performance of the microfluidic channels imposed in the alumina ceramic slide, it was covered with a thick ($\sim 5 \text{ mm}$) layer of transparent PDMS (Sylgard® 148, Dow Corning Corp.) allowing interface tubing and visual investigation of the fluid mixing process. The PDMS cover in this case was used only for validation, as it would otherwise defeat the purpose of alumina in the case of aggressive substance manipulation in which case the PDMS cover should be replaced by an alumina cover and microwave processing methods should be employed for bonding [57]. Two syringe pumps, LA-100 (single channel) and LA-120 (two channels) from Landgraf Laborsysteme HLL GmbH, were used to drive the fluids through the device. 5 ml and 10 ml syringes as well as a 0.8 mm inner diameter fluorinated ethylene propylene (FEP) tubing were used. The flow rates were varied from $0.17\text{--}5.0 \mu\text{l min}^{-1}$. The focusing fluid supplied from the side channels was deionized water and the central fluid was red color stained deionized water, which accurately simulates the concentration distribution of the colloid solution, while enhancing the contrast between flows for direct observation. The microfluidic device performance was estimated by observing the change of laminar flows before the mixing structure (see figure 3(b)) at different flow rate ratios with a USB microscope BW-500X (Brightwell Technology Ltd.). Either the flow rate of the double syringe pump (figure 3(a) ‘S1’), which was connected to channels 1 and 3 (figure 1), or that of the single syringe pump (figure 3(a) ‘S2’), connected to channel 2 (figure 3) were varied. The obtained images were compared with the modeled ones (figure 3(c)). Colored pictures of the flow geometry were acquired at regular intervals (every 1 s), they were converted to binary mode and the lateral width of the focused central flow was measured using a custom algorithm prepared in MatLab (figure 3(b)).

3. Results and discussion

3.1. Various structures and their mixing performance

First, the influence of the Tesla valve loop geometry had to be investigated. So, the main framework for the simulations

Table 2. Femtosecond laser ablation experimental parameters.

Experimental structure matrix size	Square dimensions (μm)	No. of lines within one square	Distance between lines (μm)	Energy density (J cm^{-2})	Scanning speed (mm s^{-1})	Pulse overlap (%)
6 × 5	500 × 500	400, 200, 133, 100, 80	1.25–6.25 (step 1.25)	0.56–11.2 (step 2.1)	50, 60, 76, 92, 100, 108, 124, 140, 150, 200, 250	60.9, 68.8, 76.6, 78.1, 80.6, 83.1, 84.4, 85.6, 88.1, 90.6, 92.2

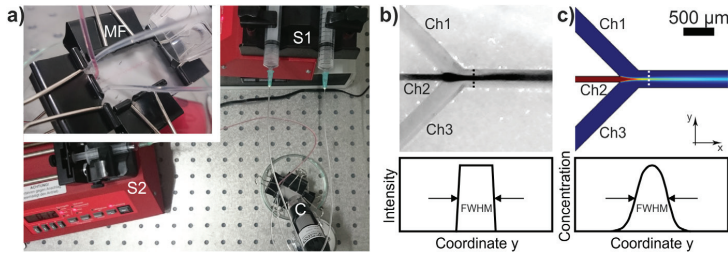


Figure 3. (a) Camera image of the experimental setup for evaluation of microfluidic mixing performance (MF—laser micromachined microfluidic device in alumina ceramics sealed with a PDMS film, S1—two channel syringe pump (clear water) supplying focusing liquids, S2—syringe pump (dyed water) supplying central liquid, C—USB microscope); USB microscope image (b) and simulated laminar flow (c) analysis used for comparison of geometries (Ch1, Ch3—focusing liquids; Ch2—central liquid).

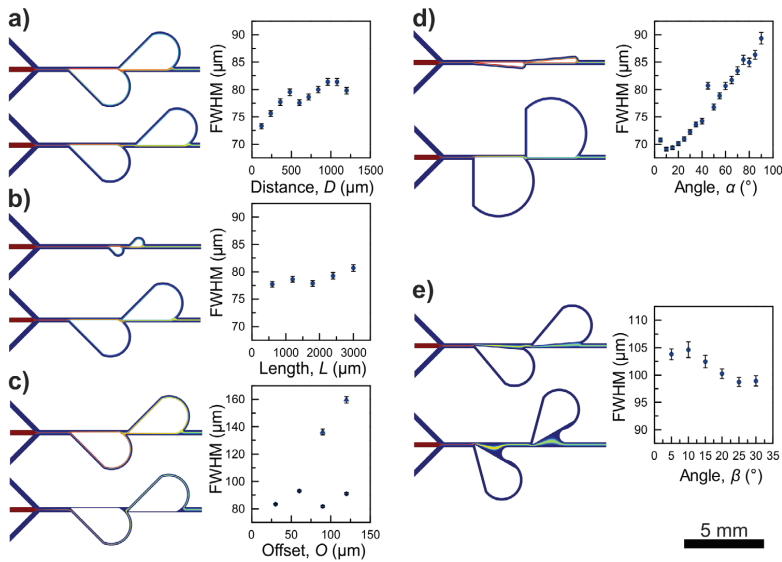


Figure 4. Results of the simulations: 2D concentration maps of lowest (top image) and highest (bottom image) investigated parameter value together with the width of central flow at the outlet (FWHM value) dependence on the corresponding parameter (a) distance D (120–1200 μm), (b) length L (600–3000 μm), (c) offset O (30–120 μm), (d) angle α (5° – 90°), (e) angle β (5° – 30°).

was a basic 4-way junction, with three inlets and one outlet, together with one or several mixing loops inbetween (as described in section 2.1). The width of the main channels was 300 μm , whereas the width of the mixing structure channels was 150 μm . The selected simulated 2D concentration maps and the graphs of the FWHM value of the concentration

Table 3. Obtained optimal Tesla structure based mixer geometry parameters.

α ($^\circ$)	β ($^\circ$)	L (μm)	D (μm)	O (μm)
45	0	1200	480	0

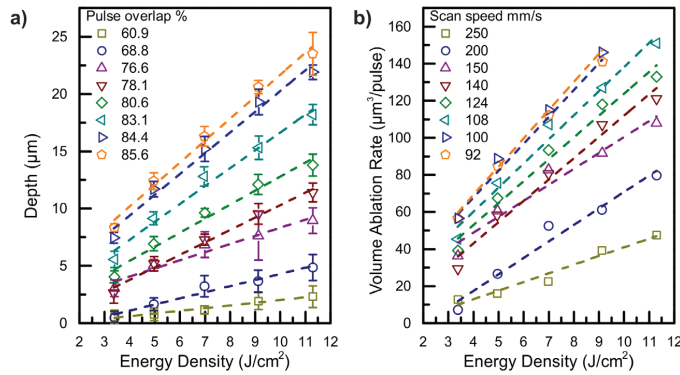


Figure 5. Laser ablation processing results with respect to the used parameters: structure depth with respect to the energy density and pulse overlap (a) and volume ablation rate with respect to the energy density and scanning speed (b). The ablation overlap at the corresponding scan speeds is indicated in the legends.

distribution at the outlet are shown in figure 4. In most cases, the flow pattern showed a regular behavior with a slight dispersion of the central flow. However, a couple of points are worth noticing. First, when varying the offset (O) (figure 4(c)), at some point the central flow switched to the looping channel as opposed to the regular splitting-recombining effect, which occurred in other cases. Also in this case, as the offset increased, the central channel shrunk to a point, where the used mesh was of insufficient fineness, which resulted in a nonconverging mesh. Therefore, the maximum element size had to be decreased to $5 \mu\text{m}$ (see graph in figure 4(c), triangles mark data points obtained using the nonconverging mesh) to reestablish the mesh convergence. However, this also removed the obvious high dependence of the FWHM value on the offset parameter. In the case where the structure angle (β) was varied (figure 4(e)), the central flow experienced a shift of trajectory and dispersion as the channel width increased with the angle. This led to an immediate increase of the FWHM value at the outlet. However, it started dropping as soon as the β parameter was increased further, showing a weak negative dependence. As for the rest of the parameters (D, L, O), for the analyzed Tesla valve based mixer, no strong dependence on the mixing performance was found for any of them, except for the angle with relation to the channel axis (α), which showed a strong linear dependence. Based on the mixing performance analysis and some structure size and experimental setup considerations, the Tesla loop parameters shown in table 3 were regarded as optimal and selected for further full-scale device modeling, implementation and experimental investigation.

3.2. Optimization of laser ablation parameters

The surface morphology of pulsed-laser micromachined structures in alumina highly depends on the spatial distribution of pulses. Furthermore, by changing the pulse energy, the volume ablation rate can be adjusted. Both parameters are of high importance for the manufacturing of microfluidic devices. Therefore, experiments using different laser

processing regimes were carried out, which yielded results allowing for an optimal material processing mode. Surface quality of the ablated areas was dependent on the regimes applied. At a high pulse overlap (92% and 90.6%) a layer of melted ablation debris was deposited, which resulted in a decline of the surface quality. This agrees well with [58], which states that a high pulse overlap as well as a high energy density results in an increase of local temperature and unwanted effects, and therefore these ablation modes are not practical. A further decrease of the pulse overlap (76.6%–85.6%) improved the surface quality and the melted debris was no longer observed. However, a further decrease of the pulse overlap to (68.8%–60.9%) showed only a negligible volume ablation rate at energy densities of $0.56\text{--}3.37 \text{ J cm}^{-2}$ (figure 5(a)).

The volume ablation rate can be defined as the volume of material removed per laser pulse (figure 5(b)). It was evaluated by measuring the depth of the structures using a profilometer. The ablated trench depth and volume ablation rate demonstrate linear dependencies with respect to the applied energy density. The higher pulse overlaps (or smaller scan speeds) resulted in deeper structures. Based on these results, a 100 mm s^{-1} scanning speed (84.4% pulse overlap) and 11.2 J cm^{-2} energy density were selected. The volume ablation rate in this case was $165 \mu\text{m}^3/\text{pulse}$, and in order to reach a microfluidic channel depth of $\sim 200 \mu\text{m}$ the ablation of the designed pattern was repeated 10 times.

3.3. Modeling and implementation of a full-scale device

A microfluidic layout was specifically designed to accommodate the needs for the direct introduction of colloid droplets in the CAPA setup. With that in mind, the length and width of the whole layout (25 by 75 mm) was selected to fit a common microscope's glass slide dimensions, which the designed device was supposed to replace [47]. The change of flow direction and branching of the channels were introduced to be able to produce precise droplets of solution on the substrate through holes where the assembly was to be performed.

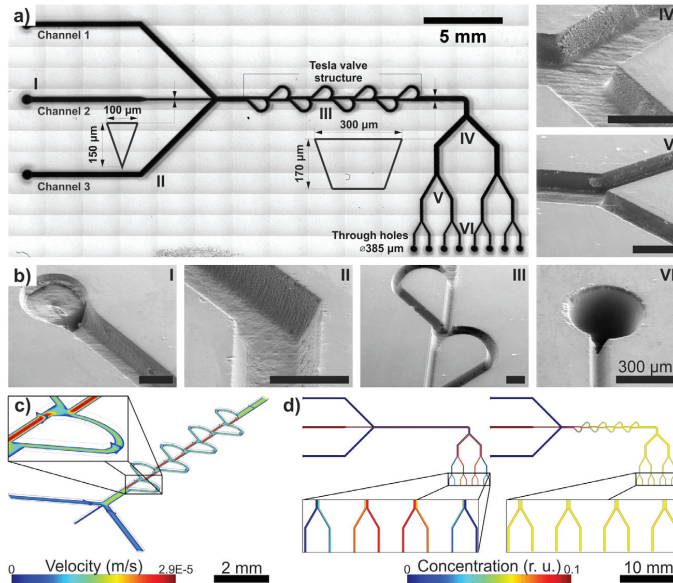


Figure 6. (a) Stacked optical micrograph of the microfluidic device, ablated in alumina ceramics and linear dimensions of the structure (typical cross-section shapes (V-shape, trapezium) of the channels are shown in the insets). (b) SEM images of characteristic channels of the microfluidic device (the corresponding positions are marked on the optical micrograph using Roman numerals) (c) 3D velocity profile of a microfluidic flow through the Tesla mixer (inset depicts first mixing structure). (d) Comparison of 2D concentration profiles without and with the Tesla mixer (insets depict magnified branching outlets).

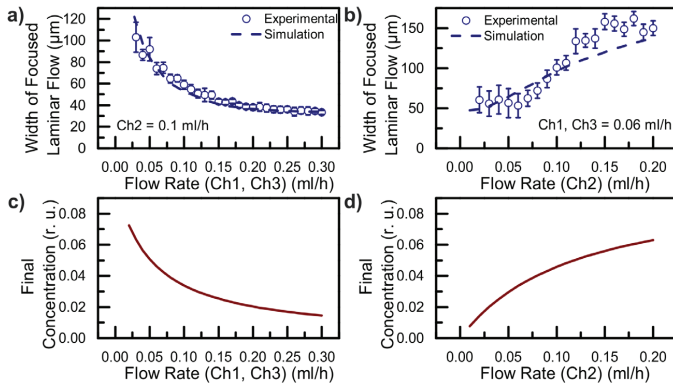


Figure 7. (a) and (b) Experimental and simulated widths of the laminar central channel flow (Ch2) while varying focusing channels' flow rates (Ch1) and (Ch3) ((a), please see the supplementary data online (stacks.iop.org/JMM/28/015013/mmedia)) and central channel flow rate (b). Simulated output concentration curves depending on the focusing channels' (c) and central channel (d) flow rates.

The microfluidic device was realized in an alumina employing femtosecond laser ablation. The laser micro-machining parameters were selected based on the investigation described in section 3.2. The stitched optical micrograph of the structures is shown in figure 6(a). The lateral dimensions of the structures close to the surface are spot on, however, there is a certain channel width (see figures 6(a) and (b) (VI)), after which the channel loses its flat bottom surface and its cross-section turns into a V-shape.

Figure 6(c) shows a numerically simulated 3D flow velocity distribution of the actually fabricated microfluidic

device taking into account the slightly tapered walls of the channels. As it can clearly be seen from figure 6(c), the flow velocity is much higher within the central channel, compared to the velocity within the loops. This suggests that mixing occurs due to two effects, i.e. different velocity magnitudes and different velocity directions. These effects are created by the passive mixer, enforcing the mixing of fluids at the interface of laminar flows.

Since the flow profile did not show much dependence on the channel cross-section geometry, further simulation of the device, not unlike the structure optimization, was performed

in 2D. As described in section 2.2, the laminar flow module was employed to calculate the velocity distribution, which was then fed to the mixture model to calculate the concentration distribution of the dispersed phase. Figure 6(d) shows the contribution of the loops to the mixing. It is evident, that a simple, straight channel results in a very varied concentration at the branching outputs, whereas after the mixing structure consisting of optimized geometry loops is introduced, the concentration distribution is completely uniform. It can also be noted, that efficient mixing is achieved after 5–6 loops, which brings the total length of the mixing channel structure to less than 10 mm.

3.4. Experimental investigation of the full-scale device

The assembled device, as described in the experimental section, was experimentally investigated by observing the flow profiles within the channels, while changing the flow rates of channels 1 and 2 or 3 (figure 7). By applying a picture analysis algorithm, which converts it to binary format and measures the dimensions of the flow profile, the device performance was compared to the simulated values. As it can be seen, the flow profile is very consistent with the simulation results, when the flow rate of the focusing flows is changed (figure 7(a), please see the supplementary data online). However, the other mode, where the focused flow rate was varied (figure 7(b)), showed a slight deviation from the simulated values, i.e. the experimental points seem to converge at both ends, whereas the numerical curve shows a monotonical increase. These errors may be attributed to the inconsistent flow rate delivered by the pump and/or insufficient side pressure from the focusing flows. Overall, the graphs demonstrate the same trends and provide sufficient evidence that: (a) structures imposed in alumina ceramics do not introduce any changes to the regular flow patterns in microfluidics and (b) the simulated dependencies of the mean concentration at the output of the microfluidic device (figures 7(c) and (d)) may be used as guides for the precise selection of the input velocities in order to achieve the desired concentration in the output. Concerning the efficiency of mixing of our designed and produced microfluidic device, it should be noted that similar results have been shown by authors [21, 43], however, our design possesses a distinct advantage of performing at a smaller than 10 mm mixing structure length scale not to mention the unique, hard and highly resistant material the device was made of—alumina—the most widely used ceramic, employing the novel lithography technology based on femtosecond laser microfabrication.

4. Conclusions

A static three port microfluidic mixer based on Tesla structures was designed, optimized and implemented in an alumina ceramic substrate via femtosecond laser micromachining. The numerical simulations, performed using the commercial FEM modeling software, were employed to explain the mixing tendencies and to find optimal structure geometry. It was

concluded, that, in fact, most of the investigated parameters have little to no effect on the mixing efficiency, except for the structure angle with respect to the channel axis. Optimal parameters ($\alpha = 45^\circ$, $\beta = 0^\circ$, $L = 1200 \mu\text{m}$, $D = 480 \mu\text{m}$, $O = 0 \mu\text{m}$) were selected for the full-scale device, which was also modeled. It was demonstrated, that the introduction of the optimal mixing structures improves the homogeneity of the concentration at the output of the device. The very same design was used to implement microfluidic structures in a very environmentally resistant, albeit tough to process material—alumina ceramic. Femtosecond laser ablation was employed to fulfill this task, as standard lithography methods simply do not work for this material. Optimal laser micromachining parameters were selected: 100 mm s^{-1} scanning speed (84.4% pulse overlap) and 11.2 J cm^{-2} energy density. Although rectangular channel geometry could not be achieved in this case, the simulations showed only a slight difference due to the tapered channel walls. The device was experimentally investigated by measuring the laminar flow geometry. After the comparison of the experimental results with the simulated curves, it was concluded that they matched well. Therefore, such laser ablation based microfabrication method of alumina is perfectly viable for the direct fabrication of microfluidic devices dedicated to aggressive substance manipulation and mixing.

Acknowledgments

This work was supported by the Research Council of Lithuania Lithuanian–Japan bilateral cooperation partnership program, project ‘PLAS’, grant No: LJB-1/2015.

ORCID iDs

M Juodėnas  <https://orcid.org/0000-0002-0517-8620>

T Tamulevičius  <https://orcid.org/0000-0003-3879-2253>

S Tamulevičius  <https://orcid.org/0000-0002-9965-2724>

References

- [1] Leman M, Abouakil F, Griffiths A D and Tabeling P 2015 Droplet-based microfluidics at the femtoliter scale *Lab Chip* **15** 753–65
- [2] Shim J, Ranasinghe R T, Smith C A, Ibrahim S M, Hollfelder F, Huck W T S, Klenerman D and Abell C 2013 Ultrarapid generation of femtoliter microfluidic droplets for single-molecule-counting immunoassays *ACS Nano* **7** 5955–64
- [3] Choi G, Song D, Shrestha S, Miao J, Cui L and Guan W 2016 A field-deployable mobile molecular diagnostic system for malaria at the point of need *Lab Chip* **16** 4341–9
- [4] Yeo J C, Kenry K and Lim C T 2016 Emergence of microfluidic wearable technologies *Lab Chip* **16** 4082–90
- [5] Kilic O *et al* 2016 Brain-on-a-chip model enables analysis of human neuronal differentiation and chemotaxis *Lab Chip* **16** 4152–62
- [6] Harink B, Le Gac S, Truckenmüller R, van Blitterswijk C and Habibovic P 2013 Regeneration-on-a-chip? The perspectives on use of microfluidics in regenerative medicine *Lab Chip* **13** 3512

- [7] Marasso S L, Giuri E, Canavese G, Castagna R, Quaglio M, Ferrante I, Perrone D and Cocuzza M 2011 A multilevel lab on chip platform for DNA analysis *Biomed. Microdevices* **13** 19–27
- [8] Xia H M, Wan S Y M, Shu C and Chew Y T 2005 Chaotic micromixers using two-layer crossing channels to exhibit fast mixing at low Reynolds numbers *Lab Chip* **5** 748
- [9] Bhagat A A S, Peterson E T K and Papautsky I 2007 A passive planar micromixer with obstructions for mixing at low Reynolds numbers *J. Micromech. Microeng.* **17** 1017–24
- [10] Wang S, Huang X and Yang C 2011 Mixing enhancement for high viscous fluids in a microfluidic chamber *Lab Chip* **11** 2081
- [11] Cheng S B, Skinner C D, Taylor J, Attiya S, Lee W E, Picelli G and Harrison D J 2001 Development of a multichannel microfluidic analysis system employing affinity capillary electrophoresis for immunoassay *Anal. Chem.* **73** 1472–9
- [12] Nguyen N-T and Wu Z 2005 Micromixers—a review *J. Micromech. Microeng.* **15** R1–16
- [13] Lee C-Y Y, Chang C-L L, Wang Y-N N and Fu L-M M 2011 Microfluidic mixing: a review *Int. J. Mol. Sci.* **12** 3263–87
- [14] Sonato A, Agostini M, Ruffato G, Gazzola E, Liuni D, Greco G, Travagliati M, Cecchini M and Romanato F 2016 A surface acoustic wave (SAW)-enhanced grating-coupling phase-interrogation surface plasmon resonance (SPR) microfluidic biosensor *Lab Chip* **16** 1224–33
- [15] Lee C-Y, Chang T-C, Wang S-C, Chien C-W and Cheng C-W 2010 Using femtosecond laser to fabricate highly precise interior three-dimensional microstructures in polymeric flow chip *Biomicrofluidics* **4** 46502
- [16] Matsubara K and Narumi T 2016 Microfluidic mixing using unsteady electroosmotic vortices produced by a staggered array of electrodes *Chem. Eng. J.* **288** 638–47
- [17] Venancio-Marques A, Barbaud F and Baigl D 2013 Microfluidic mixing triggered by an external LED illumination *J. Am. Chem. Soc.* **135** 3218–23
- [18] Wen C-Y, Yeh C-P, Tsai C-H and Fu L-M 2009 Rapid magnetic microfluidic mixer utilizing AC electromagnetic field *Electrophoresis* **30** 4179–86
- [19] Juodėnas M, Hoyland J D, Jurenas V and Bubulis A 2013 Piezoelectric actuation for microfluidic cell sorting *J. Meas. Eng.* **1** 228–32
- [20] Chung Y-C, Hsu Y-L, Jen C-P, Lu M-C and Lin Y-C 2004 Design of passive mixers utilizing microfluidic self-circulation in the mixing chamber *Lab Chip* **4** 70
- [21] Hong C-C, Choi J-W and Ahn C H 2004 A novel in-plane passive microfluidic mixer with modified Tesla structures *Lab Chip* **4** 109
- [22] Park S-G, Lee S-K, Moon J H and Yang S-M 2009 Holographic fabrication of three-dimensional nanostructures for microfluidic passive mixing *Lab Chip* **9** 3144
- [23] Lin Y-C, Chung Y-C and Wu C-Y 2007 Mixing enhancement of the passive microfluidic mixer with J-shaped baffles in the tee channel *Biomed. Microdevices* **9** 215–21
- [24] Lee C-Y, Wang W-T, Liu C-C and Fu L-M 2016 Passive mixers in microfluidic systems: a review *Chem. Eng. J.* **288** 146–60
- [25] Faustino V, Catarino S O, Lima R and Minas G 2016 Biomedical microfluidic devices by using low-cost fabrication techniques: a review *J. Biomech.* **49** 2280–92
- [26] Friend J and Yeo L 2010 Fabrication of microfluidic devices using polydimethylsiloxane *Biomicrofluidics* **4** 26502
- [27] Wu J and Gu M 2011 Microfluidic sensing: state of the art fabrication and detection techniques *J. Biomed. Opt.* **16** 80901
- [28] Kuemin C, Stutz R, Spencer N D and Wolf H 2011 Precise placement of gold nanorods by capillary assembly *Langmuir* **27** 6305–10
- [29] Henzie J, Andrews S C, Ling X Y, Li Z and Yang P 2013 Oriented assembly of polyhedral plasmonic nanoparticle clusters *Proc. Natl Acad. Sci.* **110** 6640–5
- [30] Lee J N, Park C and Whitesides G M 2003 Solvent compatibility of poly(dimethylsiloxane)-based microfluidic devices *Anal. Chem.* **75** 6544–54
- [31] Yoshimura M and Bowen H K 1981 Electrical breakdown strength of alumina at high temperatures *J. Am. Ceram. Soc.* **64** 404–10
- [32] Dörre E and Hübner H 1984 *Alumina—Processing, Properties, and Applications* (Berlin: Springer)
- [33] © KYOCERA Corporation Alumina (aluminum oxide, Al₂O₃) <https://global.kyocera.com/prdct/fc/list/material/alumina/index.html> (Accessed: 12 May 2017)
- [34] Suriano R, Kuznetsov A, Eaton S M, Kiyari R, Cerullo G, Osellame R, Chichkov B N, Levi M and Turri S 2011 Femtosecond laser ablation of polymeric substrates for the fabrication of microfluidic channels *Appl. Surf. Sci.* **257** 6243–50
- [35] Waddell E A 2006 Laser ablation as a fabrication technique for microfluidic devices *Microfluidic Techniques* vol 321 (Totowa, NJ: Humana Press) pp 27–38
- [36] Chen Q Q, Chen Q Q, Maccioni G, Sacco A, Scaltrito L, Ferraris M and Ferrero S 2011 Fabrication of large-area microfluidics structures on glass by imprinting and diode-pumped solid state laser writing techniques *Microsyst. Technol.* **17** 1611–9
- [37] Chen Q Q, Chen Q Q, Maccioni G, Sacco A, Ferrero S and Scaltrito L 2012 Fabrication of microstructures on glass by imprinting in conventional furnace for lab-on-chip application *Microelectron. Eng.* **95** 90–101
- [38] LoTurco S, Osellame R, Ramponi R and Vishnubhatla K C 2013 Hybrid chemical etching of femtosecond laser irradiated structures for engineered microfluidic devices *J. Micromech. Microeng.* **23** 85002
- [39] Sugioka K, Xu J, Wu D, Hanada Y, Wang Z, Cheng Y and Midorikawa K 2014 Femtosecond laser 3D micromachining: a powerful tool for the fabrication of microfluidic, optofluidic, and electrofluidic devices based on glass *Lab Chip* **14** 3447–58
- [40] Bellouard Y, Said A, Dugan M and Bado P 2004 Fabrication of high-aspect ratio, micro-fluidic channels and tunnels using femtosecond laser pulses and chemical etching *Opt. Express* **12** 2120
- [41] Sugioka K and Cheng Y 2012 Femtosecond laser processing for optofluidic fabrication *Lab Chip* **12** 3576
- [42] Marcinkevičius A, Juodkaziš S, Watanabe M, Miwa M, Matsuo S, Misawa H and Nishii J 2001 Femtosecond laser-assisted three-dimensional microfabrication in silica *Opt. Lett.* **26** 277
- [43] Wang C-T, Chen Y-M, Hong P-A and Wang Y-T 2014 Tesla valves in micromixers *Int. J. Chem. React. Eng.* **12**
- [44] Yang A-S, Chuang F-C, Chen C-K, Lee M-H, Chen S-W, Su T-L and Yang Y-C 2015 A high-performance micromixer using three-dimensional Tesla structures for bio-applications *Chem. Eng. J.* **263** 444–51
- [45] Hossain S, Ansari M A, Husain A and Kim K-Y 2010 Analysis and optimization of a micromixer with a modified Tesla structure *Chem. Eng. J.* **158** 305–14
- [46] Tesla N 1920 Valvular conduit *US Patent Specification* 1,329,559
- [47] Virganavičius D, Juodėnas M, Tamulevičius T, Schiff H and Tamulevičius S 2017 Investigation of transient dynamics of capillary assisted particle assembly yield *Appl. Surf. Sci.* **406** 136–43
- [48] Malaquin L, Kraus T, Schmid H, Delamarque E and Wolf H 2007 Controlled particle placement through convective and capillary assembly *Langmuir* **23** 11513–21

- [49] Ni S, Klein M J K, Spencer N D and Wolf H 2015 Capillary assembly of cross-gradient particle arrays using a microfluidic chip *Microelectron. Eng.* **141** 12–6
- [50] Ni S, Klein M J K, Spencer N D and Wolf H 2014 Cascaded assembly of complex multiparticle patterns *Langmuir* **30** 90–5
- [51] Klein M J K, Kuemin C, Tamulevičius T, Manning M and Wolf H 2012 Note: a microfluidic chip setup for capillarity-assisted particle assembly *Rev. Sci. Instrum.* **83** 86109
- [52] Zhu T and Ye W 2010 Theoretical and numerical studies of noncontinuum gas-phase heat conduction in micro/nano devices *Numer. Heat Transfer. B* **57** 203–26
- [53] Liu H, Xu K, Zhu T and Ye W 2012 Multiple temperature kinetic model and its applications to micro-scale gas flows *Comput. Fluids* **67** 115–22
- [54] Ménégaud V, Jossierand J and Girault H H 2002 Mixing processes in a zigzag microchannel: finite element simulations and optical study *Anal. Chem.* **74** 4279–86
- [55] Collins D J, Ma Z, Han J and Ai Y 2017 Continuous micro-vortex-based nanoparticle manipulation via focused surface acoustic waves *Lab Chip* **17** 91–103
- [56] Tamulevičius T, Šimatonis L, Ulčinas O, Tamulevičius S, Žukauskas E, Rekuviėnė R and Mažeika L 2016 Micromachining and validation of the scanning acoustic microscope spatial resolution and sensitivity calibration block for 20–230 MHz frequency range *Microscopy* **65** 429–37
- [57] Das S, Mukhopadhyay A K, Datta S and Basu D 2008 Prospects of microwave processing: an overview *Bull. Mater. Sci.* **31** 943–56
- [58] Leone C, Genna S, Tagliaferri F, Palumbo B and Dix M 2016 Experimental investigation on laser milling of aluminium oxide using a 30 W Q-switched Yb:YAG fiber laser *Opt. Laser Technol.* **76** 127–37

M. Juodėnas, T. Tamulevičius, J. Henzie, D. Erts, S. Tamulevičius

Surface Lattice Resonances in Self-Assembled Arrays of Monodisperse Ag Cuboctahedra

We used CAPA to self-assemble SLR-capable hexagonal arrays of Ag cuboctahedra (edge length, $a = 123 \text{ nm} \pm 2 \text{ nm}$) on the surface of a PDMS replica mold. The parameters of the assembly method enabled us to generate large $\sim 1 \text{ cm}^2$ arrays that were relatively free of defects ($< 1\%$), thus their angle and polarization-dependent transmission properties were able to be measured using a simple free-space optical setup. The spectra were compared to a coupled dipole approximation model to examine the emergence of the SLR, and a finite element method (FEM) model transmission to investigate the in-plane and out-of-plane spatial distribution of the local EM field at peak wavelength values. At orthogonal incidence, the SLR peak appears at 757 nm wavelength and has a Q -factor of ~ 30 . At oblique illumination angles, SLR peaks follow the RAs and reach a Q -factor of ~ 80 . To our knowledge, no one has been able to use template-assisted self-assembly to reproducibly generate high Q -factor SLRs.

ACS Nano, **13**(8), 2019, pp. 9038–9047

DOI: 10.1021/acsnano.9b03191

Surface Lattice Resonances in Self-Assembled Arrays of Monodisperse Ag Cuboctahedra

Mindaugas Juodėnas,^{*,†,‡} Tomas Tamulevičius,^{†,‡,§} Joel Henzie,^{*,§} Donats Erts,^{||} and Sigitas Tamulevičius^{†,‡}

[†]Institute of Materials Science, Kaunas University of Technology, K. Baršausko St. 59, Kaunas LT-51423, Lithuania

[‡]Department of Physics, Kaunas University of Technology, Studentų St. 50, Kaunas LT-51368, Lithuania

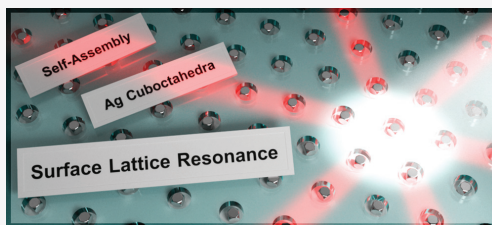
[§]International Center for Materials Nanoarchitectonics (WPI-MANA), National Institute for Materials Science (NIMS), 1-1 Namiki, Tsukuba, Ibaraki 305-0044, Japan

^{||}Institute of Chemical Physics, University of Latvia, 19 Raina Blvd., Riga LV-1586, Latvia

Supporting Information

ABSTRACT: Plasmonic metal nanoparticles arranged in periodic arrays can generate surface lattice plasmon resonances (SLRs) with high Q -factors. These collective resonances are interesting because the associated electromagnetic field is delocalized throughout the plane of the array, enabling applications such as biosensing and nanolasing. In most cases such periodic nanostructures are created *via* top-down nanofabrication processes. Here we describe a capillary-force-assisted particle assembly method (CAPA) to assemble monodisperse single-crystal colloidal Ag cuboctahedra into nearly defect-free $>1\text{ cm}^2$ hexagonal lattices. These arrays are large enough to be measured with conventional ultraviolet–visible spectroscopy, which revealed an extinction peak with a Q -factor of 30 at orthogonal illumination and up to 80 at oblique illumination angles. We explain how the experimental extinction changes with different light polarizations and angles of incidence, and compare the evolution of the peaks with computational models based on the coupled dipole approximation and the finite element method. These arrays can support high Q -factors even when exposed to air, because of the high aspect ratio of the single-crystal nanoparticles. The observation of SLRs in a self-assembled system demonstrates that a high level of long-range positional control can be achieved at the single-particle level.

KEYWORDS: surface lattice resonance, colloidal nanoparticles, template-assisted self-assembly, lattice plasmons, metal nanoparticle arrays



Noble metal nanostructures support collective oscillations of conduction electrons called localized surface plasmon resonances (LSPRs).^{1,2} LSPRs can be excited with an electromagnetic (EM) field that matches the resonant frequency of the nanostructure depending on its size, shape, and dielectric environment. The extinction peaks of LSPRs are often quite broad because of losses attributed to radiative damping and depolarization, resulting in Q -factors ($Q = \lambda_{\text{max}}/\Delta\lambda$) that seldom exceed 10 to 20 in experiment.³ One way to improve the intrinsic Q -factor of a NP is to pattern them in regular arrangements to generate a collective plasmonic response. These collective plasmon resonances were initially proposed in theoretical papers of Markel⁴ and Schatz.⁵ They showed that individual NPs in an array could couple diffractively if their LSPRs were within the range of the Rayleigh anomaly (RA). The behavior of RAs has been previously characterized in substrates such as linear dielectric diffraction gratings and plasmonic nanohole arrays.^{6–9} Under

these conditions, each metal NP in the array can experience light scattered by adjacent particles, generating a self-reinforcing collective resonance that creates a narrow dip in the optical transmission spectrum,^{3,10,11} although in some cases it can enhance transparency.¹² Scientists have used these collective resonances to generate surfaces with very narrow extinction peaks,^{13–17} even supporting Q -factors an order of magnitude larger than the LSPR of isolated particles.¹⁸ By changing the lattice parameters in relation to the nanostructures, it is possible to tune this resonant peak across the visible and near-infrared spectrum. This type of collective resonance is called a plasmonic surface lattice resonance (SLR) and it has been used in numerous applications in optics,¹⁹ light

Received: April 25, 2019

Accepted: July 22, 2019

Published: July 22, 2019

emission,^{20,21} protein biosensing,^{22,23} nanolasing,^{24–27} photoluminescence enhancement,²⁸ *et cetera*.

Learning how to generate surface lattice plasmon resonances (SLRs) with arrays of particles exposed to the environment is especially useful in sensing applications, because the analyte may access the EM hotspot and noticeably affect the SLR resonance. Nanoparticle arrays can generate stronger radiative interparticle coupling when the energy associated with the resonance is localized primarily in the superstrate. Thus, arrays composed of taller, high-aspect ratio particles are desired in order to generate stronger SLRs. Top-down nanofabrication techniques can create tall particles, but masking techniques tend to generate tapered particles whose diameter varies with height.^{9,29} In addition, physical vapor deposition methods generate particles that are highly polycrystalline, which broadens the LSPRs of individual NPs by increasing electron scattering at grain boundaries and lowering the lifetime of the plasmon resonance.³⁰ On the other hand, researchers have used DNA-assisted assembly to generate arrays of single-crystal colloidal nanocubes. These self-assembled structures can support lattice modes, but the *Q*-factors are still relatively low compared to the modeled structures.^{31,32}

Self-assembly using templates is a good route to achieve a sufficient level of control over the position and spacings of NPs while simultaneously exploiting the advantages of synthesized colloids. Shaped metal NPs have intrinsically higher single-particle *Q*-factors because they possess atomically smooth facets and can be monocrystalline. The templates can be generated by replicating patterns in hard materials such as silicon (Si) *via* soft-lithography using elastomeric polymers, *e.g.*, polydimethylsiloxane (PDMS). This feature helps limit but not eliminate the need for expensive e-beam lithography steps in the process flow. Assembling NPs on elastomers may have additional advantages in the generation of SLRs, because stretching/compression can enable dynamic tuning of the interparticle spacing.^{33–36} Such templates have been used to self-assemble arrays of metal and organic NPs³⁷ with diameters spanning tens of nanometers to micrometers in 1 cm² scale areas.^{38–40} Capillary-force-assisted assembly^{38,41} is a template-assisted method that uses convective currents and confining capillary forces at the air/liquid/template interface to selectively deposit NPs inside patterned obstacles (*e.g.*, protrusions or voids) by tailoring the wetting, temperature, and assembly speed conditions in a temperature-controlled single-axis translation setup.⁴² In the field of plasmonics, CAPA-based methods have been used to generate patterns of NPs for surface-enhanced Raman spectroscopy (SERS),⁴³ anticounterfeiting security features,⁴⁴ light upconversion,⁴⁵ *et cetera*. To our knowledge, no one has been able to use template-assisted self-assembly to reproducibly generate high *Q*-factor SLRs. In addition, SLRs provide insight into the positional control of single-particle assembly with these template-assisted methods.

We used CAPA to self-assemble SLR-capable hexagonal arrays of Ag NPs on the surface of a PDMS replica mold. The parameters of the assembly method enabled us to generate large ~ 1 cm² arrays that were relatively free of defects (<1%). Thus, the angle and polarization-dependent transmission properties of the arrays were able to be measured using a simple free-space optical setup. The spectra were compared to a coupled dipole approximation model to examine the emergence of the SLR and a finite element method (FEM) model transmission to investigate the in-plane and out-of-plane

spatial distribution of the local EM field at peak wavelength values. At orthogonal incidence, the SLR peak appears at 757 nm wavelength and has a *Q*-factor of ~ 30 . At oblique illumination angles, SLR peaks follow the RAs and reach a *Q*-factor of ~ 80 .

RESULTS AND DISCUSSION

An overview of the NPs and their optical properties is displayed in Figure 1. The particles were synthesized using a

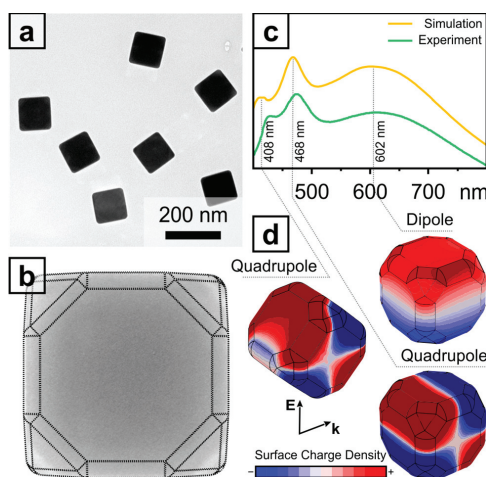


Figure 1. NPs used in the experiment. (a) TEM micrograph of colloidal Ag cuboctahedra with an edge length of 122 ± 3 nm. (b) TEM micrograph of a single NP with overlaid contours of the model shape. (c) Modeled and measured optical extinction spectra of the NPs dispersed in ethanol. (d) Charge density plots of the quadrupolar and dipolar plasmonic modes denoted in panel c.

modified polyol method described previously.⁴⁶ This method generates monodisperse single-crystal Ag nanoparticles coated with polyvinylpyrrolidone (PVP) polymer surfactant. We used the method to generate particles that approximately match the shape of a cuboctahedron with an edge length (*a*) of 122 ± 3 nm. A deeper examination of the 3D shape of the NP using SEM is included in Figure S1. We created a model matching the shape of the average particle and simulated its optical properties in the FEM. Figure 1c shows the extinction spectrum of the NPs in ethanol *versus* the simulated FEM spectrum. 3D surface polarization plots obtained in the FEM show that the peak at 602 nm is a dipolar mode, while the peaks at 408 and 468 nm are quadrupolar modes (Figure 1d). The quadrupolar mode at 408 nm is excited when the incident plane wave is normal to the edge or corner of the NP, while the 468 nm quadrupole is excited in most excitation schemes we examined. The dipolar mode is excited regardless of nanoparticle orientation. A more detailed analysis of the local surface plasmon modes under the different excitation schemes is included in Figure S2. The experimental and calculated spectra do not differ significantly aside from a slight red-shift of the experimental spectrum, which may be due to inaccurate definition of edge rounding in the model or influence of the surfactant. The match between experiment and theory was

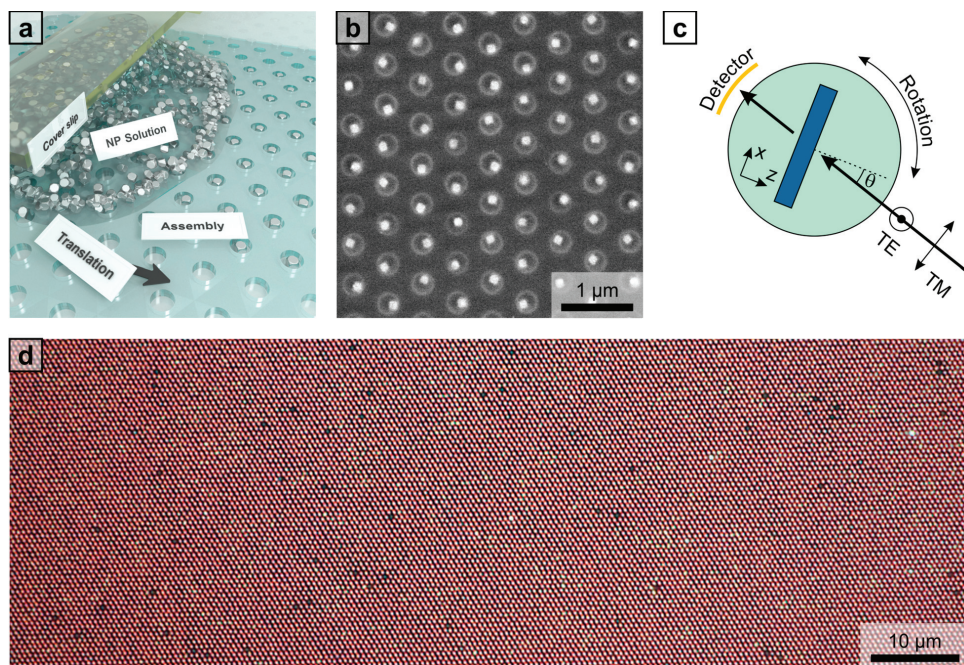


Figure 2. NP assembly. (a) A 3D visualization of the CAPA assembly method. (b) SEM micrograph of a randomly selected assembly area showing the deposition of single NPs. (c) Simplified layout of the optical measurement setup used to characterize the angle and polarization dependence of the NP arrays. TE or TM polarized light beam excites the sample at an incident angle θ , which is changed by rotating the sample around a vertical axis. The transmitted light is collected by a stationary detector. (d) Dark-field optical micrograph of a randomly selected assembly area. Each red point is a single NP, while yellowish points correspond to dimers.

deemed sufficient to accurately simulate the optical properties of dipolar interactions in the arrays we examined.

Figure 2a shows an illustration of the CAPA method used to organize the cuboctahedra into 270 nm diameter pits. The method has a >99% yield, where yield is defined as the number of filled traps divided by the total number of traps. The deposition area is $>1 \text{ cm}^2$ using optimized conditions, which are set at $15 \text{ }^\circ\text{C}$ above the dew point and $0.8 \text{ }\mu\text{m/s}$ translation speed using a Peltier-based translation stage. Dimethylformamide (DMF) was chosen as the assembly medium because it is a good solvent for the PVP polymer surfactant and enables reversible interactions between nanoparticles even in crowded environments.¹⁷ Some additional insights into single-particle deposition can be found in the Supporting Information. Dark-field (DF) microscopy is used to initially assess the quality of the deposition. Figure 2d shows a DF image of the hexagonal periodic array of NPs. SEM images were collected in different places around the pattern and show that the cuboctahedra are oriented randomly and are typically in an off-center position within the traps (Figure 2b). The trap size in this case was large enough to accommodate up to two NPs. Dimers did assemble in some locations of the patterned template (see Figure S3). Such homogeneous dimer areas were quite rare under the assembly conditions and occurred only around template defects and edges, where the translation speed of the meniscus is lower and causes more particles to accumulate. Throughout the sample, about 10% of all filled traps were

dimers (Figure S4a,d). In order for dimers to contribute to the SLR, they must be aligned, which is difficult to achieve with circular traps because the dimers are highly anisotropic. Moreover, if dimers were contributing to the optical spectra in any way other than serving as a defect, we would see polarization dependence at orthogonal excitation due to different short-axis and long-axis resonances (see Figure S4b,c). We consider only single NPs because this dependence was not observed in any of the experiments.

The samples are large enough so that simple free-space optical methods such as ultraviolet–visible (UV–vis) spectrophotometry can be used to study them. This feature is important because it allows us to avoid the use of focusing optics that might broaden the SLR peaks by introducing spatial incoherence in the source.^{3,48} The patterns were illuminated with a collimated incandescent source with a diameter of 5 mm. This corresponds to 6×10^7 assembled NPs under orthogonal incidence (particle density = $3.2 \text{ p}/\mu\text{m}^2$). The optical investigations were performed in transmission mode, where the source and detector are both stationary and the sample is rotated to change the angle of incidence (see Figure 2c and Experimental Methods for further information on the optical setup).

We converted the obtained transmission data to momentum space to generate dispersion diagrams in panels a and b of Figure 3 for Γ –M and Γ –K k -space directions, respectively, and for TM (left) and TE (right) polarized illumination. We

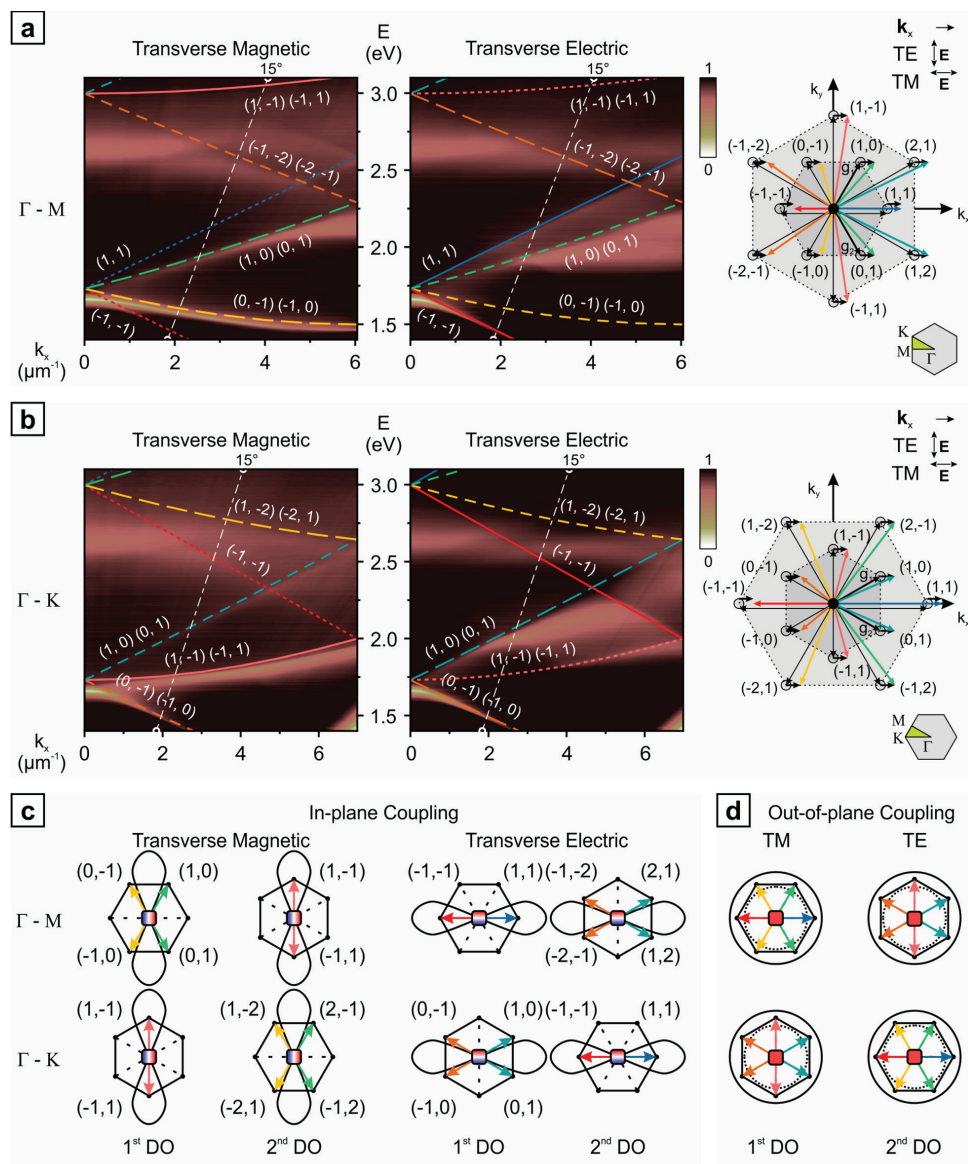


Figure 3. Experimental investigation of angular dependencies. The dispersion diagrams obtained from transmission data for (a) Γ - M_{TM} , Γ - M_{TE} and (b) Γ - K_{TM} , Γ - K_{TE} cases. The white dashed line signifies the cut for modeling analysis. Colored dashed lines overlaid on top of the graphs correspond to diffraction orders (DOs) plotted on reciprocal lattice diagrams. Lines with longer dashes indicate modes with stronger in-plane coupling and are color-coded for degeneracy. (c) Comparison between in-plane coupling strengths corresponding to the alignment of dipolar scattering patterns for all explored cases. (d) Illustration of out-of-plane coupling.

will be referring to these four cases as Γ - M_{TM} , Γ - M_{TE} , Γ - K_{TM} , and Γ - K_{TE} . Even though we have performed measurements for the full 180° angles of incidence, we plot only the first Brillouin zone to avoid redundancy. The rightmost panels in Figure 3a,b show the corresponding

reciprocal lattice diagrams. In these diagrams, we have plotted the lattice vectors \mathbf{g}_1 and \mathbf{g}_2 , which we use to define the other members of the lattice. On the basis of the formalism (see Experimental Methods) recently described by Guo *et al.* in their evaluation of different plasmonic lattices,⁴⁹ we added the

in-plane wave vector component to the resulting lattice vectors to produce the diffraction directions, which are color-coded for degeneracy and plotted on top of the experimental dispersion diagrams.

The quadrupolar LSPR can be observed in all spectra as a broad feature at ~ 2.6 eV (475 nm) that only weakly interacts with the RAs. This may be due to a complicated quadrupolar scattering pattern as well as possible mode hybridization because of asymmetric interaction with PDMS. The dipolar SLR can be observed at 1.65 eV (757 nm) at an orthogonal angle of incidence (i.e., $k_x = 0$). The SLR is typically stronger and narrower when excited on the red side of the LSPR as expected.¹³ The PDMS trap depth was ~ 300 nm based on the height of the Si-master. Thus, the particles are deep below the top surface of the PDMS and touching the PDMS walls. Therefore, the energy of the SLR best matches the Γ point

$$E_{\Gamma} = \frac{hc}{n} \cdot \frac{2\pi}{\Lambda \cdot \sin\left(\frac{2\pi}{3}\right)}$$
 for our lattice geometry when we use the

refractive index of PDMS ($n = 1.38$). Furthermore, there were no observable air-propagating SLR peaks ($E_{\Gamma}^{\text{air}} = 2.39$ eV). We concluded that the NP arrays behave like they are in a homogeneous environment for in-plane dipolar interactions—even though they are obviously not because SEM measurements show they are physically exposed inside the holes. The insight gained here suggests that SLR-capable arrays in recessed holes may be a fruitful research direction for sensing applications because the analyte will still be able to access the region near the particles, which supports the strongest EM fields in the array.

At this point it is important to note that in the four different cases we present, the coupling strength as determined by the alignment of NP scattering pattern to the diffraction mode propagation direction is not the same (Figure 3c). For in-plane coupling, when the scattering pattern of the NPs lies on a plane that is perpendicular to the surface, we show four coupling strengths indicated by the dash length of RAs on the dispersion diagrams. The solid line represents the strongest coupling. In the case of out-of-plane polarization, all nanoparticle dipoles are aligned perpendicular to the surface (Figure 3d); thus, the scattered light is primarily located in the plane of the array. This feature of the out-of-plane dipolar coupling leads to stronger overall coupling compared to in-plane coupling.

The highest Q -factor peaks (up to ~ 80) follow either the $(-1, -1)$ mode in the Γ - M_{TE} or $(0, -1)$ and $(-1, 0)$ for both Γ - K_{TM} and Γ - K_{TE} . These peaks are absent in the case of Γ - M_{TM} because the scattered light is orthogonal to the mode direction and therefore there is no coupling. Regardless, some modicum of coupling can still be observed at very small angles of incidence, which could be evidence of out-of-plane coupling. Instead, the excitation of Γ - M_{TM} generates very strong and high-quality coupling at the $(0, -1)$ and $(-1, 0)$ modes. This mode is narrow throughout the first Brillouin zone, maintaining high Q -factor even up to very large excitation angles. This allowed us to tune the SLR response in the near-infrared spectrum between 1.5 and 1.65 eV.

We can observe four different cases of coupling to RAs that increase in energy with the in-plane wave vector. In Γ - M_{TM} , the SLR follows the $(1, 0)$ and $(0, 1)$ RAs. Significant broadening occurs as the peak approaches the edge of the Brillouin zone. This may be attributed to the RA shifting toward the LSPR of NPs as opposed to away from it, which is known to increase the width of the peak.⁵ A similar situation is

encountered in Γ - M_{TE} , except the broadening is much stronger, possibly because of even weaker coupling to these modes. For the Γ - K_{TM} case, the SLR follows the $(1, -1)$ and $(-1, 1)$ modes with an average Q -factor of ~ 40 . In the Γ - K_{TE} case we see broad coupling to the $(1, 0)$ and $(0, 1)$ modes with a Q -factor of ~ 20 .

To expand upon our experimental observations and improve the understanding of the underlying phenomena, we performed numerical calculations with CDA and FEM. Figure 4a (top) shows the CDA-calculated extinction cross sections of a single dipole and a dipole in an array excited by an orthogonally incident ($k_x = 0$) plane wave. The CDA calculations assume an infinite array of particles with individual polarizabilities (α) that express the properties of the nanoparticle and the dipole sum (S) representing the collective contributions of the lattice. These values can be further split into real and imaginary contributions which to some extent represent magnitude and width of the resulting SLR peaks, respectively. The total polarization of a particle in an array (α_{ar} , see Experimental Methods for a full explanation) is then expressed as

$$\alpha_{\text{ar}} = \frac{1}{\frac{1}{\alpha_{\text{MLWA}}} - S} \quad (1)$$

Figure 4a (bottom) plots the members of the denominator in the equation above, showing the real and imaginary components of $1/\alpha$ and S . SLRs are possible when the real contributions of $1/\alpha$ and S intersect because it indicates a local maximum of α_{ar} . However, the imaginary component of the polarizability must be small to limit damping. As a result, we observed an SLR at ~ 740 nm because the α_{ar} is large and the imaginary parts of $1/\alpha$ and S are negative and similar in magnitude. The CDA result matches our hexagonal resonance at 764 nm relatively well considering it is an analytical solution.

For a glimpse at a microscopic picture of the lattice and EM fields associated with these experimental peaks, we employed COMSOL software to model the periodic unit cell with FEM. Because we deduced the optical homogeneity of our structure and validated the shape model through the extinction spectrum, we modeled the sample as a hexagonal array of cuboctahedra in a homogeneous environment with the refractive index of PDMS. Figure 4b shows the transmission spectrum of the array at orthogonal incidence ($k_x = 0$). The modeled spectrum closely matches the experimental data. In the simulation, the RAs are clearly visible and are at higher energies than the SLR peaks. The calculated Q -factor is higher in the model, which may be due to deviations in the periodicity of the self-assembled array or some rotational disorder of the particles. The EM field distribution maps were plotted for this sample at 764 nm in the plane of the array (x - y) and in the plane of incidence (x - z) in Figure 4b(1). It matches the standing wave pattern of a dipolar SLR mode. The electric field is strongest around the nanoparticles compared to the interstitial space. Animations of the EM behavior are available in the Supporting Information.

To explore all the major SLR peaks, we modeled a spectrum for each of the cases at 15° angle of incidence as indicated by the dashed white lines in Figure 3a,b. The transmission spectra are displayed in Figure 5a,b. Most of the simulated peaks can be mapped to the experimental ones (dashed lines). The subtle divergence of spectral positions could be attributed to inaccuracies of the experimental optical setup. When the two

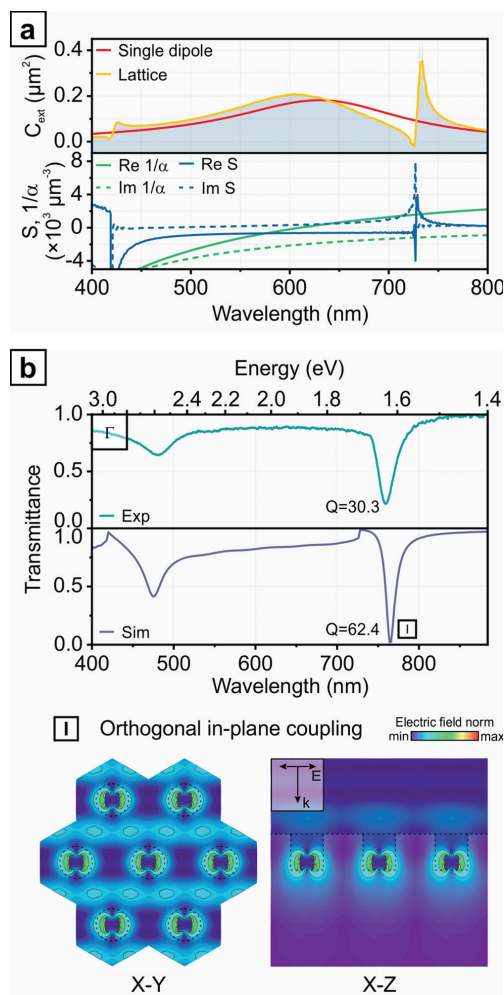


Figure 4. Analytical and numerical computations of orthogonal excitation. (a) Spectra of CDA-calculated extinction generated by an isolated and in-array dipole; real and imaginary parts of the dipole sum and inverse polarizability. (b) FEM modeled (below) and experimental (above) transmission spectra at orthogonal incidence and FEM modeled electric field distributions for the peak indicated by panel I: orthogonal in-plane coupling at 764 nm (animations are available in Animations SA1 and SA2). Dashed contours depict the PDMS template.

simulated polarization cases are compared, it is easy to recognize the same RAs have associated SLRs with different strengths. This is due to the coupling strengths discussed earlier and displayed in Figure 3c.

The strongest experimental peak at this specific 15° excitation angle occurs at 818 nm in the Γ - M_{TM} case and has a Q -factor ~ 60 . The EM field distribution cuts corresponding to this case are displayed in Figure 5a(II). In contrast to the example discussed above, here the electric field

is much more delocalized between the NPs but still significantly weaker than around them. Note how the dipolar EM field around the nanoparticle matches the polarization direction of the incident light in the x - z cut, which will not be the case for the narrowest peaks.

The narrowest simulated peaks are associated with the most red-shifted RAs in all four excitation/polarization conditions. Although corresponding experimental peaks are not as sharp, they do generate relatively large Q -factors of ~ 80 . Upon thorough investigation of each peak, two cases of OP coupling were found in the simulations, both excited using TM polarized illumination. One of them is in the simulation of Γ - M_{TM} at ~ 920 nm. Here, coupling happens to a mode that would be orthogonal to the in-plane polarized particles (*i.e.*, no coupling), which is a signature of OP coupling. The second case was found in Γ - K_{TM} . In this case, two very sharp peaks are associated with the $(0, -1)$ and $(-1, 0)$ modes. The higher-energy peak is an in-plane resonance (see Figure S5). Unlike the previous case, this mode is not orthogonal to the in-plane polarized particles; therefore, in-plane coupling is possible. The lower-energy peak is an out-of-plane (OP) resonance. Figure 5b(III) shows the EM field plot of this OP resonance (see also Animations SAS and SA6). It generates an enormous local electric intensity that is strongest between the particles and extends both vertically and horizontally. The OP condition has smaller nonradiative losses because less optical energy is being stored in the metal. It is interesting that the EM fields attributed to these narrowest peaks are oriented either parallel (in the case of in-plane) or perpendicular (in the case of OP) to the plane of array, instead of being aligned with the polarization of excitation like in Figure 5a(II) (see orthogonally excited in-plane resonance in Figure 4b(I) and off-normal excited in-plane resonance in Figure S5). This must be a signature of the strongest coupling, which is also why the peaks are narrowest, as predicted by ref 5 where red-shifting away from single-NP LSPR generally creates narrower peaks. The OP peak in Γ - M_{TM} is clearly visible in the simulation but is absent in the experiments; thus, we concluded it is just the in-plane peak we observe in the experiment of Γ - K_{TM} . The inability to excite out-of-plane resonances is likely due to the asymmetry of the refractive index in the normal direction of our samples. Addition of an index-matching layer could enable these out-of-plane peaks; however, it would deny analyte accessibility to the strongest EM fields, although for nanolasing applications it could turn out to be beneficial.

To examine the stability of the NP arrays and the effect of environment on the SLR resonance, the UV-vis spectrum of a typical sample was measured, and then the sample was left at room temperature in air for 5 months and measured again (Figure S6a). The wavelength of the SLR is unaffected over time, indicating it is not sensitive to local changes in the nanoparticle structure. The peak associated with the quadrupolar LSPR at 475 nm did red-shift over time ($\Delta\lambda \approx 7$ nm), indicating it could be affected by oxidation, sulfidation, or rounding. We imaged the edge of the PDMS pattern left out over several months and observed clumps of particles that provided enough contrast to observe the surface of the Ag (Figure S6b). The particles appear to be oxidized in places, which has been shown to round the edges/corners of the particles.⁵⁰ Although rounding is expected to blue-shift the quadrupolar LSPR mode at 475 nm (Figure S7), the subtle red-shift is attributed to the increase in the local refractive index of AgO_x versus PDMS or air.⁵¹ These results indicate that

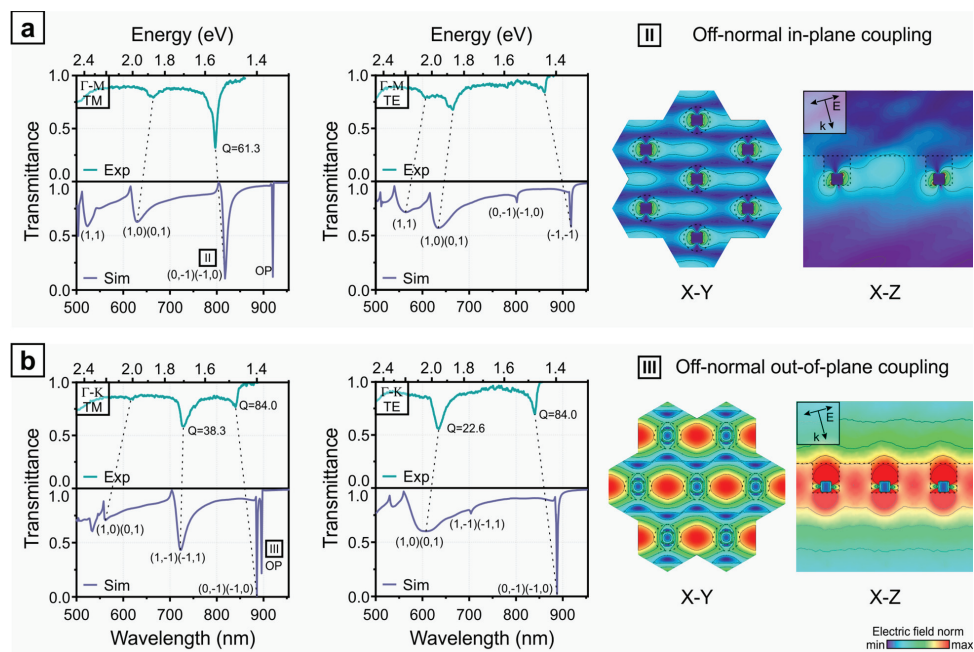


Figure 5. Numerical computations of off-normal excitation. FEM modeled and experimental transmission spectra at 15° angle of incidence for (a) $\Gamma\text{-}M_{TM}$, $\Gamma\text{-}M_{TE}$ and (b) $\Gamma\text{-}K_{TM}$, $\Gamma\text{-}K_{TE}$ cases and FEM modeled electric field distributions for the selected cases: (II) off-normal in-plane coupling at 818 nm (Animations SA3 and SA4) and (III) off-normal out-of-plane coupling at 896 nm (Animations SA5 and SA6). Dashed contours depict the PDMS template.

Ag is a reasonable choice in applications exploiting SLRs at visible wavelengths.

CONCLUSIONS

In summary, we successfully used colloidal self-assembly to generate high Q -factor SLR-capable arrays. The CAPA technique can precisely position cuboctahedral Ag NPs with high yield (>99%) and over a large area (>1 cm²). Because of the geometry of NPs and the template, the resulting lattice unit cell turned out to be asymmetric, with the NP situated off-center and touching the wall of the trap, which together with the depth of the void made the environment optically homogeneous in the plane of the array. The large area of the assembly allowed us to use conventional UV-vis spectroscopy and perform angle and polarization dependent measurements without the need for focusing optics. Sharp dips in transmission were observed, and dependencies on the mentioned parameters were characterized. The SLR nature of the observed phenomenon was confirmed by coupled dipole approximation computations. Furthermore, finite element method analysis of the unit cell showed well-fit results. Overall, the observation of SLRs in a self-assembled system is proof that we have achieved long-range positional control of single nanoparticles. It also suggests that SLRs are somewhat tolerant to defects such as dimers and local changes in the structure of the particle caused by oxidation/sulfidation. Even more complex 3D structures are possible with self-assembly

methods like CAPA, because they are not limited to a specific particle size, shape, or material composition.

EXPERIMENTAL METHODS

NP Synthesis. The Ag polyol synthesis method was used to generate the monodisperse Ag cuboctahedra.⁴⁶ The average edge length (a) of the ensemble of cuboctahedra was measured using a JEOL-1010 TEM operating at 100 kV with a minimum magnification of <0.5 nm/pixel. $n = 210$ particles were counted, and the average edge length (a) of the cuboctahedra was 122 ± 3 nm. The edge length of the cuboctahedra is summarized in the histogram in Figure S8. Fewer than 2% of the particles were twinned triangular bipyramids. The particles were suspended in DMF at a concentration of 8.55×10^7 particles/mL as determined by inductively coupled plasma mass spectrometry. In self-assembly experiments, polyvinylpyrrolidone (PVP; S5 000 MW) polymer surfactant serves as a steric barrier to minimize uncontrolled NP aggregation even at very high concentrations.^{43,47}

Capillary-Force-Assisted NP Assembly. PDMS templates patterned with small pits were used to facilitate the assembly of Ag NPs. These PDMS templates were produced using soft-lithography on an electron-beam generated 20×20 mm² Si master pattern (EBPG S000Plus, Vistec) composed of a hexagonal array of 270 nm diameter Si pillars, which are 300 nm tall and spaced 600 nm center-to-center.⁴² The master pattern was treated once with trichloro-(1H,1H,2H,2H-perfluorooctyl)-silane in a desiccator to prevent bonding with the PDMS in subsequent replication cycles. A small droplet containing a 10:1 mixture of polymer base and curing agent (Sylgard 184, Dow-Corning) was put on the stamp and constrained by a thin glass slide; the sample was then cured at 100 °C for 35 min. Once the PDMS had fully polymerized, the glass/PDMS pattern

could be detached from the master. A custom-built assembly setup was used to generate NP assemblies. Its main components are an optical microscope system (BX51, Olympus), motorized linear precision translator (LS-110, PI Micos), and a temperature control system (TEC-1090, Meerstetter Engineering GmbH).⁴² The PDMS pattern was placed on top of the stage, and a 50 mL droplet of the Ag NP colloid solution was put on top and confined by a stationary glass slide fixed at a slight inclination which is used by most doctor-blade patterning methods. DMF was used as the assembly solution because it is a theta solvent for PVP.⁴³ The template was then translated 1 $\mu\text{m/s}$ while keeping the glass slide fixed. The droplet moved along the surface, with a meniscus orthogonal to the moving direction (Figure 2a). A combination of viscous drag and evaporation-induced flux causes particles to accumulate at the edge of the meniscus. Initially, the temperature of the stage was fixed at 10 °C above the dew point and then was gradually increased until the number of particles accumulated at the meniscus was high enough and assembly in the pits could be observed in dark-field. At this point, the translation speed was reduced by 100–200 nm/s to sustain the high-yield deposition.

Characterization Methods. Optical imaging of both the deposition process and the final assemblies was performed using the microscope system described above equipped with a 100 \times dark-field objective (MPlanFLN 100 \times 0.90BD FN26.5, Olympus) and a CCD camera (Micropublisher 3.3, QImaging). Scanning electron microscopy (Quanta 200 FEG, FEI) imaging of NPs was performed at low vacuum in a water vapor atmosphere to reduce charging effects. Spectroscopy was performed using a custom-built motorized goniometric setup (Figure 2c) consisting of an incandescent light bulb source, a collimator, and a Glan-Taylor polarizer. The source and detector positions were held constant, and the sample was rotated around a vertical axis in order to change the angle of incidence. The transmitted light was collected via a 6 mm diameter lens coupled to an optical fiber and an optical spectrometer (AvaSpec-2048, Avantes; 1.2 nm resolution).⁷ The acquired spectra were normalized to transmission through an unused template at the same geometry conditions and then converted into E-k diagrams.⁴⁹ The calculations of the theoretical diffraction edges were done through the following formula:⁴⁹

$$E = \frac{\hbar c}{n} |\vec{k}_{\parallel}| + \vec{G} \quad (2)$$

FEM Simulations. FEM modeling was performed using the COMSOL Multiphysics suite in the wave optics module. A three-way periodic boundary condition was set up to simulate the hexagonal pattern. The unit cell was modeled as close to the real geometry as possible based on TEM measurements of NPs and SEM measurements of the assemblies: the NP size (122 nm) and its shape (cuboctahedron with a 0.33 truncation parameter). The lattice periodicity of 600 nm was used as measured with the SEM. The optical constants of Ag were taken from the literature,⁵² and a default piecewise cubic interpolation was used to get values between the data points.

Coupled Dipole Approximation. In this approximation, every particle is considered a dipole with a polarizability α . When particles have a spheroidal shape, the static polarizability can be expressed as in eq 3:⁵³

$$\alpha_{st} = \frac{abc}{3} \frac{(\epsilon_m - \epsilon_s)}{\epsilon_s + L(\epsilon_m - \epsilon_s)} \quad (3)$$

where a , b , and c are the semiaxes of the spheroid; ϵ_m and ϵ_s are relative permittivities of the NP and the surrounding medium (we used a nondispersive refractive index of PDMS 1.4), respectively; L is the shape factor as defined in ref 53 (for a sphere, the shape factor is 1/3). Retardation effects within the volume of the particle must be considered because they are large. Therefore, to account for radiative damping and dynamic depolarization, the static polarizability is changed by the modified long-wavelength approximation (MLWA),⁵⁴ as defined in eq 4:

$$\alpha_{MLWA} = \frac{\alpha_{st}}{1 - \frac{2}{3} ik^3 \alpha_{st} - \frac{k^2}{a} \alpha_{st}} \quad (4)$$

where k is the wavenumber of the incident light in the medium and a is a size dimension along the polarization direction. When the NPs are in an array, they scatter light in accordance with their dipole moment. The electric field affecting a particle is a sum of the incident field and scattered fields by every other NP in the array. We used a 5000 \times 5000 hexagonal array of particles and excited it with orthogonal incidence. The polarizability of a NP in an array can be expressed as in eq 1 described earlier, where the dipole sum (S) is the contribution of the surrounding NPs and is mostly dependent on the geometry as defined by eq 5:⁵

$$S = \sum_{j \neq i} \left[\frac{(1 - ikr_{ij})(3 \cos^2 \theta_{ij} - 1)e^{ikr_{ij}}}{r_{ij}^3} + \frac{k^2 \sin^2 \theta_{ij} e^{ikr_{ij}}}{r_{ij}} \right] \quad (5)$$

where r_{ij} is the distance to a dipole and θ is the angle between the induced dipole (or polarization of incident field) and the position vector. Finally, a formulation (eq 6) introduced in ref 53 is used to calculate the extinction cross section, which is a sum of absorption (first term) and scattering (second term) cross sections:

$$C_{ext} = 4\pi k \text{Im}(\alpha) + \frac{8}{3} \pi k^4 |\alpha|^2 \quad (6)$$

ASSOCIATED CONTENT

Supporting Information

The Supporting Information is available free of charge on the ACS Publications website at DOI: 10.1021/acsnano.9b03191.

Insights into single-particle assembly; SEM micrograph of cuboctahedra (Figure S1); plasmonic mode analysis (Figure S2); SEM micrograph of dimer assembly (Figure S3); evaluation of dimers in the assembly (Figure S4); EM field distribution of the narrowest in-plane peak in Γ - K_{TM} (Figure S5); discussion about oxidation of nanoparticles (Figure S6); FEM model of NP edge rounding (Figure S7); histogram of nanoparticle size distribution (Figure S8) (PDF)

Animation SA1 (AVI)

Animation SA2 (AVI)

Animation SA3 (AVI)

Animation SA4 (AVI)

Animation SA5 (AVI)

Animation SA6 (AVI)

Animation SA7 (AVI)

Animation SA8 (AVI)

AUTHOR INFORMATION

Corresponding Authors

*E-mail: mindaugas.juodenas@ktu.lt.

*E-mail: joelhenzie@protonmail.com.

ORCID

Mindaugas Juodenas: 0000-0002-0517-8620

Tomas Tamulevičius: 0000-0003-3879-2253

Joel Henzie: 0000-0002-9190-2645

Notes

The authors declare no competing financial interest.

ACKNOWLEDGMENTS

M.J., T.T., D.E., and S.T. acknowledge the joint Lithuanian–Latvian–Chinese (Taiwanese) Tripartite Cooperation Program project cofinanced by the Research Council of Lithuania

(Grant No. S-LLT-18-2) and the Ministry of Science and Technology of Taiwan (Contract SV3-0618). J.H. acknowledges support from the World Premier International Research Center Initiative on “Materials Nanoarchitectonics (WPI-MANA)” from MEXT, the Grant-in-Aid for User Facilities at NIMS, and the Japan Society for the Promotion of Science (JSPS) for financing the “Plasmonic properties of silver NPs and self-assembled clusters (PLAS)” research project between Japan and Lithuania.

REFERENCES

- (1) Anker, J. N.; Hall, W. P.; Lyandres, O.; Shah, N. C.; Zhao, J.; Van Duyne, R. P. Biosensing with Plasmonic Nanosensors. *Nat. Mater.* **2008**, *7*, 442–453.
- (2) Mayer, K. M.; Hafner, J. H. Localized Surface Plasmon Resonance Sensors. *Chem. Rev.* **2011**, *111*, 3828–3857.
- (3) Kravets, V. G.; Kabashin, A. V.; Barnes, W. L.; Grigorenko, A. N. Plasmonic Surface Lattice Resonances: A Review of Properties and Applications. *Chem. Rev.* **2018**, *118*, 5912–5951.
- (4) Markel, V. A. Coupled-Dipole Approach to Scattering of Light from a One-Dimensional Periodic Dipole Structure. *J. Mod. Opt.* **1993**, *40*, 2281–2291.
- (5) Zou, S.; Janel, N.; Schatz, G. C. Silver Nanoparticle Array Structures That Produce Remarkably Narrow Plasmon Lineshapes. *J. Chem. Phys.* **2004**, *120*, 10871–10875.
- (6) Tamulevičius, T.; Šeperys, R.; Andrulevičius, M.; Kopustinskas, V.; Meškiniš, Š.; Tamulevičius, S. Refractive Index Sensor Based on the Diamond Like Carbon Diffraction Grating. *Thin Solid Films* **2011**, *519*, 4082–4086.
- (7) Tamulevičius, T.; Gražulevičiūtė, I.; Urbonas, D.; Gabalis, M.; Petruškevičius, R.; Tamulevičius, S. Numerical and Experimental Analysis of Optical Response of Sub-Wavelength Period Structure in Carbonaceous Film for Refractive Index Sensing. *Opt. Express* **2014**, *22*, 27462.
- (8) McMahon, J. M.; Henzie, J.; Odom, T. W.; Schatz, G. C.; Gray, S. K. Tailoring the Sensing Capabilities of Nanohole Arrays in Gold Films with Rayleigh Anomaly-Surface Plasmon Polaritons. *Opt. Express* **2007**, *15*, 18119.
- (9) Henzie, J.; Lee, M. H.; Odom, T. W. Multiscale Patterning of Plasmonic Metamaterials. *Nat. Nanotechnol.* **2007**, *2*, 549–554.
- (10) Wang, W.; Ramezani, M.; Väkeväinen, A. I.; Törmä, P.; Rivas, J. G.; Odom, T. W. The Rich Photonic World of Plasmonic Nanoparticle Arrays. *Mater. Today* **2018**, *21*, 303–314.
- (11) Hicks, E. M.; Zou, S.; Schatz, G. C.; Spears, K. G.; Van Duyne, R. P.; Gunnarsson, L.; Rindzevicius, T.; Kasemo, B.; Käll, M. Controlling Plasmon Line Shapes through Diffractive Coupling in Linear Arrays of Cylindrical Nanoparticles Fabricated by Electron Beam Lithography. *Nano Lett.* **2005**, *5*, 1065–1070.
- (12) Kravets, V. G.; Schedin, F.; Pisano, G.; Thackray, B.; Thomas, P. A.; Grigorenko, A. N. Nanoparticle Arrays: From Magnetic Response to Coupled Plasmon Resonances. *Phys. Rev. B: Condens. Matter Mater. Phys.* **2014**, *90*, 125445.
- (13) Auguie, B.; Barnes, W. L. Collective Resonances in Gold Nanoparticle Arrays. *Phys. Rev. Lett.* **2008**, *101*, 143902.
- (14) Chu, Y.; Schonbrun, E.; Yang, T.; Crozier, K. B. Experimental Observation of Narrow Surface Plasmon Resonances in Gold Nanoparticle Arrays. *Appl. Phys. Lett.* **2008**, *93*, 181108.
- (15) Markel, V. A. Divergence of Dipole Sums and the Nature of Non-Lorentzian Exponentially Narrow Resonances in One-Dimensional Periodic Arrays of Nanospheres. *J. Phys. B: At., Mol. Opt. Phys.* **2005**, *38*, L115–L121.
- (16) Rodriguez, S. R. K.; Schaafsma, M. C. C.; Berrier, A.; Gómez Rivas, J. Collective Resonances in Plasmonic Crystals: Size Matters. *Phys. B* **2012**, *407*, 4081–4085.
- (17) Humphrey, A. D.; Barnes, W. L. Plasmonic Surface Lattice Resonances on Arrays of Different Lattice Symmetry. *Phys. Rev. B: Condens. Matter Mater. Phys.* **2014**, *90*, 075404.
- (18) Kravets, V. G.; Schedin, F.; Grigorenko, A. N. Extremely Narrow Plasmon Resonances Based on Diffraction Coupling of Localized Plasmons in Arrays of Metallic Nanoparticles. *Phys. Rev. Lett.* **2008**, *101*, 087403.
- (19) Chen, W.; Tymchenko, M.; Gopalan, P.; Ye, X.; Wu, Y.; Zhang, M.; Murray, C. B.; Alu, A.; Kagan, C. R. Large-Area Nanoimprinted Colloidal Au Nanocrystal-Based Nanoantennas for Ultrathin Polarizing Plasmonic Metasurfaces. *Nano Lett.* **2015**, *15*, S254–S260.
- (20) Ma, Z.; Ni, X.; Zhang, W.; Jiang, X.; Yang, H.; Yu, J.; Wang, W.; Xu, L.; Xu, J.; Chen, K.; Feng, D. Hexagonal Ag Nanoarrays Induced Enhancement of Blue Light Emission from Amorphous Oxidized Silicon Nitride via Localized Surface Plasmon Coupling. *Opt. Express* **2014**, *22*, 28180.
- (21) Vecchi, G.; Giannini, V.; Gómez Rivas, J. Shaping the Fluorescent Emission by Lattice Resonances in Plasmonic Crystals of Nanoantennas. *Phys. Rev. Lett.* **2009**, *102*, 146807.
- (22) Adato, R.; Yanik, A. A.; Amsden, J. J.; Kaplan, D. L.; Omenetto, F. G.; Hong, M. K.; Erramilli, S.; Altug, H. Ultra-Sensitive Vibrational Spectroscopy of Protein Monolayers with Plasmonic Nanoantenna Arrays. *Proc. Natl. Acad. Sci. U. S. A.* **2009**, *106*, 19227–19232.
- (23) Yanik, A. A.; Cetin, A. E.; Huang, M.; Artar, A.; Mousavi, S. H.; Khanikaev, A.; Connor, J. H.; Shvets, G.; Altug, H. Seeing Protein Monolayers with Naked Eye through Plasmonic Fano Resonances. *Proc. Natl. Acad. Sci. U. S. A.* **2011**, *108*, 11784–11789.
- (24) Hakala, T. K.; Rekola, H. T.; Väkeväinen, A. I.; Martikainen, J.-P. P.; Nečada, M.; Moilanen, A. J.; Törmä, P. Lasing in Dark and Bright Modes of a Finite-Sized Plasmonic Lattice. *Nat. Commun.* **2017**, *8*, 13687.
- (25) Zhou, W.; Dridi, M.; Suh, J. Y.; Kim, C. H.; Co, D. T.; Wasielewski, M. R.; Schatz, G. C.; Odom, T. W. Lasing Action in Strongly Coupled Plasmonic Nanocavity Arrays. *Nat. Nanotechnol.* **2013**, *8*, 506–511.
- (26) Ramezani, M.; Halpin, A.; Fernández-Domínguez, A. I.; Feist, J.; Rodríguez, S. R.-K.; Garcia-Vidal, F. J.; Gómez Rivas, J. Plasmon-Exciton-Polariton Lasing. *Optica* **2017**, *4*, 31.
- (27) Schokker, A. H.; Koenderink, A. F. Lasing at the Band Edges of Plasmonic Lattices. *Phys. Rev. B: Condens. Matter Mater. Phys.* **2014**, *90*, 155452.
- (28) Lee, B.; Park, J.; Han, G. H.; Ee, H.-S.; Naylor, C. H.; Liu, W.; Johnson, A. T. C.; Agarwal, R. Fano Resonance and Spectrally Modified Photoluminescence Enhancement in Monolayer MoS₂ Integrated with Plasmonic Nanoantenna Array. *Nano Lett.* **2015**, *15*, 3646–3653.
- (29) Kwak, E.-S.; Henzie, J.; Chang, S.; Gray, S. K.; Schatz, G. C.; Odom, T. W. Surface Plasmon Standing Waves in Large-Area Subwavelength Hole Arrays. *Nano Lett.* **2005**, *5*, 1963–1967.
- (30) Chen, K.-P.; Drachev, V. P.; Borneman, J. D.; Kildishev, A. V.; Shalae, V. M. Drude Relaxation Rate in Grained Gold Nanoantennas. *Nano Lett.* **2010**, *10*, 916–922.
- (31) Lin, Q.-Y.; Li, Z.; Brown, K. A.; O'Brien, M. N.; Ross, M. B.; Zhou, Y.; Butun, S.; Chen, P.-C.; Schatz, G. C.; Dravid, V. P.; Aydin, K.; Mirkin, C. A. Strong Coupling between Plasmonic Gap Modes and Photonic Lattice Modes in DNA-Assembled Gold Nanocube Arrays. *Nano Lett.* **2015**, *15*, 4699–4703.
- (32) Lin, Q.-Y.; Mason, J. A.; Li, Z.; Zhou, W.; O'Brien, M. N.; Brown, K. A.; Jones, M. R.; Butun, S.; Lee, B.; Dravid, V. P.; Aydin, K.; Mirkin, C. A. Building Superlattices from Individual Nanoparticles via Template-Confined DNA-Mediated Assembly. *Science* **2018**, *359*, 669–672.
- (33) Alexander, K. D.; Skinner, K.; Zhang, S.; Wei, H.; Lopez, R. Tunable SERS in Gold Nanorod Dimers through Strain Control on an Elastomeric Substrate. *Nano Lett.* **2010**, *10*, 4488–4493.
- (34) Yang, A.; Hryn, A. J.; Bourgeois, M. R.; Lee, W.-K.; Hu, J.; Schatz, G. C.; Odom, T. W. Programmable and Reversible Plasmon Mode Engineering. *Proc. Natl. Acad. Sci. U. S. A.* **2016**, *113*, 14201–14206.
- (35) Malynych, S.; Chumanov, G. Light-Induced Coherent Interactions between Silver Nanoparticles in Two-Dimensional Arrays. *J. Am. Chem. Soc.* **2003**, *125*, 2896–2898.

- (36) Wang, D.; Bourgeois, M. R.; Lee, W.-K.; Li, R.; Trivedi, D.; Knudson, M. P.; Wang, W.; Schatz, G. C.; Odom, T. W. Stretchable Nanolasing from Hybrid Quadrupole Plasmons. *Nano Lett.* **2018**, *18*, 4549–4555.
- (37) Flauraud, V.; Mastrangeli, M.; Bernasconi, G. D.; Butet, J.; Alexander, D. T. L.; Shahabi, E.; Martin, O. J. F.; Brugger, J. Nanoscale Topographical Control of Capillary Assembly of Nanoparticles. *Nat. Nanotechnol.* **2017**, *12*, 73–80.
- (38) Ni, S.; Isa, L.; Wolf, H. Capillary Assembly as a Tool for the Heterogeneous Integration of Micro- and Nanoscale Objects. *Soft Matter* **2018**, *14*, 2978–2995.
- (39) Hanske, C.; Tebbe, M.; Kuttner, C.; Bieber, V.; Tsukruk, V. V.; Chanana, M.; König, T. A. F.; Fery, A. Strongly Coupled Plasmonic Modes on Macroscopic Areas via Template-Assisted Colloidal Self-Assembly. *Nano Lett.* **2014**, *14*, 6863–6871.
- (40) Mayer, M.; Tebbe, M.; Kuttner, C.; Schnepf, M. J.; König, T. A. F.; Fery, A. Template-Assisted Colloidal Self-Assembly of Macroscopic Magnetic Metasurfaces. *Faraday Discuss.* **2016**, *191*, 159–176.
- (41) Malaquin, L.; Kraus, T.; Schmid, H.; Delamarche, E.; Wolf, H. Controlled Particle Placement through Convective and Capillary Assembly. *Langmuir* **2007**, *23*, 11513–11521.
- (42) Virganavičius, D.; Juodėnas, M.; Tamulevičius, T.; Schiff, H.; Tamulevičius, S. Investigation of Transient Dynamics of Capillary Assisted Particle Assembly Yield. *Appl. Surf. Sci.* **2017**, *406*, 136–143.
- (43) Henzie, J.; Andrews, S. C.; Ling, X. Y.; Li, Z.; Yang, P. Oriented Assembly of Polyhedral Plasmonic Nanoparticle Clusters. *Proc. Natl. Acad. Sci. U. S. A.* **2013**, *110*, 6640–6645.
- (44) Kuemin, C.; Nowack, L.; Bozano, L.; Spencer, N. D.; Wolf, H. Oriented Assembly of Gold Nanorods on the Single-Particle Level. *Adv. Funct. Mater.* **2012**, *22*, 702–708.
- (45) Greybush, N. J.; Saboktakin, M.; Ye, X.; Della Giovampaola, C.; Oh, S. J.; Berry, N. E.; Engheta, N.; Murray, C. B.; Kagan, C. R. Plasmon-Enhanced Upconversion Luminescence in Single Nanophosphor–Nanorod Heterodimers Formed through Template-Assisted Self-Assembly. *ACS Nano* **2014**, *8*, 9482–9491.
- (46) Tao, A.; Sinsersuksakul, P.; Yang, P. Polyhedral Silver Nanocrystals with Distinct Scattering Signatures. *Angew. Chem., Int. Ed.* **2006**, *45*, 4597–4601.
- (47) Henzie, J.; Grünwald, M.; Widmer-Cooper, A.; Geissler, P. L.; Yang, P. Self-Assembly of Uniform Polyhedral Silver Nanocrystals into Densest Packings and Exotic Superlattices. *Nat. Mater.* **2012**, *11*, 131–137.
- (48) Haynes, C. L.; McFarland, A. D.; Zhao, L.; Van Duyne, R. P.; Schatz, G. C.; Gunnarsson, L.; Prikulis, J.; Kasemo, B.; Käll, M. Nanoparticle Optics: The Importance of Radiative Dipole Coupling in Two-Dimensional Nanoparticle Arrays. *J. Phys. Chem. B* **2003**, *107*, 7337–7342.
- (49) Guo, R.; Hakala, T. K.; Törmä, P. Geometry Dependence of Surface Lattice Resonances in Plasmonic Nanoparticle Arrays. *Phys. Rev. B: Condens. Matter Mater. Phys.* **2017**, *95*, 155423.
- (50) Grillet, N.; Manchon, D.; Cottancin, E.; Bertorelle, F.; Bonnet, C.; Broyer, M.; Lermé, J.; Pellarin, M. Photo-Oxidation of Individual Silver Nanoparticles: A Real-Time Tracking of Optical and Morphological Changes. *J. Phys. Chem. C* **2013**, *117*, 2274–2282.
- (51) Qiu, J.-H.; Zhou, P.; Gao, X.-Y.; Yu, J.-N.; Wang, S.-Y.; Li, J.; Zheng, Y.-X.; Yang, Y.-M.; Song, Q.-H.; Chen, L.-Y. Ellipsometric Study of the Optical Properties of Silver Oxide Prepared by Reactive Magnetron Sputtering. *J. Korean Phys. Soc.* **2005**, *46*, S269–S275.
- (52) Johnson, P. B.; Christy, R. W. Optical Constants of the Noble Metals. *Phys. Rev. B* **1972**, *6*, 4370–4379.
- (53) Bohren, C. F.; Huffman, D. R. Particles Small Compared with the Wavelength. In *Absorption and Scattering of Light by Small Particles*; Wiley-VCH Verlag GmbH: Weinheim, Germany, 1998; pp 130–157.
- (54) Moroz, A. Depolarization Field of Spheroidal Particles. *J. Opt. Soc. Am. B* **2009**, *26*, 517.

D. Peckus, H. Rong, L. Stankevičius, M. Juodėnas, S. Tamulevičius,
T. Tamulevičius, J. Henzie

Hot Electron Emission Can Lead to Damping of Optomechanical Modes in Core-Shell Ag@TiO₂ Nanocubes

In this research paper, we describe the first synthesis of core-shell Ag@TiO₂ nanocubes, deliberately maintaining the size and anisotropic shape of the Ag core. The LSPR is known to enhance the photocatalytic activity in composite noble metal/TiO₂ nanostructures beyond pure TiO₂.^{146–148} Cubic nanoparticles support stronger LSPR modes and generate more hot carriers than spherical particles; thus, we hypothesized that a TiO₂ shell would further enhance hot carrier generation in Ag and also help stabilize the Ag metal against chemical corrosion.^{108,149,150} Because the particles are highly monodisperse, free-standing in solution, and separated from each other by several microns, the optical properties of the solution are representative of single, isolated Ag nanocubes surrounded by an isotropic dielectric environment. TAS was used to compare the ultrafast decay of the Ag and Ag@TiO₂ nanocubes, and tracked longer decay pathways, as this energy is converted into acoustic phonons (i.e., optomechanical modes) and eventually into sound waves. Interestingly, the TiO₂ shell caused no significant shift in the frequency of the optomechanical mode of the Ag nanocubes. Previously, Crut et al. explored spherical core-shell nanoparticles with an analytical model and explained that weak coupling between the core and shell would cause no shift in the optomechanical mode.^{151,152} Our finite element method (FEM) simulations of Ag@TiO₂ nanocubes further confirm there would have to be minimal mechanical coupling between core and shell to result in no shift in the frequency of the optomechanical mode. Taken together, analysis of TAS at fast (<2 ps) and slow (~10–500 ps) time scales indicates that some of the photoexcitation energy absorbed by the Ag nanocube LSPR is absorbed by the TiO₂ shell as hot electrons at ultrafast time scales, and the “fingerprint” of that energy loss eventually shows up as an ~36% attenuation in the optomechanical mode.

The Journal of Physical Chemistry C, **121**(43), 2017, pp. 24159–24167

DOI: 10.1021/acs.jpcc.7b06667

Hot Electron Emission Can Lead to Damping of Optomechanical Modes in Core–Shell Ag@TiO₂ Nanocubes

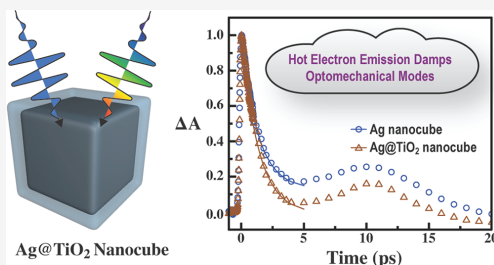
Domantas Peckus,[†] Hongpan Rong,[‡] Lukas Stankevičius,[†] Mindaugas Juodėnas,[†] Sigitas Tamulevičius,[†] Tomas Tamulevičius,^{*,†} and Joel Henzie^{*,‡}

[†]Institute of Materials Science of Kaunas University of Technology, K. Bašausko St. 59, Kaunas LT-51423, Lithuania

[‡]International Center for Materials Nanoarchitectonics (MANA), National Institute for Materials Science (NIMS), 1-1 Namiki, Tsukuba, Ibaraki 305-0044, Japan

Supporting Information

ABSTRACT: Interactions between light and metal nanostructures are mediated by collective excitations of free electrons called surface plasmons, which depend primarily on geometry and dielectric environment. Excitation with ultrafast pulses can excite optomechanical modes that modulate the volume and shape of nanostructures at gigahertz frequencies. Plasmons serve as an optical handle to study the ultrafast electronic dynamics of nanoscale systems. We describe a method to synthesize core–shell Ag@TiO₂ nanocubes—while successfully maintaining the size and shape of the nanocube. Transient absorbance spectroscopy (TAS) is used to track photophysical processes on multiple time scales: from the ultrafast creation of hot carriers to their decay into phonons and the formation of optomechanical modes. Surprisingly, the TiO₂ shell surrounding the Ag nanocubes caused no appreciable change in the frequency of the optomechanical mode, indicating that mechanical coupling between the core and shell is weak. However, the optomechanical mode was strongly attenuated by the TiO₂ shell and TAS decay at ultrafast time scales (0–5 ps) was much faster. This observation suggests that up to ~36% of the energy coupled into the plasmon resonance is being lost to the TiO₂, as hot carriers instead of coupling to the optomechanical mode. Analysis of both ultrafast decay and characterization of optomechanical modes provides a dual accounting method to track energy dissipation in hybrid metal–semiconductor nanosystems for plasmon-enhanced solar energy conversion and chemical fuel generation.



1. INTRODUCTION

Metal nanoparticles support collective excitations of free electrons called local surface plasmons (SPs) that can couple and focus light down to nanometer length scales.^{1–3} Light that couples to the SP sets off a complex cascade of relaxation processes as energy is transferred from the free electron distribution and eventually into lattice vibrations in the metal.⁴ There are, however, numerous points in this process where energy can dissipate, initially as hot electrons and then as sound and/or heat into the environment. Exploring this process is an essential part in developing high frequency chemical/biological sensors,^{5–7} controlling heat dissipation on the nanoscale in thermal devices,⁸ and improving light absorbance efficiencies in photovoltaics and solar fuel generation.⁹ However, these photophysical relaxation processes are still not well understood at either the ensemble or the single nanoparticle level, especially in hybrid metal/semiconductor systems where the plasmon resonance at least partially overlaps with the band gap of the semiconductor. Plasmon generation of hot free carriers in adjacent semiconductors is well established,^{10,11} and explaining the ultrafast transient dynamics of these systems is important to the development of various technologies.^{12–14}

This is because plasmon resonances can induce hot electron transfer from metal to the semiconductor, effectively circumventing the energy loss mechanisms of the metal and donating that energy to the semiconductor for solar energy conversion or photocatalysis.^{15,16} We hypothesized that ultrafast carrier dynamics occurring at the metal–semiconductor interface leaves some “fingerprint” or “residue” on the slower processes such as optomechanical modes. Comparing both fast and slow processes should reveal information on the total flow of energy in metal–semiconductor systems.

The SP serves as a built-in optical “handle” to monitor light–matter interactions in metallic nanosystems.⁴ Transient absorbance spectroscopy (TAS) is one of the most common techniques used to examine the ultrafast electronic dynamics of nanosized systems because tiny changes in absorbance indicate the flow of energy over short time scales—starting with absorption and then dephasing of the plasmon (~20 fs), electron–electron scattering (~100 fs), electron–phonon

Received: July 7, 2017

Revised: October 4, 2017

Published: October 5, 2017

scattering (~ 1 ps), and finally ending with mechanical oscillations and coupling to the environment (~ 1 ns).⁴ Initial excitation with the pump pulse shifts the SP resonance because hot electrons modify the dielectric constant of the metal.¹⁷ The hot electrons relax into phonons after a few picoseconds (ps), significantly driving the expansion of the lattice coordinate.¹⁸ When the time scale of the excitation source is faster than the period of expansion/contraction, it causes the particles to vibrate coherently to form breathing modes. These optomechanical modes modulate the volume and shape of the nanoparticle at gigahertz frequencies, which in turn affects the relative position of its plasmon resonance. We reasoned that the optomechanical modes embody the sum of most, if not all, of the optical energy absorbed by an isolated metal nanoparticle. Thus, comparison of an identical nanoparticle in an insulator-like environment versus one surrounded by a semiconductor shell would allow us to observe how much energy is being lost to the semiconductor, and/or show how the core-shell nanoparticle radiates sound waves into the environment.

The intensity and spatial distribution of SP modes depend sensitively on the size, shape, and dielectric environment of the nanoparticle. Cubic nanoparticles (i.e., nanocubes) in particular are very efficient at converting plasmonic fields into hot carriers.¹⁹ Silver (Ag) nanocubes support numerous bright SP modes.^{20,21} When the Ag nanocubes come in contact with a surface, the anisotropic dielectric environment initiates the hybridization of dipolar (bright) and quadrupolar (dark) SP modes with complex 3D spatial distributions and unusual absorption properties.^{22–24} Energy can be transferred to the surface primarily by plasmon induced carriers or thermal dissipation.²⁵ Previous studies using ultrafast TAS measurements have shown that ensemble measurements of Ag nanocubes in solution support optomechanical resonances that depend on the average edge length (a) of the cube.²⁶ Single-particle TAS measurements confirm that the period of the mode (T) is correlated with edge length, but edge length (a) in these measurements is only weakly correlated with its quality factor, $Q = \pi\tau/T$, where τ is the damping time.¹⁶ Detailed examination of optomechanical modes in metals is often performed on single particles, because colloids with narrow size/shape distributions are challenging to synthesize. There are some high quality measurements of ensembles of nanoparticles in solution, but these colloids typically have highly anisotropic shapes (bipyramids, nanorods) with resonances in the near-infrared (NIR). The plasmon resonances of typical impurities (spheres or polyhedra) are located at shorter wavelengths and do not interfere with these measurements.⁵ There are numerous experimental and theoretical investigations of core-shell nanoparticles. These can be classified into three groups on the basis of chemical composition: bimetallic core-shell structures (Au–Ag, Au–Pd, Ni–Ag),^{27–32} metal-dielectric core-shell nanohybrids,^{33–35} and nanoassemblies composed of heterodimers.³⁶ Careful experimental and theoretical analysis of such complex systems enables researchers to divine the nature and relationship between the component fractions^{27,29,32} and their internal structure³¹ and provides a unique avenue to probe the interface between the core-shell nanohybrid systems.^{33,34}

To our knowledge, there have been no comparable TAS investigations of free-standing core-shell nanoparticles where the band gap of the semiconductor shell is near the wavelength of the local SP resonance. However, the above references

collectively indicate that dissipation of the energy from photoexcitation generates optomechanical modes that are quite sensitive to the local environment.³⁷ Thus, the mechanism of energy dissipation likely follows one of two pathways: (i) The local dielectric environment enables more efficient transfer of sound into the environment. This pathway requires strong mechanical coupling between the metal core and the shell—mechanical coupling causes a shift in the mechanical eigenmode frequency. (ii) The shell consumes some hot carriers that otherwise would have generated phonons that contribute to the optomechanical mode—hot carrier coupling would cause faster decay of the TAS signal in the 0–5 ps time scale, and a subsequent attenuation in the optomechanical mode because less of the photoexcitation energy is being converted into phonons. Another pathway for loss could include absorbance of the shell, but this pathway can be neglected if the shell is thin and its optical absorbance is minimal at the pump/probe wavelengths.

In this research paper, we describe the first synthesis of core-shell Ag@TiO₂ nanocubes, deliberately maintaining the size and anisotropic shape of the Ag core. The SP is known to enhance the photocatalytic activity in composite noble metal/TiO₂ nanostructures beyond pure TiO₂.^{38–40} Cubic nanoparticles support stronger SP modes and generate more hot carriers than spherical particles; thus, we hypothesized that a TiO₂ shell would further enhance hot carrier generation in Ag and also help stabilize the Ag metal against chemical corrosion.^{19,41,42} Because the particles are highly monodisperse, free-standing in solution, and separated from each other by several microns, the optical properties of the solution are representative of single, isolated Ag nanocubes surrounded by an isotropic dielectric environment. TAS was used to compare the ultrafast decay of the Ag and Ag@TiO₂ nanocubes, and also tracked longer decay pathways, as this energy is converted into acoustic phonons (i.e., optomechanical modes) and eventually into sound waves. Interestingly, the TiO₂ shell caused no significant shift in the frequency of the optomechanical mode of the Ag nanocubes. Previously, Crut et al. explored spherical core-shell nanoparticles with an analytical model and explained that weak coupling between the core and shell would cause no shift in the optomechanical mode.^{33,34} Our finite element method (FEM) simulations of Ag@TiO₂ nanocubes further confirm there would have to be minimal mechanical coupling between core and shell to result in no shift in the frequency of the optomechanical mode. Taken together, analysis of TAS at fast (<2 ps) and slow (~ 10 –500 ps) time scales indicates that some of the photoexcitation energy absorbed by the Ag nanocube SP is absorbed by the TiO₂ shell as hot electrons at ultrafast time scales, and the “fingerprint” of that energy loss eventually shows up as an $\sim 36\%$ attenuation in the optomechanical mode.

2. METHODS

A more detailed explanation of the methods is included in the Supporting Information. The monodisperse solutions of Ag nanocubes were prepared using a modified procedure based on the Ag polyol synthesis method.^{43,44} In a typical synthesis to grow the surrounding TiO₂ shell, 2 mL of the Ag nanocube seed solution is combined with 50 μ L of dimethylamine (DMA) in a glass vial sonicated for 5 min and then stirred for 25 min. While the sample was stirring, 5 μ L of tetra-*n*-butyl orthotitanate (TBOT) was combined with 5 mL of ethanol while working in a nitrogen-filled glovebox. This vial of TBOT

solution was eventually transferred back into the lab environment (i.e., air) and added dropwise to the solution of nanocubes and stirred for ~ 1 h. The solution was then poured into a Teflon-lined autoclave and heated in an oven at 160 °C for 12 h. The Ag@TiO₂ nanocubes were centrifuged and washed with ethanol.

Steady state optical properties of the monodisperse Ag and Ag@TiO₂ nanocube colloidal solutions were analyzed with a UV–vis spectrophotometer, while ultrafast processes were investigated with a HARPIA TAS setup built by Light Conversion. The samples were excited using a Pharos ultrafast Yb:KGW laser (Light Conversion) with a regenerative amplifier at a 66.7 kHz repetition rate and 290 fs duration pulses at 1030 nm wavelength. The pump beam wavelength was tuned with an Orpheus collinear optical parametric generator and harmonic generator Lyra (Light Conversion) to 400 nm and an energy density of 32 mJ/cm². The samples were probed with a white light supercontinuum generated using a 2 mm thickness sapphire plate excited with the fundamental laser wavelength (1030 nm). The spectral range of the supercontinuum probe as well as the detection range of the TAS dynamics spanned wavelengths from 480 to 790 nm. The excitation beam was focused to an ~ 700 μ m diameter spot, while the diameter of the supercontinuum probe was ~ 500 μ m.

3. RESULTS AND DISCUSSION

Creating Ag nanoparticles conformally coated with TiO₂ shells using colloidal methods is challenging because hydrolysis of the titanium precursors requires acidic or alkaline environments that are not typically compatible with Ag metal.^{45,46} Top down techniques such as atomic layer deposition (ALD) have been used to coat Ag with TiO₂,^{47,48} but the method is quite challenging in part because Ag migrates at elevated temperatures and tends to pollute the ALD chamber. However, by simply mixing Ag and TiO₂ nanoparticles together, it has already been shown that plasmonic enhancement of photocatalysis and photodegradation reactions is possible,^{38,39} so there is a tangible benefit in further exploring plasmonic processes that enhance the emission of hot carriers with a more precisely controlled metal–semiconductor interface.⁴⁹ There has been some effort to adapt colloidal methods to coat Ag nanoparticles with TiO₂, but these methods have been applied to spherical Ag nanoparticles.⁵⁰ To our knowledge, no one has succeeded in coating anisotropic particles such as cubes because the TiO₂ colloidal growth conditions are quite harsh and tend to attack high index facets at the tips and edges of nanoparticles where most of the electromagnetic enhancement is localized.⁵¹ However, it is known that some amine catalysts are compatible with Ag nanoparticles and can drive the hydrolysis of silica precursors in the Stöber method,⁵² so it is possible that TiO₂ could be similarly hydrolyzed with dimethylamine (DMA). A scheme for the reaction is shown in Figure 1a. The Ag nanocubes are synthesized using a modified polyol method described in the Supporting Information. The Ag particles are initially coated with PVP polymer surfactant that is highly porous in ethanol and stabilizes the colloid so they do not irreversibly aggregate even in a condensed phase.⁴⁴

Transmission electron microscopy (TEM) shows that even our smallest Ag nanocube seeds (Figure 1b) are cubic with an average edge length (a) of 39 ± 3 nm. The nanocubes appeared to be unchanged by the TiO₂ coating step, retaining their sharp corners and edges in the diaphanous TiO₂ shell (Figure 1c). The thickness of the TiO₂ was 12 ± 4 nm for the 39 nm cubes,

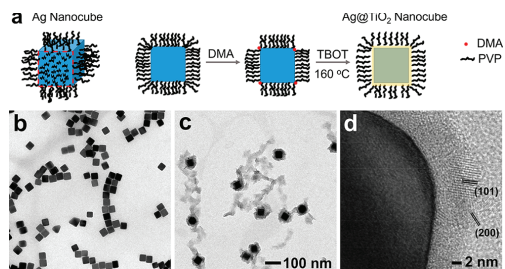


Figure 1. (a) Illustration showing the procedure for conformally coating Ag nanocubes with TiO₂ shells (DMA = dimethylamine, TBOT = tetra-*n*-butyl orthotitanate, PVP = polyvinylpyrrolidone). TEM micrographs show a dispersion of Ag nanocubes ($a = 39$ nm) (b) and Ag@TiO₂ nanocubes (c) using the same magnification. (d) HRTEM micrograph of the TiO₂ shell showing it is polycrystalline and in intimate contact with the Ag nanocube. The lattice spacings match the {101} and {200} planes of anatase phase TiO₂.

and HRTEM images show the TiO₂ shell is polycrystalline with 0.35 and 0.19 nm lattice spacings corresponding to the (101) and (200) planes of anatase TiO₂ (Figure 1d). A zoom-in image of the lattice fringes with TEM cross sections is provided in the Supporting Information (Supplemental Figure 1). The TiO₂ shell was noticeably thicker (18 ± 8 nm, Figure 2a) when we doubled the concentration of the titanium precursor. X-ray diffraction (XRD) of a larger reaction preparation of TiO₂ without adding Ag cubes showed that the reaction produced the anatase phase (Supplemental Figure 2).

The resonant wavelength of the SP depends sensitively on the local refractive index, and provides a simple and independent way to confirm that the particles maintain their shape and acquire the TiO₂ shell.⁵³ In UV–VIS spectrometer measurements, the dipolar resonance of the 39 nm Ag cubes shifted by $\Delta\lambda = 47$ nm and $\Delta\lambda = 57$ nm for the 12 and 18 nm TiO₂ shells, respectively (Figure 2a). We performed finite difference time domain (FDTD) calculations of a 39 nm Ag nanocube coated with 5, 10, and 20 nm TiO₂ and observed $\Delta\lambda_{\text{FDTD}}$ shifts of 10, 38, and 64 nm, matching the trend of the experimental data (Supplemental Figure 3). The UV–VIS data also shows that the spectra retain a similar shape with multipolar resonances that are characteristic for a cube of this size,²¹ which combined with the TEM results proves that the cubes retain their size and shape after the TiO₂ coating step. This coating method was also applied to nanocubes with larger edge lengths: $a = 77 \pm 3$ nm (Figure 2b) and $a = 92 \pm 4$ nm (Figure 2c). The TEM images show that the particles maintain their shapes, although the TiO₂ shell was thinner: 6 ± 3 and 8 ± 4 nm for the $a = 77 \pm 3$ nm and $a = 92 \pm 4$ nm Ag nanocubes, respectively.

To assess the impact of the TiO₂ shell on the ultrafast electron dynamics of the Ag nanocubes, we measured both Ag and Ag@TiO₂ cubes using TAS. Figure 3 shows the change in the TAS spectra over time (a so-called “carpet”) of Ag nanocubes (Figure 3a) and core–shell Ag@TiO₂ nanocubes (Figure 3b) in ethanol. We chose ethanol as the solvent because it is sufficiently insulating and not as strong of an electron acceptor compared to TiO₂. The samples were excited with a $\lambda = 400$ nm pump laser and monitored with a continuum white light probe ($\lambda = 480$ – 765 nm). The pump pulse wavelength was chosen so that it would be slightly lower in

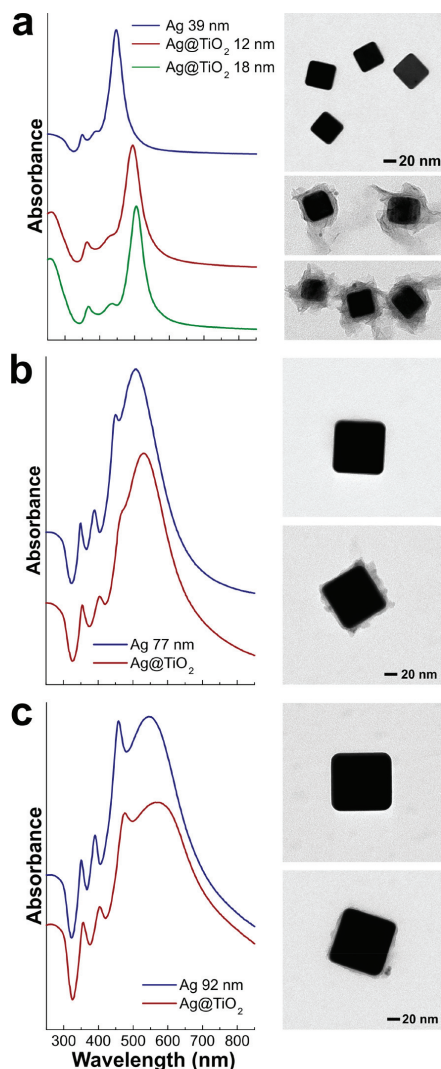


Figure 2. Steady-state UV–VIS absorption spectra of Ag and Ag@TiO₂ nanocubes with (a) 39 nm, (b) 77 nm, and (c) 92 nm edge lengths. TEM micrographs of the nanocubes are to the right of their corresponding spectra.

energy than the band gap of anatase phase TiO₂ ($\lambda \sim 386$ nm)⁵⁴ but still able to excite the SP resonance at the prototypical C2 and C3 cube modes described by Fuchs and others.^{20,21,23} This setup enabled efficient excitation of the nanocube and ability to observe the breathing modes by monitoring wavelengths associated with the lower energy primitive bright dipolar (C6) SP mode. The TiO₂ shell will cause the LSP of the Ag nanoparticle to red-shift; thus, the two-dimensional TAS carpets are useful in order to locate the maximum TAS signal for the positive (right-most) phase of the

dipolar SP resonance for accurate comparison of each particle. Choosing the dipole is important because it is better to compare SP modes with roughly the same spatial distribution and absorption cross section. Measuring the particles in solution rather than surfaces is advantageous not only because there is no vibrational damping with the surface but also because surfaces create an anisotropic dielectric environment that causes hybridization of bright and dark plasmon modes with vastly different absorption cross sections.^{22–25} Figure 3c shows TAS traces for multiple Ag and Ag@TiO₂ nanocubes ($a = 39 \pm 3$, 77 ± 3 , and 92 ± 4 nm) collected nearest to the wavelength where the cube dipole exhibited maximum ΔA . The initial increase in amplitude is caused by excitation of the electron distribution, which quickly relaxes via electron–electron scattering followed by electron–phonon scattering. The second peak originates from the expansion of the lattice coordinate that is determined by the electron–phonon coupling constant of the particle. The pulse width of the pump laser is faster than the period of expansion/contraction of the particle; thus, it is possible to efficiently excite coherent optomechanical modes that modulate absorbance by shifting the position of the SP peak.

Two functions were used to fit the TAS traces, corresponding to (1) the fast exponential decay and (2) the slow exponential decay modulated by a damped harmonic oscillator function. First, the data was separated manually, selecting characteristic time constant t_b typical for two characteristic processes^{30,55}

$$f_1(t) = a_0 e^{-t/b_0} + c_0; \quad t < t_b \quad (1)$$

$$f_2(t) = a e^{-t/b} + c + A e^{-t/\tau} \cos\left(\frac{2\pi}{T}t + \varphi\right); \quad t > t_b \quad (2)$$

containing the amplitudes of the fast decaying component (a_0), slow decaying background (a), and harmonic oscillation (A). The fast (b_0) and slow (b) decay time constants account primarily for electron–electron scattering, electron–phonon scattering, and exchange of heat with the environment, respectively. T is the oscillation period, τ is the damping time of oscillations, while φ is the phase. Fitting the TAS traces for the smallest Ag and Ag@TiO₂ nanocubes ($a = 39 \pm 3$ nm) shows that the period of oscillation (T) is almost unchanged by the TiO₂ shell (e.g., 20.0 ps for Ag and 19.5–19.6 ps for Ag@TiO₂ for 39 \pm 3 nm sized cubes), hinting that the Ag nanocube core and the TiO₂ shell are not mechanically coupled. However, the Q -factor of the Ag@TiO₂ nanocubes decreased by $\sim 40\%$ so the TiO₂ shell causes significant damping overall (Figure 4a). Furthermore, the Fourier transforms (Figure 4b) show that the same ($a = 39 \pm 3$ nm) Ag cube has a sharp resonance at ~ 50 GHz, but the TiO₂ shell broadens the peak in FFT significantly (Figure 4b). Previously, Petrova et al. used finite element analysis to show that the reduced frequency of the Ag cube fundamental breathing mode is $\omega = 6.04$ when excited by a uniform initial strain.²⁶ We fit the TAS traces for three Ag nanocube sizes ($a = 39 \pm 3$, 77 ± 3 , and 92 ± 4 nm) and show that T is correlated with size. Using this plot, we obtained $\omega = 6.17 \pm 0.13$ for Ag nanocubes and $\omega = 6.16 \pm 0.01$ for Ag@TiO₂ nanocubes. The ω values are roughly the same, adding further proof that the core and shell are decoupled (Figure 4c, top).

It was surprising that the frequency of the breathing mode of the Ag cube was largely unaffected by the TiO₂ coating (Ag =

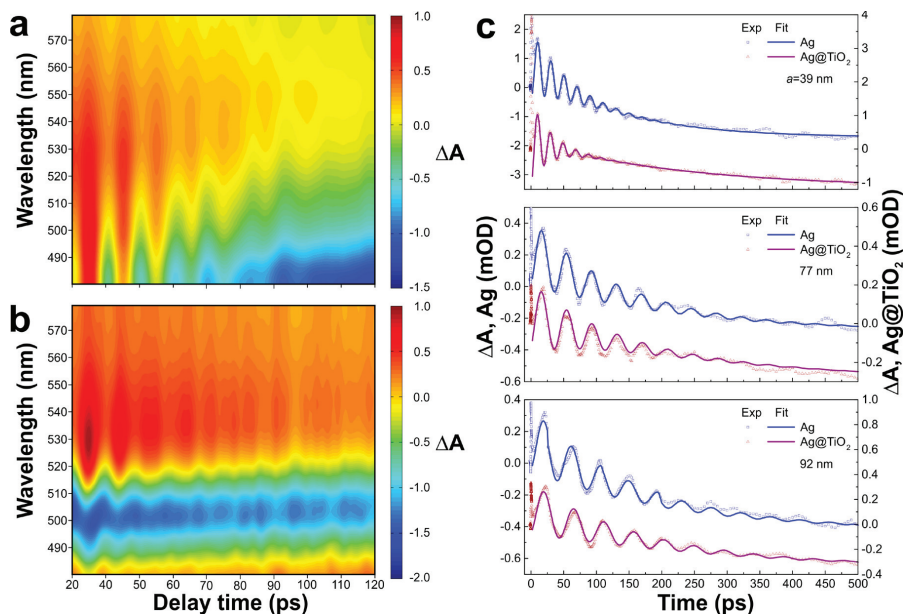


Figure 3. TAS carpets for (a) solution of 39 nm Ag nanocubes and (b) the same cubes coated with a 12 nm TiO_2 shell ($\lambda_{\text{pump}} = 400$ nm, intensity $\sim 32 \mu\text{J}/\text{cm}^2$; $\lambda_{\text{probe}} = 480\text{--}785$ nm; ΔA is expressed in mOD). (c) TAS relaxation traces were chosen at the maximum positive ΔA value for Ag (blue squares) and Ag@TiO₂ (red triangles) with three different edge lengths. (c, top): $a = 39$ nm Ag nanocubes (Ag, $\lambda_{\text{probe}} = 480$ nm; Ag@TiO₂, $\lambda_{\text{probe}} = 511$ nm). (c, middle): $a = 77$ nm Ag nanocubes (Ag, $\lambda_{\text{probe}} = 565$ nm; Ag@TiO₂, $\lambda_{\text{probe}} = 569$ nm). (c, bottom): $a = 92$ nm Ag nanocubes (Ag, $\lambda_{\text{probe}} = 605$ nm; Ag@TiO₂, $\lambda_{\text{probe}} = 602$ nm). The solid lines show the data fit to a damped oscillator function in eq 2.

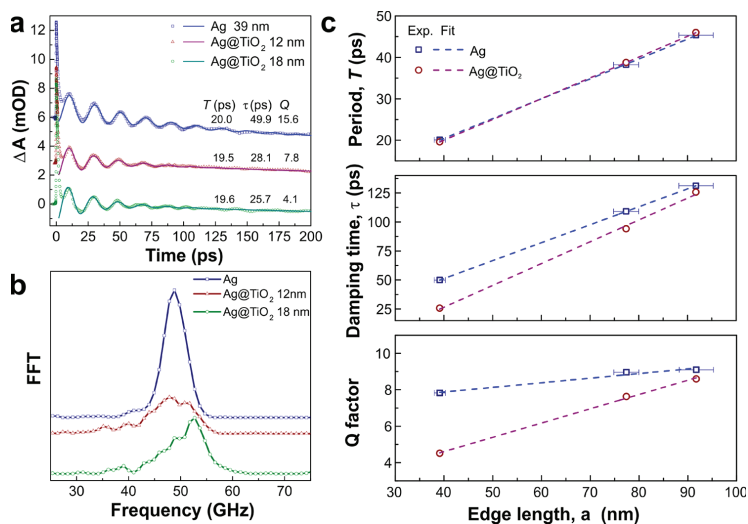


Figure 4. (a) TAS traces for Ag and Ag@TiO₂ nanocubes ($a = 39$ nm) with 12 and 18 nm thick TiO_2 shells ($\lambda_{\text{probe}} = 480, 511,$ and 517 nm, respectively). The solid lines correspond to the damped oscillator fitting, accompanied by the periods of oscillation (T), damping times (τ), and quality (Q) factors of each trace. (b) FFT spectra of the TAS traces in part a. (c) Size-dependent optomechanical properties of Ag and Ag@TiO₂ nanocubes: T (c, top), τ (c, middle), and Q (c, bottom). Edge length corresponds to the size of the Ag nanocube core, and the dotted lines are the linear fits of the experimental data.

49.9 GHz, whereas Ag@TiO₂ = 51.2 and 51.1 GHz). In order to understand this observation, we initially used a simple analytical method developed for spherical core–shell nanoparticles.^{33,35} For all of our samples, the reduced period $T_{\text{Ag@TiO}_2}/T_{\text{Ag}}$ varied from 0.98 to 1.01 with standard deviation of 0.02, indicating the core and shell were mechanically decoupled (Supplemental Figure 4). This observation suggests that the decay of the optomechanical mode is not caused by the shell enhancing the radiation of sound but rather by some other phenomena. We went further and modeled the influence of coupling strength on the oscillation frequency of a bare Ag cube ($a = 39$ nm) and one surrounded by a TiO₂ shell ($t = 12$ nm) using a finite element method (FEM) simulation. As expected, the weakly coupled core–shell Ag@TiO₂ nanocubes had an oscillation frequency similar to a bare Ag cube (Supplemental Figure 5). By steadily increasing the coupling strength from 0.01 to 10 GPa/nm, we observed a shift in the frequency of the optomechanical mode. Together, these results show that the (i) TiO₂ shell does not change the experimental frequency of the Ag nanocube, (ii) the reduced frequencies of the nanocubes are identical regardless of the presence of the TiO₂ shell, (iii) the estimation of the analytical reduced period indicates mechanical decoupling, and (iv) the FEM result shows that strong coupling is necessary to shift the frequency of the optomechanical mode. Thus, we concluded that the shell is not enhancing the decay of photoexcitation energy mechanically via sound waves, but rather some other effect is driving the attenuation of the optomechanical mode.

The damping time τ is known to be strongly affected by the surrounding medium (homogeneous broadening) and dephasing due to the size distribution of the nanoparticles (inhomogeneous broadening).⁵⁶ The Ag nanocubes are monodisperse, and the dimensions of the Ag core are largely unchanged by the coating step, as illustrated by TEM and the lack of change in T . We hypothesized that the oscillations of the Ag@TiO₂ nanocubes are damped from the very beginning because of electron losses. Since conventional energy loss via mechanical vibrations is not important in this particular system (for mechanical losses, $t > t_b$), the primary loss mechanism should be energy transfer to the TiO₂ shell (for electronic losses, $t < t_b$) (Figure 4c, middle). The homogeneous Q -factor ($Q = \pi\tau/T$) allows us to remove the influence of size and isolate the effect of energy loss (Figure 4c, bottom). We can see that the Q -factors of the Ag cubes are relatively unchanged by size ($Q = 8$ –9). Interestingly, the Q -factors for Ag@TiO₂ nanocubes had a much wider range ($Q = 5$ –9). If the systems are equivalent, then the smaller nanocubes have additional energy loss due to the enhanced absorption losses of small metal nanoparticles. In this system, energy will be lost as hot electrons, and is not mechanical as explained above.

Following initial light excitation, the local plasmon resonance of the particle can either scatter the photon or transfer its energy into nonradiative relaxation processes. As mentioned, for smaller metal particles (<50 nm), this nonradiative relaxation channel is dominant and creates hot carriers that would normally redistribute energy via electron–electron scattering and dissipate into the environment as heat/sound. However, hot electrons extend further from the surface than the normal electron distribution and can transfer into the electronic states of an adjacent electron acceptor, as clearly illustrated by emerging applications such as plasmon-enhanced photodetection and photocatalysis.^{57–62} Ag suffers less absorption losses than other plasmonic metals such as gold

(Au) and copper (Cu),⁶³ but small Ag nanoparticles are still quite lossy. To find evidence of enhanced hot electron loss, we reexamined the ultrafast TAS traces of the 39 nm Ag and Ag@TiO₂ nanocubes (Figure 5). The normalized and backgrounded

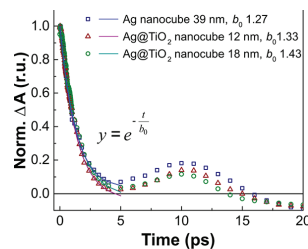


Figure 5. Normalized and backgrounded TAS traces for Ag and Ag@TiO₂ nanocubes ($a = 39$ nm) with 12- and 18-nm thick TiO₂ shells ($\lambda_{\text{probe}} = 480, 511, \text{ and } 517$ nm, respectively) showing the first 20 ps from Figure 4a. The symbols represent the experimental data, and solid lines are the exponential fits using the inset exponential equation.

traces show that the initial decay is faster for both Ag@TiO₂ nanocube solutions. Moreover, the intensity of the first part of the breathing mode (10 ps) was highly attenuated, representing a decrease in $\Delta A \sim 36\%$. Faster decay and smaller oscillations for Ag@TiO₂ nanocubes reveals that electron–phonon coupling has less impact on the TAS signal because there is an alternative relaxation path. Additionally, the transient behaviors of Ag and Ag@TiO₂ particles in Figure 5 were examined at various excitation powers and there was no dependence on pump power (Supplemental Figure 6). The geometry of the core–shell influences the ultrafast and picosecond time dynamics instead of pump power at the excitation energies used in the experiments. Collectively, the TAS results show that the TiO₂ shell can harvest hot electrons from the SP of the Ag nanocube. However, the fate of hot electrons and specifically how efficiently they move into the semiconductor—or migrate back into the metal—is still an open area of research and will impact the efficiency of the conversion process from light into hot electrons. Optomechanical oscillations can serve as an additional accounting tool to observe the effects of hot electron emission in mechanically uncoupled interfaces to help engineer the performance of plasmonic devices for energy and chemical fuel generation.⁶⁴

4. CONCLUSION

In conclusion, we have demonstrated a simple colloidal method to coat Ag nanocubes in TiO₂ while maintaining their size and shape. This is possible because the amine catalyst can hydrolyze TiO₂ precursors but is a relatively gentle base that does not etch Ag nanocubes under these conditions. Monodisperse Ag nanocubes were analyzed with TAS to establish a baseline for the size-dependent optomechanical properties of PVP-coated Ag nanocubes in ethanol. Our Q -factors for ensembles of Ag nanocubes in ethanol are in the same range as single-particle Q -factors for Ag nanocubes on a glass substrate in air.^{37,65} Coating the Ag nanocubes with TiO₂ had little to no effect on the frequency of the optomechanical mode but severely damped it. FEM simulations indicate that the Ag nanocube core and TiO₂ shell must be mechanically uncoupled to generate no shift in frequency. Although these core–shell nanoparticles are mechanically uncoupled, they are still electronically coupled

because ultrafast decay is faster and the optomechanical mode is attenuated by $\sim 36\%$. This result shows that electron–phonon coupling has less impact on the TAS response and there is a parallel competing relaxation path that enables hot electrons to be diverted into the TiO_2 layer. Ag is more Earth abundant than Au metal, and enhancing its absorbance and stability makes technologies based on hot-carrier emission more feasible. We plan to explore how excitation of different SP modes might affect the electron dynamics of the Ag@TiO_2 nanocubes and evaluate them in realistic photocatalytic reactions. We consider optomechanical oscillations to be a simple and complementary method to monitor the flow of energy in the nanosystem and will help researchers optimize the metal–semiconductor interface in plasmonic nanocatalysts and nanodevices.

■ ASSOCIATED CONTENT

Supporting Information

The Supporting Information is available free of charge on the ACS Publications website at DOI: 10.1021/acs.jpcc.7b06667.

Details on sample preparation, structural characterization, optical characterization, and numerical analysis are included. We provide a detailed version of the Ag and Ag@TiO_2 nanocube synthesis, an atomically resolved image of the interface between Ag and TiO_2 , and the XRD pattern for anatase TiO_2 generated with this method. We also provide a model using finite difference time domain (FDTD) to describe the optical properties of Ag nanocubes and core–shell Ag@TiO_2 nanocubes with varying thicknesses of TiO_2 . The coupling strength between the core and shell was initially examined with an analytical method. Finite element method (FEM) simulations were used to examine the influence of coupling strength in the core–shell structure on the oscillation mode frequency. TAS traces for $a = 39$ nm Ag and Ag@TiO_2 nanocubes were measured to show the influence of the pump power. Details of the ultrafast optical setup and the fitting parameters for analysis of the TAS spectra are also included. (PDF)

■ AUTHOR INFORMATION

Corresponding Authors

*E-mail: Tomas.Tamulevicius@ktu.lt

*E-mail: HENZIE.Joeladam@nims.go.jp

ORCID

Tomas Tamulevicius: 0000-0003-3879-2253

Joel Henzie: 0000-0002-9190-2645

Notes

The authors declare no competing financial interest.

■ ACKNOWLEDGMENTS

This work was supported by the World Premier International Research Center Initiative on “Materials Nanoarchitectonics (WPI-MANA)” from MEXT, Japan, and the Bilateral Lithuania-Japan Joint Research Program project “Plasmonic properties of silver nanoparticles and self-assembled clusters (PLAS)” co-financed by the Research Council of Lithuania (Grant No. LJB-1/2015) and the Japan Society for the Promotion of Science (JSPS). J.H. also acknowledges the user proposal (#4446) program at the Molecular Foundry, which is supported by the Office of Science, Office of Basic

Energy Sciences, of the U.S. Department of Energy under Contract No. DE-AC02-05CH11231. T.T. acknowledges The Lithuanian Academy of Sciences for Young Researchers Grant.

■ REFERENCES

- (1) Barnes, W. L.; Dereux, A.; Ebbesen, T. W. Surface Plasmon Subwavelength Optics. *Nature* **2003**, *424*, 824–830.
- (2) Schuller, J. A.; Barnard, E. S.; Cai, W.; Jun, Y. C.; White, J. S.; Brongersma, M. L. Plasmonics for Extreme Light Concentration and Manipulation. *Nat. Mater.* **2010**, *9*, 193–204.
- (3) Henzie, J.; Lee, J.; Lee, M. H.; Hasan, W.; Odom, T. W. Nanofabrication of Plasmonic Structures. *Annu. Rev. Phys. Chem.* **2009**, *60*, 147–165.
- (4) Hartland, G. V. Optical Studies of Dynamics in Noble Metal Nanostructures. *Chem. Rev.* **2011**, *111*, 3858–3887.
- (5) Pelton, M.; Sader, J. E.; Burgin, J.; Liu, M.; Guyot-Sionnest, P.; Gosztoła, D. Damping of Acoustic Vibrations in Gold Nanoparticles. *Nat. Nanotechnol.* **2009**, *4*, 492–495.
- (6) Wu, H.-J.; Henzie, J.; Lin, W.-C.; Rhodes, C.; Li, Z.; Sartorel, E.; Thomer, J.; Yang, P.; Groves, J. T. Membrane-Protein Binding Measured with Solution-Phase Plasmonic Nanocube Sensors. *Nat. Methods* **2012**, *9*, 1189–1191.
- (7) Henzie, J.; Andrews, S. C.; Ling, X. Y.; Li, Z.; Yang, P. Oriented Assembly of Polyhedral Plasmonic Nanoparticle Clusters. *Proc. Natl. Acad. Sci. U. S. A.* **2013**, *110*, 6640–6645.
- (8) Maldovan, M. Sound and Heat Revolutions in Phononics. *Nature* **2013**, *503*, 209–217.
- (9) Atwater, H. A.; Polman, A. Plasmonics for Improved Photovoltaic Devices. *Nat. Mater.* **2010**, *9*, 865–865.
- (10) Kang, Y.; Najmaei, S.; Liu, Z.; Bao, Y.; Wang, Y.; Zhu, X.; Halas, N. J.; Nordlander, P.; Ajayan, P. M.; Lou, J.; et al. Plasmonic Hot Electron Induced Structural Phase Transition in a MoS_2 Monolayer. *Adv. Mater.* **2014**, *26*, 6467.
- (11) Fang, Z.; Wang, Y.; Liu, Z.; Schlather, A.; Ajayan, P. M.; Koppens, F. H. L.; Nordlander, P.; Halas, N. J. Plasmon-Induced Doping of Graphene. *ACS Nano* **2012**, *6*, 10222.
- (12) Harutyunyan, H.; Martinson, A. B. F.; Rosenmann, D.; Khorashad, L. K.; Besteiro, L. V.; Govorov, A. O.; Wiederrecht, G. P. Anomalous Ultrafast Dynamics of Hot Plasmonic Electrons in Nanostructures with Hot Spots. *Nat. Nanotechnol.* **2015**, *10*, 770–774.
- (13) Li, J.; Cushing, S. K.; Meng, F.; Senty, T. R.; Bristow, A. D.; Wu, N. Plasmon-Induced Resonance Energy Transfer for Solar Energy Conversion. *Nat. Photonics* **2015**, *9*, 601–607.
- (14) Wu, K.; Chen, J.; McBride, J. R.; Lian, T. Efficient Hot-Electron Transfer by a Plasmon-Induced Interfacial Charge-Transfer Transition. *Science* **2015**, *349*, 632–635.
- (15) Lincic, S.; Aslam, U.; Boerigter, C.; Morabito, M. Photochemical Transformations on Plasmonic Metal Nanoparticles. *Nat. Mater.* **2015**, *14*, 744–744.
- (16) Wu, K.; Lian, T. Quantum Confined Colloidal Nanorod Heterostructures for Solar-to-Fuel Conversion. *Chem. Soc. Rev.* **2016**, *45*, 3781–3810.
- (17) Baida, H.; Mongin, D.; Christofilos, D.; Bachelier, G.; Crut, A.; Maioli, P.; Del Fatti, N.; Vallée, F. Ultrafast Nonlinear Optical Response of a Single Gold Nanorod near Its Surface Plasmon Resonance. *Phys. Rev. Lett.* **2011**, *107*, 57402.
- (18) Voisin, C.; Del Fatti, N.; Christofilos, D.; Vallée, F. Time-Resolved Investigation of the Vibrational Dynamics of Metal Nanoparticles. *Appl. Surf. Sci.* **2000**, *164*, 131–139.
- (19) Zhang, H.; Govorov, A. O. Optical Generation of Hot Plasmonic Carriers in Metal Nanocrystals: The Effects of Shape and Field Enhancement. *J. Phys. Chem. C* **2014**, *118*, 7606–7614.
- (20) Fuchs, R. Theory of the Optical Properties of Ionic Crystal Cubes. *Phys. Rev. B* **1975**, *11*, 1732–1740.
- (21) Cortie, M. B.; Liu, F.; Arnold, M. D.; Niidome, Y. Multimode Resonances in Silver Nanocuboids. *Langmuir* **2012**, *28*, 9103–9112.

- (22) Sherry, L. J.; Chang, S.; Schatz, G. C.; Van Duyne, R. P.; Wiley, B. J.; Xia, Y. Localized Surface Plasmon Resonance Spectroscopy of Single Silver Nanocubes. *Nano Lett.* **2005**, *5*, 2034–2038.
- (23) Zhang, S.; Bao, K.; Halas, N. J.; Xu, H.; Nordlander, P. Substrate-Induced Fano Resonances of a Plasmonic Nanocube: A Route to Increased-Sensitivity Localized Surface Plasmon Resonance Sensors Revealed. *Nano Lett.* **2011**, *11*, 1657–1663.
- (24) Nicoletti, O.; de la Peña, F.; Leary, R. K.; Holland, D. J.; Ducati, C.; Midgley, P. A. Three-Dimensional Imaging of Localized Surface Plasmon Resonances of Metal Nanoparticles. *Nature* **2013**, *502*, 80–84.
- (25) Li, G.; Cherqui, C.; Bigelow, N. W.; Duscher, G.; Straney, P. J.; Millstone, J. E.; Masiello, D. J.; Camden, J. P. Spatially Mapping Energy Transfer from Single Plasmonic Particles to Semiconductor Substrates via STEM/EELS. *Nano Lett.* **2015**, *15*, 3465–3471.
- (26) Petrova, H.; Lin, C. H.; De Liejer, S.; Hu, M.; McLellan, J. M.; Siekkinen, A. R.; Wiley, B. J.; Marquez, M.; Xia, Y.; Sader, J. E.; et al. Time-Resolved Spectroscopy of Silver Nanocubes: Observation and Assignment of Coherently Excited Vibrational Modes. *J. Chem. Phys.* **2007**, *126*, 094709.
- (27) Cardinal, M. F.; Mongin, D.; Crut, A.; Maioli, P.; Rodríguez-González, B.; Pérez-Juste, J.; Liz-Marzán, L. M.; Del Fatti, N.; Vallée, F. Acoustic Vibrations in Bimetallic Au@Pd Core-Shell Nanorods. *J. Phys. Chem. Lett.* **2012**, *3*, 613–619.
- (28) Crut, A.; Maioli, P.; Del Fatti, N.; Vallée, F. Acoustic Vibrations of Metal Nano-Objects: Time-Domain Investigations. *Phys. Rep.* **2015**, *549*, 1–43.
- (29) Kirakosyan, A. S.; Shahbazyan, T. V. Vibrational Modes of Metal Nanoshells and Bimetallic Core-Shell Nanoparticles. *J. Chem. Phys.* **2008**, *129*, 034708.
- (30) Hodak, J. H.; Henglein, A.; Hartland, G. V. Coherent Excitation of Acoustic Breathing Modes in Bimetallic Core-Shell Nanoparticles. *J. Phys. Chem. B* **2000**, *104*, 5053–5055.
- (31) Stoll, T.; Maioli, P.; Crut, A.; Rodal-Cedeira, S.; Pastoriza-Santos, I.; Vallée, F.; Del Fatti, N. Time-Resolved Investigations of the Cooling Dynamics of Metal Nanoparticles: Impact of Environment. *J. Phys. Chem. C* **2015**, *119*, 12757–12764.
- (32) Sader, J. E.; Hartland, G. V.; Mulvaney, P. Theory of Acoustic Breathing Modes of Core-Shell Nanoparticles. *J. Phys. Chem. B* **2002**, *106*, 1399–1402.
- (33) Mongin, D.; Juvé, V.; Maioli, P.; Crut, A.; Del Fatti, N.; Vallée, F.; Sánchez-Iglesias, A.; Pastoriza-Santos, I.; Liz-Marzán, L. M. Acoustic Vibrations of Metal-Dielectric Core-Shell Nanoparticles. *Nano Lett.* **2011**, *11*, 3016–3021.
- (34) Crut, A.; Juvé, V.; Mongin, D.; Maioli, P.; Del Fatti, N.; Vallée, F. Vibrations of Spherical Core-Shell Nanoparticles. *Phys. Rev. B: Condens. Matter Mater. Phys.* **2011**, *83*, 205430.
- (35) Crut, A.; Maioli, P.; Del Fatti, N.; Vallée, F. Time-Domain Investigation of the Acoustic Vibrations of Metal Nanoparticles: Size and Encapsulation Effects. *Ultrasonics* **2015**, *56*, 98–108.
- (36) Lombardi, A.; Grzelczak, M. P.; Crut, A.; Maioli, P.; Pastoriza-Santos, I.; Liz-Marzán, L. M.; Del Fatti, N.; Vallée, F. Optical Response of Individual Au-Ag@SiO₂ Heterodimers. *ACS Nano* **2013**, *7*, 2522–2531.
- (37) Staleva, H.; Hartland, G. V. Vibrational Dynamics of Silver Nanocubes and Nanowires Studied by Single-Particle Transient Absorption Spectroscopy. *Adv. Funct. Mater.* **2008**, *18*, 3809–3817.
- (38) Christopher, P.; Ingram, D. B.; Linic, S. Enhancing Photochemical Activity of Semiconductor Nanoparticles with Optically Active Ag Nanostructures: Photochemistry Mediated by Ag Surface Plasmons. *J. Phys. Chem. C* **2010**, *114*, 9173–9177.
- (39) Gomathi Devi, L.; Kavitha, R. A Review on Plasmonic Metal-TiO₂ Composite for Generation, Trapping, Storing and Dynamic Vectorial Transfer of Photogenerated Electrons across the Schottky Junction in a Photocatalytic System. *Appl. Surf. Sci.* **2016**, *360*, 601–622.
- (40) Mubeen, S.; Lee, J.; Singh, N.; Krämer, S.; Stucky, G. D.; Moskovits, M. An Autonomous Photosynthetic Device in Which All Charge Carriers Derive from Surface Plasmons. *Nat. Nanotechnol.* **2013**, *8*, 247–251.
- (41) Ung, T.; Liz-Marzán, L. M.; Mulvaney, P. Controlled Method for Silica Coating of Silver Colloids: Influence of Coating on the Rate of Chemical Reactions. *Langmuir* **1998**, *14*, 3740–3748.
- (42) Yin, Y.; Lu, Y.; Sun, Y.; Xia, Y. Silver Nanowires Can Be Directly Coated with Amorphous Silica to Generate Well-Controlled Coaxial Nanocables of Silver/Silica. *Nano Lett.* **2002**, *2*, 427–430.
- (43) Tao, A.; Sinsermsuksakul, P.; Yang, P.; Signatures, S. Polyhedral Silver Nanocrystals with Distinct Scattering Signatures. *Angew. Chem., Int. Ed.* **2006**, *45*, 4597–4601.
- (44) Henzie, J.; Grünwald, M.; Widmer-Cooper, A.; Geissler, P. L.; Yang, P. Self-Assembly of Uniform Polyhedral Silver Nanocrystals into Densest Packings and Exotic Superlattices. *Nat. Mater.* **2011**, *11*, 131–137.
- (45) Sajan, C. P.; Wageh, S.; Al-Ghamdi, A. A.; Yu, J.; Cao, S. TiO₂ Nanosheets with Exposed {001} Facets for Photocatalytic Applications. *Nano Res.* **2016**, *9*, 3–27.
- (46) Xiang, G.; Li, T.; Zhuang, J.; Wang, X. Large-Scale Synthesis of Metastable TiO₂(B) Nanosheets with Atomic Thickness and Their Photocatalytic Properties. *Chem. Commun.* **2010**, *46*, 6801.
- (47) Standridge, S. D.; Schatz, G. C.; Hupp, J. T. Toward Plasmonic Solar Cells: Protection of Silver Nanoparticles via Atomic Layer Deposition of TiO₂. *Langmuir* **2009**, *25*, 2596–2600.
- (48) Deng, Y.; Tüysüz, H.; Henzie, J.; Yang, P. Templated Synthesis of Shape-Controlled, Ordered TiO₂ Cage Structures. *Small* **2011**, *7*, 2037–2040.
- (49) Brongersma, M. L.; Halas, N. J.; Nordlander, P. Plasmon-Induced Hot Carrier Science and Technology. *Nat. Nanotechnol.* **2015**, *10*, 25–34.
- (50) Hirakawa, T.; Kamat, P. V. Charge Separation and Catalytic Activity of Ag@TiO₂ Core-Shell Composite Clusters under UV-Irradiation. *J. Am. Chem. Soc.* **2005**, *127*, 3928–3934.
- (51) Chandrasekhar, P. S.; Chander, N.; Anjaneyulu, O.; Komarala, V. K. Plasmonic Effect of Ag@TiO₂ Core-Shell Nanocubes on Dye-Sensitized Solar Cell Performance Based on Reduced Graphene Oxide-TiO₂ Nanotube Composite. *Thin Solid Films* **2015**, *594*, 45–55.
- (52) Kobayashi, Y.; Katakami, H.; Mine, E.; Nagao, D.; Konno, M.; Liz-Marzán, L. M. Silica Coating of Silver Nanoparticles Using a Modified Stöber Method. *J. Colloid Interface Sci.* **2005**, *283*, 392–396.
- (53) Anker, J. N.; Hall, W. P.; Lyandres, O.; Shah, N. C.; Zhao, J.; Van Duyne, R. P. Biosensing with Plasmonic Nanosensors. *Nat. Mater.* **2008**, *7*, 442–453.
- (54) Reyes-Coronado, D.; Rodríguez-Gattorno, G.; Espinosa-Pesqueira, M. E.; Cab, C.; de Coss, R.; Oskam, G. Phase-Pure TiO₂ Nanoparticles: Anatase, Brookite and Rutile. *Nanotechnology* **2008**, *19*, 145605.
- (55) Hartland, G. V. Coherent Vibrational Motion in Metal Particles: Determination of the Vibrational Amplitude and Excitation Mechanism. *J. Chem. Phys.* **2002**, *116*, 8048–8055.
- (56) Marty, R.; Arbouet, A.; Girard, C.; Mlayah, A.; Paillard, V.; Lin, V. K.; Teo, S. L.; Tripathy, S. Damping of the Acoustic Vibrations of Individual Gold Nanoparticles. *Nano Lett.* **2011**, *11*, 3301–3306.
- (57) Goykhman, I.; Desiatov, B.; Khurgin, J.; Shappir, J.; Levy, U. Locally Oxidized Silicon Surface-Plasmon Schottky Detector for Telecom Regime. *Nano Lett.* **2011**, *11*, 2219–2224.
- (58) Knight, M. W.; Sobhani, H.; Nordlander, P.; Halas, N. J. Photodetection with Active Optical Antennas. *Science* **2011**, *332*, 702–704.
- (59) Linic, S.; Christopher, P.; Ingram, D. B. Plasmonic-Metal Nanostructures for Efficient Conversion of Solar to Chemical Energy. *Nat. Mater.* **2011**, *10*, 911–921.
- (60) Mukherjee, S.; Libisch, F.; Large, N.; Neumann, O.; Brown, L. V.; Cheng, J.; Lassiter, J. B.; Carter, E. a.; Nordlander, P.; Halas, N. J. Hot Electrons Do the Impossible: Plasmon-Induced Dissociation of H₂ on Au. *Nano Lett.* **2013**, *13*, 240–247.
- (61) Wang, G.; Wang, X.; Liu, J.; Sun, X. Mesoporous Au/TiO₂ Nanocomposite Microspheres for Visible-Light Photocatalysis. *Chem. - Eur. J.* **2012**, *18*, 5361–5366.

(62) Brongersma, M. L.; Halas, N. J.; Nordlander, P. Plasmon-Induced Hot Carrier Science and Technology. *Nat. Nanotechnol.* **2015**, *10*, 25–34.

(63) Palik, E. D. *Handbook of Optical Constants of Solids*; Academic Press: 1998; Vol. 4.

(64) Moskovits, M. The Case for Plasmon-Derived Hot Carrier Devices. *Nat. Nanotechnol.* **2015**, *10*, 6–8.

(65) Staleva, H.; Hartland, G. V. Transient Absorption Studies of Single Silver Nanocubes. *J. Phys. Chem. C* **2008**, *112*, 7535–7539.

Effect of Ag Nanocube Optomechanical Modes on Plasmonic Surface Lattice Resonances

In this manuscript, we examine how dynamics on the ultrafast time scale affect optical properties that manifest on the photonic length scale. We initially compare the steady-state optical properties of free-standing, disordered Ag nanocubes in solution vs. the same Ag nanocubes assembled into 2D arrays that are specifically patterned to generate SLRs. The dispersion diagrams of NP arrays with various spacings were measured in an angle-dependent optical spectroscopy setup and compared to electromagnetic (EM) models generated with the finite element method (FEM). Both experiment and theory show the emergence of both dipolar and quadrupolar SLR modes in the nanoparticle arrays. These samples were then measured with TAS at normal incidence and 30° to examine how the in-plane vs. out-of-plane (OP) SLRs evolve as the optomechanical modes ring down over time. Finally, the dominant eigenmode shapes corresponding to the tip (27 GHz) and face (38 GHz) optomechanical modes were isolated using a FEM model. These dynamic nanoparticle shapes were then imported into the EM model to examine how the subtle change in shape modulated the dispersion diagram and specifically the SLRs of the nanocube array. These results show that the dynamic nature of the nanoparticles can play a role in applications of SLRs (e.g., nanolasing, light collection, *etc.*) and suggests new applications that leverage the ability of the SLR to shift and modulate in energy to create new functions.

Effect of Ag Nanocube Optomechanical Modes on Plasmonic Surface Lattice Resonances

Mindaugas Juodėnas,* Domantas Peckus, Tomas Tamulevičius, Yusuke Yamauchi, Sigita Tamulevičius, and Joel Henzie*

Cite This: *ACS Photonics* 2020, 7, 3130–3140

Read Online

ACCESS |

Metrics & More

Article Recommendations

Supporting Information

ABSTRACT: Noble metal nanoparticles patterned in ordered arrays can interact and generate hybrid plasmonic–photonic resonances called surface lattice resonances (SLRs). Dispersion curves help explain how the Bragg coupling conditions and radiation patterns create dipolar and quadrupolar SLRs, but they assume that the nanoparticles are static structures, which is inaccurate at ultrafast time scales. In this article, we examine how local surface plasmon resonances (LSPRs) supported by cubic Ag nanocrystals are modulated by ultrafast photophysical processes that generate optomechanical modes. We use transient absorbance spectroscopy measurements to demonstrate how the LSPRs of the nanoparticles modulate the SLR of the array over time. Two primary mechanical breathing modes of Ag nanocubes were identified in the data and input into electromagnetic models to examine how fluctuations in shape affect the dispersion diagram. Our observations demonstrate the impact of optomechanical processes on the photonic length scale, which should be considered in the design of SLR-based devices.

KEYWORDS: plasmonics, optomechanics, photoacoustics, self-assembly, surface lattice resonances, lattice plasmons



Decades ago theorists predicted that arrays of plasmonic nanostructures could interact collectively and generate hybrid plasmonic–photonic resonances far narrower than is possible with single nanoparticles.^{1–4} In these systems, the local surface plasmon resonances (LSPRs)⁵ of each particle couple with their neighbors via in-plane diffracted waves called Rayleigh anomalies (RAs). The resulting spectral peaks have quality factors (Q -factors, $Q = \lambda/\Delta\lambda$) an order of magnitude larger than single particles. Over time, experimentalists developed nanofabrication and optical measurement tools to observe and study these plasmonic–photonic modes.^{6–12} This phenomenon is now commonly called a plasmonic surface lattice resonance (SLR) or a lattice plasmon.^{6,13,14} Researchers can now engineer surfaces supporting SLRs with wide tunability and narrow spectral line width for use in novel light-emitting and light-manipulating devices.^{15–19}

Transient absorption spectroscopy (TAS) has enabled researchers to better understand the dynamics of individual or isolated metal nanoparticles following the absorption of photons.^{20–25} The ensuing cascade of photophysical processes underpins many of the applications of plasmonic nanostructures, but very little is known about the dynamics of highly ordered plasmonic arrays and how the ultrafast optical response of its nanoparticle constituents affect the hybrid long-range plasmonic–photonic modes of the array. At the individual nanoparticle level, the absorbed energy is transferred

from the plasmon to electronic transitions and then to phonons; these phonons raise the lattice temperature and expand the lattice coordinate. Coherent optomechanical modes in metal nanoparticles can be excited when the laser pump pulse is shorter than the vibrational mode period of the particle. Ag nanoparticles with diameters >10 nm have vibrational modes at picosecond time scales.²⁶ The resulting ultrafast change in shape, electron density, and deformation potential modulates the intensity and wavelength of the nanoparticle LSPR at gigahertz frequencies.^{25,27}

Figure 1 illustrates the length scales of the LSPR and SLR modes (x -axis), in addition to the time scales (y -axis) of their decay processes, following the absorption of a photon and generation of optomechanical modes. The optomechanical modes of individual Ag nanocubes have been studied in detail.^{20,21,25,28} In brief, after a nanocube absorbs a photon, it expands and then evolves into a sum of its breathing eigenmodes. Ag nanocubes have two dominant breathing modes associated with its tips and faces.^{25,27} The tip and face

Received: July 28, 2020

Published: October 20, 2020



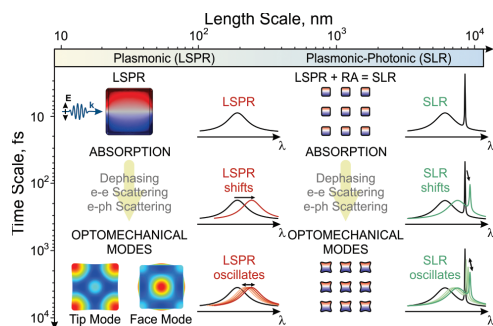


Figure 1. Overview of the relevant length scales and time scales described in this article. The illustration describes the processes following the excitation of individual nanoparticles (left) and nanoparticles in arrays (right) as the absorbed energy decays into optomechanical modes over time. The spectra show how a typical LSPR or SLR changes in the TAS spectrum.

modes have different frequencies and modulate the LSPR over time.²⁵ In the absorption spectrum of a typical dipole LSPR (“D-LSPR”) (Figure 1, left), these processes cause the LSPR to shift and then oscillate as the breathing modes dissipate energy into the environment. Nanoparticles can also generate quadrupolar LSPRs (“Q-LSPRs”), which have longer dephasing times,²⁹ but should dissipate energy via the same process. Overall, TAS studies have demonstrated that plasmonic nanoparticles are not the static structures that appear in most computational electromagnetic models; they have a dynamic shape that affects the LSPR.²⁷

Individual nanoparticles patterned into arrays with spacings on the order of the wavelength of light can couple with each other via RAs to form ultranarrow SLRs (Figure 1, right). SLRs can be composed of dipoles (“D-SLRs”) or quadrupoles (“Q-SLRs”) depending on the spectral overlap of the LSPR mode with RAs supported by the array. A SLR is strongly dependent on nanoparticle size/shape and its corresponding LSPR,³⁰ thus, we hypothesized that the optomechanical modes would also affect the time-dependent plasmonic–photonic properties. This phenomenon would be observed as an oscillation in the SLR at picosecond time scales. Other researchers have noted that the propagation of optomechanical modes on textured metal films is affected by lattice spacing,³¹ and researchers in the field of Si-based optomechanical photonic crystals³² have experimented with structures that support photonic/plasmonic bandgaps.³³ But the latter studies rely on high refractive index (n) dielectrics as opposed to a system that is mainly plasmonic and enables strong light–matter interactions at visible wavelengths.

In this article, we examine how dynamics on the ultrafast time scale affect optical properties that manifest on the photonic length scale. We initially compare the steady-state optical properties of free-standing, disordered colloidal Ag nanocubes suspended in solution versus the same Ag nanocubes assembled into 2D arrays that are designed to generate SLRs. The dispersion diagrams of nanoparticle arrays with various spacings were measured in an angle-dependent optical spectroscopy setup and compared to electromagnetic (EM) models generated with the finite element method (FEM). Both D-SLRs and Q-SLRs emerged from our

experimental and computational dispersion diagrams. Ultrafast TAS spectroscopy was then used to measure the arrays excited at normal incidence and at 30° incidence with polarized light to examine how the in-plane versus out-of-plane SLRs evolve as the optomechanical modes ring down over time. The frequencies of the optomechanical modes were similar in colloidal solution versus in arrays because of a similar acoustic impedance of the environments. A FEM model was used to identify the dominant breathing eigenmode shapes by their frequencies: a tip mode at 27 GHz and face mode at 38 GHz. These dynamic nanoparticle shapes were then imported into the EM model to examine how the subtle change in shape modulated the dispersion diagram and affected the SLRs of the nanocube array.

RESULTS AND DISCUSSION

Self-Assembly of Ag Nanocube Arrays. Researchers have used a variety of methods to generate arrays of single nanocrystals.^{34–36} We used the capillary-force assisted particle assembly (CAPA)³⁷ technique, with PDMS patterns consisting of a square array of pits with 300, 350, and 400 nm spacings (center-to-center). PDMS templates were not preconditioned prior to assembly experiments. The assembled nanocubes have no adhesion layer and are sitting directly in circular pits patterned on a PDMS surface. The patterns were filled with monodisperse Ag nanocubes (edge length $a = 77 \text{ nm} \pm 3 \text{ nm}$), which were generated using a variation of the polyol method.³⁸ Details of the CAPA method, fabrication of PDMS patterns, and synthesis of Ag nanocubes are described in more detail in **Methods**. The nanocubes are coated with a thin surfactant layer of 55000 molecular weight (MW) polyvinylpyrrolidone (PVP). CAPA experiments were performed using a dense solution of colloidal Ag nanocubes ($3.59 \times 10^{11} \text{ p/mL}$) in dimethylformamide (DMF) because it is a good solvent for the PVP polymer and prevents irreversible interactions between Ag nanoparticles, enabling them to behave like hard particles.^{39,40} DMF also has nearly identical n value as PDMS at visible wavelengths. Steady-state and TAS optical measurements on the colloidal Ag nanocube solutions were also performed in DMF ($0.28 \times 10^{11} \text{ p/mL}$). Particle concentrations were estimated using inductively coupled plasma atomic emission spectroscopy (ICP-AES). Further information can be found in previous papers^{41,42} and in **Methods**.

Figure 2A shows a real photograph of CAPA assembly in progress on a $15 \times 15 \text{ mm}^2$ array. Dark-field optical micrographs of these assemblies are shown in Figure 2B. A SEM image is shown in the close-up in Figure 2C. These images indicate a high assembly yield, which we estimate to be >99% in a $>1 \text{ cm}^2$ area (estimated from a randomly selected $40 \times 40 \mu\text{m}^2$ area with $n = 10000$ events). The selected nanoparticle patterns could be left exposed to air to generate an asymmetric dielectric environment or fully encapsulated by polymerizing an additional layer of PDMS following deposition to create a uniform dielectric environment. We mainly focused on the asymmetric patterns with nanoparticles exposed to the environment because this configuration may be advantageous for sensing applications as it leaves the superstrate open for the introduction of different analytes.

UV–Vis Measurements of Colloidal Ag Nanocubes in Solution versus Ordered Arrays. Figure 3A shows the absorbance spectrum of a solution of colloidal Ag nanocubes ($a = 77 \text{ nm}$) suspended in DMF. Free-standing Ag nanocubes support numerous bright and dark plasmon modes.^{43–45} We

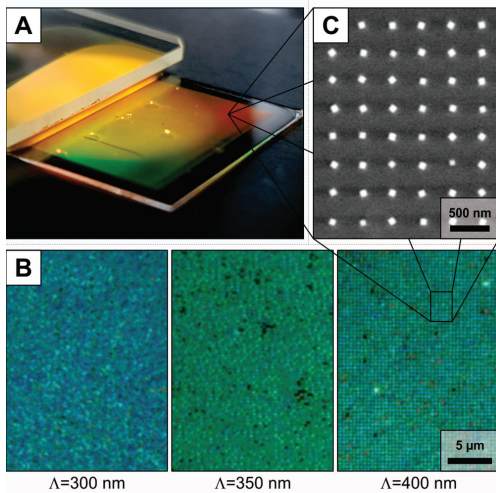


Figure 2. Nanoparticle self-assembly. (A) Photograph of the CAPA assembly process drawing a nanoparticle ink across a $15 \times 15 \text{ mm}^2$ template. (B) Dark-field optical micrographs (100 \times , NA = 0.9) of nanocube arrays with 300, 350, and 400 nm spacings. (C) SEM micrograph of a self-assembled nanocube lattice.

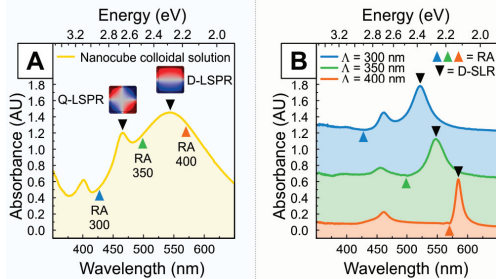


Figure 3. Optical properties of nanocubes in solution vs in arrays. (A) Steady-state UV-vis spectrum of a colloidal solution of Ag nanocubes ($a = 77 \text{ nm}$). The location of the D-LSPR and Q-LSPR peaks and RAs are labeled on the spectrum. (B) Steady-state UV-vis spectrum of nanocube arrays with spacings of 300, 350, and 400 nm excited at normal incidence. The spectra are offset for clarity. The SLRs and RA wavelengths at normal incidence (Γ points) of each lattice spacing are marked with triangles.

calculated the charge distribution plots of the D-LSPR and Q-LSPR of the nanocubes and labeled their location in Figure 3A. The RAs are also labeled in the graph to show where they would overlap with the LSPRs. Arrays containing the same cubes were assembled, and their transmission properties were measured at normal incidence with a collimated incandescent light source and a 6 mm diameter lens fiber coupled to a spectrometer (Figure 3B). The RA wavelengths at normal incidence for square gratings in PDMS are $\lambda_{\text{RA}} = \Lambda \times n$. Thus, for $\Lambda = 300, 350,$ and 400 nm square gratings in PDMS ($n = 1.425$), λ_{RA} is 428, 499, and 570 nm (marked with colored triangles). Their corresponding SLRs are located at wave-

lengths of 522, 549, and 585 nm (marked with black triangles in Figure 3B). The wavelengths are expressed in both nanometers and electron volts (eV) to help the reader identify these resonances in the dispersion diagrams later in this article.

The relative spectral position between the RA and LSPR resonance is the most critical factor for SLR coupling.^{3,4,8} Of all the arrays described here, only the 400 nm lattice RA is on the red side of the single nanoparticle D-LSPR at normal incidence, giving a narrow dipolar SLR (D-SLR) peak ($Q = \lambda / \Delta\lambda \approx 48$). The other two arrays have similar line widths ($Q \approx 18$ and $Q \approx 14$ for 350 and 300 nm lattices, respectively) at different spectral positions, which is associated with the relative positions of their respective RAs. Neither of the normal incidence RAs match the wavelength of the narrow Q-LSPR peak at $\sim 460 \text{ nm}$. Therefore, the quadrupolar SLR (Q-SLR) can only be observed with off-normal excitation because it affects the spectral position of the RA according to the energy dispersion relation: $E = \frac{\hbar c}{n} \left| \vec{G} + k_{\parallel} \right|$, where n is the refractive

index of the medium, \vec{G} is the reciprocal lattice vector, and k_{\parallel} is the in-plane projection of the wavevector. The PDMS- and air-propagating RAs are shown in Figure 4A.

Dispersion Diagrams of Nanocube Arrays and the Relevance of Single-Nanocube Radiation Patterns. The energy dispersion diagrams for each array were collected from 0–90° incidence with TM and TE polarization in transmission mode (Figure 4B–D). The calculated RA lines are overlaid on top. In between each dispersion diagram is a greyscale bar representing the UV-vis absorption spectrum of the free-standing Ag nanocubes suspended in solution for reference in order to compare the location of the LSPRs with the SLRs. To eliminate redundancy and allow a better comparison between the three cases (i.e., the in-plane k -vector range $-\pi/\Lambda$ to π/Λ). These results clearly show the dependence of coupling on the in-plane polarization of the nanoparticle arrays, which we previously described using a hexagonal lattice of Ag nanoparticles.⁴² When the nanocube is excited with TM-polarized light, its radiation pattern couples most strongly to the $(0, \pm 1)$ modes. TE-polarized nanoparticles couple most strongly to the $(\pm 1, 0)$ modes. This is easily observed in the dispersion diagram of the $\Lambda = 400 \text{ nm}$ (Figure 4B) lattice because its RA is on the red side of the nanocube D-LSPR; hence, the peak is very narrow. The TM case shows a parabolic SLR following the $(0, \pm 1)$ modes, whereas the TE case has a strongly red-shifting SLR peak following the $(\pm 1, 0)$ modes. This coupling preference persists in all nanoparticle array samples examined in this article.

When the arrays are excited with TM-polarized light at larger angles of incidence, the electric field vector becomes increasingly polarized perpendicular to the plane of the array. These conditions enable out-of-plane SLRs that have been observed by us⁴² and other research groups.^{12,46–50} In out-of-plane excitation, the radiation pattern of a dipole lies in the array plane, enabling coupling to any of the modes. It manifests in the experiment as coupling to unexpected directions, such as coupling to $(\pm 1, 0)$ modes using TM polarization. Out-of-plane resonances are challenging to observe experimentally because the nanoparticle patterns are typically designed to achieve the narrowest SLR peaks at normal incidence; the RA is usually designated further to the red-side of particle LSPR, but the RA shifts quickly as the angle of incidence is changed,

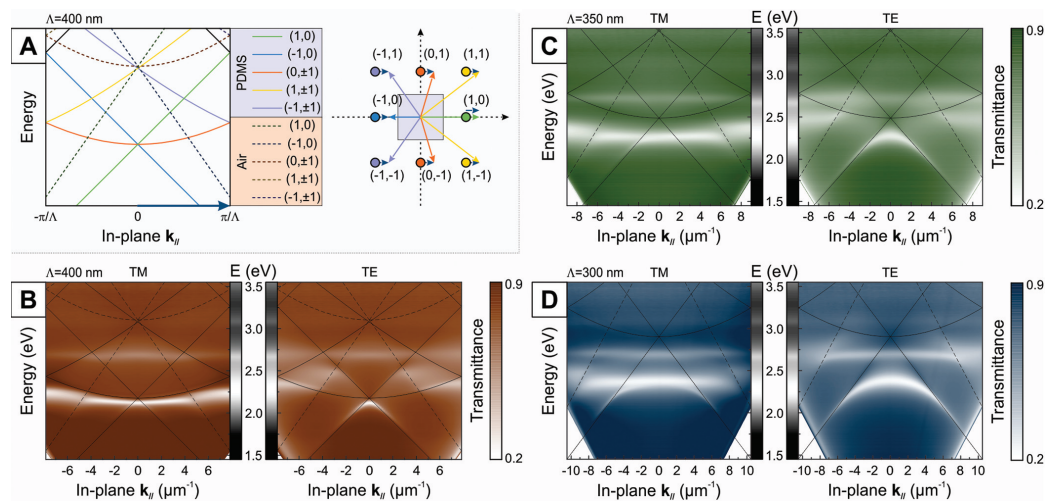


Figure 4. Energy dispersion diagrams of the self-assembled nanocube arrays. (A) Energy dispersion structure of a square lattice; diffraction orders propagating in two interfacing media are plotted: PDMS $n = 1.425$ and air $n = 1$. A reciprocal lattice diagram shows the modification of lattice vectors because of additional in-plane light momentum provided by off-normal excitation; (B–D) Steady-state E - k dispersion diagrams of nanocube arrays with 400 (B), 350 (C), and 300 nm (D) spacings. The E - k diagrams were collected in transmission mode using a collimated white light that is TM- or TE-polarized. The calculated RA lines are overlaid on top. The vertical greyscale bars represent the transmission spectrum of colloidal Ag nanocubes in solution (see Figure 3A).

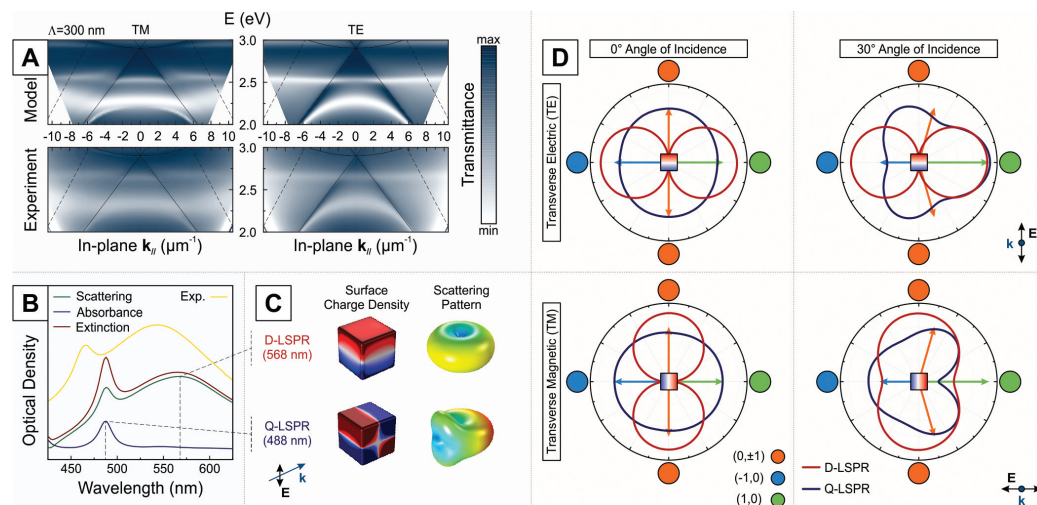


Figure 5. FEM modeled nanocubes and their arrays. (A) Simulated (top) and experimental (bottom) energy dispersion diagrams of a 300 nm spaced nanocube lattice in a homogeneous slab of PDMS. Transmittance is normalized (actual value ranges are 0.015–0.98 in the model and 0.15–0.625 in the experiment). (B) Experimental and simulated absorption spectra of the nanocube colloid solution. (C) Respective surface charge density and radiation pattern surfaces. (D) Polar plots of in-plane radiation patterns generated by the Q-LSPR and D-LSPR modes at normal incidence and at 30° incidence.

and large angles required to polarize nanoparticles out-of-plane causes the RA to red-shift too far away from the single-particle LSPR. Thus, coupling is weak, but the SLR retains its narrow line width. This phenomenon is evident in the TM polarized excitation of the $\Lambda = 400$ nm (Figure 4B) and 350 nm spaced

arrays (Figure 4C). There are sharp features following the $(\pm 1, 0)$ PDMS-propagating modes (marked as solid green and blue lines in Figure 4A). However, they quickly fade because the RA red-shifts too far away from the single-particle LSPR. Strong out-of-plane coupling extends further in the 300 nm (Figure

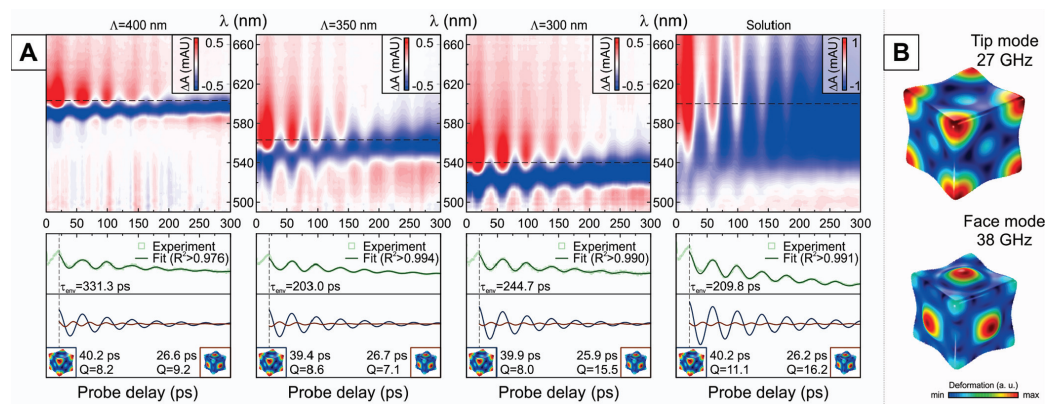


Figure 6. Transient absorption measurements of arrays exhibit the signature of fundamental optomechanical modes of single nanocubes. (A) Transient absorption spectroscopy carpets were collected on arrays with spacings $\Lambda = 400, 350,$ and 300 nm at normal probe incidence and compared to a colloidal solution containing the same nanocubes. The horizontal dashed lines indicate the traces used to fit the optomechanical modes ($\lambda_{\text{probe}} = 603, 563, 540,$ and 601 nm for each respective case, left to right). The traces were fit using a sum of a decaying exponent and two damped cosines starting from $t = 21$ ps to eliminate the uncertainties introduced by a mixed contribution to the TAS signal from e-ph equilibration and crystal lattice expansion. (B) The two dominant eigenshapes were modeled with FEM: tip mode (27 GHz) and face mode (38 GHz).

4D) spaced lattice ($Q \approx 78$ at $\theta = 35^\circ$) because the RAs still intersect the single-particle LSPR at oblique angles of incidence, allowing the nanoparticles to be polarized normal to the surface. These types of SLRs are particularly interesting because their EM field is concentrated out-of-plane instead of in-plane, which may enable extreme sensitivity to changes in the dielectric environment.

The Q-LSPR peak, observed in all dispersion diagrams at ~ 2.65 eV, remained relatively constant and independent of array spacing. The colloidal solution spectrum in Figure 3A shows that the Q-LSPR and D-LSPR should be similar in intensity, whereas the latter is invisible in the arrays. The number of particles probed in solution (5.42×10^8 nanoparticles) versus in the arrays ($1.23 \times 10^8, 1.6 \times 10^8,$ and 2.18×10^8 nanoparticles for 400, 350, and 300 nm patterns, respectively) is on the same order of magnitude. So we attribute this feature to the combined effects of phase retardation and substrate-induced quadrupole-dipole hybridization.^{44,51}

The Q-SLR could be observed at larger angles and appears in TE illumination in the 300 nm spaced arrays (Figure 4D). Interestingly, it is formed next to the air-RA ($\pm 1, 0$) at $k \approx 8 \mu\text{m}^{-1}$ instead of the PDMS-RA ($\pm 1, 0$) at $k \approx 2 \mu\text{m}^{-1}$ (marked with solid and dashed lines in Figure 4A, respectively). This behavior can be explained by extending the plasmon hybridization theory for single nanocubes on surfaces to SLRs.⁴⁴ The nanocube array is partially exposed to air, so there are two RAs available in this asymmetric dielectric environment—one propagating above the array in air, and one propagating in PDMS below. The D-LSPR EM intensity is expected to be localized in the larger n medium and thus interacts strongly with the PDMS-RA. The dispersion diagrams in Figure 4 illustrate this point because the strong dipolar SLR peaks are close to the PDMS-RAs. In contrast, substrate-induced hybridization causes the Q-LSPR mode to shift primarily into the air superstrate⁴⁴ and interact with the air-RA.

We performed EM modeling using FEM with a single nanocube, and nanocubes in $\Lambda = 300$ nm spaced square arrays. The arrays were suspended in a homogeneous dielectric environment ($n = 1.43$) to simplify the calculations. To make a direct comparison, we also prepared a nanocube array sample fully encapsulated in PDMS (Figure 5A). The modeled $E-k$ dispersion maps match the experiment almost perfectly. However, there is a slight red-shift in the modeled peaks due to the unavoidable mismatch between nanoscale features and bulk-derived optical constants. The red-shift is also observed in the single-nanocube model (Figure 5B). As expected, the features previously attributed to air-RAs have disappeared in uniform n , and the D-SLRs remain mostly unchanged compared to air-exposed samples in Figure 4D because the PDMS-RAs dominate the D-SLRs in both cases.

Interestingly, the Q-SLR coupling has shifted from TE to TM polarization in both the simulation and experiment. We use the radiation patterns of the D-LSPR and Q-LSPR modes to help explain this observation. The radiation pattern of the nanocube D-LSPR mode has a characteristic torus shape that allows it to best couple to RAs that match the radiation direction (Figure 5C,D). As a result of the symmetry of the D-LSPR in TE excitation, coupling preference does not change with the angle of incidence. In the TM case, the toroidal radiation pattern progressively rotates with the angle of incidence, allowing out-of-plane coupling described earlier. Figure 5D shows cross sections of the radiation patterns when the angle of incidence is normal (left) and 30° (right). The radiation pattern of the nanocube in the lattice will be different due to fields generated by neighboring particles, but the coupling rules are similar. The radiation pattern of the Q-LSPR is different; it has a fishtail-like shape in the backscattering direction, which shifts the radiation pattern node away from the center of the particle. Thus, the radiation pattern cross-section in the plane of the array is an ellipse at normal incidence, which means that the quadrupole radiates in-plane in all directions, enabling it to couple to any RA. But the

quadrupolar peak is very narrow and thus extremely sensitive to lattice spacing. Predicting the correct lattice spacing with imperfect optical constants is challenging; thus, we did not observe Q-SLR at normal incidence in the arrays tested, but it should be possible. Figure 5D also shows the profile of the Q-LSPR radiation pattern at a 30° angle. In TE excitation, scattering is strongest in the (1, 0) direction. However, this direction corresponds to an RA with energy that increases with the angle of incidence, and the quadrupole is already smaller in energy than the RA, so coupling is not possible in TE excitation. In TM excitation, there is stronger radiation in the (-1, 0) direction, which corresponds to an RA with decreasing energy, allowing it to intersect with the quadrupolar LSPR and couple into the Q-SLR at high angles of incidence. The reason for the switch of the Q-SLR from TE to TM is not completely clear; we speculate that the radiation pattern of Q-LSPR in an asymmetric environment might be modified in a way that reverses the coupling priority observed in a homogeneous environment.

TAS Measurements of Colloidal Ag Nanocubes in Solution versus in Ordered Arrays. Figure 6A shows TAS plots with ΔA modulations that are characteristic of optomechanical modes supported by plasmonic nanoparticles. We measured all array samples ($\Lambda = 400, 350,$ and 300 nm) in addition to colloidal Ag nanocubes suspended in DMF (i.e., “Solution”). There have been efforts to examine the collective mechanical modes of small clusters of Au nanoparticles,⁵² nanowire arrays composed of indium tin oxide (ITO),⁵³ and various nanoparticle arrays.^{54,55} In particular, the experiments on Au clusters show that near-field coupling can enable the hybridization of vibrational modes of closely spaced nanoparticles.⁵² The work on ITO nanowires shows how vibrational modes can modulate transmittance over time. To our knowledge, there are no previous experiments explaining how optomechanical modes affect plasmonic SLRs at ultrafast frequencies.

Cubes are known to support two vibrational breathing modes that dominate its mechanical response.^{25,27} The strongest mode results from a deformation of the eight corners of the cube. We call this the “Tip Mode” and it is known to strongly affect the position and intensity of the LSPR. The second mode is a higher-frequency overtone resulting from the deformation of the six faces of the cube. We call this the “Face Mode” and note that it has a smaller effect on the LSPR. An eigenmode analysis was performed on a single Ag nanocube suspended in a vacuum with FEM. A menagerie of these eigenmodes is shown in Supporting Information, Figure S1. The two most dominant breathing modes were selected based on fitting results and plotted in Figure 6B. To understand the impact of each vibrational mode on TAS data, we selected TAS traces with the highest signal amplitude and plotted in the bottom row of Figure 6A. Each trace was analyzed using a machine learning (ML) algorithm (Eureqa) by fitting it with a decaying exponential ($e^{-t/\tau_{\text{env}}}$; τ_{env} is the decay constant) and two damped cosine functions.²⁵ The fit was initiated at $t = 21$ ps to minimize the contribution of e-ph equilibration and focus on lattice expansion/contraction. In the ML code, the face mode was constrained to be smaller in amplitude than the tip mode. In addition, frequencies were selected to best match those acquired after performing a fast Fourier transform (FFT) on the data (Supporting Information, Figure S2). The ML code was allowed to run until it achieved a high goodness-of-fit ($R^2 > 0.97$). The optomechanical mode-defining parameters

are given in Supporting Information, Table S1. The mechanical quality factors for each mode is expressed as $Q = \frac{\pi}{T}$, where τ and T are the decay constant and the period of the damped cosine function in $e^{-t/\tau} \cdot \cos\left(\frac{2\pi t}{T} - \varphi\right)$. These equations are used to compare how each array affects the damping of optomechanical modes.

The mechanical Q -factors of nanoparticles depend on their materials and dimensions, in addition to the acoustic impedances of the surrounding media.⁵⁶ Previously, Hartland et al. measured individual Ag nanocubes cast with poly(vinyl alcohol) on glass substrates and observed Q -factors from 14 to 25.²⁸ Damping of the Q -factor of metal nanostructures is highly dependent on the orientation of the particle and its interaction with a solid substrate. Since our nanoparticles are randomly oriented in the circular pits and exposed to the air-PDMS interface, we expect larger inhomogeneous broadening that will lead to some decrease in Q -factor.

In the colloidal solution, the D-LSPR of the nanocubes is very broad due to the intrinsic radiative damping of bright plasmon modes. The Q -factors of the tip and face modes were 11.1 and 16.2, respectively, at $\lambda_{\text{probe}} = 601$ nm. Interestingly, the Q -factor should be larger in ethanol,²¹ because ethanol has a smaller acoustic impedance (0.9 MPa-s/m) than DMF (1.37 MPa-s/m). But DMF is a much better solvent for PVP polymer (1.2 MPa-s/m). Swelling the PVP surfactant with DMF may lead to a smaller average acoustic impedance resulting in the larger observed Q -factor. The Q -factors of the optomechanical modes in arrays excited at normal incidence (0°) are smaller than the colloidal solution measurements ($Q \approx 8$ for the tip mode and $Q \approx 7$ –15 for face mode). A few points are worth noting are as follows: (i) The tip mode has a near-constant Q -factor in all array samples; (ii) The face mode varies between samples and becomes strongest in the $\Lambda = 300$ nm pattern.

Influence of Optomechanical Modes on SLRs. The SLR depends on the RA and LSPR in a nanoparticle array. The position of the RA is fixed in our experiment. Thus, any change in the LSPR will affect coupling to the RA and modify the SLR peak. The effect of chemically deforming Ag nanocubes on the LSPR has been studied by colloidal chemists and serves here as a useful guide.⁵⁷ They show that the LSPR progressively redshifts as the faces become concave and tips extend away from the body center of the cube. Conversely, Ag nanocubes with rounded edges and tips have blue-shifted LSPRs. To understand how dynamic mechanical deformation of the nanocube affects the SLR, we used TAS to measure the $\Lambda = 300$ nm array using a pump/probe incidence angle of 30° with TE and TM excitation (Figure 7). At 30° incidence, TM polarization produces two peaks, one in-plane and one out-of-plane; we will consider the former and compare it to TE-generated in-plane coupling. The EM intensity plots in Figure 7 demonstrate the characteristic in-plane and out-of-plane intensity distribution, and the out-of-plane mode generates stronger fields. Regarding optomechanical modes, the tip mode maintained the same Q -factor in both in-plane and out-of-plane coupling and matched previous experiments at 0° incidence ($Q \approx 9$). Interestingly, the face mode Q -factor was larger in the in-plane case ($Q \approx 12$). The larger Q in-plane could be a consequence of increased elastic environment homogeneity in the plane of the array versus out of plane, because the latter has one facet strongly adsorbed to the polymer surface.

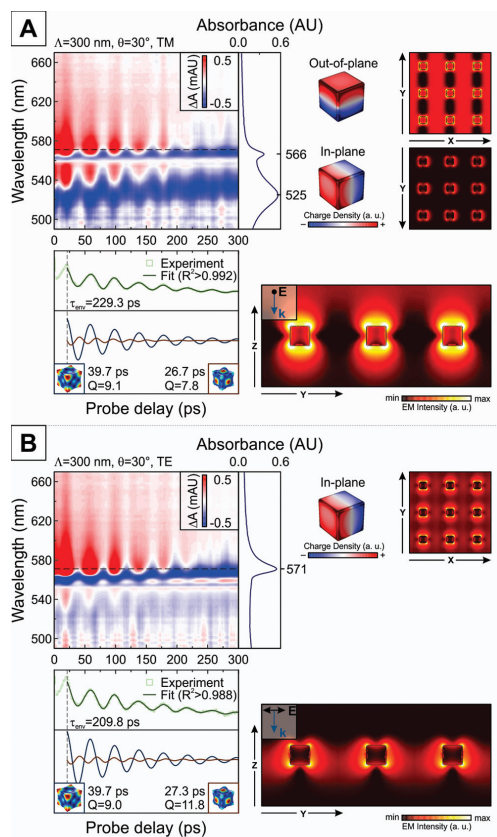


Figure 7. Transient absorption measurements at an angle. Transient absorption data taken from 300 nm spaced nanocube arrays at 30° probe angle of incidence and two polarizations: (A) TM and (B) TE. Traces used for fitting are marked with a horizontal dashed line ($\lambda_{\text{probe}} = 571$ nm). The absorption spectra next to the 2D maps are steady-state measurements taken at the same angle of incidence. Surface charge density maps of the nanocubes are presented next to the respective absorption peaks, and the electric field time average is plotted in the XY and YZ planes of the nanoparticle array.

A finite element study in the frequency domain was performed on a $\Lambda = 300$ nm square array with the tip and face mode eigenshapes to study how the SLR was affected by them over time. Initially, we performed a frequency sweep of a nanocube (a displacement relation of characteristic points on a nanocube can be found in Supporting Information, Figure S3). As predicted by the eigenmode analysis, the edge mode and face mode are very close in frequency, becoming convoluted when isotropic damping is used, yielding a combined shape at the face mode frequency.^{25,27} Therefore, to produce pure tip and face mode shapes, we used the frequencies of dominant eigenmodes with Rayleigh damping, which damps all but two predefined frequencies. The initial strain was selected to yield a deformation of 3 nm to observe clear shapes. A comparison to the TAS signal generated by a 1 nm maximum amplitude can be found in Supporting Information, Figure S4, which shows

that the general shape of the TAS curves remains the same. We select the phase of both modes with the tips of the nanocubes extended outward (the shapes at π -shifted phases can be found in Supporting Information, Figure S5). Each array was modeled using an incident excitation from 0–30° and then subtracted from the E - k diagram acquired from a lattice of Ag nanocubes with the original undistorted cubic shape (Figure 8A).

The dispersion diagrams in Figure 8A are strongly affected by the deformed shapes that represent the optomechanical modes. Both modes cause a red-shift in the spectrum. We only consider the influence of shape on LSPR, but changes in electron density and interband transitions will also play a role but to a lesser extent in cubes.²⁷ The tip mode dominates the overall change of the optical response, which is demonstrated by the amplitude and distance between the positive and negative ΔA peaks. The D-SLRs of both tip and face modes generate similar patterns in both TE and TM excitation, including the out-of-plane mode. The Q-SLR available in TM excitation is most strongly affected, + ΔA contributions from the tip and face mode almost do not overlap in energy. This strong contrast difference between the Q-SLRs of the tip and face modes could be caused by the Fano line shape of quadrupolar modes,⁴⁴ which is very sensitive to changes in the shape of the corners and edges of nanocubes.⁵⁸

The simulated ΔA spectra from 0° and 30° (TM/TE) illumination schemes were compared to the $\Lambda = 300$ nm arrays in the experiments (Figure 8B). We focus on the D-SLR here because its features are well within the bandwidth of the probe in our experimental TAS setup. Under normal excitation, both arrays cause the SLR to red-shift versus the undeformed nanocube array, matching the shape and general shift in the experiment. The experimental trace also features a slightly asymmetric line shape, indicating a broadening of the SLR peak. TE and TM excitation generated slightly smaller red-shifting of the SLR in the simulated arrays. Probing at an angle and especially at the sharpest out-of-plane mode wavelength enables us to exploit the narrow line shape of the SLR, even though the shift is smaller, the amplitude of the signal is larger than normal excitation because very small changes of a sharp feature can generate strong differences in the TAS signal. Overall, the simulations have an excellent qualitative match with the experiments, even with the large deformation of the simulated eigenmodes. These results indicate that the dynamic shape of the nanoparticle may also be considered when designing SLR-employing devices for ultrafast applications such as lasers.⁵⁹ For example, SLRs could be designed with strong ΔA that modulates the intensity and position of the SLR. If the modulation generates strong enough ΔA it may enable pulsed light emission at gigahertz frequencies in an appropriate gain medium.

CONCLUSIONS

Previous work on SLRs has focused on the fundamental interaction between LSPRs and RAs in Bragg scattering conditions. Our work shows how absorption can modify the LSPR and alter the dynamic optical properties of the SLR over time. First, we investigated steady-state optics of nanocube arrays and explained how LSPRs interact via RAs and form in-plane and out-of-plane D-SLRs and Q-SLRs. Later we compared the optomechanical properties of free-standing Ag nanocubes suspended in solution vs nanocubes in arrays under Bragg coupling conditions. The arrays generate similar

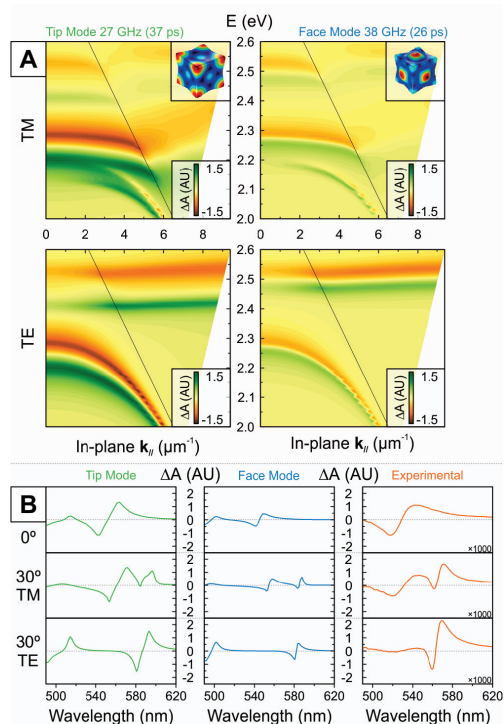


Figure 8. Influence of the isolated eigenmodes on the $E-k$ diagrams. (A) Absorbance difference maps on $E-k$ diagrams, showing the individual contribution of the two primary modes to the TAS signal. The calculated RA is overlaid on top; (B) Absorbance difference traces generated by tip mode (left), face mode (middle), and experimental measurement (right, multiplied by a factor of 1000 for clarity) at normal (top) and 30° incidence with TM/TE polarizations (bottom).

mechanical quality factors even though their viscoelastic environment is anisotropic. TAS measurements at high angles revealed that the in-plane mode couples more effectively to the mechanical modes compared to out-of-plane mode, but the latter has the advantage of narrower spectral line width. A full eigenmode analysis of the mechanical modes of cubes was performed to determine the shapes of the two dominant eigenmodes. These two eigenshapes were imported into our electromagnetic model to show how deformation affects the dispersion diagram of the nanocube array. The dynamic shape of the nanocube affects the SLR over time and matches our experimental TAS data showing the contribution of each optomechanical mode. This work shows how local vibrational modes can shift and modulate photonic/plasmonic modes at ultrafast time scales. This phenomenon may impact applications such as nanolasing and light collection and perhaps be used to create new functions.

METHODS

Nanoparticle Synthesis/Characterization. The particles are synthesized using a variation of the Ag polyol method.³⁸

The average edge length (a) of the ensemble of cuboctahedra was measured using a JEOL-1010 TEM operating at 100 kV with a minimum magnification of <0.5 nm/pixel. A total of 200 nanoparticles were measured, and the average size was $a = 77 \pm 3$ nm. The particles were suspended in DMF at a concentration of 3.59×10^{11} p/mL, as determined by inductively coupled plasma atomic emission spectrometry. The Ag nanocubes are coated with a layer of polyvinylpyrrolidone (PVP; 55000 MW) polymer surfactant. The PVP serves as a steric barrier to minimize uncontrolled aggregation even at high nanoparticle concentrations.^{39,40}

Capillary Force Assisted Assembly (CAPA). The master stamps (Si) featuring pillars for template preparation were fabricated using e-beam lithography, Al lift-off, and reactive ion etching using $\text{SF}_6/\text{C}_4\text{F}_8$ plasma. These stamps were coated with a self-assembled monolayer of perfluorooctyltrichlorosilane as an antiadhesion layer. Soft lithography was employed to create polymer templates by casting and thermally curing polydimethylsiloxane. The resulting patterned substrates were used in a custom capillary force assisted assembly setup.⁴¹

During the deposition process, a temperature-controlled stage translates the vacuum chucked sample relative to a stationary microscope glass slide. A droplet of colloidal nanocubes suspended in DMF is confined between the substrate and the glass slide. The recirculation currents because of the movement and evaporation flow bring nanoparticles from the bulk of solution close to the meniscus, where nanoparticles accumulate and eventually deposit into pits defined by the master stamp. The nanoparticle assemblies are investigated using optical darkfield and scanning electron microscopy as well as a custom free-space UV-vis angular spectrophotometry setup.⁶⁰

Transient Absorption Measurements. Ultrafast relaxation processes in Ag nanocubes (both in solution and regular 2-D structures) were investigated by means of transient absorption spectroscopy (TAS). HARPIA spectrometer built by Light Conversion was used for TAS measurements. The samples were excited using a Pharos ultrafast Yb:KGW laser (Light Conversion) with a regenerative amplifier at a 66.7 kHz repetition rate and 290 fs duration pulses at 1030 nm wavelength. The pump beam wavelength was tuned with a collinear optical parametric generator Orpheus and harmonic generator Lyra (Light Conversion) to 350 nm and an energy density of $40 \mu\text{J}/\text{cm}^2$. The samples were probed with a white light supercontinuum generated using a 2 mm thickness sapphire plate excited with a fundamental laser wavelength. The spectral range of the supercontinuum probe as well as the detection range of the TAS dynamics spanned wavelengths from 489 to 793 nm. The excitation beam was focused down to a $\sim 700 \mu\text{m}$ diameter spot. The supercontinuum probe was $\sim 500 \mu\text{m}$ in diameter. The steady-state absorption of samples was rechecked after each measurement to ensure there was no damage from the laser irradiation.

Modeling. Finite element modeling was performed using COMSOL Multiphysics suite. The Structural Mechanics Module was employed for the mechanical response of the nanoparticle. Eigenmode analysis and the frequency response was modeled using the geometry of the synthesized nanoparticles and mechanical material properties provided by the integrated material library. Optical modeling was done using the RF Module. For single-particle modeling, a nanoparticle was placed in a uniform dielectric environment, surrounded by a perfectly matched layer, and the background field was designed as a plane wave. The far-field border layer was

designated as the surface between the physical dielectric domain and the perfectly matched layer. The optical constants of silver were implemented in the model using data collected by Johnson and Christy.⁶¹ For array modeling, the nanoparticle was placed in a dielectric with Floquet boundary conditions relating to the square pattern. The array was illuminated from a port above the nanoparticle at varying incidence angles and polarizations, and a secondary port below collected the transmitted light, yielding transmittance spectra.

■ ASSOCIATED CONTENT

SI Supporting Information

The Supporting Information is available free of charge at <https://pubs.acs.org/doi/10.1021/acsp Photonics.0c01187>.

Eigenmode analysis of a Ag nanocube (Figure S1); FFT of a TAS trace (Figure S2); A table containing the fitting parameters (Table S1); Frequency domain analysis of a Ag nanocube's deformation (Figure S3); A comparison between two TAS spectra modeled with different deformation amplitudes (Figure S4); π -shifted phases of the Ag nanocube mechanical modes (Figure S5) (PDF)

■ AUTHOR INFORMATION

Corresponding Authors

Mindaugas Juodėnas – Institute of Materials Science, Kaunas University of Technology, Kaunas LT-51423, Lithuania; orcid.org/0000-0002-0517-8620; Email: mindaugas.juodenas@ktu.lt

Joel Henzie – International Center for Materials Nanoarchitectonics (WPI-MANA), National Institute for Materials Science (NIMS), Ibaraki 305-0044, Japan; JST-ERATO Yamauchi Materials Space-Tectonics Project, Saitama 332-0012, Japan; orcid.org/0000-0002-9190-2645; Email: joelhenzie@protonmail.ch

Authors

Domantas Peckus – Institute of Materials Science, Kaunas University of Technology, Kaunas LT-51423, Lithuania; orcid.org/0000-0002-4224-2521

Tomas Tamulevičius – Institute of Materials Science and Department of Physics, Kaunas University of Technology, Kaunas LT-51423, Lithuania; orcid.org/0000-0003-3879-2253

Yusuke Yamauchi – Australian Institute for Bioengineering and Nanotechnology (AIBN) and School of Chemical Engineering, The University of Queensland, Brisbane, Queensland 4072, Australia; JST-ERATO Yamauchi Materials Space-Tectonics Project, Saitama 332-0012, Japan; orcid.org/0000-0001-7854-927X

Sigitas Tamulevičius – Institute of Materials Science and Department of Physics, Kaunas University of Technology, Kaunas LT-51423, Lithuania; orcid.org/0000-0002-9965-2724

Complete contact information is available at: <https://pubs.acs.org/doi/10.1021/acsp Photonics.0c01187>

Author Contributions

The manuscript was written via the contributions of all authors. All authors have given approval to the final version.

Notes

The authors declare no competing financial interest.

■ ACKNOWLEDGMENTS

M.J., D.P., T.T., and S.T. acknowledge funding from the Research Council of Lithuania (LMTLT) (Agreement No. S-LLT-18-2) and the Ministry of Science and Technology of Taiwan. J.H. acknowledges the World Premier International Research Center Initiative on Materials Nanoarchitectonics (WPI-MANA) from MEXT, and the Japan Society for the Promotion of Science (JSPS) KAKENHI Program (Grant No. 20K05453).

■ REFERENCES

- (1) Mayer, K. M.; Hafner, J. H. Localized Surface Plasmon Resonance Sensors. *Chem. Rev.* **2011**, *111* (6), 3828–3857.
- (2) Anker, J. N.; Hall, W. P.; Lyandres, O.; Shah, N. C.; Zhao, J.; Van Duyne, R. P. Biosensing with Plasmonic Nanosensors. *Nat. Mater.* **2008**, *7* (6), 442–453.
- (3) Markel, V. A. Coupled-Dipole Approach to Scattering of Light from a One-Dimensional Periodic Dipole Structure. *J. Mod. Opt.* **1993**, *40* (11), 2281–2291.
- (4) Zou, S.; Janel, N.; Schatz, G. C. Silver Nanoparticle Array Structures That Produce Remarkably Narrow Plasmon Lineshapes. *J. Chem. Phys.* **2004**, *120* (23), 10871–10875.
- (5) Mulvaney, P. Surface Plasmon Spectroscopy of Nanosized Metal Particles. *Langmuir* **1996**, *12* (3), 788–800.
- (6) Kravets, V. G.; Kabashin, A. V.; Barnes, W. L.; Grigorenko, A. N. Plasmonic Surface Lattice Resonances: A Review of Properties and Applications. *Chem. Rev.* **2018**, *118* (12), 5912–5951.
- (7) Malynych, S.; Chumanov, G. Light-Induced Coherent Interactions between Silver Nanoparticles in Two-Dimensional Arrays. *J. Am. Chem. Soc.* **2003**, *125* (10), 2896–2898.
- (8) Auguie, B.; Barnes, W. L. Collective Resonances in Gold Nanoparticle Arrays. *Phys. Rev. Lett.* **2008**, *101* (14), 143902.
- (9) Hicks, E. M.; Zou, S.; Schatz, G. C.; Spears, K. G.; Van Duyne, R. P.; Gunnarsson, L.; Rindzevicius, T.; Kasemo, B.; Käll, M. Controlling Plasmon Line Shapes through Diffractive Coupling in Linear Arrays of Cylindrical Nanoparticles Fabricated by Electron Beam Lithography. *Nano Lett.* **2005**, *5* (6), 1065–1070.
- (10) Henzie, J.; Lee, M. H.; Odom, T. W. Multiscale Patterning of Plasmonic Metamaterials. *Nat. Nanotechnol.* **2007**, *2* (9), 549–554.
- (11) Kravets, V. G.; Schedin, F.; Grigorenko, A. N. Extremely Narrow Plasmon Resonances Based on Diffraction Coupling of Localized Plasmons in Arrays of Metallic Nanoparticles. *Phys. Rev. Lett.* **2008**, *101* (8), No. 087403.
- (12) Zhou, W.; Odom, T. W. Tunable Subradiant Lattice Plasmons by Out-of-Plane Dipolar Interactions. *Nat. Nanotechnol.* **2011**, *6* (7), 423–427.
- (13) Cherqui, C.; Bourgeois, M. R.; Wang, D.; Schatz, G. C. Plasmonic Surface Lattice Resonances: Theory and Computation. *Acc. Chem. Res.* **2019**, *52* (9), 2548–2558.
- (14) Wang, W.; Ramezani, M.; Väkeväinen, A. I.; Törmä, P.; Rivas, J. G.; Odom, T. W. The Rich Photonic World of Plasmonic Nanoparticle Arrays. *Mater. Today* **2018**, *21* (3), 303–314.
- (15) Goerlitzer, E. S. A.; Mohammadi, R.; Nechayev, S.; Volk, K.; Rey, M.; Banzer, P.; Karg, M.; Vogel, N. Chiral Surface Lattice Resonances. *Adv. Mater.* **2020**, *32*, 2001330.
- (16) Wang, D.; Bourgeois, M. R.; Guan, J.; Fumani, A. K.; Schatz, G. C.; Odom, T. W. Lasing from Finite Plasmonic Nanoparticle Lattices. *ACS Photonics* **2020**, *7* (3), 630–636.
- (17) Guan, J.; Sagar, L. K.; Li, R.; Wang, D.; Bappi, G.; Watkins, N. E.; Bourgeois, M. R.; Levina, L.; Fan, F.; Hoogland, S.; Voznyy, O.; Martins de Pina, J.; Schaller, R. D.; Schatz, G. C.; Sargent, E. H.; Odom, T. W. Engineering Directionality in Quantum Dot Shell Lasing Using Plasmonic Lattices. *Nano Lett.* **2020**, *20* (2), 1468–1474.
- (18) Liu, Y.; Teitelboim, A.; Fernandez-Bravo, A.; Yao, K.; Altoe, M. V. P.; Aloni, S.; Zhang, C.; Cohen, B. E.; Schuck, P. J.; Chan, E. M. Controlled Assembly of Upconverting Nanoparticles for Low-

Threshold Microlasers and Their Imaging in Scattering Media. *ACS Nano* **2020**, *14* (2), 1508–1519.

(19) Vaskin, A.; Kolkowski, R.; Koenderink, A. F.; Staudé, I. Light-Emitting Metasurfaces. *Nanophotonics* **2019**, *8* (7), 1151–1198.

(20) Hartland, G. V. Optical Studies of Dynamics in Noble Metal Nanostructures. *Chem. Rev.* **2011**, *111* (6), 3858–3887.

(21) Peckus, D.; Rong, H.; Stankevičius, L.; Juodėnas, M.; Tamulevičius, S.; Tamulevičius, T.; Henzie, J. Hot Electron Emission Can Lead to Damping of Optomechanical Modes in Core–Shell Ag@TiO₂ Nanocubes. *J. Phys. Chem. C* **2017**, *121* (43), 24159–24167.

(22) Link, S.; El-Sayed, M. A. Spectral Properties and Relaxation Dynamics of Surface Plasmon Electronic Oscillations in Gold and Silver Nanodots and Nanorods. *J. Phys. Chem. B* **1999**, *103* (40), 8410–8426.

(23) Voisin, C.; Del Fatti, N.; Christofilos, D.; Vallée, F. Ultrafast Electron Dynamics and Optical Nonlinearities in Metal Nanoparticles. *J. Phys. Chem. B* **2001**, *105* (12), 2264–2280.

(24) Besteiro, L. V.; Kong, X.-T.; Wang, Z.; Hartland, G.; Govorov, A. O. Understanding Hot-Electron Generation and Plasmon Relaxation in Metal Nanocrystals: Quantum and Classical Mechanisms. *ACS Photonics* **2017**, *4* (11), 2759–2781.

(25) Petrova, H.; Lin, C.-H. H.; De Liejer, S.; Hu, M.; McLellan, J. M.; Siekkinen, A. R.; Wiley, B. J.; Marquez, M.; Xia, Y.; Sader, J. E.; Hartland, G. V. Time-Resolved Spectroscopy of Silver Nanocubes: Observation and Assignment of Coherently Excited Vibrational Modes. *J. Chem. Phys.* **2007**, *126* (9), No. 094709.

(26) Hodak, J. H.; Martini, J.; Hartland, G. V. Spectroscopy and Dynamics of Nanometer-Sized Noble Metal Particles. *J. Phys. Chem. B* **1998**, *102* (36), 6958–6967.

(27) Ahmed, A.; Peltom, M.; Guest, J. R. Understanding How Acoustic Vibrations Modulate the Optical Response of Plasmonic Metal Nanoparticles. *ACS Nano* **2017**, *11* (9), 9360–9369.

(28) Staleva, H.; Hartland, G. V. Transient Absorption Studies of Single Silver Nanocubes. *J. Phys. Chem. C* **2008**, *112* (20), 7535–7539.

(29) Sun, Q.; Yu, H.; Ueno, K.; Kubo, A.; Matsuo, Y.; Misawa, H. Dissecting the Few-Femtosecond Dephasing Time of Dipole and Quadrupole Modes in Gold Nanoparticles Using Polarized Photoemission Electron Microscopy. *ACS Nano* **2016**, *10* (3), 3835–3842.

(30) Tretnak, V.; Hohenester, U.; Krenn, J. R.; Hohenau, A. The Role of Particle Size in the Dispersion Engineering of Plasmonic Arrays. *J. Phys. Chem. C* **2020**, *124* (3), 2104–2112.

(31) Robillard, J.-F.; Devos, A.; Roch-Jeune, I.; Mante, P. A. Collective Acoustic Modes in Various Two-Dimensional Crystals by Ultrafast Acoustics: Theory and Experiment. *Phys. Rev. B: Condens. Matter Mater. Phys.* **2008**, *78* (6), No. 064302.

(32) Eichenfield, M.; Chan, J.; Camacho, R. M.; Vahala, K. J.; Painter, O. Optomechanical Crystals. *Nature* **2009**, *462* (7269), 78–82.

(33) El-Jallal, S.; Mrabti, A.; Lévêque, G.; Akjouj, A.; Pennec, Y.; Djafari-Rouhani, B. Phonon Interaction with Coupled Photonic-Plasmonic Modes in a Phoxonic Cavity. *AIP Adv.* **2016**, *6* (12), 122001.

(34) Zhang, H.; Kinneer, C.; Mulvaney, P. Fabrication of Single-Nanocrystal Arrays. *Adv. Mater.* **2020**, *32* (18), 1904551.

(35) Lin, Q.-Y.; Li, Z.; Brown, K. A.; O'Brien, M. N.; Ross, M. B.; Zhou, Y.; Butun, S.; Chen, P.-C.; Schatz, G. C.; Dravid, V. P.; Aydin, K.; Mirkin, C. A. Strong Coupling between Plasmonic Gap Modes and Photonic Lattice Modes in DNA-Assembled Gold Nanocube Arrays. *Nano Lett.* **2015**, *15* (7), 4699–4703.

(36) Lin, Q.-Y.; Mason, J. A.; Li, Z.; Zhou, W.; O'Brien, M. N.; Brown, K. A.; Jones, M. R.; Butun, S.; Lee, B.; Dravid, V. P.; Aydin, K.; Mirkin, C. A. Building Superlattices from Individual Nanoparticles via Template-Confined DNA-Mediated Assembly. *Science (Washington, DC, U. S.)* **2018**, *359* (6376), 669–672.

(37) Ni, S.; Isa, L.; Wolf, H. Capillary Assembly as a Tool for the Heterogeneous Integration of Micro- and Nanoscale Objects. *Soft Matter* **2018**, *14* (16), 2978–2995.

(38) Tao, A.; Sinsersuksakul, P.; Yang, P. Polyhedral Silver Nanocrystals with Distinct Scattering Signatures. *Angew. Chem., Int. Ed.* **2006**, *45* (28), 4597–4601.

(39) Henzie, J.; Grünwald, M.; Widmer-Cooper, A.; Geissler, P. L.; Yang, P. Self-Assembly of Uniform Polyhedral Silver Nanocrystals into Densest Packings and Exotic Superlattices. *Nat. Mater.* **2012**, *11* (2), 131–137.

(40) Henzie, J.; Andrews, S. C.; Ling, X. Y. Y.; Li, Z.; Yang, P. Oriented Assembly of Polyhedral Plasmonic Nanoparticle Clusters. *Proc. Natl. Acad. Sci. U. S. A.* **2013**, *110* (17), 6640–6645.

(41) Virganičiūsis, D.; Juodėnas, M.; Tamulevičius, T.; Schift, H.; Tamulevičius, S. Investigation of Transient Dynamics of Capillary Assisted Particle Assembly Yield. *Appl. Surf. Sci.* **2017**, *406* (11), 136–143.

(42) Juodėnas, M.; Tamulevičius, T.; Henzie, J.; Erts, D.; Tamulevičius, S. Surface Lattice Resonances in Self-Assembled Arrays of Monodisperse Ag Cuboctahedra. *ACS Nano* **2019**, *13* (8), 9038–9047.

(43) Fuchs, R. Theory of the Optical Properties of Ionic Crystal Cubes. *Phys. Rev. B* **1975**, *11* (4), 1732–1740.

(44) Zhang, S.; Bao, K.; Halas, N. J.; Xu, H.; Nordlander, P. Substrate-Induced Fano Resonances of a Plasmonic Nanocube: A Route to Increased-Sensitivity Localized Surface Plasmon Resonance Sensors Revealed. *Nano Lett.* **2011**, *11* (4), 1657–1663.

(45) Sherry, L. J.; Chang, S.-H.; Schatz, G. C.; Van Duyne, R. P.; Wiley, B. J.; Xia, Y. Localized Surface Plasmon Resonance Spectroscopy of Single Silver Nanocubes. *Nano Lett.* **2005**, *5* (10), 2034–2038.

(46) Huttunen, M. J.; Dolgaleva, K.; Törmä, P.; Boyd, R. W. Ultra-Strong Polarization Dependence of Surface Lattice Resonances with out-of-Plane Plasmon Oscillations. *Opt. Express* **2016**, *24* (25), 28279.

(47) Li, G. H. Y.; Li, G. Necessary Conditions for Out-of-Plane Lattice Plasmons in Nanoparticle Arrays. *J. Opt. Soc. Am. B* **2019**, *36* (4), 805.

(48) Zhou, W.; Hua, Y.; Huntington, M. D.; Odom, T. W. Delocalized Lattice Plasmon Resonances Show Dispersive Quality Factors. *J. Phys. Chem. Lett.* **2012**, *3* (10), 1381–1385.

(49) Yang, X.; Xiao, G.; Lu, Y.; Li, G. Narrow Plasmonic Surface Lattice Resonances with Preference to Asymmetric Dielectric Environment. *Opt. Express* **2019**, *27* (18), 25384.

(50) Hua, Y.; Fumani, A. K.; Odom, T. W. Tunable Lattice Plasmon Resonances in 1D Nanogratings. *ACS Photonics* **2019**, *6* (2), 322–326.

(51) McMahon, J. M.; Wang, Y.; Sherry, L. J.; Van Duyne, R. P.; Marks, L. D.; Gray, S. K.; Schatz, G. C. Correlating the Structure, Optical Spectra, and Electrodynamics of Single Silver Nanocubes. *J. Phys. Chem. C* **2009**, *113* (7), 2731–2735.

(52) Yi, C.; Dongare, P. D.; Su, M.-N.; Wang, W.; Chakraborty, D.; Wen, F.; Chang, W.-S.; Sader, J. E.; Nordlander, P.; Halas, N. J.; Link, S. Vibrational Coupling in Plasmonic Molecules. *Proc. Natl. Acad. Sci. U. S. A.* **2017**, *114* (44), 11621–11626.

(53) Guo, P.; Schaller, R. D.; Ocola, L. E.; Ketterson, J. B.; Chang, R. P. H. Gigahertz Acoustic Vibrations of Elastically Anisotropic Indium–Tin-Oxide Nanorod Arrays. *Nano Lett.* **2016**, *16* (9), 5639–5646.

(54) Huang, W.; Qian, W.; El-Sayed, M. A. Coherent Vibrational Oscillation in Gold Prismatic Monolayer Periodic Nanoparticle Arrays. *Nano Lett.* **2004**, *4* (9), 1741–1747.

(55) Wang, L.; Nishijima, Y.; Ueno, K.; Misawa, H.; Tamai, N. Near-IR Vibrational Dynamics of Periodic Gold Single and Pair Nanocuboids. *Appl. Phys. Lett.* **2009**, *95* (5), No. 053116.

(56) Devkota, T.; Chakraborty, D.; Yu, K.; Beane, G.; Sader, J. E.; Hartland, G. V. On the Measurement of Relaxation Times of Acoustic Vibrations in Metal Nanowires. *Phys. Chem. Chem. Phys.* **2018**, *20* (26), 17687–17693.

(57) Rycenga, M.; Langille, M. R.; Personick, M. L.; Ozel, T.; Mirkin, C. A. Chemically Isolating Hot Spots on Concave Nanocubes. *Nano Lett.* **2012**, *12* (12), 6218–6222.

(58) Pellarin, M.; Ramade, J.; Rye, J. M.; Bonnet, C.; Broyer, M.; Lebeault, M.-A.; Lermé, J.; Marguet, S.; Navarro, J. R. G.; Cottancin, E. Fano Transparency in Rounded Nanocube Dimers Induced by Gap Plasmon Coupling. *ACS Nano* **2016**, *10* (12), 11266–11279.

(59) Wang, W.; Watkins, N.; Yang, A.; Schaller, R. D.; Schatz, G. C.; Odom, T. W. Ultrafast Dynamics of Lattice Plasmon Lasers. *J. Phys. Chem. Lett.* **2019**, *10* (12), 3301–3306.

(60) Tamulevičius, T.; Gražulevičiūtė, I.; Urbonas, D.; Gabalis, M.; Petruškevičius, R.; Tamulevičius, S. Numerical and Experimental Analysis of Optical Response of Sub-Wavelength Period Structure in Carbonaceous Film for Refractive Index Sensing. *Opt. Express* **2014**, *22* (22), 27462.

(61) Johnson, P. B.; Christy, R. W. Optical Constants of the Noble Metals. *Phys. Rev. B* **1972**, *6* (12), 4370–4379.

SL344. 2021-01-12, 16,25 leidyb. apsk. l. Tiražas 12 egz. Užsakymas 3.
Išleido Kauno technologijos universitetas, K. Donelaičio g. 73, 44249 Kaunas
Spausdino leidyklos „Technologija“ spaustuvė, Studentų g. 54, 51424 Kaunas

